ALMA MATER STUDIORUM
UNIVERSITÀ DI BOLOGNA

DOTTORATO DI RICERCA IN

ASTROFISICA

CICLO XXXVII

Settore Concorsuale: 02/C1 – Astronomia, Astrofisica, Fisica della Terra e dei Pianeti

Settore Scientifico Disciplinare: FIS/05 – Astronomia e Astrofisica

Studying gas circulation in star-forming galaxies in simulations with explicit ISM and feedback models

Presentata da:
Filippo Barbani

Coordinatore dottorato:
Chiar.mo Prof.
Andrea Miglio

Supervisore:
Chiar.mo Prof.
Federico Marinacci

Co-supervisore:
Dr. Raffaele Pascale

Esame Finale Anno 2025

Ai miei nonni

"He felt all at once like an ineffectual moth,
fluttering at the windowpane of reality,
dimly seeing it from outside."

— Philip K. Dick, Ubik

Contents

Abstract

This Thesis presents a comprehensive study of the baryon cycle in star-forming galaxies, with a particular focus on gas circulation between the galactic disc and the circumgalactic medium (CGM) and its role in sustaining star formation. To explore the complex interactions between these galactic components, I use cutting-edge hydrodynamical N-body simulations of Milky Way-like galaxies, incorporating a CGM around the disc. These simulations are performed with the moving-mesh code Arepo coupled with the *SMUGGLE* model, which includes essential stellar feedback processes, enabling the realistic simulation of the interstellar medium and the generation of multiphase outflows. In the first part of this Thesis, I analyze the role of the CGM as a reservoir for star formation, finding that stellar feedback effectively acts as a positive feedback mechanism, generating galactic fountains that recycles gas between the disc and the corona. This circulation enhances gas cooling and accretion from the CGM, fueling the star formation in the disc at a sustained rate of $\approx 3\ \mathrm{M}_\odot\ \mathrm{yr}^{-1}$. In the second part, I go through the vertical and radial gas flows that transport CGM gas to the galactic disc and from the outer disc to the central regions, respectively. These processes support continuous star formation, with coronal gas preferentially accreting at larger radii before being funneled inward. Finally, using hybrid-cosmological simulations, I examine galactic outflows as a multiphase phenomenon, revealing distinct cold, warm, and hot gas phases, each with unique roles in mass and energy transport. The cold phase primarily transports mass, while the hot phase dominates in energy and momentum, reaching greater distances from the disc. This Thesis will provide deeper insights into the evolution of star-forming galaxies, contributing to a more comprehensive understanding of galaxy formation and evolution.

Chapter 1

Introduction

The Λ Cold Dark Matter (ΛCDM) model is the most widely accepted cosmological framework describing the formation and evolution of the Universe. According to the ΛCDM scenario (Planck Collaboration et al., 2020), the total mass-energy budget of the Universe consists of three main components: dark energy ($\approx 70\%$), matter ($\approx 30\%$), and radiation, which has a negligible contribution at redshift zero. The matter component is further divided into cold dark matter, which constitutes $\approx 85\%$ of the total matter content, and baryonic matter, which makes up the remaining $\approx 15\%$. Cold dark matter plays a crucial role in the hierarchical structure formation of the Universe. Due to its weak interaction with radiation and other forces beyond gravity, CDM can begin collapsing under its own gravity at very small mass scales ($\approx 10^4 - 10^5$ $M_\odot$). Over cosmic time, these small overdensities grow through gravitational instability, forming larger structures through successive mergers. As a result, the evolution of cosmic structures follows a bottom-up process (White & Rees, 1978), where small-scale dark matter halos form first and later assemble into more massive systems through mergers and accretion. These dark matter halos provide the gravitational potential wells in which baryons can cool and condense, leading to the formation of the first stars and stellar systems. Even though this bottom-up assembly scenario appears relatively simple, it results in the formation of an heterogeneous variety of large-scale structures and galaxies with different chemo-dynamical properties.

One of the first systematic classifications of galaxies was introduced by Hubble (1926), whose empirical Hubble sequence remains widely used today. This classification organizes

galaxies based on their morphological and dynamical properties into a bifurcated diagram, commonly known as the Hubble tuning fork (Figure 1.1).

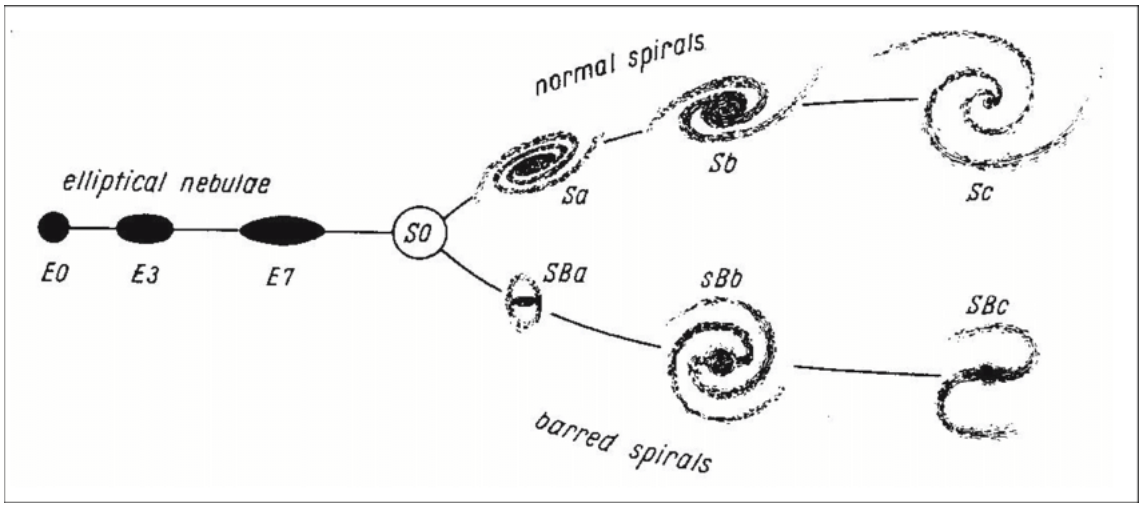

Figure 1.1: Schematic representation of the Hubble tuning fork. From left to right we see elliptical galaxies (E), lenticular galaxy (S0), spiral galaxies (S or SB). Figure taken from Hubble (1936).

In general, galaxies can be divided into two broad categories based on their morphology and star formation activity:

- **Early-type galaxies**: These include elliptical and lenticular galaxies, which are predominantly composed of old stellar populations and exhibit little to no ongoing star formation.

- **Late-type galaxies**: These include spiral and irregular galaxies, which are actively forming stars and contain significant reservoirs of cold gas.

Elliptical galaxies are among the most massive galaxies in the Universe ($\sim 10^{10} - 10^{13}$ $M_\odot$), with the most massive examples found at the centers of galaxy clusters (Cimatti et al., 2019). These galaxies are characterized by red, old stellar populations (age $\gg 1$ Gyr; De Jong & Davies 1997) and a lack of significant star formation, leading to their classification as quiescent or passive galaxies. Their interstellar medium is dominated by hot, X-ray emitting gas ($T \sim 10^7$ K) with high metallicity ($Z > 0.5\ Z_\odot$), but some cases exhibit residual cold gas,

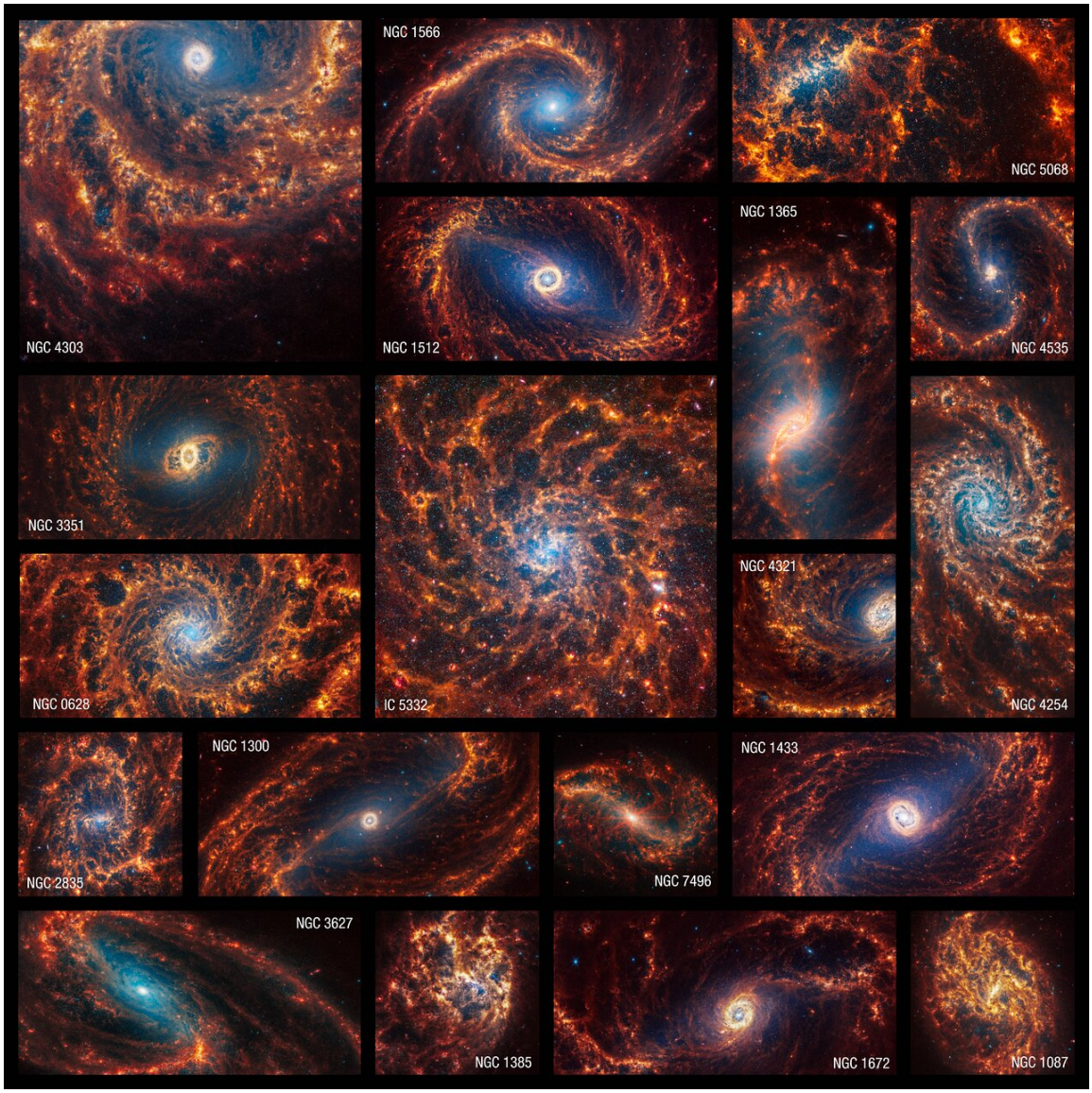

Figure 1.2: A collection of 19 face-on spiral galaxies observed in near- and mid-infrared light as part of the PHANGS-JWST survey (e.g., Lee et al., 2023). These images reveal millions of stars and intricate gas and dust structures. Notably, the galaxy discs exhibit large cavities in the gas, shaped by stellar feedback over time.

dust, and weak star formation, likely due to interactions with gas-rich galaxies (e.g., Morganti et al., 2006). Lenticular (S0) galaxies share structural similarities with both ellipticals and spirals. They contain a prominent disc but lack significant star formation and gas reservoirs. They are often considered quenched spiral galaxies, having exhausted or lost their cold gas through processes such as ram-pressure stripping and harassment in dense environments (e.g., Spitzer Jr & Baade, 1951).

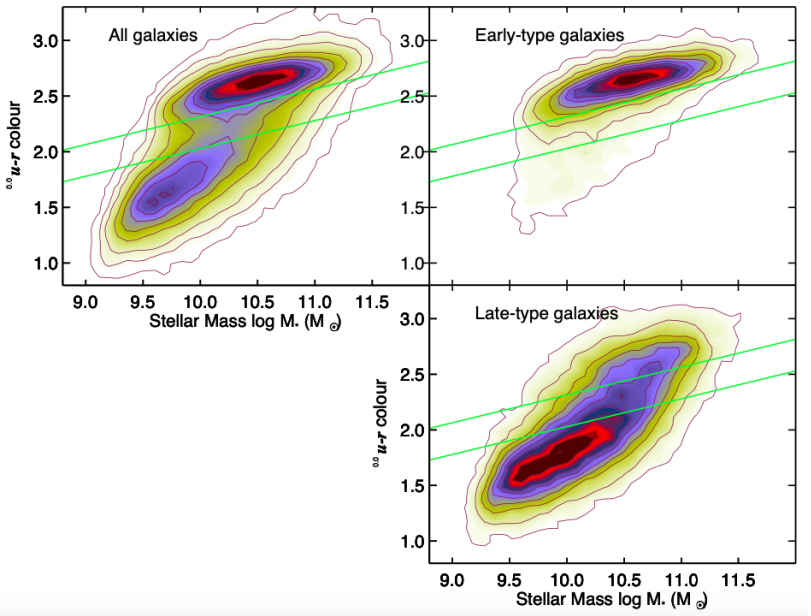

Figure 1.3: $u-r$ color as a function of stellar mass diagram from the Sloan Digital Sky Survey. The left panel shows all galaxies, the top right panel isolates early-type galaxies, and the bottom right panel isolates late-type galaxies. Early-type galaxies predominantly occupy the red sequence, while late-type galaxies reside in the blue cloud. Figure adapted from Schawinski et al. (2014).

Spiral galaxies, in contrast, are gas-rich systems with an ongoing, non-negligible level of star formation. Their interstellar medium is a complex, multi-phase environment, where cold, warm, and hot gas coexist, fueling continuous star formation. Their structure typically includes a stellar disc, a bulge, and in some cases, a central bar that redistributes angular momentum within the galaxy. Irregular galaxies are typically low-mass systems that lack well-defined structures like discs or bulges. They often exhibit turbulent star formation and can be shaped by interactions with larger galaxies, internal feedback processes, or external

environmental effects. Figure 1.2 shows 19 different spiral galaxies observed with the James Webb Space Telescope, highlighting how stellar feedback can strongly influence the structure of the discs.

With the advent of large-scale galaxy surveys, such as the Sloan Digital Sky Survey (York et al., 2000; Privatus & Goswami, 2025), a fundamental bimodality in galaxy colors has been observed (e.g., Baldry et al., 2006). This bimodality, seen in color-stellar mass diagrams, reveals the presence of two main populations of galaxies: the red sequence and the blue cloud. The former is a tight correlation where more massive galaxies exhibit redder colors, dominated by old stellar populations, whereas the latter is a broader distribution of star-forming galaxies with blue colors, indicating ongoing star formation. As shown in Figure 1.3, early-type galaxies reside almost exclusively in the red sequence, reflecting their passive evolution due to the absence of ongoing star formation. In contrast, late-type galaxies are found in the blue cloud, maintaining their blue colors due to continuous star formation. The evolutionary connection between these populations suggests that galaxies tend to transition from the blue cloud to the red sequence, but rarely in the opposite direction (Peng et al., 2010). This transition, driven by mechanisms such as gas exhaustion, feedback, and environmental effects, is a key and still not fully understood aspect of galaxy evolution.

Galaxies are not isolated systems, but they interact with the external environment through their whole life. Apart from environmental effects in galaxy clusters such as mergers (Conselice et al., 2022) and ram pressure stripping (Roediger & Hensler, 2005; Ebeling & Kalita, 2019; Boselli et al., 2022), interactions of galaxies with gas are one of the key drivers of galaxy evolution. In particular, a galaxy can either eject material from its disc thanks to feedback processes or accrete material from the environment. When both mechanisms occur simultaneously, they create a circulation of gas. In this Thesis I will focus on the interaction that star-forming galaxies can have with the surrounding gas and on the consequences of such an interaction for the evolution of these objects.

Gas circulation refers to the dynamics of gas within and around star-forming galaxies and includes all the physical processes for which the gas moves from the disc to the intergalactic or circumgalactic space and vice versa. This circulation forms the so-called **baryon cycle** and has a crucial role in galaxy evolution. Figure 1.4 depicts a cartoon scheme of the different processes involved in the circulation of gas of star-forming galaxies. In particular, gas can be

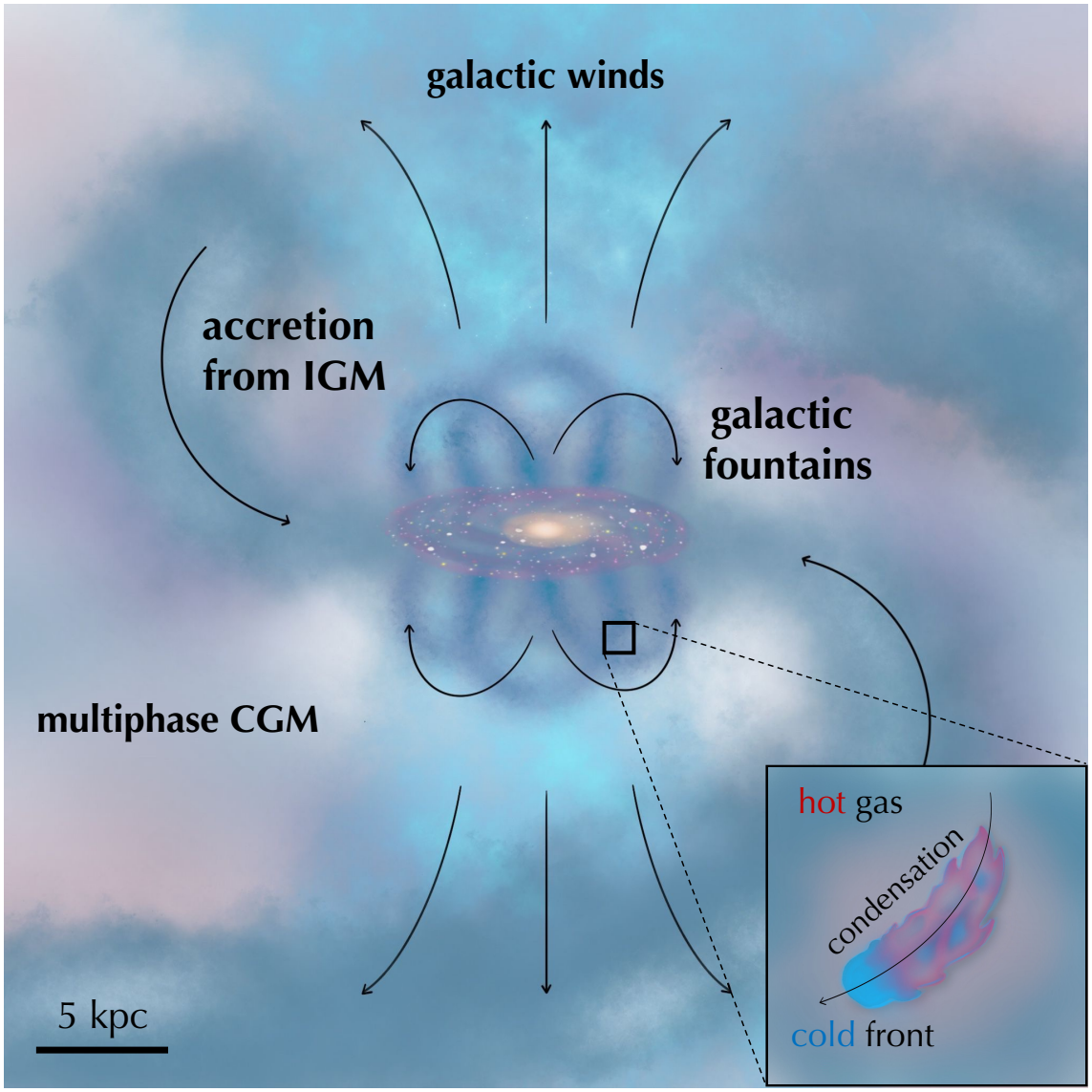

Figure 1.4: Cartoon scheme depicting the main processes involved in the baryon cycle of star-forming galaxies. On the smaller scales, close to the galactic disc, outflows not strong enough to travel far from the galactic disc generate cold gas clouds that form the **galactic fountains**. When there is a burst in star formation, outflows can reach velocities higher than the escape velocity and reach a distance of hundreds of kpc from the disc, forming **galactic winds** that bring metals outside the galaxy. Gas can be accreted directly from the **IGM** or from the **CGM**, in the latter case the cooling can be enhanced by the presence of the cold galactic fountains. In the bottom right panel I show a zoom of a single galactic fountain cloud, this cold gas, travelling through the CGM can mix with it, generating a warm phase that helps the cooling of the circumgalactic gas. Arrows indicates the direction of the gas flows. Figure taken from Barbani et al., in preparation.

accreted onto the disc both from the **intergalactic medium** (IGM; see McQuinn 2016 for a review) and from the **circumgalactic medium** (CGM; see Tumlinson et al. 2017 for a review). Stars form from the collapse of high-density and low-temperature gas clouds in the galactic disc. During their evolution they inject energy and momentum into the interstellar medium (ISM), a process known as **stellar feedback**, eventually pushing the gas outside the galactic disc and generating outflows. Within the disc, stellar feedback acts mainly as negative feedback which heats the gas in the ISM and disrupts the cold dense clumps, thereby stopping or slowing down the formation of new stars. Moreover, strong outflows can decrease the rate of gas accretion into the disc, which is needed to keep forming new stars over time. The consequence of this is the formation of a self-regulated cycle in which inflow-dominated phases are followed by burst in the star formation rate (SFR) and therefore by outflow-dominated phases, driving a gas circulation. These outflows can form **galactic winds** if their velocity is higher than the escape velocity of the system or **galactic fountains**, which are one of the main focus of this Thesis work. The ejected gas is bound to interact with the material in the CGM and this interaction modifies the thermodynamic state of the CGM gas, its dynamics, and its chemical composition. A fraction of the ejected gas eventually makes its way back to the disc, thus becoming the material from which new stars are born. The interaction between galactic fountains and the CGM can create a mixture of warm gas which decreases the cooling time of the circumgalactic gas. I will investigate this phenomenon and its broad implications for galaxy evolution in the next Chapters.

1.1 Circumgalactic medium

Before delving into the processes involved in the baryon cycle of star-forming galaxies, I briefly describe the properties of the medium that surrounds the galactic disc. The CGM is confirmed to be a multiphase medium by observations (e.g. Tumlinson et al., 2011; Putman et al., 2012; Anderson et al., 2016; Prochaska et al., 2017), containing cold ($T \lesssim 10^4$ K), warm ($10^4 \lesssim T \lesssim 10^6$ K) and hot ($T \gtrsim 10^6$ K) gas, with a complex distribution of metallicities and densities and is also a prediction of theoretical models (e.g., White & Rees 1978; Fukugita & Peebles 2006). Furthermore, this component of the galactic ecosystem contains a significant fraction of the baryons associated to Milky Way-like galaxies (up to 50%, see Werk et al. 2014;

Bregman et al. 2018). This makes the CGM the primary reservoir from which star-forming galaxies can get the fresh gas they need to sustain star formation. This medium is fundamental for the evolution of star-forming galaxies owing to its mutual interplay with the galactic disc, that is mediated by outflows and inflows.

The CGM can be observed through several methods (Tumlinson et al., 2017). For the warm and cold phases of the CGM one common approach is using absorption line studies, where the cold CGM is detected in absorption against the spectrum of a bright background source, such as a quasar (Yao et al., 2012; Gupta et al., 2012; Miller & Bregman, 2013; Troitsky, 2017; Kaaret et al., 2020). This technique offers advantages like the ability to detect very low column densities and probe a wide range of gas densities. However, a limitation is that each observation typically samples only a single line of sight per galaxy due to the scarcity of background quasars, requiring a large sample of galaxies to construct a radial profile of the CGM properties (Lehner et al., 2015; Bowen et al., 2016). This method has been extensively used both in the local Universe and at high redshift (Rauch & Haehnelt, 2011; Rubin et al., 2015). Another technique involves stacking analysis (Bordoloi et al., 2011; Peek et al., 2015), where multiple spectra are combined to detect weak absorption features. Although this approach enhances signal detection, it averages out individual absorber profiles, limiting detailed characterization of each absorber.

Despite its presence in the CGM has been confirmed by absorption line observations, the origin of the cold gas is still unclear. Although gas can cool through the spontaneous growth of thermal instabilities, this scenario has been ruled out by linear perturbation analysis (see, e.g., Binney et al., 2009; Nipoti, 2010) but could be still relevant in case of a substantial rotation of the gas in the inner regions of the CGM (Sormani & Sobacchi, 2019). Another key mechanism for the formation of cold gas could be the interaction between the cold outflows from the galactic disc and the CGM, which will be discussed in this Chapter. The cold CGM mass in the Milky Way has been estimated as $\lesssim 10^9$ $M_\odot$ including the contribute from the Magellanic stream ($\approx 3\times10^8$ $M_\odot$), which is accounting for a small fraction of the total CGM mass ($\approx 10^{10}-10^{11}$ $M_\odot$). Cold gas mass has also been measured in L^* galaxies using stacked optical spectra, finding again similar values as in the Milky Way.

Alternatively, the hot phase of the CGM (the so-called galactic corona) can be observed in emission from the gas itself. As the emissivity scales with the square of the gas number

density ($\propto n^2$), a direct detection is challenging due to the extremely low values of density involved ($n \sim 10^{-3} - 10^{-4}$ cm^{-3}). Furthermore, these hot gaseous haloes have a temperature higher than 0.1 keV (i.e. around the virial temperature of the halo), thus, the hot gas is expected to thermally emit X-ray photons through bremsstrahlung emission. In recent times many observations have been attempted to find and study the properties of these hot haloes around spiral galaxies (e.g. Li et al., 2008; Rasmussen et al., 2009; Li et al., 2011; Bogdán et al., 2015), but, due to their temperature range and the low-densities, a large fraction of the thermal emission falls under the Galactic absorption threshold (0.2-0.3 keV) making this component very faint and highly contaminated by the X-ray background. Nevertheless, this direct detection method has successfully detected hot CGM emission in some external galaxies (Anderson et al., 2016). For instance, around four massive (with total masses $\sim 10^{13}$ M$_\odot$) spiral galaxies (NGC 1961, UGC 12591, NGC 266, and NGC 6753) using Chandra, XMM-Newton, and ROSAT. In NGC 1961, Anderson & Bregman (2011) estimated a total hot gas mass of $1 - 3 \times 10^{11}$ M$_\odot$, assuming a metallicity of 0.5 Z$_\odot$, though precise metallicity measurements are crucial for accurate mass estimates. In UGC 12591, Dai et al. (2012) detected X-ray emission out to 80 kpc, placing an upper limit on the corona mass of 4.5×10^{11} M$_\odot$ and estimating a temperature of around 7.42×10^6 K. Similarly, Bogdán et al. (2013) found the hot gas mass in NGC 266 to be comparable to that in NGC 1961 and UGC 12591, suggesting that these massive spiral galaxies, with similar virial masses, exhibit comparable corona properties.

Studying the interaction between star-forming galaxies and their coronae is one of the goals of this Thesis. Due to their nature galactic coronae in elliptical and spiral galaxies exhibit distinctly different physical properties. In early-type galaxies, the coronae have metallicities close to solar (Ji et al., 2009), indicating significant enrichment from material ejected by evolved stars through stellar feedback (Ciotti & Ostriker, 1997). These galaxies typically lack significant cold gas and have little or no star formation, suggesting inefficient cooling of their coronae. Although cooling may occur in the galaxy core, where densities are the highest, the cold gas is rapidly accreted by the central supermassive black hole, triggering AGN feedback that reheats the corona (Liu et al., 2024). In contrast, spiral galaxies present a different structure, with coronae characterized by lower metallicities and longer cooling times on the order of a few Gyrs near the disc (Hodges-Kluck & Bregman, 2013). In these galaxies, an effi-

cient cooling mechanism seems to be in place, allowing the corona to cool and accrete onto the galactic disc. This cooling process appears to be effective only in spiral galaxies, where a cold gaseous disc is present, but not in early-type galaxies, where such a mechanism fails to operate efficiently. Yet, the mechanism that enables the cooling of the corona remains poorly understood. This Thesis will examine this phenomenon in detail, providing a comprehensive analysis of gas circulation in Milky Way-like galaxies.

1.2 Gaseous inflows

Galaxies like the Milky Way have formed stars at an almost constant rate for about their entire life (Twarog, 1980; Cignoni et al., 2006; Bernard, 2017; Alzate et al., 2021). Figure 1.5 (left panel) depicts the star formation history in the Milky Way obtained from [Si/Fe] abundance measurements (Haywood, 2014), which is a key indicator of the SFR in galaxies because it reflects the contributions of different types of supernovae to chemical enrichment over time[1]. These observations show how at $z < 1$ the SFR has remained approximately constant in a range between $1 - 5$ $M_\odot$ yr^{-1}. However, the mass of gas located in the discs of Milky Way-like galaxies is not sufficient to sustain their current SFR (i.e. $\approx 1.65 \pm 0.19$ $M_\odot$ yr^{-1} in the Milky Way, Licquia & Newman 2015) for more than a few Gyr. Given the fact that the gas depletion time in Milky Way-like galaxies is $\approx 1 - 2$ Gyr (Saintonge et al., 2013; Tacconi et al., 2018), keeping a constant SFR would not be possible without a substantial accretion of gas onto the star-forming disc over time. Therefore, inflows of gas are necessary to prevent the quenching of star formation (e.g. Fraternali, 2014). The necessity of gas accretion is also required by galactic chemical evolution models (e.g. Spitoni et al., 2021): an example is the so-called G-dwarf problem (van den Bergh, 1962; Alibés et al., 2001), that is a deficit of metal-poor stars in the solar neighbourhood. This suggests the presence of an evolution for star-forming galaxies very different from total isolation. The preferred solution to this problem is to require a continuous accretion of low-metallicity gas (~ 0.1 $Z_\odot$, Larson 1972; Tosi 1988; Matteucci & Francois 1989; Colavitti et al. 2008) that fuels star formation (Chiappini et al.,

[1] α elements (such as oxygen, neon, and silicon) are predominantly produced by Type II supernovae, which rapidly enrich the interstellar medium following star formation. In contrast, iron is mainly produced by Type Ia supernovae, which take a longer time to spread this element to the interstellar medium owing to the longer lifetime of the progenitors.

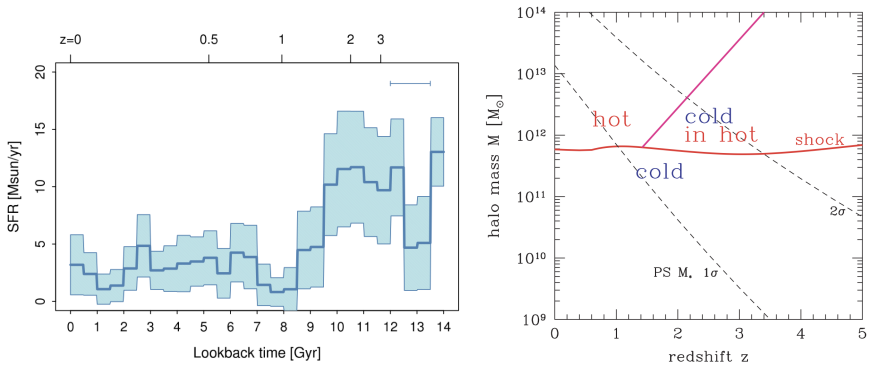

Figure 1.5: *Left*: Star formation history for the Milky Way, obtained from [Si/Fe] abundance measurements, indicating that the SFR has remained nearly constant for the past $\approx$ 10 Gyr. Figure taken from Haywood (2014). *Right*: critical halo mass as a function of redshift, showing the halo mass at which accretion mode transition from cold to hot. This threshold is set by the balance between gravitational potential and radiative cooling, determining whether inflowing gas is shock-heated or able to condense efficiently. Figure taken from Dekel & Birnboim (2006).

2001), this process can self-regulate, producing a gas close to solar metallicity. Therefore what seems to be a deficit of metal-poor G-dwarf stars would be in reality an excess of solar metallicity G-dwarf stars. Thus, accretion of gas from surrounding environment is crucial to understand the formation and evolution of the Milky Way and galaxies in general.

Numerical simulations suggest that gas accretion occurs primarily in two main modes: cold and hot accretion. In the cold accretion mode (Rees & Ostriker, 1977; Silk, 1977), that is typically dominant at high redshift ($z \gtrsim 2$), cold filaments from the intergalactic medium can survive their journey through the galaxy halo and deliver cold gas directly into the star-forming disc. On the other hand, in the hot accretion mode (Dekel & Birnboim, 2006; Kereš et al., 2009; Nelson et al., 2013; Stern et al., 2020) the gas that is falling into the dark matter potential well is shock-heated to the virial temperature, forming a halo of hot gas that subsequently must cool before being accreted onto the galaxy. This mode is generally prevailing at lower redshifts ($z \lesssim 2$) for galaxies like the Milky Way.

The right panel of Figure 1.5 shows the different accretion regimes as a function of the halo mass M_h and of the redshift z. In practice, the panel reveals the existence of a critical

halo mass ($M_{cr} \sim 10^{12}$ $M_{\odot}$), below which halos cannot efficiently shock-heat infalling gas, this allows cold gas to penetrate and accrete directly onto the galactic disc. However, halos with $M_h > M_{cr}$ are effective at shock-heating gas, and for redshifts $z < 2$, the hot accretion mode becomes dominant. At $z > 2$, while gas is still heated to the virial temperature, it primarily accretes through dense gas filaments from the intergalactic medium, which remain intact and can reach the galaxy without being disrupted (Ocvirk et al., 2008). Thus, galaxies shift their dominant mode of gas accretion over time. At high redshift, star-forming galaxies with masses $M_h < M_{cr}$ primarily accrete gas via the cold mode. As these galaxies grow in mass, many eventually surpass the critical halo mass, switching to hot mode accretion at the virial temperature and forming a gas reservoir, which constitutes the hot phase of the CGM, around the galaxy. For a Milky Way-like galaxy ($M_h \sim 10^{12}$ $M_{\odot}$), this transition typically occurs around $z \sim 1 - 2$ (Kereš et al., 2009), with the hot gaseous halo forming at that time. In contrast, more massive galaxies tend to develop their hot coronae at earlier epochs. This hot gaseous halo is a large reservoir of gas that could be accreted into the galaxy to feed star formation over time.

Gas accretion does not occur uniformly across the entire disc but is expected to happen predominantly in the outer regions due to angular momentum conservation and to a larger cross-section of the external disc regions. The majority of star formation is located in the central regions, where gas density is highest, therefore a mechanism that moves the accreted gas from the outskirts to the center of the galaxy is needed to keep forming new stars. Lacey & Fall (1985) proposed three mechanisms that could generate these radial flows: if the specific angular momentum of the infalling gas is lower than the one of the gas in the disc a radial flow towards the center is expected. Other mechanisms proposed by Lacey & Fall (1985) are the presence of viscosity in the gas layer and gravitational interaction between the gas in the disc and spiral arms and bars. The HI 21 cm emission line is the best way to investigate these radial motions in the outskirts of spiral galaxies, but it is still unclear if the radial inflows are sufficient to bring enough gas to the center to sustain the star formation (Wong et al., 2004; Schmidt et al., 2016; Di Teodoro & Peek, 2021). Finally, these radial flows are necessary also to reproduce the metallicity gradients (e.g. Mott et al., 2013) and the exponential density profiles (e.g. Wang et al., 2014) observed in spiral galaxies.

1.3 Gaseous outflows

Young massive stars eject energy and momentum in the ISM during their life. This usually happens through stellar winds (Owocki, 2013; Rickard et al., 2022), radiative feedback (Murray et al., 2010; Walch et al., 2012) and supernovae (SNe) explosions (Woosley & Weaver, 1986; Burrows & Vartanyan, 2021; Liu et al., 2023). SNe are considered to be the dominant feedback phenomenon, but radiative feedback and stellar winds, generally called early stellar feedback (Stinson et al., 2013), also have a very important role, heating and pre-processing the medium that surrounds stars, that will be swept more easily when the SNe occur thanks to the reduced density of the ISM. Young stars are usually embedded in cold dense gas and when they explode as core-collapse (type II) SNe they sweep away the cold gas creating a bubble of low density hot gas. Eventually the generated cavity can reach the edge of the disc and can breakout releasing cold, warm and cold gas into the CGM and generating gaseous outflows. A big number of SNe exploding in a short period of time is capable of accelerating the gas and ejecting it at a velocity greater than the escape velocity v_{esc} of the galaxy, generating the so-called galactic winds. These, can bring the multi-phase metal-rich gas from the dense galactic disc to distances farther than the virial radius, eventually escaping the galaxy gravitational potential. These winds can be observed through Doppler shift of absorption lines in galaxies spectra (e.g. Rubin et al., 2010; Burchett et al., 2021). Gas outflows can also have velocities smaller than v_{esc}, in which case the gas can not travel far from the disc and will fall back again into it in another location, enriching the ISM with a fraction of pristine low-metallicity gas, forming the so-called galactic fountains. The multiphase nature of outflows has been confirmed by observations, showing cold molecular outflows (Bolatto et al., 2013; Leroy et al., 2015; Martini et al., 2018; Bolatto et al., 2021), warm outflows (Chisholm et al., 2015; Heckman et al., 2015; Weldon et al., 2024) and hot outflows (Lehnert et al., 1999; Strickland & Heckman, 2007; Lopez et al., 2020).

Detecting cool, warm and hot outflows in external galaxies is very challenging (see Veilleux et al. 2020 for a review). Observations in the Milky Way identify outflows of different phases (see Figure 1.6 for examples of outflows observations towards the center of the galactic disc in the Milky Way). High energy emission in the direction of the galactic center is generated by the so-called Fermi bubbles (GRAVITY Collaboration et al., 2019), which have been

detected as γ-ray emitting bubbles in the energy range 1-100 GeV (Dobler et al., 2010; Ackermann et al., 2014). The power that is needed to generate the Fermi bubbles is $10^{42} - 10^{44}$ erg s^{-1}, which is possible only through feedback from a supermassive black hole rather than a starburst event (Ruszkowski et al., 2014; Bland-Hawthorn et al., 2019). Other emissions found looking towards the galactic center are radio (Sofue & Handa, 1984; Anderson et al., 2024) and X-ray (Bland-Hawthorn & Cohen, 2003) emitting shells indicating the presence of a large bipolar warm-hot outflow. The thermal energy of this structure is consistent with being generated from stellar feedback coming from the central star cluster (Ponti et al., 2019). Bland-Hawthorn & Cohen (2003) have also shown the presence of cool dust emission outflows extending 140 pc over and under the galactic plane. A population of $\sim$ 200 HI high velocity clouds have been detected within 1.5 kpc from the galactic midplane (McClure-Griffiths et al., 2013; Di Teodoro et al., 2018; Lockman et al., 2020), which are consistent with a biconical outflow with a radial velocity of $\approx$ 300 km s^{-1} and a constant neutral outflow rate of 0.1 $M_\odot$ yr^{-1} (Di Teodoro et al., 2018). Given the properties of these HI clouds the energetics of this outflow is consistent with a past starburst event rather than AGN.

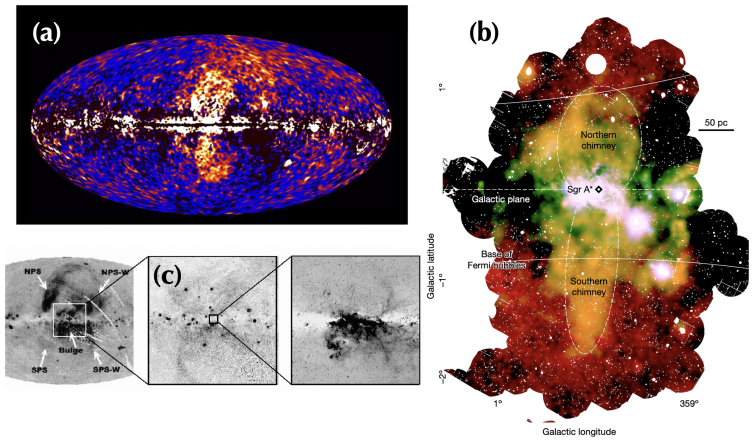

Figure 1.6: (a) All-sky γ-ray emission map from Fermi, showing the Fermi bubbles, large lobes extending 50° above and below the Galactic center, likely driven by past AGN activity (Su et al., 2010); (b) X-ray emission towards the Galactic center, tracing hot plasma and energetic feedback processes (Ponti et al., 2019); (c) large-scale bipolar wind in the Galactic center, detected in optical emission lines and indicative of past starburst or AGN-driven outflows (Bland-Hawthorn & Cohen, 2003). Figure adapted from Veilleux et al. (2020).

The majority of warm and cold outflows will not reach large distances from the disc but they will rather fall again onto it generating a galactic fountain cycle, a crucial mechanism for the evolution of Milky Way-like galaxies, that will be discussed in Chapter 4.

1.4 Galactic fountains: the mediators of gas circulation

Galactic fountains are clouds of gas ejected from the disc owing to stellar feedback which generally are located close to the disc. Galactic coronae have high temperature ($T \approx 10^6$ K) and low metallicities ($Z \approx 0.1\ Z_\odot$), thus they have cooling times of several Gyrs, reaching a few Gyrs close to the disc (Hodges-Kluck & Bregman, 2013). Nonetheless, star-forming galaxies have to accrete gas from this hot reservoir in order to keep forming stars. A possible mechanism that could help with the cooling and accretion of the coronal gas is represented by the interaction between the cold high-metallicity gas ejected from the disc and the metal-poor hot corona. As mentioned, star-forming galaxies can eject gas in the form of galactic fountains or galactic winds (Oppenheimer et al., 2010); if this gas efficiently mixes with the corona it can decrease its cooling time forming an intermediate temperature and metallicity gas. As the cloud of gas ejected from the disc travels through the hot corona there is the development of a Kelvin-Helmoltz instability[2], that helps the mixing of the gas, and the formation of a wake of gas behind it. In the wake some of the coronal gas can condensate thanks to its reduced cooling time, increasing the mass of the cold gas that then rains down on the disc, supplying it with fresh fuel for star formation (see the inset in Figure 1.4 for a sketch of this interaction). This phenomenon has been studied with very high resolution (on parsec-scale) simulations of the interface region between the corona and the cold gas clouds (Marinacci et al., 2010, 2011). In this way the nature of the interaction is captured but not inserted in a realistic galaxy model. Also, from parsec-scale simulations it has been found that a higher temperature of the corona reduces the ability of its condensation onto the galactic fountains, meaning that more massive galaxies (that have a higher virial temperature) will be less efficient in accreting gas from the external environment, bringing to a quenching of the star formation (Armillotta et al., 2016). Therefore, reaching high galaxy masses ($\sim$

[2]The Kelvin-Helmoltz instability is a hydrodynamical instability that occurs when two different fluids are in relative shearing motion.

10^{13} $M_{\odot}$) blocks the gas inflows that sustain the formation of new stars. Understanding the phenomenon of galactic fountain-CGM interaction can shed light on how star-forming galaxies evolve from being star-forming to quiescent, with profound implications for galaxy evolution.

1.5 This Thesis

In this Thesis I focus on the study of gas circulation between the disc and the CGM in Milky Way-like galaxies, studying how the SFR can be sustained over several Gyrs, in particular focusing on how the CGM gas can be accreted into the disc and then used to form new stars. I focus on different aspects of the baryon cycle, from gas accretion to gaseous outflows and their importance for galaxy evolution in the mutual interplay between the disc and the CGM. To do so, I use cutting-edge galaxy evolution simulations performed with advanced numerical techniques, which are described in **Chapter 2**. In particular, I use the moving-mesh code Arepo, an N-body hydrodynamical code coupled with the *SMUGGLE* model, a stellar feedback and explicit interstellar medium model which implements crucial phenomena for the evolution of spiral galaxies such as cooling and heating of the gas, stellar evolution and stellar feedback. In **Chapter 3**, I describe the process of setting up the initial conditions for my simulations of Milky Way-like galaxies. These conditions include not only the star-forming disc but also the surrounding galactic corona. The presence of the hot phase of the CGM is crucial for the gas circulation analysis that I perform in this work. In **Chapter 4**, I investigate the interaction between galactic fountains and the galactic corona. My findings show that cold clouds from galactic fountains passing through the hot coronal gas can trigger condensation of the hot gas onto the clouds, forming a warm gas phase with a shorter cooling time than the hot gas. This process facilitates the accretion of coronal gas onto the disc, making the CGM the primary gas reservoir for sustaining star formation over long timescales. Therefore, stellar feedback not only regulates star formation but also helps to sustain it over billions of years. In **Chapter 5** I focus on how the gas accreted from the CGM can become accessible for the formation of new stars. To study this phenomenon, I examine the distribution of gas accretion and ejection. I find that most accretion takes place at the disc outer edge. The majority of star formation occurs in the central regions of the disc, therefore to efficiently

fuel star formation in the center, a mechanism is needed to transport the gas inward. My simulations reveal that vertical gas inflows in the disc central regions, combined with radial inflows from the outskirts, are sufficient to sustain star formation in the inner regions of the disc. This radial motion from the outskirts to the center and the consequent formation of new stars is closing the baryon cycle, which started with the ejection of gas and the formation of galactic fountains operated by stellar feedback. In **Chapter 6**, I focus on studying galactic fountain cycle and the energetics of large-scale outflows in a cosmological context, employing an innovative method to simulate a more realistic CGM, which consists in extracting a box containing the galaxy from a cosmological zoom-in simulation and then use it to run isolated simulation. This approach reduces significantly computational time while still providing a realistic simulation environment for the galaxy. Finally, in **Chapter 7**, I summarize the key findings and conclusions of my work.

Chapter 2

Numerical methods for galaxy formation simulations

Understanding how (star-forming) galaxies form and evolve is a fundamental problem in modern astrophysics. Studying these objects from a theoretical perspective is extremely demanding, especially from a computational point of view. Indeed, to properly simulate a galaxy and its environment it is necessary to simultaneously model scales ranging from the Mpc of the galactic halos to the sub-pc of supernovae explosions. Moreover, high resolution is required in order to faithfully describe the involved physical processes with a sufficient level of detail. Despite these difficulties, hydrodynamical simulations of galaxy formation have been playing an essential role in furthering our understanding of the complex processes driving galaxy formation and evolution. The present Chapter is dedicated to the discussion of the numerical methods used to perform the hydrodynamical N-body simulations analyzed in this Thesis. In the following, I summarize the main computational methods that can be used to solve hydrodynamics (Section 2.1) and gravity (Section 2.2) equations. Then, in Section 2.3 I describe the moving-mesh code Arepo. In Section 2.4 I describe the *SMUGGLE* model, which implements crucial processes for galaxy evolution.

2.1 Hydrodynamics schemes

Baryons constitute approximately $\approx 5\%$ of the Universe's matter-energy content, with about $\approx 7\%$ in stars and the remaining $\approx 93\%$ in gas. Although baryons contribute only a small fraction of the Universe's total mass, hydrodynamic processes play a crucial role across a wide range of scales, driving key phenomena such as star formation, AGN feedback, stellar feedback, turbulence, shock waves, cooling flows etc. These processes collectively shape the evolution of astrophysical structures, from individual stars to entire galaxy clusters. In particular, the behavior of gas is essential for understanding the formation and evolution of galaxies, as outlined in Chapter 1.

If an idealized inviscid fluid is considered, i.e. with zero viscosity, neglecting the presence of magnetic fields, its dynamics is governed by the Euler equations, a set of hyperbolic, non-linear partial differential equations

$$\begin{cases} \dfrac{\partial \rho}{\partial t} + \nabla \cdot (\rho \boldsymbol{v}) = 0 \\ \\ \dfrac{\partial (\rho \boldsymbol{v})}{\partial t} + \nabla \cdot (\rho \boldsymbol{v} \otimes \mathbf{v} + P \mathbb{1}) = 0 \\ \\ \dfrac{\partial E}{\partial t} + \nabla \cdot (E + P) \boldsymbol{v} = 0 \end{cases} , \tag{2.1.1}$$

where ρ is the fluid density, $\boldsymbol{v}$ is the velocity field, P is the pressure, E is the total energy density of the fluid and $\mathbb{1}$ is the identity matrix. Equations (2.1.1) represent, from top to bottom, the conservation of mass, momentum and energy of the fluid. The total energy density is defined as

$$E = \frac{\rho \boldsymbol{v}^2}{2} + \frac{P}{\gamma - 1}, \tag{2.1.2}$$

where the first term on the right hand side is the kinetic energy per unit volume of the fluid and the second term is its internal energy per unit volume. In order to close and solve the system another equation is needed, that is an equation of state relating gas pressure, density and internal energy. Such equation for an ideal fluid (the case that I treat in this Thesis work)

reads

$$P = (\gamma - 1)\rho e, \tag{2.1.3}$$

where γ is the adiabatic index, defined as $\gamma = (1+c_v)/c_v$, with c_v the specific heat at constant volume, and e the internal energy per unit mass. In order to solve the hydrodynamics equations (2.1.1), three families of methods are widely used, Eulerian, Lagrangian and arbitrary Lagrangian-Eulerian codes. These types of methods have both advantages and disadvantages and they will be briefly outlined below.

- **Eulerian codes**. Here, the simulated volume is discretized on a mesh that partitions the volume in cells and the evolution of the fluid is obtained studying the variables that define its state, in particular the primitive $\mathbf{W} = (\rho, \mathbf{v}, P)$ or the conservative $\mathbf{Q} = (m, \mathbf{p}, E)$ variables ($\mathbf{p}$ is the momentum of the fluid), inside such cells. Between the cell interfaces there are exchanges of mass, momentum and energy. Therefore, this method is focused on given volumes in space and its based on how the properties of the fluid vary over time. There are different types of Eulerian methods, for instance *finite differences methods* (e.g. Ryu & Jones 1995, Ryu et al. 1995), in which it is studied how the variables evolve at the center of the cells, and the *finite volume methods* (e.g. Zachary & Colella 1992, Dai & Woodward 1994, Janhunen 2000, Ziegler 2004, Balsara 2004) where volume-averaged quantities are used. Nowadays, finite-volume Godunov methods (Godunov, 1959) are widely adopted. In such methods (see Section 2.3.2), the fluxes across cell interfaces are computed by solving a set of Riemann problems at these interfaces and the variables are updated consequently with a conservative scheme. If constant values for the variables inside the cells are considered, the method has a first-order accuracy; to reach the second or higher-order accuracy it is possible to use extrapolation methods, such as the piecewise parabolic method (Colella & Woodward, 1984). One disadvantage of Eulerian methods is that the resolution has to be modified explicitly in different zones of the simulation in order to resolve phenomena that occur on different spatial scales.

- **Lagrangian codes**. In these type of codes the motion of individual fluid elements is followed and the variation of their properties over time is analysed (in this case there is no volume, but rather mass discretization). The more used codes are the so-called

Smoothed Particles Hydrodynamics techniques (Lucy, 1977; Gingold & Monaghan, 1977; Springel, 2010a), which use particles to sample the fluid elements. In this way the resolution is always automatically adapted to the flow. This is extremely attractive in some applications that need to model a large dynamic range of spatial scales, such as cosmological simulations, and the resolution does not need to be explicitly adjusted in different regions of the simulation. The main disadvantage of these types of codes is their inability in accurately representing discontinuities, which are very common in astrophysical problems, for instance shock waves or contact instabilities (Springel, 2010a).

- **Arbitrary Lagrangian-Eulerian codes**. The third case combines both Eulerian and Lagrangian codes, thus mitigating their shortcomings. In this case, the volume is discretized but the cells are allowed to move with the fluid. The numerical methods using this approach are called Arbitrary Lagrangian-Eulerian codes. These codes are particularly important as they are becoming commonly used in galaxy evolution simulations nowadays for their flexibility. This family of methods has had a great development in recent years with the creation of new arbitrary Lagrangian-Eulerian codes (Duffell & MacFadyen, 2011; Vandenbroucke & De Rijcke, 2016; Hopkins, 2015). These also include the Arepo code (see Section 2.3), which has been used in this Thesis work.

2.2 Gravity schemes

Gravity is the driving force behind numerous astrophysical phenomena that shape the evolution of the Universe, from the motion of planets and stars to the complex instability processes that lead to the formation of cosmic structures. To determine the evolution of intricate systems like galaxies it is necessary to compute the evolution of a large ensemble of particles, either collision-less or collisional (in the case of gas particles), evolving under their own self-gravity. This configuration constitutes what is referred to as the *N-body problem*. Each particle in the system interacts gravitationally with the others, feels a given gravitational acceleration and moves according to it. The only way to address in full detail the N-body problem (if $N > 2$) is to use numerical methods. The problem at hand is to determine the acceleration acting on each particle and solve for its motion that is governed by the second order system

of differential equations

$$\ddot{\mathbf{x}}_i = -\nabla\Phi(\mathbf{x}_i), \tag{2.2.1}$$

where $\mathbf{x}_i$ is the coordinate of the i-th particle, $\ddot{\mathbf{x}}_i$ is its acceleration and Φ is the gravitational potential determined by all the particles present in the system and that can be computed numerically as

$$\Phi(\mathbf{x_i}) = -G\sum_{j\neq i}\frac{m_j}{[||\mathbf{x}_i - \mathbf{x}_j||^2 + \varepsilon^2]^{1/2}}, \tag{2.2.2}$$

where G is the gravitational constant and m_j is the mass of the j-th particle. Also, it is worth noting the presence of the parameter ε, which did not appear in the Newtonian form of the gravitational potential. This is a numerical expedient called *gravitational softening* that is necessary to ensure that the potential does not become exceedingly large for close encounters between particles. Evaluating the potential for each particle in the system directly with equation (2.2.2) brings to the **direct summation technique**, with which the sum of N individual contributions to the gravitational potential given by all other particles is taken. Obtaining the gravitational potential allows to compute the acceleration with equation (2.2.1), from which the evolution of velocity and position of the particles can be determined, solving the following system of differential equations for each particle i

$$\begin{cases} \dot{\mathbf{v}}_i = -\nabla\Phi(\mathbf{x}_i) \\ \\ \dot{\mathbf{x}}_i = \mathbf{v}_i \end{cases}. \tag{2.2.3}$$

Equations (2.2.3) can be numerically integrated with different ordinary differential equations solving methods, but a widely used method is the Leapfrog scheme. As I will discuss in Section 2.3.3, AREPO uses this scheme to integrate equations (2.2.3).

The direct summation technique does not introduce approximations – except for the gravitational softening – in the solution of Equations (2.2.3), thus it is the method with the highest accuracy. However, to solve for the gravitational N-body problem requires more efficient techniques. In fact the sum in equation (2.2.2) requires $N-1$ operations and has to be repeated for N particles. This requires $N(N-1) \sim N^2$ operations and it quickly becomes computationally prohibitive for a large number of particles, as it is customary in astrophysical

applications. Fortunately, there are other techniques which allow to solve this problem in a more efficient (but approximated) way reducing the numerical complexity of the solver from N^2 to N or $N\log N$. Some of the most commonly used techniques include the Particle-Mesh method, the Tree Method and the Tree-PM method, that I will describe below.

- The **Particle-mesh** (PM) **method** (Eastwood & Hockney, 1981) exploits the fact that the Poisson's equation (that connects the gravitational potential to the density distribution)

$$\nabla^2\Phi = 4\pi G\rho(\mathbf{x}), \tag{2.2.4}$$

  can be simply rewritten in Fourier space as

$$\mathbf{k}^2\hat{\Phi}(\mathbf{k}) = 4\pi G\hat{\rho}(\mathbf{k}), \tag{2.2.5}$$

  i.e. a simple product of terms, where $\mathbf{k}$ is the wave vector. The method is performed on a Cartesian mesh: from a given distribution of particles a scheme is used to assign a mass to each grid cell[1], based on the particles inside each cell, from which it is possible to derive a smooth density field. From equation (2.2.5) it is possible, after finding the Fourier transform of the density field $\hat{\rho}$, to estimate the Fourier transform of the gravitational potential $\hat{\Phi}$. The gravitational potential is then obtained with an inverse Fourier transform. The gravitational accelerations are subsequently computed from equation (2.2.1) with a finite-difference approach and interpolated to the particle positions. The main advantage of the PM method is that it is fast and simple, in fact its complexity scales with the number of particle N. The problem is that the computation of the force is bound to the mesh resolution, the force resolution cannot go below the size of a single mesh cell. This is particularly problematic in cosmological simulations, where a high dynamic range of scales is present. For this reason, the method is particularly suited to compute the force field from almost homogeneous distributions of matter on large scale (Springel, 2016a).

- The **Tree method** (Barnes & Hut, 1986) works by recursively dividing the simulation domain into eight subdomains[2] (nodes), a process that continues until each subdomain

[1] In particular Arepo uses the cloud-in-cell scheme (Eastwood & Hockney, 1981).
[2] For this reason it is also called an Oct-Tree method.

contains either one or zero particles (these are called the leaves of the tree). The purpose of the Tree method is to group together particles at a relatively large distance from the particle for which the gravitational force is needed, in order to approximate their collective gravitational potential with a multipole expansion, significantly speeding up the calculation over direct summation techniques and reducing the computational cost to $N\log N$. A schematic view of the domain division in 2 dimensions is shown in Figure 2.1. A further optimization to a complexity of N can be achieved through the use of the fast multipole method (Greengard & Rokhlin, 1987), where forces are calculated between two nodes of the tree rather than between individual particles and nodes. For its nature this method is well-suited to compute the gravitational forces coming from highly clustered particles and when a high force resolution (i.e. when the forces have to be computed at small scales) is needed, in fact the resolution automatically increases in regions where the matter is more clustered. The main disadvantage is that for large-scale, homogeneous matter distributions the computation becomes very onerous (and might also lose accuracy), due to the many gravitational terms that have to be computed to obtain an almost vanishing force. This method is used to solve for the gravitational potential in this Thesis, thus it will be described in more details in Section 2.3.3.

- In order to overcome their disadvantages and to combine the high resolution of the Tree method and the high speed of the PM method, many N-body codes implement a combination of these two algorithms, the so-called **Tree-PM method** (Bode et al., 2000; Bode & Ostriker, 2003; Springel, 2005; Springel et al., 2021). In these methods the gravitational potential is divided in a short-range component (computed with the Tree method) and in a long-range component (computed with a PM method). This is an approach that is particularly used in large-scale cosmological simulations in order to achieve high efficiency.

2.3 The moving-mesh code Arepo

The Arepo code (Springel, 2010b; Weinberger et al., 2020) is a cutting-edge moving-mesh code that employs a finite volume solver on an unstructured Voronoi mesh for hydrody-

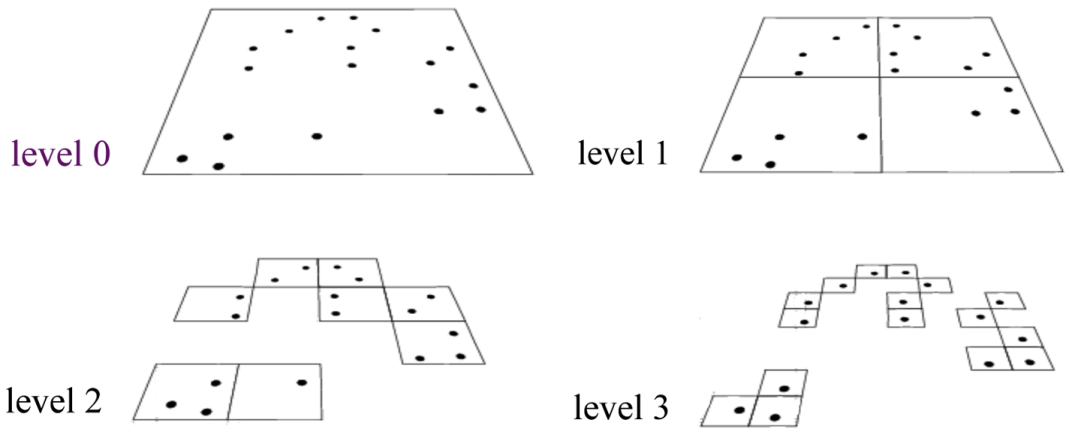

Figure 2.1: Schematic view of the Barnes & Hut (1986) scheme in 2 dimensions. All particles are enclosed in a square-shaped box that is then hierarchically subdivided until each particle finds itself in a node alone. Figure adapted from Springel (2016b).

namics, paired with a Tree-PM method to solve the Poisson equation. The use of a mesh that moves with the fluid flow provides a key advantage that mitigates issues that typically challenge both Eulerian and Lagrangian codes: it combines the high spatial adaptability of Lagrangian methods with the ability to accurately resolve discontinuities, a feature of Eulerian approaches. This dual capability is the primary reason Arepo was chosen for this Thesis work. In the last years Arepo has been successfully used in computational astrophysics in a vast number of topics, for instance in state-of-the-art cosmological simulations of galaxy formation and evolution, such as *Illustris* (Genel et al., 2014; Vogelsberger et al., 2014), *IllustrisTNG* (Naiman et al., 2018; Nelson et al., 2018; Pillepich et al., 2018; Marinacci et al., 2018; Springel et al., 2018) and *Auriga* (Monachesi et al., 2016; Gómez et al., 2017; Marinacci et al., 2017; Grand et al., 2017), but also in smaller scale simulations of different astrophysical objects, such as dwarf galaxies (Besla et al., 2012), isolated galaxies (Jacob et al., 2018; Pascale et al., 2021; Nobels et al., 2024), globular clusters (Gutcke, 2024), supermassive black holes (Ward et al., 2024; Bhowmick et al., 2024), molecular filaments in galaxies (Smith et al., 2014; Kong et al., 2024), type Ia supernovae (Pakmor et al., 2013) and protoplanetary discs (Muñoz

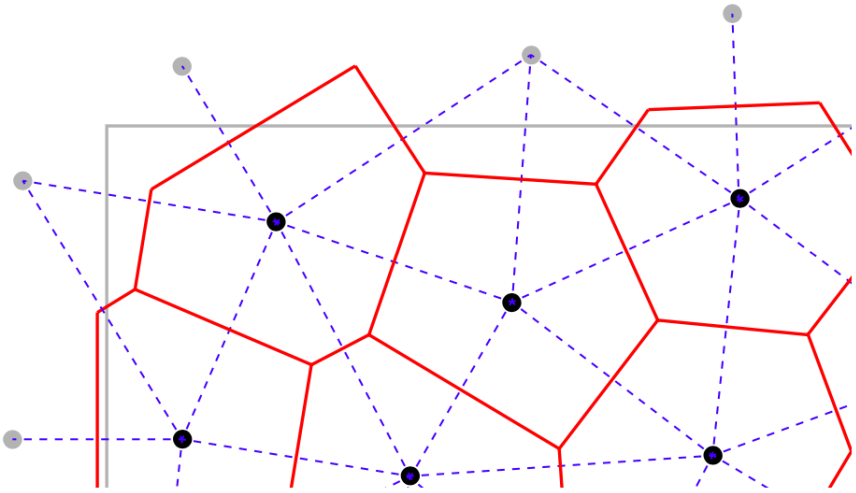

Figure 2.2: Schematic view of the Voronoi tessellation in two dimensions. The red lines show the Voronoi cells and the blue dashed lines shows the corresponding Delaunay triangulation. Black filled circles are the mesh generating points. Figure taken from Weinberger et al. (2020).

et al., 2014).

In this section, I provide a brief overview of the Arepo code structure, the distinctive properties of the mesh (Section 2.3.1), the time integration scheme for both hydrodynamics (Section 2.3.2) and gravity (Section 2.3.3), and the time-step constraints employed in the code (Section 2.3.4).

2.3.1 Moving mesh

In Arepo, the simulated volume is partitioned using a mesh with unique geometric and topological properties known as a **Voronoi mesh**. The mesh is generated by points, called mesh-generating points, which are the centers around which Voronoi cells are constructed. A Voronoi tessellation of space consists of non-overlapping cells, where each cell encloses the region of space that is closer to its mesh-generating point than to any other.

In general, it is more simple to generate a Delaunay triangulation and derive from it the Voronoi tessellation. Therefore, this is what is done to build the mesh in Arepo (see Figure 2.2 for an illustration of the constituting elements of the mesh). The Delaunay triangulation, formed by tetrahedra (triangles in two dimensions) that have the mesh generating points as

vertices, and each circumsphere around one of these tetrahedra is not allowed to contain any other mesh-generating point inside it.

A fundamental property of AREPO is that it allows the grid cells to move with the fluid. At each time-step each mesh generating point is moved according to the gas bulk velocity and the Voronoi mesh is reconstructed consistently. In particular the velocity of the i-th mesh generating point is assigned as

$$\mathbf{w}_i = \mathbf{v}_i + \mathbf{v}_{\text{corr,i}} \tag{2.3.1}$$

where $\mathbf{v}_i$ is the velocity of the fluid in the cell i and $\mathbf{v}_{\text{corr,i}}$ is a corrective velocity (equation 2.3.4), described below. The bulk velocity accounts for accelerations arising from local pressure gradients and gravity, using the expected velocity at the next half time-step. This approach naturally results in a quasi-Lagrangian behavior, allowing the mesh to adapt to the flow of the fluid. However, this alone does not guarantee that the mesh remains well-structured at all times. Indeed, local fluid motions can still distort the mesh, leading to cells with high aspect ratios. Therefore, it can happen that in the reconstructed grid may be present highly distorted cells due to the fact that the mesh generating points can largely step away from the geometric center of the cell. Such feature can increase discretization errors and introduce mesh noise, which may, in turn, degrade the accuracy of the scheme, particularly in the linear reconstruction step (equation 2.3.15). Therefore, the geometric center and the mesh generating point have to remain as close as possible, this can also reduce the rate at which the mesh faces can rotate during their motion. These highly distorted cells are identified by the maximum angle α_{max} within which each cell face is seen from the mesh generating point

$$\alpha_{\text{face}} = (A_{\text{face}}/\pi)^{1/2}/h_{\text{face}}, \tag{2.3.2}$$

$$\alpha_{\text{max}} = \max(\alpha_{\text{face}}), \tag{2.3.3}$$

where A_{face} is the area of each face of the cell and h_{face} is the distance between the face and the mesh generating point.

In particular, if α_{max} is greater then 0.75β, where β is a free parameter called "*cell roundness criterion*", set to $\beta = 2.25$ in our simulations, the cell is considered distorted and the velocity

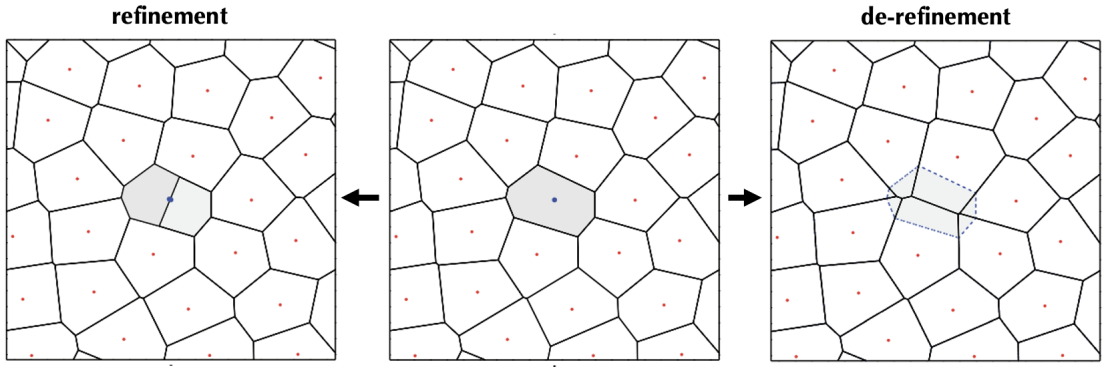

Figure 2.3: Schematic view of a refinement and de-refinement example of a Voronoi cell. In the central panel a Voronoi cell is highlighted in grey. The cell is refined in the left panel (dividing it into two different cells) and de-refined in the right panel (removing the cell and distributing its thermodynamic properties to the neighbour cells). Figure adapted from Springel (2010b).

assigned to its mesh generating point is corrected with a velocity that points toward the center of mass of the cell, as follows (Vogelsberger et al., 2012; Weinberger et al., 2020)

$$\mathbf{v}_{\rm corr} = \begin{cases} 0 & \text{for } \alpha_{\rm max} \leq 0.75\beta \\ f_{\rm shaping} \frac{\alpha_{\rm max} - 0.75\beta}{0.25\beta} v_{\rm char} \hat{\mathbf{n}} & \text{for } 0.75\beta < \alpha_{\rm max} \leq \beta \\ f_{\rm shaping} v_{\rm char} \hat{\mathbf{n}} & \text{for } \alpha_{\rm max} > \beta \end{cases} \tag{2.3.4}$$

where $f_{\rm shaping}$ is called "*cell deformability parameter*" and is set to $f_{\rm shaping} = 0.5$, $\hat{\mathbf{n}}$ is the normal vector to the cell and $v_{\rm char}$ is a characteristic velocity, corresponding to the sound speed in this work.

Another key feature of the AREPO mesh is its ability to undergo dynamic refinement and de-refinement, ensuring that the mass of gas cells remains tightly distributed around the prescribed mass resolution. During refinement, a mesh-generating point is split into two closely spaced points, with a distance $0.025 r_{\rm cell}$, with $r_{\rm cell}$ defined as

$$r_{\rm cell} = \left(\frac{3V}{4\pi} \right)^{1/3}, \tag{2.3.5}$$

effectively dividing the cell. In contrast, de-refinement removes a mesh-generating point and its corresponding Voronoi cell, redistributing its volume and thermodynamic properties to neighboring cells (see Figure 2.3). These processes are triggered when a cell mass falls below half (de-refinement) or exceeds twice (refinement) the target mass resolution. Additionally, the mesh structure can be modified through a process known as conversion. For example, when a new stellar particle is formed (see Section 2.4.2), the corresponding gas cell is removed, and its mass is transferred entirely to the stellar particle. The surrounding gas cells then expand to occupy the empty volume as the mesh is reconstructed. Due to the semi-Lagrangian nature of the code, in this Thesis I will use the terms gas particles and gas cells interchangeably.

2.3.2 Hydrodynamic solver

To solve the equations of hydrodynamics, AREPO employs a finite-volume Godunov method on an unstructured Voronoi-mesh. The aim of this method is to perform a conservative update for the variables that describes the state of the fluid, this is done discretizing the conservative form of the Euler equations (2.3.8).

At each time-step AREPO carries out the following steps to solve the hydrodynamics equations:

(i) derive the primitive variables of the fluid $\mathbf{W} = (\rho, \mathbf{v}, P)$ in each cell from the conserved variables $\mathbf{Q} = (m, \mathbf{p}, E)$;
(ii) compute the gradients of the primitive variables in each cell;
(iii) assign a velocity $\mathbf{w}^n$ to each mesh generating point (equation 2.3.1);
(iv) determine the time-step from the time-step criteria (Section 2.3.4);
(v) compute the first fluxes across each cell interface using a Riemann solver;
(vi) move the mesh generating points consistently with their velocity $\mathbf{w}^n$;
(vii) compute a new Voronoi mesh, based on the new generating mesh points coordinates $\mathbf{r}'$;
(viii) compute the second fluxes on an updated mesh;
(ix) update the conserved variables in each cell, with a second order Runge-Kutta scheme (2.3.10), using the derived fluxes and obtaining the new variables $\mathbf{Q}_i^{n+1}$.

I now explain in more detail how the time integration through a finite-volume Godunov method works in Arepo. The gradients computation (step (ii)) is described in more detail later in a separate paragraph. First, for each grid cell, I define the state vector

$$\mathbf{U} = \begin{bmatrix} \rho \\ \rho\mathbf{v} \\ \rho e \end{bmatrix}, \tag{2.3.6}$$

containing, from top to bottom, density, momentum density and total energy density of the fluid. The fluxes of these variables are defined as

$$\mathbf{F}(\mathbf{U}) = \begin{bmatrix} \rho\mathbf{v} \\ \rho\mathbf{v}\mathbf{v}^T + P\mathbb{1} \\ \rho e\mathbf{v} + P\mathbf{v} \end{bmatrix}. \tag{2.3.7}$$

With these definitions the Euler equations can be written in the following compact conservative form

$$\frac{\partial \mathbf{U}}{\partial t} + \nabla \cdot \mathbf{F} = 0, \tag{2.3.8}$$

which emphasizes their character as conservation laws for mass, momentum and energy.

In Arepo a finite-volume strategy is employed, therefore the variables $\mathbf{U}$ are averaged inside each cell volume, obtaining the conservative variables

$$\mathbf{Q} = \int_{V_i} \mathbf{U}\, \mathrm{d}V = (m_i, \mathbf{p}_i, E_i), \tag{2.3.9}$$

where m_i, $\mathbf{p}_i$ and E_i are the mass, the momentum and the total energy (kinetic + internal) of the i-th cell.

The conservative update of the variables $\mathbf{Q}$ in each time-step is done through a second order Runge-Kutta scheme, similar to the Heun's method[3] (see Pakmor et al. 2016)

[3]The scheme can also be thought as a hybrid method between a Runge-Kutta and a MUSCL-Hancock scheme and it has been employed instead of the original MUSCL-Hancock scheme presented in Springel (2010b).

$$\mathbf{Q}_i^{n+1} = \mathbf{Q}_i^n - \frac{\Delta t}{2}\left(\sum_j A_{ij}^n \hat{\mathbf{F}}_{ij}^n(\mathbf{W}^n) + \sum_j A'_{ij}\hat{\mathbf{F}}'_{ij}(\mathbf{W}')\right), \tag{2.3.10}$$

where $\mathbf{Q}_i^n$ represents the variable $\mathbf{Q}$ in the i-th cell at the n-th time-step, Δt is the time-step and A_{ij} is the oriented area of the face between cells i and j. Here, the quantities with the apex n are computed in the grid from the previous time-step, the quantities with the apex $'$ are computed in the newly created Voronoi mesh. Therefore, in these scheme the fluxes have to be computed twice in two different grids for each time-step. This method ensures that only a single mesh construction is required for each time-step while obtaining formal second-order convergence in time.

The coordinates of the new j-th mesh generating points are computed as follows

$$\mathbf{r}'_j = \mathbf{r}_j^n + \Delta t \mathbf{w}_j^n, \tag{2.3.11}$$

where $\mathbf{r}^n$ are the mesh generating points coordinates of the previous time-step and $\mathbf{w}^n$ are the mesh generating points velocities, computed with equation (2.3.1). The velocities of the mesh generating points are kept constant inside a time-step. At the end of the time step these coordinates should be updated as

$$\mathbf{r}_j^{n+1} = \mathbf{r}_j^n + \frac{\Delta t}{2}(\mathbf{w}_j^n + \mathbf{w}'_j), \tag{2.3.12}$$

but, since the velocities are kept constant inside each time-step: $\mathbf{w}' = \mathbf{w}^n$, it is easy to demonstrate that

$$\mathbf{r}^{n+1} = \mathbf{r}' \tag{2.3.13}$$

This is fundamental because it allows to have only one mesh computation for each time-step, since it is a very onerous computational operation.

The fluxes are first computed from the primitive variables obtained in the previous time-step, and then from new primitive variables found with a time extrapolation as

$$\mathbf{W}'_i = \mathbf{W}_i^n + \Delta t \frac{\partial \mathbf{W}}{\partial t}. \tag{2.3.14}$$

Equation (2.3.10) is used in step (vii) to update the conservative variables inside each cell. To compute the changes of the variables inside a given cell, it is necessary to obtain the variable fluxes at each interface of the cell, quantities that measure how much mass, momentum and energy have entered and exited from the cell. Therefore, the code has to compute an approximation of the conservative variables fluxes at each interface (step v), which is done solving a so-called Riemann problem, a configuration in which two different constant states (left and right) are present, separated by a single discontinuity, at each interface. This is performed with a **Riemann solver** (see Toro 2013), in particular, AREPO gives the possibility to use different types of Riemann solvers for the Euler equations (in the case of pure hydrodynamics): an exact Riemann solver or an approximate one, called HLLC (Toro et al., 1994). I used the exact Riemann solver (the default mode of operation in AREPO for hydrodynamics) for this work.

Gradients computation

The gradients are computed (step (ii)) using a least-square gradient estimate (Pakmor et al., 2016). This method differs from the original one by Springel (2010b), which was slightly inaccurate for distorted cells. This computation is required in order to reach a higher order spatial accuracy of the Godunov method. The primitive variables are defined at the center of each cell and finding their values at the cell interfaces allows to solve a more accurate Riemann problem at each interface.

The gradient ∇W_i of a primitive variable W_i is obtained with a linear extrapolation, such that the extrapolated value of the variable in the cell j is very close to the real one

$$\tilde{W}_j = W_i + \mathbf{d}_{ij} \nabla W_i, \tag{2.3.15}$$

where $\mathbf{d}_{ij}$ is the position vector of the j-th cell relative to the i-th cell. Of course multiple neighbour cells are involved in this computation. Therefore, to find a single value for the gradient a residuals minimization is employed, weighting the equations squared for each couple of cells ij

$$S_{\mathrm{TOT}} = \sum_j g_j (W_j - W_i - \mathbf{d}_{ij} \nabla W_i)^2. \tag{2.3.16}$$

Here, $g_j = A_{ij}/|\mathrm{d}_{ij}|$ are the weights adopted, where A_{ij} is the area of the interface between the i-th and the j-th cell. Minimizing equation (2.3.16) allows to find an estimate of the gradient ∇W_i. In this way a linear reconstruction of the primitive quantities $\mathbf{W} = (\rho, P, \mathbf{v})$ at the interface of the cell can be found with equation (2.3.15), therefore allowing a better reconstruction of the primitive variable and a more accurate solution to the Riemann problem. This scheme allows to reach second-order accuracy, but near hydrodynamical discontinuities (e.g. shock waves) it is important to reduce the order of the scheme, with a so-called slope limiter, to avoid numerical instabilities.

2.3.3 Gravitational time evolution

The gravitational time evolution is structured in the following way:

(i) Computation of the gravitational potential Φ with a Tree-based method and consequent derivation of the gravitational acceleration $\mathbf{a}$.
(ii) Determination of the time-step Δt.
(iii) Time integration with a leapfrog scheme.

Gravitational potential computation

The computation of the gravitational potential Φ in AREPO is performed in general with a Tree-PM method (Section 2.2), this happens in cosmological simulations where the application of this method is particularly efficient. In my case I simulated an isolated galaxy and therefore I used only a Tree-based method. After having created the tree structure (until the leaves of the tree) the computation of the potential is performed for each particle, starting from the bigger nodes with group of particles (using a multipole expansion) and then going to the sub-nodes if the approximation does not satisfy certain conditions. What is important is to determine an opening criterion, i.e. a criterion to understand if a certain multipole approximation does not differ too much from the real potential. In particular, a relative opening criterion is used

$$\frac{Gm}{d^2}\frac{L_{\mathrm{node}}^2}{d^2} > \alpha|\mathbf{a}|, \tag{2.3.17}$$

where m is the mass of the node, d is the distance between the node center of mass and the particle for which the potential is created, $\mathbf{a}$ is the acceleration of the particle at the previous time-step and α is a free parameter set to $\alpha = 0.0025$. If this criterion is satisfied, the node is opened and the potential computation is done in each sub-node. The gravitational acceleration is then obtained summing the contribute coming from each individual node (or single particle).

For the first time-step, a geometrical criterion is applied due to the lack of an acceleration estimate from the preceding time-step

$$L_{\text{node}} > d\theta_{\text{opening}}, \tag{2.3.18}$$

with θ_{opening} a free parameter set to 0.7. This first computation of the acceleration is then repeated using the relative opening criterion (2.3.17).

Leapfrog scheme

The positions and the velocities of the particles are updated with a second-order leapfrog scheme. The characteristic that makes this method of particular interest in astrophysical numerical simulations is that it is a symplectic integrator, therefore it is an exact solution of a discrete Hamiltonian that approximates the real one of the system and it conserves its energy. A general leapfrog scheme is constructed by an alternation of drift (coordinates update) and kick (velocities update) operations

$$\begin{cases} D(\Delta t): \quad \mathbf{x}_i \rightarrow \mathbf{x}_i + \Delta t \mathbf{v}_i & \text{(drift)} \\ \\ K(\Delta t): \quad \mathbf{v}_i \rightarrow \mathbf{v}_i + \Delta t \mathbf{a}(\mathbf{x}_i) & \text{(kick)} \end{cases}, \tag{2.3.19}$$

where $\mathbf{x}_i$ are the positions, $\mathbf{v}_i$ are the velocities and $\mathbf{a}(\mathbf{x}_i)$ are the accelerations at the time-step i. The scheme implemented in AREPO is similar to the one implemented in the GADGET-2 code (Springel, 2005), and in our case simply consists in a simple kick-drift-kick application

$$\begin{cases} \mathbf{x}_{i+1/2} = \mathbf{x}_i + \dfrac{1}{2}\Delta t \mathbf{v}_i \\ \\ \mathbf{v}_{i+1} = \mathbf{v}_i + \Delta t \mathbf{a}(\mathbf{x}_{i+1/2}) \\ \\ \mathbf{x}_{i+1} = \mathbf{x}_{i+1/2} + \dfrac{1}{2}\Delta t \mathbf{v}_{i+1} \end{cases} . \tag{2.3.20}$$

In the first step the positions are evolved for half time-step $\Delta t/2$, then the velocities are evolved for an entire time-step Δt with the gravitational accelerations $\mathbf{a}$ computed from the updated positions $\mathbf{x}_{i+1/2}$ and finally the positions are updated for another half time-step with the newly derived velocities $\mathbf{v}_{i+1}$. This method has a second-order time accuracy.

2.3.4 Time-step constraints

The time-steps Δt chosen for the time evolution of hydrodynamics and gravity are fundamental to ensure the stability of the code, in fact a time-step that is too large can lead to an unstable scheme.

The first time-step criterion, which is enforced for hydrodynamics, is the **Courant-Friedrichs-Lewy** (CFL) **criterion** (Courant, Friedrichs & Lewy, 1967)

$$\Delta t \leq C_{\rm CFL} \frac{r_{\rm cell}}{v_{\rm signal}}, \tag{2.3.21}$$

where the Courant factor $C_{\rm CFL}$ is a safety parameter set to $C_{\rm CFL} = 0.3$ in our simulations, $r_{\rm cell}$ (Eq. 2.3.5) is the cell size, V is the cell volume, and $v_{\rm signal}$ is the maximum signal velocity in the fluid

$$v_{\rm signal} = \left(\gamma \frac{P}{\rho}\right)^{1/2}, \tag{2.3.22}$$

corresponding to the sound speed. Gas bulk velocity is not taken into account (as it is done in fixed-mesh codes) because the mesh moves with the fluid flow and, therefore, *relative to the mesh*, the fluid has a small bulk velocity (much smaller than the sound speed). If magnetic fields are included, the Alfvén speed must also be considered.

The time-step for the gravitational dynamics is defined as

$$\Delta t \geq \sqrt{\frac{2C_{\text{grav}}\varepsilon_{\text{soft}}}{|\mathbf{a}|}}, \tag{2.3.23}$$

where C_{grav} is a free parameter set to $C_{\text{grav}} = 0.012$ in our simulations.

Also, another time-step criterion is needed to account for information from distant regions. For instance, if a shock wave is coming and the gas cell is unaware of that, the time step would be too large, making the code unstable. This can be avoided using

$$\Delta t_i \geq \min_{j \neq i} \left(\frac{r_{ij}}{c_i + c_j - \mathbf{v}_{ij} \cdot \mathbf{r}_{ij} r_{ij}} \right), \tag{2.3.24}$$

where $\mathbf{v}_{ij}$ is the velocity difference between two cells i and j, c_i and c_j are the sound speed in the i-th and j-th cells, respectively, and r_{ij} is the distance between them.

If a global time-step constraint is used, the time-step is chosen minimizing all the time-step just described

$$\Delta t = \min_i \Delta t_i. \tag{2.3.25}$$

Otherwise, a more flexible (and efficient) scheme that uses local time-steps can be implemented. Typically, in astrophysical simulations, a wide range of density is present. For instance, in high-density regions like a galaxy center, shorter time-steps are necessary compared to low-density areas, such as the circumgalactic or intergalactic medium. Evolving all particles with the smallest time-step would be highly inefficient, so each particle is assigned an individual time-step. This allows some particles to evolve more quickly than others, with a synchronization scheme ensuring that shorter time-steps are nested within the longer ones. Local time-stepping is also employed in the simulations presented in this work.

2.4 The *SMUGGLE* model

The **S**tars and **MU**ltiphase **G**as in **Ga**l**a**xi**E**s model (***SMUGGLE***; Marinacci et al. 2019) is an explicit stellar feedback and interstellar medium model for the moving-mesh code Arepo. *SMUGGLE* is a sub-resolution model[4] that describes the complex multiphase structure of the ISM and self-consistently generates gaseous outflows. Making realistic galaxy simulations requires the use of large volumes (in order to have a realistic environment and the natural interactions between different cosmic structures) while still resolving the smaller scales (to capture, for instance, the nature of star formation and SNe explosions).

In general, the ISM structure is very complex, with cold, warm and hot phases that coexist in the same environment. What is commonly done to numerically implement the ISM is to use an equation of state instead of resolving individually the different phases of the gas, for instance treating the gas as a two-fluid component with cold clouds inside a hot medium (Springel & Hernquist, 2003; Agertz et al., 2011). These models usually have a minimum temperature, that is roughly set to warm gas ($T \sim 10^4$ K), below which the cooling and the gravitational collapse of the gas is disabled. This could lead to an ISM model that is smooth on scales of hundreds of parsecs (comparable to or larger than molecular clouds size), missing its real complexity. In this models, increasing the numerical resolution of the simulation does not modify the ISM structure, as it is dependent on the chosen effective equation of state. In order to capture the ISM complex nature it is necessary to accurately model both the different gaseous phases and stellar feedback with its associated injection of energy, momentum and mass into the ISM.

In this Section I describe in detail the physical processes considered in the *SMUGGLE* model and their numerical implementation. The main processes implemented in the *SMUGGLE* model (schematically described in Figure 2.4) are:

(i) **Cooling**, in particular primordial and metal cooling lines, low-temperature cooling and an implementation of gas self-shielding, cosmic rays and photoelectric **heating processes** (Section 2.4.1);

[4] A subresolution model is a set of numerical prescriptions used to capture physical processes that are unresolved, i.e. that happen on scales below the resolution of the simulations.

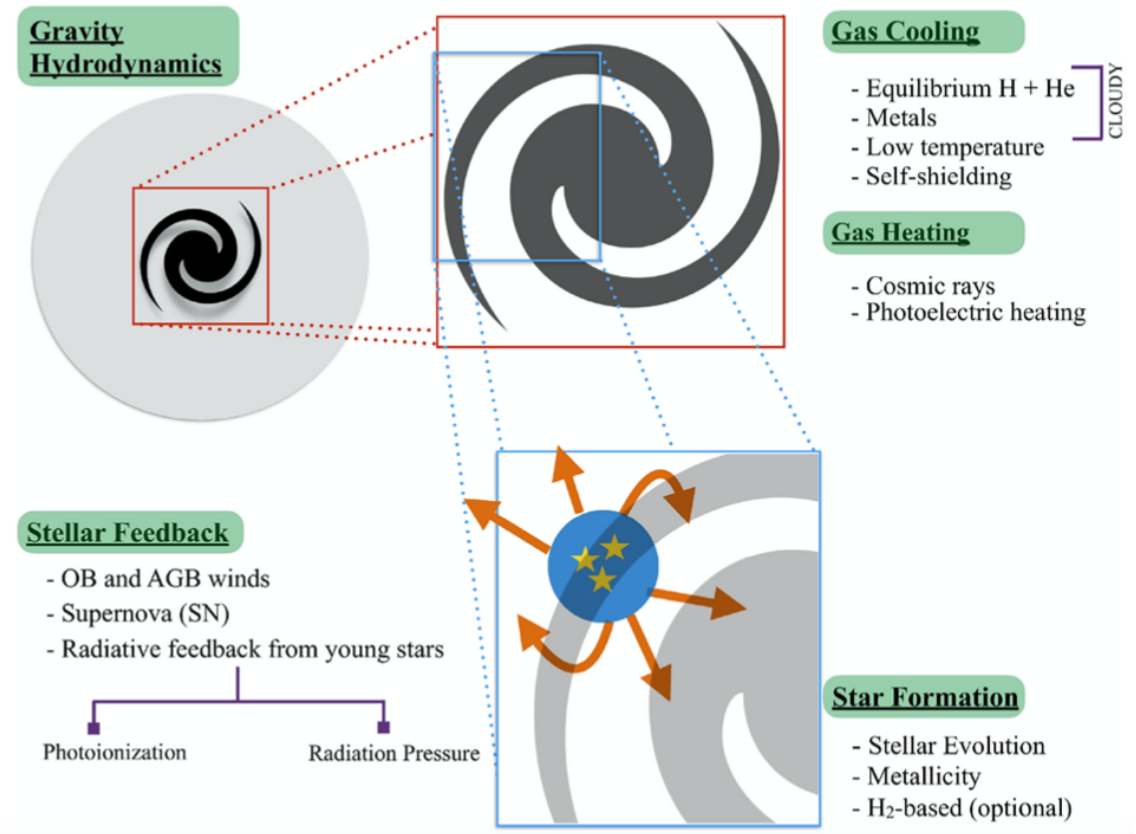

Figure 2.4: Schematic view of the main processes implemented in the *SMUGGLE* model, and their mutual interplay across different spatial scales: cooling (primordial and metal line cooling, low temperature cooling and self-shielding) and heating (cosmic rays and photoelectric heating) of the gas; star formation and stellar feedback (i.e. SNe, stellar winds and radiative feedback). Figure taken from Marinacci et al. (2019).

(ii) A stochastic implementation of the **star formation** (Section 2.4.2), complemented with a prescription for stellar evolution (Section 2.4.3) taken from Vogelsberger et al. (2013).

Furthermore, a crucial part of this model is the implementation of the stellar feedback, which occurs through three main different channels:

(iii) **Supernova feedback** (Section 2.4.4) from type II and type Ia SNe. After explaining the numerical treatment of these phenomena, I describe the implementation of the momentum boost from the $P\mathrm{d}V$ work (Section 2.4.4). Also, I explain in detail the method used to couple the energy and momentum generated to the surrounding gas (Section 2.4.4);

(iv) **Radiative feedback** (Section 2.4.5) from young and massive stars. The radiation can have an impact on the ISM mainly through **photoionization** (Section 2.4.5) and **radiation pressure** (Section 2.4.5);

(v) **Stellar winds feedback** (Section 2.4.6) from two classes of stars: OB and AGB stars.

The implementation of cooling, star formation and stellar feedback is inspired by the one in the FIRE-2 model (Hopkins et al., 2018) with some modifications.

2.4.1 Cooling and heating

Radiative cooling is the process through which gas cools down emitting photons. All these processes can be parameterized by the so-called cooling function

$$L = n^2 \Lambda_{\mathrm{cool}}(T, X, Z), \tag{2.4.1}$$

where L is the luminosity per unit volume, n is the gas number density and Λ_{cool} is the cooling function (in unit erg cm^3 s^{-1} in cgs), that depends on the temperature T, on the ionization state X and on the metallicity Z of the gas.

On the other hand, also processes that heat the gas are possible, I can therefore define a heating function Λ_{heat}. The balancing between the cooling and heating functions gives the net cooling function

$$\Lambda_{\rm net} = \Lambda_{\rm cool} - \Lambda_{\rm heat}. \tag{2.4.2}$$

In galaxy formation and evolution simulations, accounting for gas cooling and heating is crucial, as these processes significantly impact the gas thermal properties and state, either promoting or hindering star formation. The main cooling and heating mechanisms included in *SMUGGLE* are: (i) cooling from a primordial network of hydrogen (H) and helium (He), which also encompasses (ii) Compton cooling from cosmic microwave background (CMB) photons, and (iii) metal-line cooling. These processes are implemented following the approach of Vogelsberger et al. (2013). Additionally, the *SMUGGLE* model incorporates (iv) low-temperature metal lines, fine-structure, and molecular cooling, (v) cosmic ray heating, and (vi) photoelectric heating. Below, I briefly describe each of these processes.

The total cooling rate $\Lambda_{\rm cool}$ is computed as follows

$$\Lambda_{\rm cool} = \Lambda_{\rm p} + \frac{Z}{Z_{\odot}}\Lambda_{\rm m} + \Lambda_{\rm C} + (1 - f_{\rm ssh})\Lambda_{\rm mol}, \tag{2.4.3}$$

where $\Lambda_{\rm p}$ is the net primordial cooling rate from two-body processes, $\Lambda_{\rm m}$ is the net metal cooling rate and $\Lambda_{\rm C}$ is the cooling due to the Compton scattering with the CMB photons, $Z/Z_{\odot}$ is the gas metallicity in solar units, $\Lambda_{\rm mol}$ is the low temperature cooling rate (equation 2.4.5) and $f_{\rm ssh}$ is the gas self-shielding. A primordial mixture of H and He (i.e. H, H^+, He, He^+, He^{++}) is affected by different processes: two-body processes (collisional excitation and ionization, recombination, dielectric recombination and bremmstrahlung emission), photoionization from a UV background and Compton cooling with the CMB photons. The **primordial net cooling rates** $\Lambda_{\rm p}$ are computed from ionization equations using rates from Cen (1992) and Katz et al. (1996). The metal cooling lines are computed from the CLOUDY photo-ionization code[5] (Ferland et al., 1998) assuming ionization equilibrium and a optically thin gas. In this way it is possible to compute $\Lambda_{\rm m}$ considering all metal lines for a given temperature and density (Smith et al., 2008). The Compton cooling off CMB photons rate is taken from Ikeuchi & Ostriker (1986)

$$\Lambda_{\rm C} = 5.41 \times 10^{-36} n_e T (1+z)^4 \ \ {\rm erg\ cm^{-3}\ s^{-1}}, \tag{2.4.4}$$

[5]This code balances the heating and the radiative cooling to find an equilibrium solution, accounting for all the transitions of the considered atomic species.

where n_e is the electron number density, T is the temperature of the gas and z is the redshift. For both the primordial and the metal cooling rates it is important to consider also the presence of a UV background in the CLOUDY calculations, this affects the thermal and ionization state of the gas (Efstathiou, 1992; Gnedin & Hollon, 2012) decreasing the cooling rates. The photoionization and photoheating rates are obtained from the space-uniform UV background from Faucher-Giguere et al. (2009), which includes the contribute from star-forming galaxies and quasars, where galaxies are dominants at redshifts $z > 3$. In our case the simulations are performed at redshift $z = 0$ and the background is consequently taken at this redshift.

An important feature of the *SMUGGLE* model is the presence of cooling processes from **low temperature** metal lines, fine structure and molecules lines that allow the gas to reach very low temperatures ($T \sim 10$ K) and, consequently, to form stars in high density and low temperature regions. This cooling channel is parameterized with the fit to the CLOUDY tables computed by Hopkins et al. (2018)

$$\Lambda_{\rm mol} = 2.896 \times 10^{-26} \left\{ \left(\frac{T}{125.215\ K} \right)^{-4.9202} + \left(\frac{T}{1349.86\ K} \right)^{-1.7288} + \left(\frac{T}{6450.06\ K} \right)^{-0.3075} \right\}^{-1} \times \left(0.001 + \frac{0.10 n_H}{1 + n_H} + \frac{0.09 n_H}{1 + 0.1 n_H} + \frac{(Z/Z_\odot)^2}{1 + n_H} \right) \times \left(\frac{1 + (Z/Z_\odot)}{1 + 0.00143 n_H} \right) \times \exp\left(- \left[\frac{T}{158000\ K} \right]^2 \right) \ \text{erg s}^{-1}\ \text{cm}^3. \tag{2.4.5}$$

Equation (2.4.5) is multiplied for the factor $(1 - f_{ssh})$ to account for the self-shielding of the gas, that consider the phenomenon for which a very dense gas can shield itself from the ultraviolet radiation. Considering a generic hydrogen cloud, in the outer parts the UV radiation can photoionize the hydrogen, but, as the density increases, fewer and fewer photons can reach the central zones of the cloud, effectively shielding the molecular gas. The self-shielding parameter f_{ssh} is defined as

$$f_{ssh} = (1 - f) \left[1 + \left(\frac{n_H}{n_0} \right)^{\beta} \right]^{\alpha_1} + f \left[1 + \frac{n_H}{n_0} \right]^{\alpha_2}, \tag{2.4.6}$$

where n_H is the neutral hydrogen number density and the parameters (α_1, α_2, β, f, n_0) pa-

rameterize the dependence of the self-shielding from the UV background with the redshift (see Table A1 in Rahmati et al. 2013) and have been obtained applying the radiation transfer code TRAPHIC to cosmological simulations (Pawlik & Schaye, 2008). In particular, for redshift $z = 0$ the set of parameters is: $\log(n_0/\mathrm{cm}^{-3}) = -2.94$, $\alpha_1 = -3.98$, $\alpha_2 = -1.09$, $\beta = 1.29$, $f = 0.01$. The self-shielding parameter f_{ssh} suppresses the heating and ionization rates used for the primordial network and also the input radiation field (i.e. the UV spectrum) given to the CLOUDY code for the metal line cooling calculations (the optically thin approximation is not realistic). f_{ssh} is also used for the computation of the low temperature cooling.

It is also important to consider heating processes such as **cosmic ray** (Field et al., 1969) and **photoelectric heating** (Wolfire et al., 2003), in fact they are thought to have a fundamental role in maintaining the stability of both the cold ($T \sim 50$ K) and the warm ($T \sim 8000$ K) phases of the ISM (Wolfire et al., 1995). **Cosmic ray heating** is taken from Guo & Oh (2008)

$$\Lambda_{\mathrm{CR}} = -10^{-16}(0.98 + 1.65)\tilde{n}_e e_{\mathrm{CR}} n_H^{-1} \ \mathrm{erg\ s^{-1}\ cm^3}, \tag{2.4.7}$$

where $\tilde{n}_e$ is the electron number density in units of the neutral hydrogen number density n_H and e_{CR} is the cosmic rays energy density that is parameterized as follows

$$e_{\mathrm{CR}} = \begin{cases} 9 \times 10^{-12} & \mathrm{erg\ cm^{-3}\ \ for}\ n_H > 0.01\ \mathrm{cm^{-3}} \\ \\ 9 \times 10^{-12}\left(\frac{n_H}{0.01\ \mathrm{cm^{-3}}}\right) & \mathrm{erg\ cm^{-3}\ \ for}\ n_H \leq 0.01\ \mathrm{cm^{-3}} \end{cases} . \tag{2.4.8}$$

Cosmic ray heating occurs through two main channels: hadronic collisions and Coulomb interactions between the cosmic rays and the electrons of the gas[6], represented, respectively, by the first and the second term in equation (2.4.7). This heating acts mainly on the dense gas, as seen in equation (2.4.8).

The second main heating process considered is **photoelectric heating**, driven by dust grains present in the interstellar medium. Photons from the radiation field, primarily UV radiation emitted by young, high-mass stars, interact with these dust grains via the photoelectric ef-

[6]Cosmic rays protons can interact with the thermal gas particles producing a cascade of particle that is mainly composed of π^+, π^- and π^0.

fect, extracting electrons from the grains. The heating occurs through Coulomb interactions between these ejected electrons and free electrons in the ISM. Polycyclic aromatic hydrocarbons (PAHs)[7] are the primary contributors to this process. The heating rate $\Lambda_{\rm phot}$ is taken from Wolfire et al. (2003)

$$\Lambda_{\rm phot} = -1.3 \times 10^{-24} \tilde{e}_v^{\rm pe} n_H^{-1} \left(\frac{Z}{Z_\odot} \right) \times \left(\frac{0.049}{1 + (x_{\rm pe}/1925)^{0.73}} + \frac{0.037 (T/10^4 \text{ K})^{0.7}}{1 + (x_{\rm pe}/5000)} \right) \text{ erg s}^{-1} \text{ cm}^3, \tag{2.4.9}$$

where

$$x_{\rm pe} \equiv \frac{\tilde{e}_v^{\rm pe} T^{0.5}}{\Phi_{\rm PAH} n_e}. \tag{2.4.10}$$

In equation (2.4.10) $\tilde{e}_v^{\rm pe}$ is the photon energy density in Milky Way units (known as Habing field; Habing 1968) and therefore it is set to $\tilde{e}_v^{\rm pe} = e_v^{\rm pe}/(3.9 \times 10^{-14} \text{ erg cm}^3) = 1$, $\Phi_{\rm PAH}$ is a parameter that incorporates the electron-PAH collision rates and is set to $\Phi_{\rm PAH} = 0.5$ from CI observations in the galactic plane (Jenkins & Tripp, 2001). The total heating rate is thus obtained as

$$\Lambda_{\rm heat} = \Lambda_{\rm CR} + \Lambda_{\rm phot}. \tag{2.4.11}$$

After accounting for all these processes, the total net cooling rate is obtained with equation (2.4.2).

2.4.2 Star formation

Another crucial aspect of the model is the implementation of star formation. Stars are modeled via collision-less particles (called star or stellar particles) and each of them represents a simple stellar population[8] (SSP). A SSP is characterized by an initial mass function (IMF) $\Phi(m)$, a function that parameterizes the mass distribution of the newly formed stars, giving

[7] The PAHs are chemical compounds formed by multiple aromatic rings of hydrogen and carbon, the naphtalene is the simpler one, having only two aromatic rings.

[8] A simple stellar population is an ideal stellar population in which all the stars: (i) are formed at the same time; (ii) have the same chemical composition.

the fraction of stars with a given mass inside the SSP. The integral of the IMF weighted on the mass of each star, m, is equal to the mass, $M_\star$, of the SSP (in this case the star particle) at its birth, i.e.

$$M_\star(t = t_0) = \int_{M_{\rm min}}^{M_{\rm max}} m\Phi(m)\, {\rm d}m, \tag{2.4.12}$$

where t_0 is the birth time of the star particle, $M_{\rm min} = 0.1$ M$_\odot$ and $M_{\rm max} = 100$ M$_\odot$. The choice of this function is extremely important because it determines, for instance, the rate of type II SNe explosions, affecting both the energy and momentum injection in the ISM and its chemical enrichment. In particular the *SMUGGLE* model uses a Chabrier (2003) IMF, characterized by a log-normal trend for low mass stars and by a power-law for high masses

$$\Phi(m) = \begin{cases} Am^{-1}\exp\left[-\dfrac{\log(m/m_c)^2}{2\sigma^2}\right] & \text{for } m \leq 1\ M_\odot \\ \\ Bm^{-2.3} & \text{for } m > 1\ M_\odot \end{cases}, \tag{2.4.13}$$

where $A = 0.852$, $B = 0.238$, $m_c = 0.079$ and $\sigma = 0.69$ are normalized to have a continuous transition at $M = 1\ M_\odot$. This IMF is top-heavy compared to the Salpeter (1955)[9] IMF, indicating that from the formation of a population of stars fewer low-mass and more high-mass stars are expected compared to the Salpeter case.

The star formation process is treated with a probabilistic approach based on the Springel & Hernquist (2003) model, in which a gas cell can turn into a star particle under certain conditions.

(i) At first, gas density must be above a density threshold $\rho_{\rm th}$ in order to allow for its gravitational collapse. Most of the star formation happens in the dense cores of giant molecular clouds in the spiral arms of the galaxy (Herbig, 1962; Cohen & Kuhi, 1979; Ward Thompson et al., 2002). The density of these systems is $\simeq 10^2 - 10^3$ cm^{-3} (Ferriere, 2001), therefore the threshold is set to $\rho_{\rm th} = 100$ cm^{-3} and the condition is

$$\rho > \rho_{\rm th}, \tag{2.4.14}$$

[9]The first derivation of the initial mass function, often used as a comparison due to its simple analytic form $\Phi(m) = km^{-2.35}$.

where ρ is the density of the gas cell.

(ii) The second condition restricts the star formation only to the regions that cannot resist to the gravitational collapse and therefore are gravitationally bound (Semenov et al., 2017). This information is encoded in the virial parameter defined for each gas cell i as (see Hopkins et al. 2018)

$$\alpha_i = \frac{||\nabla \otimes v_i||^2 + (c_{s,i}/\Delta x_i)^2}{8\pi G \rho_i}, \tag{2.4.15}$$

where $c_{s,i}$ is the sound speed, Δx_i is the cell size, ρ_i is the cell density, G is the gravitational constant. $||\nabla \otimes v_i||^2$ is the norm of the velocity gradient tensor[10], computed as

$$||\nabla \otimes v_i||^2 \equiv \sum_{i,j} \left(\frac{\partial v_i}{\partial x_j}\right)^2, \tag{2.4.16}$$

here v_i is the gas velocity of the i-th cell. The star formation is allowed only in gas cells with $\alpha < 1$.

If these two criteria are satisfied by a given gas cell i, the star formation rate (SFR) is computed as follows

$$\dot{M}_\star = \varepsilon \frac{M_{\rm gas}}{t_{\rm dyn}}, \tag{2.4.17}$$

otherwise it is set to zero. In equation (2.4.17) $M_{\rm gas}$ is the gas cell mass, ε is the star formation efficiency, set to $\varepsilon = 0.01$ as suggested by observations (e.g. Krumholz & Tan 2007), and $t_{\rm dyn}$ is the free fall time

$$t_{\rm dyn} = \sqrt{\frac{3\pi}{32 G \rho_{\rm gas}}}, \tag{2.4.18}$$

where $\rho_{\rm gas}$ is the gas density. From the SFR $\dot{M}_\star$ of a given gas cell i it is possible to derive the stellar mass $M_{\star,i}$ that has to be formed in a time-step Δt in that cell i as

$$M_{\star,i} = M_i \left[1 - \exp\left(-\frac{\dot{M}_\star \Delta t}{M_i}\right)\right], \tag{2.4.19}$$

[10] $\otimes$ is the outer product, e.g. $(u \otimes v)_{ij} = u_i v_j$.

where M_i is the mass of the i-th gas cell. The stellar mass formed in this way would be much smaller than the gas cell mass. For numerical reasons, it would be better if an entire given gas cell turned into a star particle in a certain time-step, in order to have a star particle mass similar to the mass of the gas particles. This can be implemented with a stochastic method that, on average, recovers the correct stellar mass formed per time-step across the whole galaxy in the following way. For each cell a random variable p^* uniformly distributed between 0 and 1 is extracted at each time step. The gas cell is then converted entirely into a star particle if $p^* < p$, where $p = 1 - \exp(-\dot{M}_\star \Delta t / M_i)$ is the fraction of the gas cell mass that would be converted in stars in a single time-step. In this way the correct stellar mass is formed in the galaxy at each time-step.

2.4.3 Stellar evolution model

The stellar evolution model adopted in *SMUGGLE* is the same described in Vogelsberger et al. (2013), with the addition of stellar mass loss from OB stars (see Section 2.4.6). The main mechanisms contributing to the return of mass and metals to the ISM that have been considered in the stellar evolution model are stellar winds from young and massive OB stars and from asymptotic giant branch (AGB) stars, and supernova explosions (type II and type Ia). In this Section I briefly summarize how the stellar evolution model works; more details on single evolutionary channels are given in Sections 2.4.4 and 2.4.6.

The mass and metal return from massive stars could be approximated using an instantaneous star evolution model (e.g. Steinmetz & Müller, 1994), this approach is valid for massive stars due to their relatively short lifespans (less than 10 Myrs). However, this model cannot be accurately applied to intermediate-mass stars, as their evolutionary timescales – and thus the timescales for mass return – are similar to or exceed galactic dynamical timescales. Notably, AGB stars return a significant portion of their mass to the ISM over lifetimes that can surpass a billion years. Likewise, Type Ia SNe, despite contributing less mass to the ISM, release substantial amounts of iron after significant delay times. These variations lead to time-dependent changes in both the mass return rate and the composition of the returned material, depending on which processes are dominant.

A more comprehensive approach to enrichment can be achieved by tracking the mass and metal return of a stellar population over time (Scannapieco et al., 2005). In the *SMUGGLE*

model, the time evolution of stellar particles is simulated, calculating both mass loss and chemical enrichment as continuous processes, except for SN explosions which are implemented as discrete events. The mass and metals that are returned to the ISM are tracked as a function of time, with an approach similar to Wiersma et al. (2009). In doing so, the stellar evolution is integrated in time in order to find the mass and metal losses at each time-step (see equations 2.4.20 and 2.4.23). What is assumed is that the evolution after the main sequence happens instantaneously, this is reasonable because the post main sequence phases are much shorter ($< 1/10$ of the entire life of the star). Therefore, after a certain lifetime each star loses some fraction of its mass with a certain metallicity. This time is parameterized with the stellar lifetime function $\tau(m, Z)$, depending on the mass m and metallicity Z of the star. This function is taken from Portinari et al. (1998) and it was obtained summing the hydrogen and helium burning phases length. From this function the inverted lifetime function $M(t = t_0 + \tau, Z)$ can be evaluated, that is the mass of a star leaving the main sequence at an age t (t_0 is the birth time of the star). The mass of gas that is returned to the ISM in a single time step Δt from a SSP can be obtained from the stellar recycling fraction $f_{\rm rec}(m, Z)$, i.e. the fraction of the initial mass of the star that is released in the ISM over its entire life. Depending on the mass m and on the metallicity Z the main contribution to this recycle of mass is different. For instance, more massive stars ($> 13 M_\odot$) will lose mass mainly through type II SNe, while low mass stars will have a greater contribution from the AGB phase. The total mass released in the ISM in a time-step Δt is

$$\Delta M_{\rm rec}(t, \Delta t, Z) = \int_{M(t+\Delta t)}^{M(t)} m f_{\rm rec}(m, Z) \Phi(m) {\rm d}m. \tag{2.4.20}$$

Also it is important to track the release of each element. The mass of a given element i recycled to the ISM in a time-step is given by

$$\Delta M_i(t, \Delta t, Z) = Z_i \int_{M(t+\Delta t)}^{M(t)} m f_{\rm rec}(m, Z) \Phi(m) {\rm d}m = Z_i \Delta M_{\rm rec}, \tag{2.4.21}$$

where Z_i is the initial mass fraction of the element i. In this case the chemical enrichment was not considered and therefore the released mass has the same chemical composition of the stellar particle at its birth.

Elements are processed by thermonuclear reactions during the lifetime of a star, bringing to a chemical composition of the ejected mass that differs from the initial one of the star. To include the presence of this chemical enrichment (in the model nine elements are tracked: H, He, C, N, O, Ne, Mg, Si, Fe), it is possible to define the yield of an element i, i.e. the net created mass for each element (these have to be obtained for each mass and metal return channel), as

$$y_i(m, Z) = M_{i,\mathrm{enrich}}(m, Z) - mZ_i f_{\mathrm{rec}}(m, Z), \tag{2.4.22}$$

Then, the mass of a given element returned to the ISM in a single time-step is defined as

$$\Delta M_i(t, \Delta t, Z) = \int_{M(t+\Delta t)}^{M(t)} (y_i + mZ_i f_{\mathrm{rec}}(m, Z))\Phi(m)\mathrm{d}m. \tag{2.4.23}$$

The yields for AGB stars are taken from Karakas (2010), for core collapse SNe are taken from Portinari et al. (1998), obtained using the Padova stellar evolution tracks (e.g. Bertelli et al. 2009) and the nucleosynthesis model from Woosley & Weaver (1986). Also the stellar recycling fractions $f_{\mathrm{rec}}(m, Z)$ have been obtained from these works. The yields for thermonuclear SNe are obtained from Thielemann et al. (2003) and Travaglio et al. (2004).

2.4.4 Feedback from supernovae

Supernova feedback is one of the main feedback processes that can occur in star-forming galaxies. It is thought to be fundamental in regulating star formation and the structure of the ISM (e.g. Agertz et al. 2011; Agertz et al. 2013) through injection of momentum and energy (Martizzi et al., 2015; Kim & Ostriker, 2018), while also being capable of generating turbulence (Martizzi et al., 2016) and ejecting multiphase gas into the CGM (Fielding & Bryan, 2022), distributing gas and metals into the galactic halo. Most of the times it functions as negative feedback for the star formation in the galaxy, heating the gas and generating superbubbles[11], which can reach the physical size of the disc scale height, thus causing the formation of outflows from the disc and creating the so-called galactic fountains (Chapter 1). One of the characteristics of the *SMUGGLE* model is the ability to self-consistently generate

[11] In an OB stars association multiple SNe can explode in a short time, each single bubble generated from the explosions can merge and form a superbubble.

galactic-scale outflows. In particular, the *SMUGGLE* model accounts for type II and type Ia SNe.

• **Type II supernovae** (core-collapse SNe) are considered to be the main injectors of mass and they release the majority of the α elements[12] in the ISM. These SNe explosions originate from the collapse of high-mass stars (approximately with a mass > 8 $M_\odot$). After the formation of an iron core there are no thermonuclear reactions possible to counterbalance the force of gravity and the core collapses on itself, making the envelope fall on it and generating a shock wave that creates the SN explosion.

• **Type Ia supernovae** (thermonuclear SNe) inject the majority of iron in the ISM. Type Ia explosions occur when a white dwarf (WD) activates the burning of the carbon in a degenerate environment causing the explosion of the structure. For this to happen, the WD must be in a binary system, and two main scenarios are possible: the double degenerate and single degenerate scenarios. The *double degenerate scenario* involves the presence of a WD binary system, the merger between these two objects can form a WD with a mass greater then the Chandrasekhar mass $M_{\rm ch} \sim 1.44$ $M_\odot$ (i.e. the limit mass that can be maintained in equilibrium via electron degeneracy pressure), bringing to the collapse of the structure and to the triggering of the carbon burning. In the *single degenerate scenario* the WD is in a binary system with a star that under certain conditions can lose mass that is subsequently accreted onto the WD until the carbon burning is triggered, in this situation it can happen at a mass $< M_{\rm ch}$, bringing to the so-called *Sub-Chandrasekhar Type Ia SNe*. The uncertainties on the progenitors of these SNe and on the time after the birth of a certain population at which these SNe explode make the parameterization of these phenomena not trivial.

Energy and momentum budget derivation

Here I describe how the number of SNe and the consequent release of energy and momentum are implemented in the *SMUGGLE* model. The total energy injected in the ISM by a single SN is defined as

$$E_{\rm SN} = f_{\rm SN} E_{51}, \tag{2.4.24}$$

[12] Elements formed in an alpha capture process, such as O, Ne, Mg and Si.

in our simulations $f_{\rm SN} = 1$, as the average energy released per SN in the ISM is $E_{51} \sim 10^{51}$ erg. I assume that the velocity of the blast wave is

$$v_{\rm SN} = \sqrt{\frac{2E_{\rm SN}}{M_{\rm SN}}}, \tag{2.4.25}$$

where $M_{\rm SN}$ is the mass ejected by the SN. Therefore, the SN momentum is obtained as

$$p_{\rm SN} = M_{\rm SN} v_{\rm SN} = \sqrt{2E_{\rm SN} M_{\rm SN}}. \tag{2.4.26}$$

As mentioned in Section 2.4.2, each stellar particle represents a simple stellar population. For this reason multiple SNe can explode in a single stellar particle at a given time-step Δt. Thus, it is important to compute the number of Type Ia ($N_{\rm SNIa}$) and Type II ($N_{\rm SNII}$) SNe at each time-step. In this way the total energy $E_{\rm SN,tot}$ and momentum $p_{\rm SN,tot}$ injected in the ISM can be obtained. These are defined for each star particle and each time-step as follows

$$E_{\rm SN,tot} = f_{\rm SN} E_{51} (N_{\rm SNII} + N_{\rm SNIa}), \tag{2.4.27}$$

$$p_{\rm SN,tot} = p_{\rm SNII,tot} + p_{\rm SNIa,tot} = \sqrt{2N_{\rm SNII} E_{\rm SN} M_{\rm SNII,tot}} + \sqrt{2N_{\rm SNIa} E_{\rm SN} M_{\rm SNIa,tot}}, \tag{2.4.28}$$

where $M_{\rm SNII,tot}$ and $M_{\rm SNIa,tot}$ are the total ejecta mass of the Type II and Type Ia SNe.

The total number and the total ejecta mass of Type II SNe are found integrating the initial mass function $\Phi(m)$ (see equation 2.4.13) (Vogelsberger et al., 2013)

$$N_{\rm SNII} = \int_{\rm M(t+\Delta t)}^{\rm M(t)} \Phi(m)\, {\rm d}m, \tag{2.4.29}$$

$$M_{\rm SNII,tot} = \int_{\rm M(t+\Delta t)}^{\rm M(t)} m f_{\rm rec}(m, Z) \Phi(m)\, {\rm d}m, \tag{2.4.30}$$

where $f_{\rm rec}(m, Z)$ is the mass released from a single star with a mass m and a metallicity Z (Portinari et al., 1998) and $M(t)$ is the mass of a star leaving the main sequence at an age t (as

already explained in Section 2.4.3), it is assumed that only stars between $M_{\rm SNII,min} = 8\ M_\odot$ and $M_{\rm SNII,max} = 100\ M_\odot$ can explode as Type II SNe. It is worth noting that the number of Type II SNe is strongly dependent on the chosen IMF because the latter determines the fraction of stars with $M > 8\ M_\odot$.

The timing of Type Ia SNe, specifically the delay between the formation of a stellar population and the eventual SN explosion, remains uncertain. Unlike Type II SNe, where the explosion time can be predicted based on the progenitor star mass (more massive stars will explode at earlier times), Type Ia SNe are more difficult to constrain. This uncertainty arises from several factors: the unclear nature of their progenitors (whether they follow the single or double degenerate scenario), ambiguities in the true shape of the IMF, and the uncertain fraction of binary systems (which, as explained, are thought to be essential for Type Ia SNe). As a result of this, the rates at which Type Ia SNe occur are not well understood or tightly constrained.

In *SMUGGLE* the rate has been parameterized with a delay time distribution (DTD) of SNe Ia events (e.g. Dahlen et al., 2004; Strolger et al., 2004; Greggio, 2005; Mannucci et al., 2006; Castrillo et al., 2021). The rates of Type Ia SNe ($\rm SNR_{Ia}$) should follow the SFR of the galaxy, but with a certain delay time, as they need the presence of a WD, the final state in the evolution of low-mass stars. Hence, the $\rm SNR_{Ia}$ can be obtained with a convolution of the star formation history SFR(t) over the DTD

$$\rm SNR_{Ia} = \int_0^t SFR(t')DTD(t - t')\ dt'. \tag{2.4.31}$$

The star formation history of an SSP is a Dirac delta function centered on the birth time of the population. The number of type Ia SNe at a certain time-step Δt is, therefore,

$$N_{\rm SNIa} = \int_t^{t+\Delta t} \rm DTD(t')dt'. \tag{2.4.32}$$

The delay time distribution is defined as a power-law in time (Maoz et al., 2012)

$$\rm DTD(t) = \Theta(t - \tau_8)N_0\left(\frac{t}{\tau_8}\right)^{-s}\frac{s-1}{\tau_8}, \tag{2.4.33}$$

where $\Theta(t-\tau_8)$ is the Heaviside step function[13], which parameterizes the delay between the birth of the stellar population and the explosion of the first Type Ia SN. This means that $\mathrm{SNR_{Ia}} = 0$ for $t < \tau_8$, for this reason Type Ia and Type II SNe occur on different time scales. In equation (2.4.33) $\tau_8 = 40$ Myr is the main sequence life time of an 8 $M_\odot$ star, $s = 1.12$ and $N_0 = 2.6 \times 10^{-3}$ SN $M_\odot^{-1}$. Due to the nature of type Ia SN explosions the ejected mass is constant and given by $M_{\mathrm{SNIa}} \sim 1.37$ $\mathrm{M_\odot}$ $\mathrm{SN^{-1}}$. Therefore, the total mass ejected in a time-step by a single star particle is

$$M_{\mathrm{SNIa,tot}} = M_{\mathrm{SNIa}} N_{\mathrm{SNIa}}. \tag{2.4.35}$$

The metal return for both type II and type Ia SNe is computed from the stellar yields as mentioned in Section 2.4.3. The method used to distribute the mass and the metals in the ISM is described in detail in Section 2.4.4.

SN explosions are modelled as discrete events, so, to ensure this characteristic a particular time-step $\Delta t_\star$ for the stellar particles is imposed (see Section 2.3.4 for the AREPO time-step constraints)

$$\Delta t_\star = \min\Big(\Delta t_{\mathrm{grav}}, \Delta t_{\mathrm{evol}}\Big), \tag{2.4.36}$$

Δt_{grav} is the gravitational time-step and Δt_{evol} is defined as

$$\Delta t_{\mathrm{evol}} = \min\left(\Delta t_{\mathrm{SNII}}, \frac{t_{\mathrm{age}}}{300}\right) \mathrm{yr}, \tag{2.4.37}$$

where $\Delta t_{\mathrm{SNII}} = \tau_8 / N_{\mathrm{SNII,8}}$, $N_{\mathrm{SNII,8}}$ is the number of type II SNe over a time τ_8. These parameters are computed consistently with the stellar evolution model (Section 2.4.3). With this time-step limit a rate of ~ 1 SN per time-step is expected.

Hence, at each time-step for each star particle the total number N_{SN} of type II and type Ia SNe in a time step $\Delta t_\star$ is computed with equations (2.4.29) and (2.4.32). Then, to obtain the

[13]The Heaviside step function is defined as

$$\Theta(t-\tau_8) = \begin{cases} 1 & \text{for } t \geq \tau_8 \\ 0 & \text{for } t < \tau_8. \end{cases} \tag{2.4.34}$$

actual number of SNe, $N_{\rm SN} = \lambda$ is used as the expectation value of a Poisson distribution

$$P(n;\lambda) = \frac{\lambda^n \mathrm{e}^{-\lambda}}{n!}, \tag{2.4.38}$$

from which the actual number of events per time-step $\Delta t_\star$ is sampled; that will usually be 0 or 1 SN events per time-step due to the time-step limit. From these quantities the energy, the momentum ejected from the star particle in the ISM (equations 2.4.27 and 2.4.28) and the mass and metals return are obtained.

Sedov-Taylor phase

One problem in modeling SN feedback, that arises due to insufficient resolution of galaxy scale simulations ($\sim 10 - 100$ pc), is how to properly describe the Sedov-Taylor phase of the SN remnant in which most of the momentum imparted to ISM is generated. To accurately capture the momentum generation, the model explicitly accounts for the momentum boost occurring during the Sedov-Taylor phase with a formulation derived from individual, high-resolution SN simulations. The momentum obtained with equation (2.4.28) underestimates the real one, due to the limited resolution of galaxy formation simulations that does not allow one to fully resolve the cooling radius of the supernova remnant. An analytical expression of the cooling radius, from which it is apparent that this scale can be at best only marginally resolved in our simulations, is given by (Cioffi et al., 1988)

$$r_{\rm cool} = 28.4 E_{51}^{2/7} \langle n \rangle^{-3/7} f(Z) \text{ pc}, \tag{2.4.39}$$

where E_{51} is the SN energy in units of 10^{51} erg, $\langle n \rangle$ is the average density within the cooling radius and $f(Z)$ is defined in equation (2.4.41).

The aim is to impart to the gas the final momentum that would naturally result from SN remnant evolution if sufficient resolution were available to resolve the cooling radius and, consequently, the Sedov-Taylor phase. Instead, due to the limited resolution of our calculations, energy and mass are returned to the ISM on scales larger than $r_{\rm cool}$. The momentum boost generated by the Sedov-Taylor phase is not negligible and, therefore, it has to be accounted in the model. High-resolution simulations of the evolution of SN remnants in a

variety of environments (e.g. Cioffi et al. 1988) suggest that the value of the terminal momentum p_t (that remains constant from the momentum-conserving phase of the SN) is

$$p_t = 4.8 \times 10^5 E_{\rm SN,tot}^{13/14} \left(\frac{\langle n_H \rangle}{1\ {\rm cm}^{-3}} \right)^{-1/7} f(Z)^{3/2}\ {\rm M}_\odot\ {\rm km\ s}^{-1}, \tag{2.4.40}$$

where $\langle n_H \rangle$ is the neutral hydrogen number density averaged around the star particle with weights determined with an SPH kernel (see equation 6.2.1) and

$$f(Z) = \min \left[\left(\frac{\langle Z \rangle}{Z_\odot} \right)^{-0.14}, 2 \right], \tag{2.4.41}$$

where $Z_\odot = 0.0127$ is the solar metallicity and $\langle Z \rangle$ is the gas metallicity averaged around the star particle in the same way of $\langle n_H \rangle$.

The momentum that is added to each gas particle influenced by a SN explosion is increased by an amount

$$\Delta p_i = \tilde{w}_i {\rm min} \left[p_{\rm SN,tot} \sqrt{1 + \frac{m_i}{\Delta m_i}}, p_t \right]. \tag{2.4.42}$$

Here, the term $p_{\rm SN,tot}\sqrt{1 + m_i/\Delta m_i}$, comes from the energy conservation, m_i is the gas cell mass and $\Delta m_i = \tilde{w}_i (M_{\rm SNII,tot} + M_{\rm SNIa,tot})$. p_t is the terminal momentum and $\tilde{w}_i$ (defined in equation 6.2.3) is a weight function used to divide the energy and the momentum injected from the SN explosion. Also, to compute the correct terminal momentum for a star particle in a time-step Δt, the terminal momentum p_t has to be multiplied by the total number of SNe ($N_{\rm SNII} + N_{\rm SNIa}$) that occurs in the time-step in that star particle.

Supernova energy and momentum coupling

The energy and momentum (but also mass and metals) that come from SNe explosions (and also from other feedback channels) have to be injected in the gas cells around the star particles. This is done using weight functions. The number of neighbours cells that are influenced by stellar feedback is defined as

$$N_{\rm ngb} = \frac{4\pi}{3} h^3 \sum_i W(|\mathbf{r}_i - \mathbf{r}_s|, h), \tag{2.4.43}$$

where W is the standard cubic spline SPH kernel (Monaghan & Lattanzio, 1985), h is a search radius and $|\mathbf{r}_i - \mathbf{r}_s|$ is the distance between the gas cell and the star particle. Equation (2.4.43) is solved iteratively in order to find the parameter h with a predetermined value of $N_{\rm ngb}$. In my simulations I set $N_{\rm ngb} = 64$.

To avoid numerical instabilities, Marinacci et al. (2019) imposed a limit to the radius within which the gas cells are affected by feedback. The coupling scale $h_{\rm coupling}$ is limited to a maximum radius $R_{\rm SB}$, which in our simulations is fixed at 0.86 kpc, however, the coupling scale for the injection of mass and metals is always set to h to ensure mass and metal conservation.

Finally, for each gas cell i the weights are defined as

$$w_i = \frac{\Delta\Omega_i}{4\pi} = \frac{1}{2}\left\{1 - \frac{1}{[1 + A_i/(\pi|\mathbf{r}_i - \mathbf{r}_s|^2)]^{1/2}}\right\}, \tag{2.4.44}$$

where $A_i = \pi\Delta x_i^2$ is the gas cell area. In this way each gas cell within $h_{\rm coupling}$ receives a fraction of energy and momenta (while mass and metals are returned within the scale h) proportional to the fraction of the solid angle 4π covered by the cell as seen from the stellar particle position. The total energy and momentum (equations 2.4.27 and 2.4.28) is injected in each gas cell multiplied by the factor

$$\tilde{w}_i = \frac{w_i}{\sum_i w_i}, \tag{2.4.45}$$

which ensures that each cell receives the correct amount of momentum and energy.

2.4.5 Radiative feedback

Radiative feedback is thought to be important for the thermal and dynamical state of the ISM. It can affect its temperature through photoionization by young massive stars and it can inject additional momentum thanks to radiation pressure. Also, this feedback channel is important due to its timing, in fact the majority of energy and momentum is released before the first SN explosions (Murray et al., 2009; Lopez et al., 2011; Walch et al., 2012), therefore, it can disperse giant molecular clouds, setting a low-density environment and making SN feedback more efficient. Because it occurs before SN explosions it is also known as being part

of the so-called *early stellar feedback* (Smith et al., 2022). Observations and theoretical studies agree that radiation has an important impact on star formation at the scales of individual stars (Rosen et al., 2016), clumps (Hopkins & Grudić, 2019), giant molecular clouds (Howard et al., 2016), and clusters (Grudić et al., 2018).

Photoionization

Young and massive stars (OB stars) are one of the main sources of photoionization in disc galaxies. Photoionization is necessary to sustain HII regions, that can expand and disrupt giant molecular clouds, the warm interstellar medium , and the UV background (Tielens, 2005). Photoionization is a process in which a bound electron absorbs a photon with energy high enough to remove it from the atom. In particular, for neutral hydrogen the process is

$$\mathrm{H} + h\nu \rightarrow \mathrm{H}^{+} + e^{-}, \tag{2.4.46}$$

where the neutral hydrogen H is photoionized only by photons with an energy $E = h\nu > 13.6$ eV. These high-energy UV photons are abundantly produced by OB stars. Around these stars this process forms the HII regions (i.e. the so-called Strömgren sphere), in which the hydrogen is completely photoionized within the Strömgren radius (the size of the HII region) and neutral outside of it.

In the *SMUGGLE* model the ionizing photon rate emitted by a single star particle is parameterized as

$$N_{\star} = \frac{L_{\star}}{\langle h\nu \rangle} = \frac{\gamma_{\star} M_{\star}}{\langle h\nu \rangle}, \tag{2.4.47}$$

where $L_{\star}$ is the star particle luminosity and $M_{\star}$ is the star particle mass. $\gamma_{\star} = 10^3\ L_{\odot}/M_{\odot}$ is the mass-to-light ratio and $\langle h\nu \rangle = 17$ eV is the average photon energy above 13.6 eV, which corresponds to the peak emission of a black-body with a temperature $T \sim 40000$ K, consistent with the properties of OB stars (Rybicki & Lightman, 1991).

The photoionizing photons (E>13.6 eV) are all absorbed by the hydrogen within the Strömgren radius, that is most of the times smaller than the effective coupling scale h_{coupling}. For this reason a probabilistic approach is used. For each gas cell the probability of being photoionized can be defined as

$$\mathcal{P} = \frac{n_\star}{\alpha_{\rm rec} n_H^2 V}. \tag{2.4.48}$$

This probability is derived assuming that the ionizing photon rate, scaled by the same weights used for the SN explosions, is equal to the recombination rate $\dot{N}_{\rm rec}$ (i.e. the number of recombination per second)

$$n_\star = \dot{N}_{\rm rec} = \alpha_{\rm rec} n_H^2 V, \tag{2.4.49}$$

where $n_\star = \tilde{w}_i N_\star$, $V = 4/3\pi\Delta r^3$ is the cell volume, $n_H = X\rho/m_p$ is the average hydrogen number density in the cell (X is the hydrogen mass fraction and m_p is the proton mass) and $\alpha_{\rm rec} = 2.6 \times 10^{-13}$ cm^3 s^{-1} is the hydrogen recombination rate.

A gas cell is considered photoionized if three conditions are satisfied, in this case the temperature of the gas cell is set to $T_{\rm phot} = 1.7 \times 10^4$ K[14] and its cooling is disabled for a time $t_{\rm off}$, equal to the star particle time-step $\Delta t_\star$:

(i) First, a number $\mathcal{P}'$ is extracted randomly between 0 and 1, the gas cell is eligible for photoionization if $\mathcal{P}' < \mathcal{P}$.

(ii) The thermal energy per mass unit of the gas cell must be $u_{\rm therm} < 1.2 u_{\rm phot}$, where $u_{\rm phot}$ is the thermal energy per mass unit corresponding to $T_{\rm phot}$.

(iii) The cooling in the gas cell must be active, therefore $t_{\rm off} = 0$.

If one of the conditions (ii) and (iii) is not satisfied it means that the gas cell is already photoionized. This mechanism causes the formation of a region with a higher pressure with respect to the external neutral environment, causing the expansion of the HII region.

Radiation pressure

Another source of momentum is the pressure generated from the radiation emitted by young massive stars. The total momentum injected in a time-step Δt from a star particle is defined as

$$\Delta p = \frac{L_\star}{c}(1 + \tau_{\rm IR})\Delta t, \tag{2.4.50}$$

[14]The temperature of a hydrogen gas ionized from photons with $\langle h\nu \rangle = 17$ eV.

where $L_\star = \gamma_\star M_\star$ is the star particle luminosity, c is the light speed and $\tau_{\rm IR} = \kappa_{\rm IR}\Sigma_{\rm gas}$ is the gas optical depth to infrared radiation. $\kappa_{\rm IR} = 10(Z/Z_\odot)$ cm^2 g^{-1} is the opacity in the infrared band and $\Sigma_{\rm gas}$ is the gas column density, defined using a Sobolev approximation. In particular, the Sobolev length for each star particle j is (see Hopkins et al. 2018)

$$l_j = h_{\rm coupling,j} + \frac{\rho_j}{||\nabla\rho_j||}. \tag{2.4.51}$$

Here, ρ_j and $\nabla\rho_j$ are the gas density and its gradient, computed with a SPH approach. Then, the gas column density is obtained as

$$\Sigma_{\rm gas,j} = \langle\rho_s\rangle_j l_j, \tag{2.4.52}$$

where

$$\langle\rho_s\rangle_j = \sum_j W(|\mathbf{r}_i - \mathbf{r}_j|, h)m_i. \tag{2.4.53}$$

In equation (2.4.53), W is the cubic spline SPH kernel, $|\mathbf{r}_i - \mathbf{r}_j|$ is the distance between the gas cell and the star particle, m_i is the mass of the i-th gas cell and h is the coupling scale obtained solving equation (6.2.1).

This momentum is injected at each time-step in the gas cells around the star particle in the same way described in Section 2.4.4 for SNe (within $h_{\rm coupling}$). Also, the same maximum coupling radius $R_{\rm SB}$ is used for both photoionization and radiation pressure.

2.4.6 Feedback from stellar winds

Another important feedback source is represented by stellar winds. The *SMUGGLE* model accounts for stellar winds generated by two classes of stars: young and massive OB type stars and asymptotic giant branch (AGB) stars. These provide two channels of feedback that act at different moments. At early times winds from OB stars play an important role, in fact they can pre-process the environment dispersing the dense gas clouds, leading to a more efficient SN feedback, with a role similar to the radiative feedback (Matzner, 2002; Krumholz & Matzner, 2009). Stellar winds can also be an important feedback source at later times through AGB winds, injecting momentum and energy in the ISM.

It is worth noting that the different feedback channels considered in *SMUGGLE* have an

integrated specific momentum, defined as $\int p(t)/m_\star \mathrm{d}t$, of the same order of magnitude but that is released on different time scales. Different channels of feedback act at different times (see Agertz et al. 2013): the first is the momentum injection from stellar winds and radiative feedback that acts before the explosion of the first SNe, confirming their role in pre-processing the gas. At later times, feedback is dominated by SNe explosions.

Stellar winds in *SMUGGLE* are implemented as follows. First, the mass loss for the two type of stars is derived. The cumulative mass loss per stellar unit mass for OB stars is parameterized as

$$m_{\mathrm{closs}} = \begin{cases} f(t) \ \text{ if } \ t > 1 \ \mathrm{Myr} \\ g(t) \ \text{ if } \ 1 \ \mathrm{Myr} < t < 3.5 \ \mathrm{Myr} \\ h(t) \ \text{ if } \ 3.5 \ \mathrm{Myr} < t < 100 \ \mathrm{Myr} \end{cases} , \tag{2.4.54}$$

where

$$\begin{cases} f(t) = 4.763 \times 10^{-3}(0.01 + \tilde{Z})t \\ \\ g(t) = 4.763 \times 10^{-3}(0.01 + \tilde{Z})\dfrac{t^{2.45+0.8\log(\tilde{Z})} - 1}{2.45 + 0.8\log(\tilde{Z})} + f(1) \\ \\ h(t) = g(3.5) - 4.57 \times 10^{-2}\left[\left(\dfrac{t}{3.5}\right)^{-2.25} - 1\right] + 4.2 \times 10^{-6}(t - 3.5) \end{cases} , \tag{2.4.55}$$

here $\tilde{Z}$ is the star particle metallicity in solar units and for $t > 100$ Myr $m_{\mathrm{closs}} = h(100)$.

The mass and metal losses from AGB stars are treated with the Arepo stellar evolution model from Vogelsberger et al. (2013) (see Section 2.4.3). Then, the mass loss by a star particle with a mass $M_\star$ in a time-step Δt is computed as

$$M_{\mathrm{loss}} = M_\star[m_{\mathrm{closs}}(t + \Delta t) - m_{\mathrm{closs}}(t)]. \tag{2.4.56}$$

In particular, OB stellar winds are considered only for times smaller then the life time of a 8 $M_\odot$ star (i.e. the smaller progenitor of a type II SN).

The energy E_{winds} and momentum p_{winds} injected around the stellar particle at a given

time-step Δt are defined as

$$E_{\rm winds} = \Delta t L_{\rm kin} = M_{\rm loss} \times \Psi \times 10^{12}\ {\rm erg\ g^{-1}}, \tag{2.4.57}$$

where

$$\Psi = \frac{5.94 \times 10^4}{1 + \left(\frac{t_{\rm Myr}}{2.5}\right)^{1.4} + \left(\frac{t_{\rm Myr}}{10}\right)^{5}} + 4.83, \tag{2.4.58}$$

and

$$p_{\rm winds} = \sqrt{2 M_{\rm loss} E_{\rm winds}}. \tag{2.4.59}$$

The assignment of these two quantities to the gas cells near the star particle is performed as in the supernova case (Section 2.4.4). The main difference is that stellar winds are a continuous process, unlike SNe which explode in a discrete manner, and are implemented accordingly.

Chapter 3

Initial conditions

Initial conditions (ICs) consist of a set of N particles, each assigned with specific physical properties such as position and velocity at the beginning of the simulation, which serve as the starting point for computing the hydrodynamical N-body evolution. Collision-less particles, such as dark matter and stars, are characterized by initial positions (x, y, z) and velocities (v_x, v_y, v_z). In contrast, collisional particles, like gas particles, require additional properties, such as temperature (derived from internal energy) and metallicity. I generated the ICs for my isolated galaxy simulations (Chapters 4 and 5) extending the method described in Springel et al. (2005, see also Hernquist 1993 and Springel 2000) to include an extended hot gaseous structure surrounding the galaxy. This approach allows to build a multi-component galaxy with the different parts of the system in approximate equilibrium, including a dark matter halo and a bulge with Hernquist density profiles, exponential stellar and gaseous disks, and a galactic corona (i.e. the hot phase of the CGM) modeled with a β-profile. Each component is built following observational constraints.

I show the density profiles and velocity distributions of the dark matter halo and bulge in Section 3.1 which will be used for the sampling of the ICs. The corresponding properties for the stellar and gaseous disks are discussed in Section 3.2, while the galactic corona is covered in Section 3.3. Finally, Section 3.4 details the numerical implementation of the ICs.

3.1 Dark matter halo and bulge

In this Section we describe the structural and kinematic properties of the model used to sample the ICs of the dark matter halo and the stellar bulge.

3.1.1 Dark matter halo and bulge density profile

The **dark matter halo** is modelled using a spherical Hernquist (1990) profile

$$\rho_{\rm dm}(r) = \frac{\mathrm{M}_{\rm dm}}{2\pi}\frac{a}{r(r+a)^3}, \tag{3.1.1}$$

where a is the scale radius, $\mathrm{M}_{\rm dm}$ is the total mass of the dark matter and $r = \sqrt{x^2+y^2+z^2}$ is the spherical radius. This profile has been chosen over a Navarro, Frenk and White profile (Navarro et al., 1997) due to the fact that the Hernquist profile in the outer parts goes as $\rho(r) \propto r^{-4}$, so for $r \to +\infty$ the total mass converges, making it a more realistic configuration. Instead, the NFW profile goes as $\rho(r) \propto r^{-3}$ and a truncation of the profile is needed to have a finite mass. In my isolated simulations the dark matter is modeled as a static gravitational potential to reduce computational time, thus the properties of the dark matter density distribution are not further analyzed. If a live dark matter halo is required, it can be sampled using the same method employed for generating the ICs for the bulge, as both components use the same models.

The **bulge** is assumed to be spherical and is also modelled with a Hernquist profile

$$\rho_{\rm b}(r) = \frac{\mathrm{M}_{\rm b}}{2\pi}\frac{b}{r(r+b)^3}, \tag{3.1.2}$$

where M_b is the total mass of the bulge and b is the bulge scale length. From the Hernquist profile the cumulative mass function (i.e. the mass enclosed within a radius r) can be derived analytically integrating the density profile as

$$\mathrm{M}_{\rm b}(r) = 4\pi\int_0^r \rho_{\rm b}(r')r'^2\,\mathrm{d}r' = \mathrm{M}_{\rm b}\left(\frac{r}{r+a}\right)^2, \tag{3.1.3}$$

this physical quantity will be used to sample the particles positions (Section 3.4), making sure that they follow the analytic density profile.

The bulge mass is defined as $M_b = M_{200} m_b$, where m_b is the bulge mass fraction and M_{200} is the virial mass of the system (the mass of the system contained within the virial radius r_{200}[1]). The mass of the dark matter halo is assumed to be the difference between M_{200} and the mass of all the other components of the system (see the upcoming sections of this Chapter for their detailed description).

3.1.2 Bulge velocity structure

Here we provide a theoretical description for the bulge velocity structure (which is applicable also to the dark matter halo). This will be important to define the three velocity components (v_x,v_y,v_z) for each particle.

For spherical, non-collisional structures, it can be assumed that the distribution function depends only on the energy and the z-component of the angular momentum L_z, this happens because the bulge is a spherical structure inside an axisymmetric potential. Under this assumption, certain velocity momenta vanish: the mixed second-order momenta $\langle v_R v_\phi \rangle = \langle v_R v_z \rangle = \langle v_\phi v_z \rangle = 0$, as well as the first momenta in the radial and vertical directions $\langle v_R \rangle = \langle v_z \rangle = 0$ (Binney & Tremaine, 2011). In the case of a Hernquist profile the distribution function of the system are known and deriving the velocities can be straightforward. However, to build a more general method I rely on the Jeans equations to estimate the particle velocity distribution for the bulge, using what is known as the **Gaussian approximation**. In this approach, it is assumed that at each point r, the velocities (v_R, v_z, v_ϕ) in cylindrical coordinates follow a tri-axial Gaussian distribution. These velocities are then randomly sampled from this distribution. Specifically, v_R is treated as a normal distribution with a dispersion of σ_R and a mean value of $\langle v_R \rangle$. Similarly, v_ϕ and v_z are distributed with dispersions σ_ϕ and σ_z, and their respective mean values $\langle v_\phi \rangle$ and $\langle v_z \rangle$. While this method does not provide the exact equilibrium distribution, it offers a reasonable approximation for generating ICs that place the system in a state of near equilibrium. After the velocities have been sampled from their Gaussian distributions, they are converted into Cartesian coordinates using the procedure outlined in Section 3.4.2.

[1]The virial radius, often denoted as r_{200}, is a measure to define the boundary of a system. It represents the radius within which the average density of the galaxy is 200 times the critical density of the Universe.

The non-vanishing second-momenta can be obtained from the Jeans equations as:

$$\langle v_z^2 \rangle = \langle v_R^2 \rangle = \frac{1}{\rho} \int_z^\infty \rho(z, R) \frac{\partial \Phi}{\partial z} \, \mathrm{d}z \, , \tag{3.1.4}$$

$$\langle v_\phi^2 \rangle = \langle v_R^2 \rangle + \frac{R}{\rho} \frac{\partial (\rho \langle v_R^2 \rangle)}{\partial R} + v_c^2, \tag{3.1.5}$$

where $v_c = R \, \partial \Phi / \partial R$ is the circular velocity, ρ is the density of the bulge, $\langle v_\phi^2 \rangle$ is the azimuthal second order velocity moment, $\langle v_R^2 \rangle$ is the radial second order velocity moment and Φ is the total gravitational potential, which includes the contribution of all galaxy components. Also, a mean streaming component in the azimuthal direction $\langle v_\phi \rangle$ can be present. The velocity dispersion in the azimuthal direction is then

$$\sigma_\phi^2 = \langle v_\phi^2 \rangle - \langle v_\phi \rangle^2, \tag{3.1.6}$$

where $\langle v_\phi \rangle$ is the mean the azimuthal velocity. I assume that the bulge has no net rotation, this implies that the mean streaming component is set to zero.

3.2 Stellar and gaseous discs

In this Section we discuss the radial (Subsection 3.2.1) and vertical (Subsection 5.4) structures of both stellar and gaseous discs. Furthermore, in Subsection 3.2.3 we describe the procedure used to set the disc scale length and in Subsection 3.2.4 we describe how the velocity distribution of the discs particles are sampled.

3.2.1 Radial discs structure

Observationally it has been shown that disc galaxies have radial exponential profiles (Freeman, 1970; Van Der Kruit & Searle, 1981; Courteau et al., 1996; Portinari & Salucci, 2010), for this reason the stellar and the gaseous discs have been modeled with exponential surface density profiles

$$\Sigma_*(R) = \frac{M_*}{2\pi h_*^2}\exp(-R/h_*)\ , \tag{3.2.1}$$

where $* = \star$ for stars and $* = \mathrm{g}$ for gas. h_* is the scale length and M_* is the mass of the stellar/gaseous disc, while R is the cylindrical radius, defined as $R = \sqrt{x^2 + y^2}$. The radial cumulative mass profiles for the stellar and gaseous discs are given by

$$M_*(R) = 2\pi \int_0^R \rho_*(R')R'\,\mathrm{d}R' = M_*\left[1 - \left(1 + \frac{R}{h_*}\right)e^{-R/h_*}\right]. \tag{3.2.2}$$

I set $M_d = M_\star + M_g = m_d M_{200}$, where m_d is the mass fraction of the discs (summing the contributes from stellar and gaseous discs). All the parameters of my galaxy models are shown in Chapter 4 and 5.

3.2.2 Vertical discs structure

Vertically the stellar disc follows a sech^2 profile, that corresponds to isothermal sheets perpendicular to the disc plane (Spitzer Jr, 1942; Bahcall & Soneira, 1980; Binney & Tremaine, 2008)

$$\rho_\star(R, z) = \frac{\Sigma_\star(R)}{2z_0}\mathrm{sech}^2\left(\frac{z}{z_0}\right), \tag{3.2.3}$$

where $\rho_\star(R, z)$ is the stellar density and z_0 is a free parameter that determines the scale height of the stellar disc.

The velocity structure of the stars is set so that the vertical scale height of the stellar disc is self-maintained in equilibrium in the total gravitational potential of the galaxy. This cannot be done for the gaseous disc, where the vertical distribution has to be determined by solving the vertical hydrostatic equilibrium equation, i.e. by the balance between the gas pressure and gravity (including gas self-gravity):

$$\frac{1}{\rho_g}\frac{\partial P}{\partial z} + \frac{\partial \Phi}{\partial z} = 0. \tag{3.2.4}$$

In Eq. (3.2.4), ρ_g is the density, P is the pressure of the gas and Φ is the total gravitational potential. For a given potential Φ the solution of this equation is given by the integral con-

straint

$$\Sigma_g(R) = \int_{-\infty}^{+\infty} \rho_g(R, z)\, \mathrm{d}z, \tag{3.2.5}$$

where $\Sigma_g(R)$ is the gas surface density described in Eq. (3.2.1) and $\rho_g(R, z)$ is the gaseous disc density. The gas density distribution is obtained through an iterative method, an initial potential Φ is assumed and with this initial estimate the gas surface density is obtained solving equations (3.2.4) and (3.2.5), integrating the differential equation assuming a chosen central density at $z = 0$, this starting value is adjusted until the desired surface density is found. Then, a new potential is computed with the new surface density distribution using a hierarchical multipole expansion based on a tree code and the whole process is repeated until the convergence is reached, i.e. when the desired surface density at each radius is obtained.

3.2.3 Stellar disc scale length

The scale length of the stellar disc $h_\star$ is calculated by relating it to the angular momentum of the disc assuming that the latter is related to the total angular momentum of the dark matter halo (Mo et al., 1998; Springel & White, 1999). From cosmological N-body simulations it emerges that dark matter halos begin to rotate because of the tidal forces between them, as they are not perfectly spherical. The baryons that collapse inside the halo potential will then have a certain angular momentum. Considering a NFW profile, it is possible to calculate the total energy of the halo truncated at r_{200} from the virial theorem as

$$E = -\frac{GM^2}{2r_{200}} f_c, \tag{3.2.6}$$

where M is the virial mass of the dark matter halo and f_c can be computed from the concentration parameter

$$f_c = \frac{c}{2} \frac{1 - 1/(1+c)^2 - 2\ln(1+c)/(1+c)}{[c/(1+c) - \ln(1+c)]^2}. \tag{3.2.7}$$

It is often convenient to define a dimensionless spin parameter λ, that characterizes the angular momentum J, as

$$\lambda = \frac{J|E|^{1/2}}{GM_{200}^{5/2}}. \tag{3.2.8}$$

From which it is straightforward to derive

$$J = \lambda G^{1/2} M_{200}^{3/2} r_{200}^{1/2} \left(\frac{2}{f_c}\right)^{1/2}, \tag{3.2.9}$$

λ is a free parameter in my model, which can be chosen to set the desired disc scale length. In fact, I assume that the angular momentum of the disc is related to the angular momentum of the halo $J_d = j_d J$. With this condition the disc scale length can be derived. In the thin disc approximation the angular momentum of the disc is given by

$$J_d = M_d \int_0^\infty v_c(R) \left(\frac{R}{h_\star}\right)^2 \exp\left(-\frac{R}{h_\star}\right) \mathrm{d}R, \tag{3.2.10}$$

where v_c is the circular velocity and $h_\star$ is the scale length of the stellar disc. Then, for a given set of parameters: λ (spin parameter), m_d (disc mass fraction), M_{200} (virial mass of the galaxy) and j_d (conversion factor between the disc and the dark matter halo angular momenta), the scale length $h_\star$ is found iteratively solving equation (3.2.10) in order to obtain the best approximation for the disc angular momentum. Notice that, while the thin disc approximation assumed in equation (3.2.10) is good enough for the calculation of $h_\star$, in my ICs and in the simulations the disc has non negligible thickness, it has in fact a stratification in the z-direction (as explained in Section 3.2.2).

3.2.4 Discs velocity structure

Here I describe the derivation of the discs velocity structure. For the stellar disc I adopt a Gaussian approximation for the velocity distribution (as described in Section 3.1.2) as well. Observations suggest that $\langle v_R^2 \rangle$ is proportional to $\langle v_z^2 \rangle$ in stellar discs (Hernquist, 1993), in particular I assumed $\sigma_R = \langle v_R^2 \rangle = \langle v_z^2 \rangle$ with $f_R = 1$ as in Springel et al. (2005). This $f_R = \langle v_R^2 \rangle / \langle v_z^2 \rangle$ is a free parameter that can be changed to increase the Toomre parameter

$$Q = \frac{\sigma_R k}{3.36 G \Sigma_\star} \tag{3.2.11}$$

and hence to increase the stability of the disc[2]. In Eq. (3.2.11), k is the epicyclic frequency and $\Sigma_\star$ is the stellar surface density.

To obtain the mean streaming velocity I use the epicyclic approximation, valid for quasi-circular orbits in an axisymmetric potential

$$\sigma_\phi^2 = \frac{\sigma_R^2}{\eta^2}, \tag{3.2.12}$$

where η is defined as

$$\eta^2 = \frac{4}{R}\frac{\partial\phi}{\partial R}\left(\frac{3}{R}\frac{\partial\phi}{\partial R} + \frac{\partial^2\phi}{\partial R^2}\right)^{-1}. \tag{3.2.13}$$

The streaming component in the azimuthal direction is set to

$$\langle v_\phi \rangle = \left(\langle v_\phi^2\rangle - \frac{\sigma_R^2}{\eta^2}\right)^{1/2}. \tag{3.2.14}$$

For the gaseous disc only the azimuthal component has to be computed. This can be obtained from the stationary equation of momentum conservation in the radial direction that yields

$$v_{\phi,\mathrm{gas}}^2 = R\left(\frac{\partial\phi}{\partial R} + \frac{1}{\rho_g}\frac{\partial P}{\partial R}\right). \tag{3.2.15}$$

3.3 Hot circumgalactic medium

In addition to the components described above, I also include a hot CGM, also called galactic corona, around the galaxy. As explained in Chapter 1 the corona is essential for sustaining the star formation in the disc over a long time (> 10 Gyr). The main purpose of this Thesis work is to analyze the gas circulation between the disc and the CGM, this interaction is mediated by stellar feedback due the material that is ejected from the disc. The properties of the hot galactic corona have been modeled using the few observations available for the Milky Way, in fact the extremely low densities of this gas makes it very difficult to observe. The corona follows a β-profile

[2]The Toomre's stability criterion states that a stellar disc is stable for $Q > 1$

$$\rho_{\rm cor}(r) = \rho_0 \left[1 + \left(\frac{r}{r_c}\right)^2\right]^{-\frac{3}{2}\beta}, \tag{3.3.1}$$

where $\beta = 2/3$, ρ_0 is the central density and r_c is the core radius. The β model profile of the corona has formally infinite mass, but I truncated the resulting density distribution at $10\,R_{200}$.

I built the corona with two different configurations: a static corona and a rotating one. In the case of a static corona, the temperature profile is derived assuming that the coronal gas is in hydrostatic equilibrium in the total potential of the galaxy. In the case of a non-rotating corona, the temperature profile is derived assuming hydrostatic equilibrium in the total potential. Knowing the corona density profile $\rho_{\rm cor}(r)$ and the total cumulative mass profile $M(r)$, the temperature profile is given by

$$T(r) = \frac{\mu m_p}{k_B} \frac{1}{\rho_{\rm cor}(r)} \int_r^\infty \rho_{\rm cor}(r) \frac{GM(r)}{r^2}\, {\rm d}r, \tag{3.3.2}$$

where $\rho_{\rm cor}(r)$ is the corona density profile in Eq. (3.3.1) and $M(r)$ is the total cumulative mass profile.

In the case of a rotating corona, the net velocity is computed as a fraction of the circular velocity

$$v_\phi = \alpha \left[\frac{\partial \Phi}{\partial R} R\right]^{1/2}, \tag{3.3.3}$$

where I set $\alpha = 0.4$ in my runs, which ensures that $v_\phi \approx 80$ km s^{-1} near the disc ($z \sim 2$ kpc). In fact, the galactic corona is expected to rotate with a lag of $\approx 80 - 120$ km s^{-1} with respect to the disc of the galaxy (e.g. Marinacci et al., 2011; Afruni et al., 2022). Values $\alpha > 0.4$ can cause significant deviations from sphericity, which, for simplicity is assumed in setting all the profiles of the coronal properties. A more accurate treatment of the rotation structure will be addressed in the future.

In this non static scenario, the temperature profile can be computed assuming hydrostatic equilibrium in an effective potential

$$\Phi_{\rm eff} = \Phi(R, z) - \int_\infty^R \frac{v_\phi^2(R')}{R'}\, {\rm d}R'. \tag{3.3.4}$$

More details on the structural parameter of the galactic corona for each work are given in Chapter 4 and Chapter 5.

3.3.1 Temperature and metallicity

The gaseous components in the ICs are also characterized with a temperature profile and a metallicity distribution. The initial temperature in the disc is assumed constant at the value of 10^4 K, and from this temperature T, the internal energy per unit mass is obtained as

$$u = \frac{k_B}{\mu(\gamma - 1)m_p} T \,, \tag{3.3.5}$$

here $k_B = 1.38 \times 10^{-16}$ erg K^{-1} is the Boltzmann constant, $\gamma = 5/3$ is the adiabatic index and $\mu = 4/[8 - 5(1 - f_H)]$ is the mean molecular weight for a full ionized gas ($f_H = 0.76$ is the hydrogen mass fraction). Although the temperature is constant in the ICs, when the galaxy is evolved in time the formation of a multiphase gas is expected, with both very low ($\sim 10^2$ K) and very high ($\sim 10^6 - 10^7$ K) temperatures, due to cooling and heating mechanisms and to the stellar feedback implemented in the *SMUGGLE* model (Section 2.4), and also to the mixing and accretion of the CGM. Additionally, the metallicity of the gas in the disc can be either set to a constant value (Chapter 4) or with a metallicity gradient (Chapter 5). Finally, a uniform metallicity set to $0.1 Z_\odot$ (e.g. Tosi, 1988; Bogdán et al., 2017) is assigned to the coronal gas. The computation of the metallicity is described in Section 3.4.3.

3.4 Sampling of the initial conditions

After describing the theoretical models that are at the foundations of the ICs construction, I proceed explaining how the physical properties are actually assigned to each particle. It is important to make an accurate realization of the analytical profiles described above, because these ICs are then used as a starting point to compute the time evolution of the galaxy. To do so, it is needed to sample the particle positions in the phase space: i.e. the coordinates and the velocity of each particle. For the gas particles it is also needed to set the internal energy and the metallicity to compute their evolution in terms of metallicity and temperature. The positions and the velocities of the particles (dark matter, stars and gas) are computed directly

from their respective profiles.

3.4.1 Coordinates

The particle positions of each component are derived with the **inversion method**, a general statistical method to sample a variable X from a probability density function $f_X(X)$:

(i) Given a probability density function $f_X(X)$ I calculate the cumulative distribution function

$$F_X(X) = \int_{-\infty}^{X} f_X(\tau)\, \mathrm{d}\tau \,. \tag{3.4.1}$$

This is a monotonically non-decreasing function with values between 0 and 1.

(ii) I set $u = F_X(X)$, where u is a random number between 0 and 1 extracted from a uniform distribution.

(iii) I invert the equation to find the variable X: $X = F_X^{-1}(u)$; X will be distributed as $f_X(X)$.

In this case the density distribution is the probability density function $f_X(X)$, from which I derive F_X, i.e. the normalized cumulative mass profile.

Bulge positions

For the bulge the inversion can be carried out analitically, since it follows a Hernquist profile. In this case, the normalized cumulative mass function is

$$F_X(r) = \left(\frac{r}{r+a}\right)^2, \tag{3.4.2}$$

which, by imposing

$$u = \left(\frac{r}{r+a}\right)^2, \tag{3.4.3}$$

can be inverted to find

$$r = \frac{a\sqrt{u}}{1-\sqrt{u}}. \tag{3.4.4}$$

In equations (3.4.2) and (3.4.3) u is a number between 0 and 1 extracted from a uniform random distribution. This procedure allows us to sample the spherical distance from the galaxy center r. To find the missing components required to attribute to each particle its (x, y, z) positions I procede as follows. I set the azimuthal coordinate ϕ as

$$\phi = 2\pi v, \tag{3.4.5}$$

where v is another random variable extracted from 0 to 1. In this way $0 < \phi < 2\pi$. The polar angle θ can go from 0 to π and is derived as

$$\theta = \arccos(2w - 1), \tag{3.4.6}$$

with w being another random variable. The Cartesian coordinates (x,y,z) are then simply derived from the spherical coordinates (r,θ,ϕ):

$$x = r\sin(\theta)\cos(\phi), \tag{3.4.7}$$

$$y = r\sin(\theta)\sin(\phi), \tag{3.4.8}$$

$$z = r\cos(\theta). \tag{3.4.9}$$

Discs positions

For the stellar disc the vertical position z can be computed analitically, since the vertical profile follows a sech^2 profile (equation 3.2.3):

$$z = \frac{z_0}{2\ln(u/(1-u))}, \tag{3.4.10}$$

where u is a random number extracted from 0 to 1. For the gaseous disc the vertical position z is derived from the vertical density structure computed as described in Section 3.2.2.

Instead, for the radial component the analytical inversion of Eq. (3.2.2) is not possible, but the value of the radius of the particle can be estimated with the **Newton-Raphson method**, an iterative root-finding algorithm. Starting with an equation written in the form $f(x) = 0$,

the root is found iteratively as follows

$$x_{n+1} = x_n - \frac{f(x_n)}{f'(x_n)}, \tag{3.4.11}$$

where x_{n+1} is a better approximation of the root. For the stellar disc $x = R/h_\star$, and $f(x_n)$ is given by

$$f(x_n) = -1 + \Big(1 + x_n\Big)\exp(-x_n) + u \tag{3.4.12}$$

while the first derivative $f'(x_n)$ reads

$$f'(x_n) = -x_n \exp(-x_n). \tag{3.4.13}$$

Starting from $x_1 = 1$, the process described in equation (3.4.11) is repeated until convergence is reached, in particular until $|x_{n+1} - x_n|/x_n < 10^{-7}$. Since the cumulative mass profiles are monotonically non-decreasing functions, I expect to find a solution R_i to the problem $\mathrm{M}(R_i)/M_{\mathrm{tot}}$=$u$, where u is a random number uniformly distributed between 0 and 1. The cylindrical radius is then obtained as R=$x_n\ h_\star$. The stellar disc is sampled from 0 to ∞, while the gaseous disc extends only from 0 to $10\ h_g$. Therefore, in the latter case the functions $f(x_n)$ and $f'(x_n)$ used in the Newton-Raphson algorithm must be modified accordingly

$$f(x_n) = \frac{-1 + (1 + x_n)\exp(-x_n)}{1 - (1 + 10)\exp(-10)} + u, \tag{3.4.14}$$

$$f'(x_n) = -\frac{x_n \exp(-x_n)}{1 - (1 + 10)\exp(-10)}. \tag{3.4.15}$$

The cylindrical radius is then found as R=$x_n\ h_g$. After obtaining R and z, ϕ is sampled in the same way described in equation (3.4.5) and then it is possible to pass from cylindrical to Cartesian coordinates as follows:

$$x = R\cos(\phi), \tag{3.4.16}$$

$$y = R\sin(\phi), \tag{3.4.17}$$

$$z = z. \tag{3.4.18}$$

Galactic corona positions

For the corona the analytical inversion of the β-profile is not possible. Also in this case I used a Newton-Raphson method. The coronal gas is sampled from 0 to $10\,r_{200}$, therefore $f(x_n)$ is given by

$$f(x_n) = u + \left[10\frac{r_{200}}{r_c} - \arctan\left(10\frac{r_{200}}{r_c}\right)\right]^{-1}\left(\arctan\left(\frac{x_n}{r_c}\right) - \frac{x_n}{r_c}\right), \tag{3.4.19}$$

whereas $f'(x_n)$ is

$$f'(x_n) = -\left[10r_c\left(\frac{r_{200}}{r_c} - \arctan\left(10\frac{r_{200}}{r_c}\right)\right)\right]^{-1}\frac{x_n^2/r_c^2}{1 + x_n^2/r_c^2}. \tag{3.4.20}$$

The cartesian coordinates (x, y, z) are then obtained from the cylindrical ones with equations (3.4.16), (3.4.17) and (3.4.18).

3.4.2 Velocities

I now explain the process of sampling particle velocities. For each particle position, determined as outlined in Section 3.4.1, the velocity components are sampled from three Gaussian distributions with means and standard deviations derived in Sections 3.1.2 and 3.2.4. The first step involves calculating the velocity dispersions in the radial, vertical, and azimuthal directions by solving the differential equations described in Section 3.2.4, using a logarithmic grid in R and z. This grid consists of 512 grid points in each direction, with a total box size of $\approx$ 857 kpc to encompass the galaxy. The logarithmic spacing allows for finer sampling across all scales, from the largest to the smallest.

Next, bilinear interpolation is employed to determine the velocity dispersions at the particle positions. Once these dispersions are known, the velocities are assumed to follow a normal distribution with the mean and dispersion described in Section 3.1.2 and 3.2.4. To generate these velocities, I used the polar form of the **Box-Muller algorithm** (Box & Muller, 1958), which is an efficient method for sampling Gaussian-distributed random variables.

First, two pseudo-random numbers, y_1 and y_2, are drawn from a uniform distribution between -1 and 1. Then, $r = y_1^2 + y_2^2$ is defined. If $r = 0$ or $r \geq 1$ the pair is discarded and

new values are drawn. Otherwise, ξ_0 is computed:

$$\xi_0 = y_{1,2}\sqrt{\frac{-2\ln r}{r}}, \tag{3.4.21}$$

which results in ξ_0 being normally distributed with a mean $m = 0$ and variance $\sigma^2 = 1$. In the first instance, $y_{1,2} = y_1$ is assigned. The second time a Gaussian variable is required, $y_{1,2} = y_2$ is directly used without needing to draw another pair (y_1, y_2). Once both elements of the (y_1, y_2) pair have been used, the process repeats from the beginning.

If Gaussian distributed values with a given mean m and variance σ are need, it can be obtained by simply multiplying for σ and add m. For instance, the stellar disc has

$$v_R = \xi_0\sqrt{\sigma_R^2}, \tag{3.4.22}$$

$$v_z = \xi_0\sqrt{\sigma_z^2}, \tag{3.4.23}$$

$$v_\phi = \xi_0\sqrt{\sigma_\phi^2} + \langle v_\phi \rangle. \tag{3.4.24}$$

In this case, the mean velocities in the radial and vertical directions are zero, while a free-streaming component is present in the azimuthal direction. A similar method is used to compute the velocities for the bulge and the corona components. For the bulge I assume that there is no net rotation, $\langle v_\phi \rangle = 0$ (see Section 3.1.2). The corona is set with $v_R = v_z = 0$ and $\langle v_\phi \rangle$ as in Eq. (3.3.3). In the case of the gaseous disc, only the azimuthal velocity component needs to be calculated. This value is not sampled from a distribution but is determined directly by equation (3.2.15, see Section 3.2.4).

In all the compontents, the velocities (v_R,v_ϕ,v_z) are then converted from cylindrical to Cartesian coordinates (v_x,v_y,v_z):

$$v_x = v_R\frac{x}{R} - v_\phi\frac{y}{R}, \tag{3.4.25}$$

$$v_y = v_R\frac{y}{R} + v_\phi\frac{x}{R}, \tag{3.4.26}$$

$$v_z = v_z, \tag{3.4.27}$$

where x and y are the Cartesian coordinates of the particle (described in Section 3.4.1) and

R is the cylindrical radius.

3.4.3 Metallicity sampling

In this section, I outline how metallicity is assigned to gas particles, a crucial aspect of my simulations. Metallicity is a key factor in galaxy formation and evolution, as it enhances gas cooling, which can accelerate gravitational collapse and subsequently lead to more efficient star formation. Accurately modeling this property is vital to producing realistic simulations of galaxy evolution.

Table 3.1: Primordial abundances (these abundances are mass fractions, therefore they are defined as the ratio between the mass of a given element X and the total mass of all the elements) $f_{\rm prim}$ and solar abundances $f_{\odot}$ of different elements: Hydrogen (H), Helium (He), Carbon (C), Nitrogen (N), Oxygen (O), Neon (Ne), Magnesium (Mg), Silicon (Si) and Iron (Fe). Solar abundances are taken from Asplund et al. (2009).

	H	He	C (10^{-3})	N (10^{-3})	O (10^{-3})	Ne (10^{-3})	Mg (10^{-3})	Si (10^{-3})	Fe (10^{-3})
$f_{\rm prim}$	0.76	0.24	0	0	0	0	0	0	0
$f_{\odot}$	0.7388	0.2485	2.4	0.7	5.7	1.2	0.7	0.7	1.3

In the ICs, gas particles in both the disc and hot corona are assigned uniform, though distinct, metallicities: the hot corona particles have $Z = 0.1Z_{\odot}$, consistent with observational data (see Chapter 1), while the gaseous disc particles are either given a constant metallicity of $Z = Z_{\odot}$ or follow a metallicity gradient. Metallicity is treated as a passive scalar, meaning it evolves passively within each gas cell through a continuity equation

$$\frac{(\partial \rho Z)}{\partial t} + \nabla \cdot (\rho Z \boldsymbol{v}) = 0, \tag{3.4.28}$$

each gas cell has its own metallicity Z_i that is transported by the fluid.

The code traces not only the global metallicity but also the abundances of nine chemical elements (i.e. Hydrogen (H), Helium (He), Carbon (C), Nitrogen (N), Oxygen (O), Neon

(Ne), Magnesium (Mg), Silicon (Si) and Iron (Fe)). To different metallicities correspond different chemical abundances of the different elements. These are derived as follows.

The abundance of a given element X is computed with a linear interpolation between two sets of abundances: primordial abundances $f_{\rm prim}$ and solar abundances $f_{\odot}$, which are taken from Asplund et al. (2009) and reported on Table 3.1. Therefore, given the gas metallicity Z_i, each cell i has:

$$f_{X,i} = f_{X,{\rm prim},i} + \frac{Z_i}{Z_{\odot}}(f_{X,\odot,i} - f_{X,{\rm prim},i}) \, , \tag{3.4.29}$$

where $f_{X,{\rm prim}}$ is the primordial abundance of the element X, $f_{X,\odot}$ is the solar abundance of the element X and $Z_{\odot} = 0.0127$ is the solar metallicity (only the nine elements in Table 3.1 are considered). In each cell the sum of the abundances of the nine elements has to be $\sum_X f_{X,i} = 1$, as the total mass has to be conserved.

Chapter 4

The role of stellar feedback in gas accretion

4.1 Introduction

This Chapter is focused on the study of the gas circulation between the disc and the corona of star-forming galaxies like the Milky Way. To analyze this circulation and its implications on the properties of the corona and of the gas that is subsequently accreted onto the disc, I make use of high-resolution ($\sim 10^4$ $M_\odot$) hydrodynamical N-body simulations of an isolated Milky Way-like galaxy, with the inclusion of an observationally-motivated hot corona around the galaxy. After sampling the galaxy initial conditions, the simulations are evolved with the *SMUGGLE* model (Marinacci et al., 2019), an explicit ISM and stellar feedback model that is part of the moving-mesh code Arepo (Springel, 2010b; Weinberger et al., 2020). So far, the *SMUGGLE* model has been tested on isolated galaxies in the absence of a hot corona (e.g. Kannan et al., 2020; Li et al., 2020; Kannan et al., 2021; Jahn et al., 2021; Burger et al., 2022; Li et al., 2022; Beane et al., 2023; Smith et al., 2022; Sivasankaran et al., 2022), which is usually not included in this type of hydrodynamical N-body simulations. The calculations that I carry out in this Chapter are the first that include such an important component for galactic evolution in the *SMUGGLE* framework.

The Chapter is structured as follows: in Section 4.2 I briefly summarize the numerical methods used in this Chapter and give details on the initial conditions for my simulations. In Section 4.3 I describe the structure of the ISM and of the galactic corona that is generated in the simulations. In Section 4.4 I present the main results of this Chapter. In Section 4.5 I

Table 4.1: *Structural parameters of the Milky Way-like galaxy simulated in this Chapter.* From left to right: circular velocity of the halo at r_{200} (v_{200}); dark matter halo mass ($M_{\rm dm}$); dark matter halo scale length (r_s); bulge mass (M_b); bulge scale length (a); stellar disc mass ($M_\star$); stellar disc scale length ($h_\star$); stellar disc scale height (z_0); gaseous disc mass (M_g); gaseous disc scale length (h_g); mass of the corona ($M_{\rm cor}$) computed within the virial radius $r_{\rm vir}$; corona core radius ($r_{\rm c}$).

v_{200} [km s^{-1}]	$M_{\rm dm}$ [$M_\odot$]	r_s [kpc]	M_b [$M_\odot$]	a [kpc]	$M_\star$ [$M_\odot$]
169	1.53×10^{12}	36.46	1.5×10^{10}	1.3	4.73×10^{10}
$h_\star$ [kpc]	z_0 [pc]	M_g [$M_\odot$]	h_g [kpc]	$M_{\rm cor}$ [$M_\odot$]	$r_{\rm c}$ [kpc]
3.8	380	9×10^9	7.6	3×10^{10}	8

compare my results to previous works and I summarize them in Section 4.6.

The results of this Chapter have been published in paper form in Barbani et al. (2023).

4.2 Numerical Methods

The simulations presented in this Chapter are performed with the hydrodynamical N-body code Arepo (Springel, 2010b; Weinberger et al., 2020), described in detail in Section 2.3. I coupled Arepo with the *SMUGGLE* model. More details on *SMUGGLE* can be found in Section 2.4.

4.2.1 Initial conditions

In this Section I describe the ICs of the Milky Way-like multi-component galaxy model that I study in this Chapter by means of hydrodynamical N-body simulations. The ICs have been generated according to the method presented in Chapter 3. To summarize, the components include: a dark matter halo and a stellar bulge that follow a Hernquist profile, an exponential thick stellar disc, an exponential thick gaseous disc and a galactic hot corona.

The gaseous components in the ICs are characterized by a temperature profile and a metallicity distribution. The initial temperature in the disc is assumed to be constant at the value

of 10^4 K. However, when the galaxy is evolved in time, the formation of a multiphase gas is expected, with both very low ($\sim 10 - 100$ K) and very high temperatures ($\sim 10^6$ K), due to cooling and heating mechanisms and to the stellar feedback. The overall metallicity of the gas in the disc is set to $Z = Z_\odot$ for simplicity.

Galactic corona

The properties of the hot galactic corona have been set using some of the observational constraints available for this component in the Milky Way (Grcevich & Putman, 2009; Anderson & Bregman, 2010; Gatto et al., 2013; Salem et al., 2015; Putman et al., 2021). I modeled the corona with a β-model (Cavaliere & Fusco-Femiano, 1978), that is often used to fit the density profiles of the hot gas in galaxy clusters and that has been shown to fit well the corona density profile of the L* galaxy NGC 3221 in recent observations (e.g. Das et al., 2020)

$$\rho_{\rm cor}(r) = \rho_0 \left[1 + \left(\frac{r}{r_c}\right)^2\right]^{-\frac{3}{2}\beta}. \tag{4.2.1}$$

The parameters for the β-model are taken following Moster et al. (2011). β is set to $2/3$ and the core radius is set to $r_c = 0.22 r_s = 8$ kpc.

In Figure 4.1 I show a comparison between the number density of the coronal gas (black solid line) of the fiducial simulation (Table 4.2) with observational estimates of the Milky-Way corona (points with errorbars). The model has a mass of 3×10^{10} M$_\odot$ inside the virial radius $R_{200} \approx 240$ kpc and is well constrained by the observational points. The β-profile has a region of constant density (i.e. a core) in the center, that depends on the parameter r_c: small changes in the inner region density can have important consequences on the cooling of this component, as the cooling time is extremely dependent on the gas density and temperature. The evolution of the number density over time is also shown, in particular at 1 Gyr (blue solid line) and 2 Gyr (red solid line) after the beginning of the simulation. The galactic corona slowly accretes into the disc of the galaxy and the density is decreasing particularly in the central region (where it changes from 8×10^{-3} to 10^{-3} cm^{-3}). At large radii ($r > 50$ kpc) the density is similar to the initial one. At both times the density profile is in good agreement with the observational points.

For my simulations, I analyzed two distinct configurations: a galaxy with a static corona

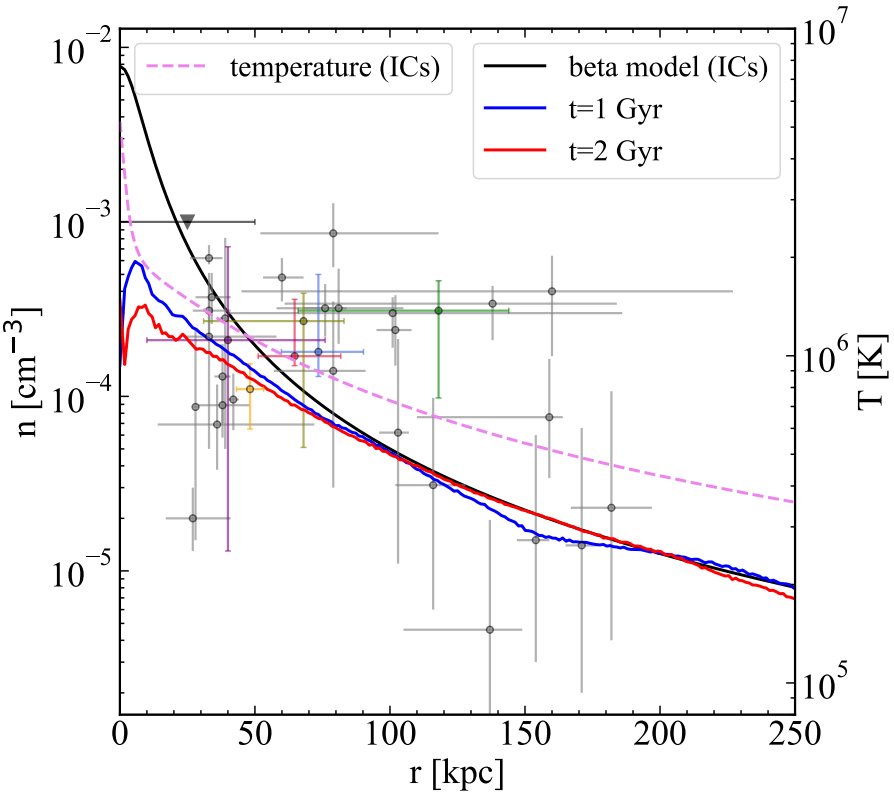

Figure 4.1: Galactic corona number density profile (black solid line) of the fiducial simulation BM_R (see Table 4.2) compared with several observational constraints of the Milky Way (points with errorbars): ram-pressure stripping from the dwarf spheroidal galaxies Fornax, Ursa Minor and Sculptor (green, purple and olive points, Grcevich & Putman 2009), Carina and Sextans (red and blue points, Gatto et al. 2013), the Large Magellanic Cloud (orange point, Salem et al. 2015) and also more recent constraints obtained from several dwarf galaxies (grey points, Putman et al. 2021); and Pulsar dispersion measures (black upper limit, Anderson & Bregman 2010). The black line represents the initial number density corona profile (i.e. a β-model), while the blue and the red solid lines represent the same profile 1 Gyr and 2 Gyr after the start of the simulation, respectively. The purple dashed line is the initial temperature of the coronal gas.

Table 4.2: Summary of the model variation of the Milky Way-like galaxy parameters in this Chapter. The fiducial simulation is BM_R, which includes a rotating corona. The other simulations are used as comparison with the main one.

Simulation name	$M_{\rm cor}$ [$M_\odot$]	Rotation	Feedback
BM_NR	3×10^{10}	no	yes
BM_R	3×10^{10}	yes	yes
NOCOR	negligible	-	yes
NOFEED_NR	3×10^{10}	no	no
NOFEED_R	3×10^{10}	yes	no

and a galaxy with a rotating one (see Chapter 3 for more details on the galactic hot corona implementation). I also assign a uniform metallicity, set to 0.1 $Z_\odot$, to the coronal gas (e.g. Tosi, 1988; Bogdán et al., 2017). In both the static and the rotating configurations the temperature is higher in the center and it decreases with radius (see purple dashed line in Figure 4.1): a temperature gradient has been observed for instance in Das et al. (2020), this is very similar to the temperature that I obtain in my ICs, with an average temperature $\sim 10^6$ K that depends on the total mass of the galaxy.

4.2.2 Simulations setup

I simulated a series of isolated non-cosmological Milky Way-like galaxies, with components as described in the previous Sections. The parameters of the galaxies simulated in this Chapter are listed in Table 4.1. These parameters are chosen in order to represent a galaxy similar to the Milky Way. The galactic corona has a mass inside the virial radius of $M_{\rm cor}(r < r_{\rm vir}) = 3 \times 10^{10}$ $M_\odot$, that is a mass similar to those derived from observations (e.g. Kaaret et al., 2020; Martynenko, 2022) and is in agreement with the observational constraints on the number density (see Figure 4.1) of the galactic corona in the Milky Way. The galaxy is inserted inside a box with a side length of 860 kpc. I have run 4 main simulations (listed in Table 4.2) changing the characteristics of the coronal gas or the feedback processes. These are:

- **BM_NR**: using a β-profile with no net rotation;
- **BM_R**: using a β-profile with rotation;

- **NOCOR**: ICs with a negligible galactic corona;
- **NOFEED_NR/NOFEED_R**: simulations with no stellar feedback.

The **BM_R** simulation has been chosen as the fiducial simulation for this Chapter, it includes a rotating corona with a beta model density profile. The results of this simulation will be compared with a static corona case (**BM_NR**), a configuration without the galactic corona (**NOCOR**) and two configurations in the absence of stellar feedback (**NOFEED_NR/NOFEED_R**) with the same ICs of **BM_NR/BM_R**. I put $N_{\rm disc} = 3.2 \times 10^6$ particles in the stellar disc, $N_{\rm bulge} = 8 \times 10^5$ in the bulge and $N_{\rm gas} \simeq 4.9 \times 10^5$ gaseous particles, with $N_{\rm gas,d} = 3.2 \times 10^5$ gaseous particles in the disc and $N_{\rm gas,cor} = 1.7 \times 10^5$ in the corona. This results in a mass resolution $m_{\rm gas} = 1.1 \times 10^4$ $M_\odot$ and a minimum gravitational softening length $\epsilon_{\rm gas} = 10$ pc for the gas. The mass of the stellar disc and bulge particles is respectively $m_{\rm disc} = 1.5 \times 10^4$ $M_\odot$ and $m_{\rm bulge} = 2 \times 10^4$ $M_\odot$, and the gravitational softening length is $\epsilon_\star = 21.4$ pc.

First, I have run adiabatic simulations using Arepo, i.e. without the presence of the dissipation processes implemented in the *SMUGGLE* model, with the different IC setups, to ensure that the different components of the galaxy are in equilibrium. This simulations confirmed the dynamical stability of the simulated galaxy model, with a configuration that remains almost unchanged for a time span of 2 Gyr. Then the ICs are evolved using Arepo with the *SMUGGLE* model for 2 Gyr, this is a sufficient time to see the effect of the corona presence on the SFR of the galaxy, given that the depletion time for a Milky Way-like galaxy is

$$\tau_{\rm dep} = \frac{M_{\rm g}}{\rm SFR} \sim \frac{10^9\ M_\odot}{1\ M_\odot\ {\rm yr}^{-1}} \sim 1\ {\rm Gyr}, \tag{4.2.2}$$

where $M_{\rm g}$ is the mass of gas in the disc and SFR is the star formation rate, $\tau_{\rm dep}$ has similar values also in my setup.

4.3 ISM and coronal gas structure

4.3.1 Scheme of the gas circulation

In Figure 4.2 I show a schematic view of the processes that contribute to the gas circulation, i.e. the balance between outflows and inflows (from and into the galactic disc), in a star-

forming galaxy like the Milky Way. The gas that is lifted from the disc (outflowing) is ejected thanks to stellar feedback ($\sim \dot{M}_{\rm out}$), mostly coming from SN explosions. The gas accreted onto the galactic disc (inflowing) can be schematically divided in two main components: (i) the galactic fountain gas that, failing to reach the galaxy escape velocity, re-accretes onto the disc ($\dot{M}_{\rm in,\,fount}$, which is $\sim \dot{M}_{\rm out}$), (ii) the gas accreted from the galactic corona that can come directly from the radiative cooling of the coronal gas ($\dot{M}_{\rm in,\,cor}$) or from the interaction between the galactic fountains and the corona ($\dot{M}_{\rm in,\,int}$). The latter interaction may act as a positive feedback for star formation, as mentioned in Section 4.1. The coexistence of these different phenomena is described in more detail in the following Sections.

4.3.2 Gas projection maps

I start by analyzing projection maps of the gas in the simulated galaxies. In Figure 4.3 I show the face-on and edge-on surface density maps of the fiducial simulation **BM_R** at different times and a comparison with other simulations. From the face-on projections of **BM_R** (first row in Figure 4.3) it is possible to appreciate the gaseous disc structure complexity of the simulated galaxy: as the simulation starts, the first stars begin to form, generating radiative feedback and stellar winds that are followed by the SN explosions, which cause the formation of low-density cavities (surface densities $< 1 M_{\odot}$ pc^{-2}). These cavities, filled with hot gas, can extend over the plane of the disc and are responsible for the production of outflows. Along the spiral arms of the galaxy, at the edges of the generated cavities, high-density gas filaments, whose presence is enhanced by stellar feedback, are present. In such regions, most of the star formation takes place, since below the density threshold $\rho_{\rm th} = 100\, cm^{-3}$ the formation of a stellar particle is not possible (see Section 2.4).

In Figure 4.3 I have also compared the disc structure of **BM_R** with the other simulations performed at $t = 1.13$ Gyr (third row). The first panel shows the **NOCOR** simulation, where the disc is more extended thanks to the lack of accretion of low-angular momentum gas from the corona. Furthermore, the overall gas surface density is visibly lower, especially in the gas filaments: the gas consumed by star formation is not replaced and the average gas density can only decrease over time. The **NOFEED_R** simulation is shown in the second panel. Here, the disc structure is unrealistic with almost no gas filaments and with small clumps of high-density gas. These clumps are formed from initial density fluctuations thanks to gravitational

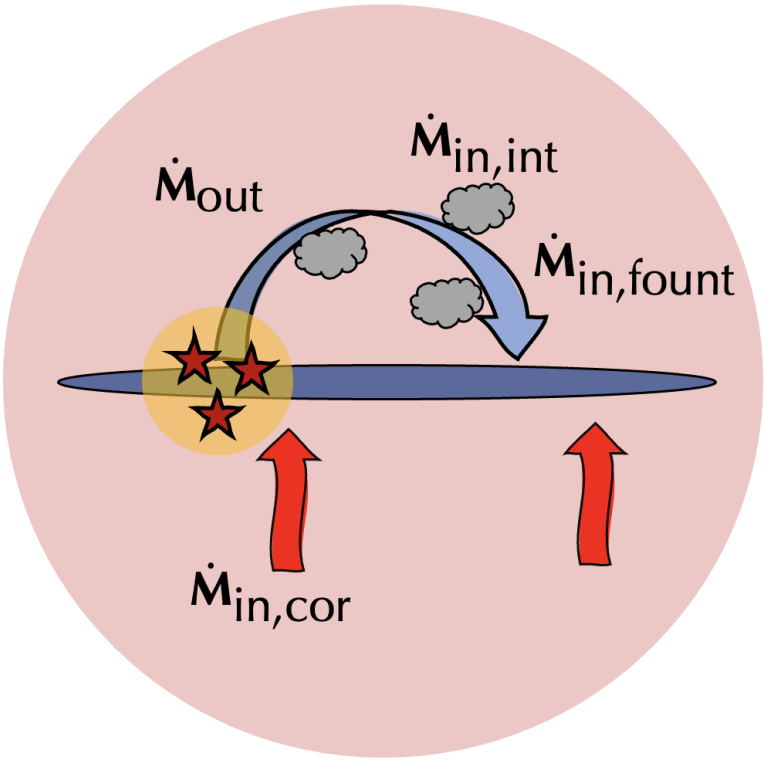

Figure 4.2: Cartoon scheme of the gas accretion/ejection processes in a Milky Way-like galaxy. The stellar feedback processes (i.e. SN, stellar winds and radiative feedback) can eject gas outside the galactic disc. The outflow rate ($\dot{M}_{out}$) is represented by the blue arrow, that schematize the trajectory of a single galactic fountain. This gas can eventually fall back onto the disc, giving a inflow rate coming from the galactic fountains ($\dot{M}_{in,\,fount}$). The interaction between the fountains and the corona (red halo) can create a mixture of gas, represented by the grey clouds, that can increase the gas accretion rate onto the disc ($\dot{M}_{in,\,int}$). The red arrows represent the inflow rate of gas accreted directly from the galactic hot corona ($\dot{M}_{in,\,cor}$).

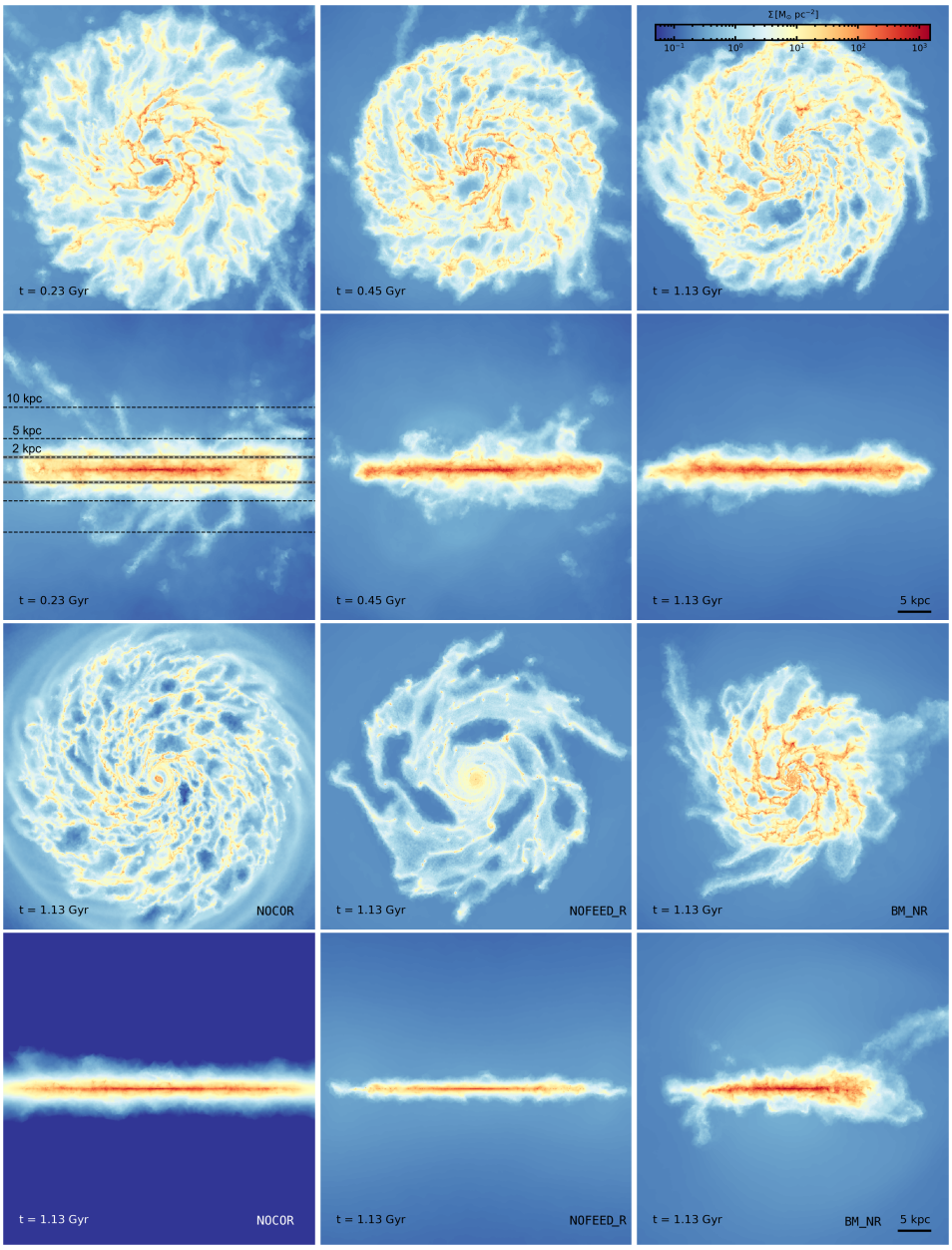

Figure 4.3: *Top panels*: Gas column density in face-on (first row) and edge-on (second row) projections of the **BM_R** simulation computed using the *SMUGGLE* model at the times indicated in each panel. The horizontal dashed lines represent three heights over the disc (2, 5 and 10 kpc). Each panel is 50 kpc across and in projection depth with a total number of 1024 × 1024 pixels that give a resolution of ~ 50 pc. *Bottom panels*: The same projections are made face-on (third row) and edge-on (forth row) at $t = 1.13$ Gyr for the **NOCOR** (first column), **NOFEED_R** (second column) and **BM_NR** (third column) simulations.

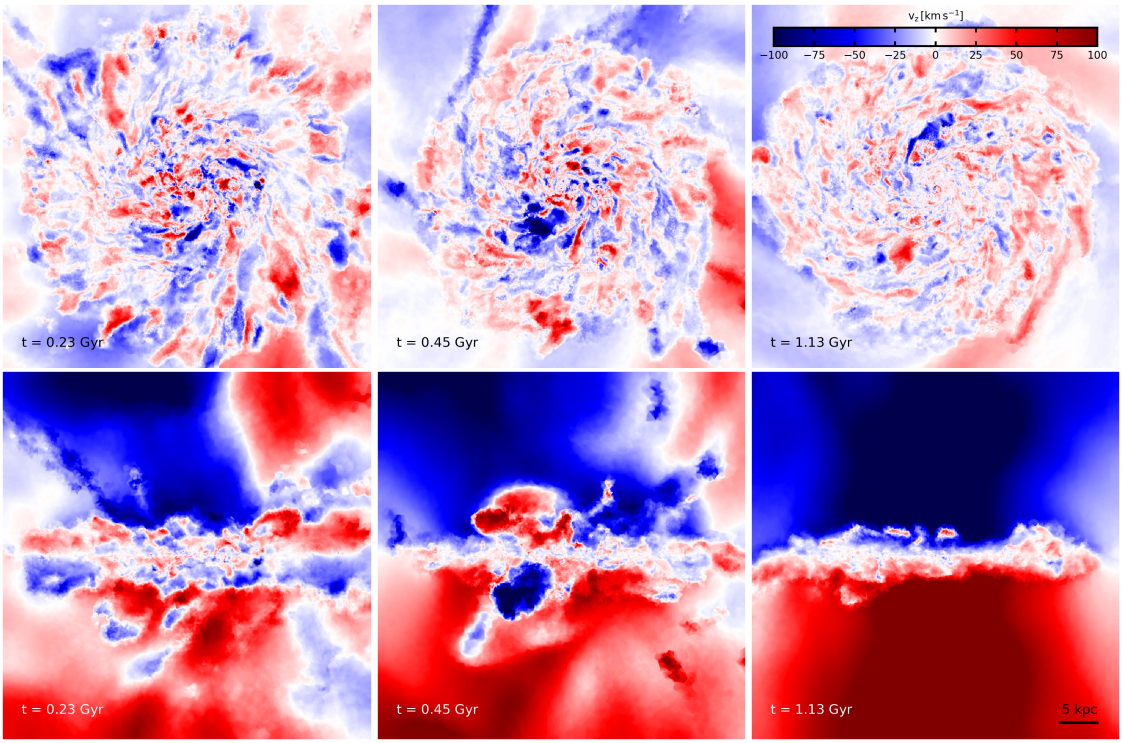

Figure 4.4: Density-weighted maps of the gas velocity perpendicular to the disc plane in face-on (top panels) and edge-on (bottom panels) projections of the **BM_R** simulation computed using the *SMUGGLE* model at the times indicated in each panel. Each panel is 50 kpc across and in projection depth with a total number of 1024 × 1024 pixels that give a resolution of $\sim$ 50 pc. The kinematic structure of the gas in the galaxy can be visually appreciated. The coronal gas is accreted onto the galaxy and outflows of gas are ejected from the disc, this generates a gas circulation between the disc and the corona.

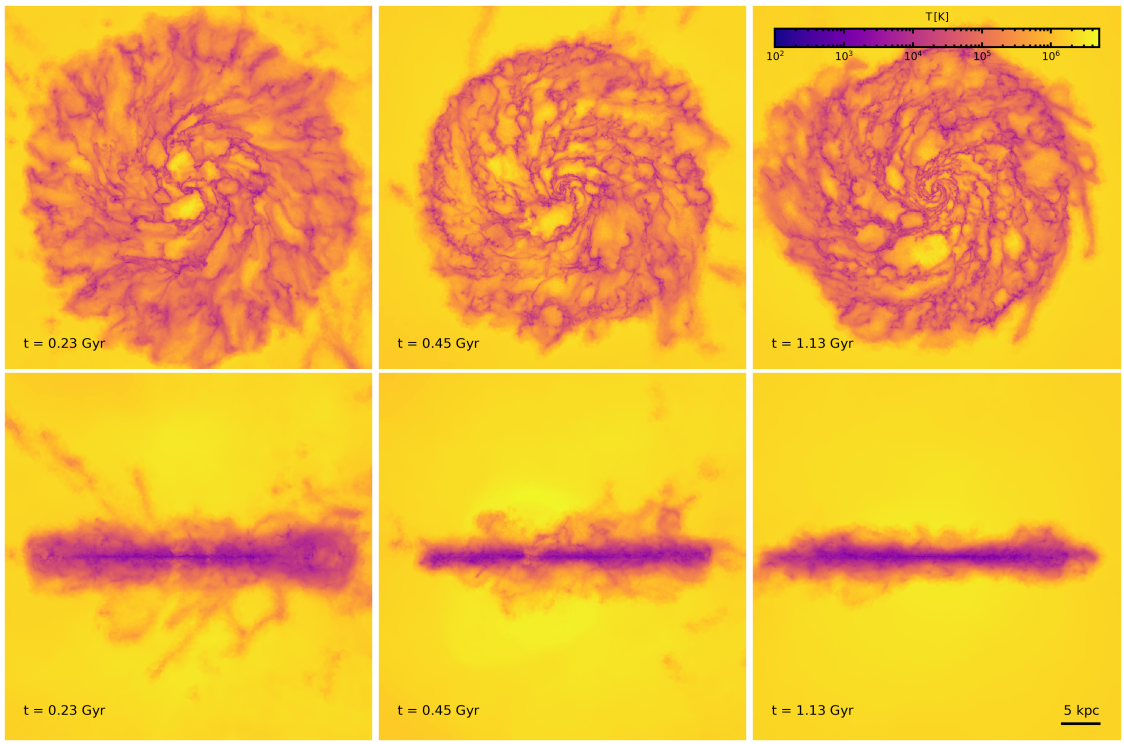

Figure 4.5: Density-weighted temperature in face-on (top panels) and edge-on (bottom panels) projections of the Milky-Way like galaxy for the **BM_R** simulation computed with the *SMUGGLE* model at the times indicated in each panel. Each panel is 50 kpc across and in projection depth with the presence of a total number of 1024 × 1024 pixels that give a resolution of $\sim$ 50 pc. The mixing between the material ejected from the disc and the hot galactic corona can be visually appreciated, with the formation of an intermediate temperature gas phase at the disc-corona interface.

attraction, they grow over time and are not torn apart from SN explosions. Also, they tend to migrate towards the center of the disc over time as a consequence of dynamical friction. This phenomenon causes a higher concentration of gas at the center of the disc, where a substantial amount of stars are then able to be formed. A few large low density cavities are still formed thanks to gas clustering and cooling. Looking at the **BM_NR** simulation (third panel), it can be noted that the gaseous disc scale length is smaller (halved approximately) then in **BM_R**. The disc shrinks in size over time in the case of a static corona, whereas it remains extended if the rotation is included. Although this might be caused by a redistribution of the angular momentum between the disc and the corona caused by the gas circulation mediated by the galactic fountains, this speculation requires further investigations and it is outside the scope of this Chapter. Overall, the disc structures found in **BM_R** are also present in this simulation.

The second row of Figure 4.3 shows the corresponding edge-on projections of the same configurations shown in the top panels. In the first panel I have highlighted three heights over the plane of the disc (2, 5 and 10 kpc) as comparison. As I will discuss in Sections 4.4.2, 4.4.3 and 4.4.4, at these heights I have computed the outflow and inflow rates (inside the shaded area). The presence of a low density halo of gas around the galactic disc can be observed. In an initial phase that lasts about 0.1 Gyr there is a substantial accretion of coronal gas onto the disc, as I will discuss in detail in Section 4.4.1. This accretion episode causes an increase of the SFR at the beginning of the simulation, after this the corona inflates again and continues its evolution. Starting from $t = 100$ Myr the galaxy develops strong outflows, ejected from the disc by stellar feedback. These outflows can reach relatively large distances from the galaxy mid-plane (over 10 kpc), traveling through the galactic corona and then falling back onto the disc in a galactic fountain cycle (e.g. Fraternali & Binney, 2006). This is clear in the 0.23 Gyr image where several galactic fountains ejected from the disc can be seen. This process is schematically depicted in Figure 4.2 and will be analyzed in detail in Sections 4.4.3 and 4.4.4.

I have analyzed the gaseous structure of the other simulations at $t = 1.13$ Gyr in comparison with **BM_R** also for the edge-on projections (see fourth row in Figure 4.3). In **NOCOR** (first panel) the disc is isolated and not surrounded by the corona, the intensity of the gaseous outflows is lower than in **BM_R**. The **NOFEED_R** simulation (second panel) features a disc immersed in a galactic corona, but in the absence of galactic outflows. From the **BM_NR** simulation (third panel) I note that the gaseous outflows are more frequent and reach higher

heights with a static corona: with a rotating corona the gas surface density is lower due to the larger scale length of the gaseous disc induced by the angular momentum exchange. Moreover, the rotation of the gas creates a different gas accretion distribution on the disc. For these reasons, the star formation is lower and consequently also the intensity of gas ejection. A more detailed outflow/inflow analysis is carried out in Section 4.4.2.

Figure 4.4 shows the face-on and edge-on projections of the density-weighted gas velocity perpendicular to the disc plane of the **BM_R** simulation. The bluer colors in the region above the galactic disc mid-plane represent gas that is falling onto the disc, the redder colors gas that is ejected from the disc, and vice versa for the regions below the disc. The face-on projections (top panels) highlight the gas that is ejected at high velocity from SN explosions: the location of this ejected gas roughly corresponds to the low-density cavities in Figure 4.3. In the edge-on projections (bottom panels) is particularly noticeable the accretion of coronal gas that is strongest in the central regions, where its density is the highest. In addition, the complex kinematic structure of the gaseous outflows is visible in Figure 4.3: these outflows can have a velocity in excess of 100 km s^{-1}. The galactic fountain kinematics is clearly visible in the projections at 0.23 and 0.54 Gyr. There is the establishment of a circulation of gas between the disc and the galactic corona: the gas is ejected at high velocities from the disc plane (with a vertical velocity directed out of the disc) and after a certain time, that depends on the initial velocity and on the angle of ejection, it falls back into another spot (with a vertical velocity directed to the disc plane).

In Figure 4.5 I show the density-weighted projected temperature of the gas for the **BM_R** simulation. In the face-on projections (top panels) the presence of a multi-phase medium in the disc can be noted, where the regions with the higher densities correspond to the colder gas ($T < 10^2$ K), this very cold gas can therefore collapse and form stars. The bubbles carved by SN feedback are filled with high temperature ($T \sim 10^6$ K) gas. The temperature distribution of the gas ejected from the disc is visible in the edge-on projections (bottom panels). At 1 kpc above and below the disc the gas is hotter than in the disc filaments, reaching $10^4 < T < 10^5$ K. Outside the disc of the galaxy the temperature is dominated by the coronal gas ($T > 5 \times 10^5$ K). The same features are present in the temperature projections of the other simulations. The temperature of the aforementioned gaseous outflows is in general at an intermediate level ($10^4 < T < 10^5$ K), this might be caused by the mixing with the

gas from the corona, that is at higher temperatures ($T \sim 10^6$ K), or it is possible that the majority of the gas is already ejected at these temperatures. As I will discuss in Section 4.4 the gas mixing has a predominant role, I found that the intermediate temperature gas is formed due to the presence of the stellar feedback that mediate the interaction between the disc and the corona.

4.3.3 Phase diagrams

I now focus on the phase diagram of the gas in the galaxy, looking in particular at the **BM_R** simulation. The analysis of the structure of the gas that surrounds and lies inside the disc of the galaxy is critical to understand how star-forming galaxies evolve. In Figure 4.6 I show the gas number density-temperature phase diagram that includes all the gas cells in the simulation (top panels) or all the gas cells within a distance from the mid-plane $1.5 < z < 4$ kpc (bottom panels). The diagrams are represented at the beginning of the simulation ($t = 0.05$ Gyr, first column) and at $t = 1$ Gyr for **BM_R** (second column) and for **NOFEED_R** (third column). The lighter colours represent higher gas masses, as indicated in the colorbar. The first noticeable thing is the presence of a complex ISM structure (blue dashed rectangle) that is already developed in the first Myr of the simulation, similarly to Marinacci et al. (2019). The gas has a wide range of temperatures and densities: the majority ($\sim 85\%$) of the gas in the disc has a temperature lower than 10^4 K, with densities ranging from 10^{-3} cm^{-3} to 10^3 cm^{-3}. The strip of gas in Figure 4.6 at 1.7×10^4 K (i.e. $\log T = 4.25$ K) at densities between 1 and 10^5 cm^{-3} is gas photoionized from the massive and hot OB stars. Around these stars the gas temperature is fixed at this value. The creation of lower temperature gas is fundamental for the star formation since only gas over certain densities ($\sim 10^{-1} - 10^{-2}$ cm^{-3}) can cool, overcoming the heating from the UV background. This gas can reach densities over 10^2 cm^{-3} and is used to form new stars if the right conditions are satisfied (Section 2.4). The cloud of gas particles with a temperature over 1.7×10^4 K and a density between 1 and 10^5 cm^{-3} represents the hot ionized medium generated from the SN explosions.

The majority of the gas in the system (over 75%) is located in the galactic corona, its gas can be identified in Figure 4.6 within the region marked by the red dashed rectangle (top left region of the diagram), in both the first and second panels. The coronal gas has a temperature between 10^5 K and 10^7 K and a low density, smaller than 10^{-1} cm^{-3} and reaching $n < 10^{-5}$

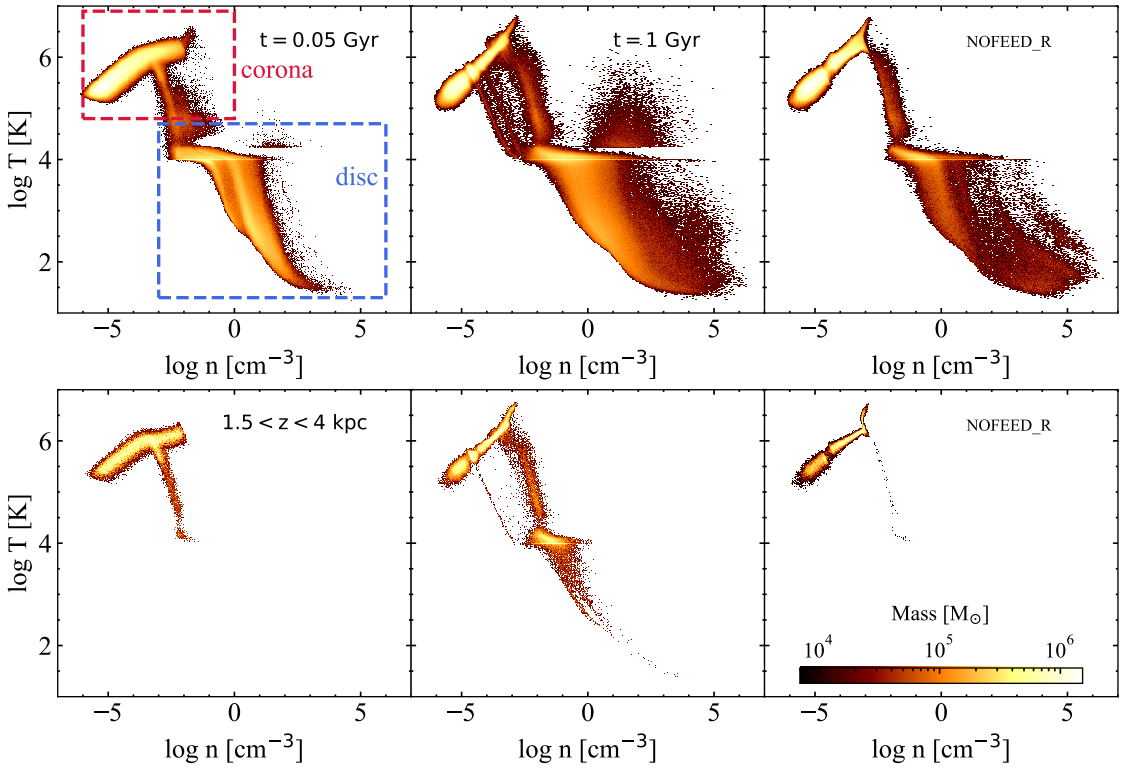

Figure 4.6: Number density-temperature diagrams for all the gas cells in the simulation box (top panels) and for the gas cells at the disc-corona interface ($1.5 < z < 4$ kpc, bottom panels) of the **BM_R** simulation at $t = 0.05$ Gyr (first column) and $t = 1$ Gyr (second column) and of the **NOFEED_R** simulation at $t = 1$ Gyr (third column). The lighter colours indicate higher gas masses. The blue and the red dashed rectangles specify the gaseous disc and the coronal gas respectively. The diagram highlights the complex structure of the ISM and of the coronal gas. The gas in the disc has a wide range of temperatures and densities thanks to the cooling processes and to the stellar feedback. The structure of the corona, that cools starting from the more dense and hot gas located at the center of the galaxy, can be seen. A different structure is present in the gas at the interface between **BM_R** and **NOFEED_R**.

cm^{-3}. In the first two panel from left to right it can be appreciated how the temperature and density of the hot gaseous halo change over time: a 'cooling bridge' forms between the corona and the gas in the disc at around 10^4 K. This represents the coronal gas that is cooling and is fueling the galaxy with new gas for the star formation. This gas can cool more rapidly thanks to the mixing with the galactic fountains. The first coronal gas that cools down is the one present in the central regions of the corona, that has the higher densities and temperatures. After 2 Gyr also lower density gas starts to cool, forming gas trails in the diagram and reaching the temperatures present in the disc.

The **NOFEED_R** simulation (third panel) has a similar overall structure, but some differences are clearly evident. The hot gas generated by the SNe is absent due to the lack of stellar feedback. Furthermore, a noticeable difference is present in the structure of the 'cooling bridge': the structures at lower densities and temperatures (present in **BM_R**) are totally absent. Looking at the lower panels, the density-temperature diagram for the gas at the disc-corona interface ($1.5 < z < 4$ kpc) can be observed. In **BM_R** at $t = 1$ Gyr (second panel) a multiphase medium, with both warm and cold gas, as well as hot gas, is present, instead, this is missing at the start of the simulation (first panel, $t = 0.05$ Gyr) since the first SNe are not exploded yet. In **NOFEED_R** (third panel) the cold and warm gas phases are completely absent. This gives a first idea on the importance of stellar feedback, and therefore the production of galactic fountains, for the creation of a multiphase medium over the plane of the disc. The formation of warm and cold gas does not seem to be caused exclusively by the coronal gas cooling, otherwise these phases of gas would be somehow present in **NOFEED**. This aspect will be better explored in Section 4.4.4.

4.4 Star formation and galactic gas circulation

4.4.1 Star formation history

In Figure 4.7 (left panel) I show the evolution of the star formation rate (SFR) over time of the **BM_NR** (blue line) and **BM_R** (orange line) simulations, and compared it with the **NOCOR** (black line) and **NOFEED_R** (dashed green line) simulations. The evolution of the SFR in the first 0.2-0.3 Gyr has to be considered cautiously. I set the corona in hydrostatic equilibrium,

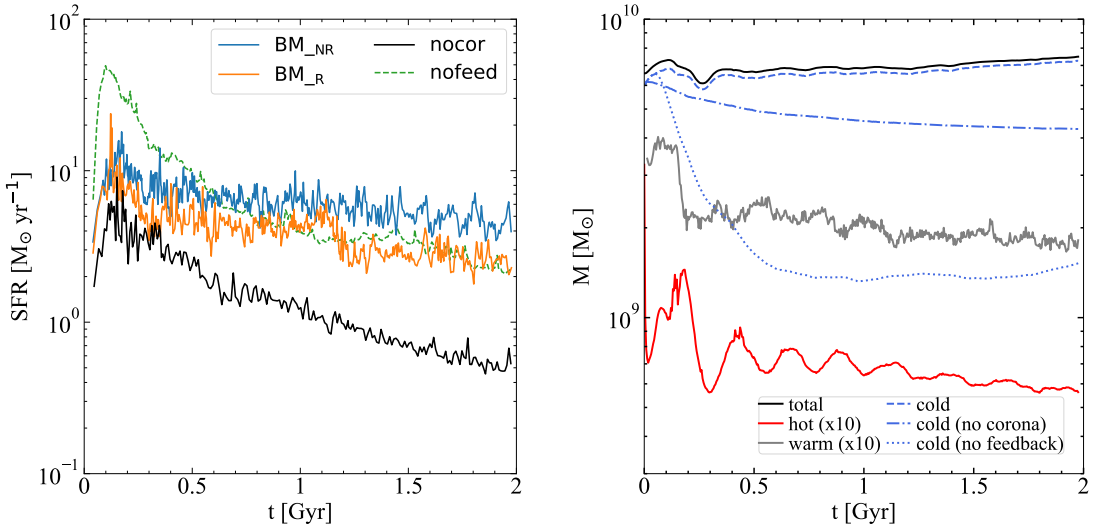

Figure 4.7: *Left:* Star formation rate (SFR) as a function of time for the four simulations performed: **BM_NR** (blue line), **BM_R** (orange line), **NOCOR** (black line) and **NOFEED_R** (green dashed line), see Table 4.2. In the **NOCOR** simulation the SFR is decreasing over time, reaching values of the SFR lower than **BM_NR**/**BM_R** at the end of the simulation. The simulations with the inclusion of the corona maintains an almost constant SFR up to 2 Gyr. **NOFEED_R** features a prominent SFR peak within the first 0.5 Gyr. *Right:* Mass of the gas in **BM_R** as a function of time at a height $|z| < 2$ kpc and a cylindrical radius R< 30 kpc, divided in three ranges of temperature: cold ($T < 10^4$ K, blue dashed line), warm ($10^4 \leq T \leq 5 \times 10^5$ K, grey line) and hot ($T > 5 \times 10^5$ K, red line). The mass of warm and hot gas is multiplied by 10 for clarity. The black line represents the total mass of gas in **BM_R**. The blue dash-dotted line is the mass of cold gas in **NOCOR** and the blue dotted line the mass of cold gas in **NOFEED_R**. The gas in the disc is almost totally cold, the warm and hot gas masses are lower by almost two orders of magnitude. In **BM_R** the mass of cold gas is approximately constant, while in **NOCOR** it decreases over time. In **NOFEED_R** the mass decreases at the beginning, reaching a constant value after 0.5 Gyr.

but the activation of the cooling processes causes a significant deviation from it and causes the corona to lose pressure support in the central regions that rapidly accrete onto the disc. This initial accretion phase is due to the fact that the corona is already in place at the beginning of the simulations. A more realistic configuration would gradually form the hot corona over time following the processes mentioned in Section 1. After ~ 0.2 Gyr the SFR stabilizes, thanks to the self-regulation between star formation and stellar feedback achieved by the *SMUGGLE* model. Also, the corona is more stable, but it slowly continues to accrete onto the disc thanks to radiative cooling.

It is worth noticing the presence of a periodicity in the SFR, this 'noisy' trend is linked to the self-regulation between the formation of stars and the stellar feedback that it causes. On the one hand, the periodic activation of the stellar feedback temporarily reduces the star formation injecting energy and momentum in the ISM, heating the gas and ejecting it from the disc. On the other hand, the periodic re-accretion of gas onto the disc can support star formation with cold gas.

In the **BM_NR** simulation the SFR is $\approx 7 - 8\ M_\odot\ \mathrm{yr}^{-1}$ after the bump and it slightly decreases over time to $\approx 4 - 5\ M_\odot\ \mathrm{yr}^{-1}$ at 2 Gyr. The **BM_R** simulation has a similar trend, where the SFR stays at $2 - 3\ M_\odot\ \mathrm{yr}^{-1}$ after 2 Gyr (starting from $\approx 5 - 6\ M_\odot\ \mathrm{yr}^{-1}$ after the bump) until the end of the simulation. These SFR are in reasonable agreement with the SFR observed nowadays in the Milky Way (e.g. Licquia & Newman, 2015) or in analogous galaxies (Fraser-McKelvie et al., 2019). The SFR is slightly higher when the coronal gas is not rotating: the rotation of the gas modifies the distribution of the gas that is accreted onto the galactic disc. When the gas is not rotating, it tends to accrete more in the central regions of the galaxy because of its negligible angular momentum. This creates a high concentration of gas in the center that is able to cool down and generate a higher SFR, that strongly depends on the gas density.

In the **NOFEED_R** simulation there is a large burst of star formation in the first 0.5 Gyr, reaching 50 $M_\odot\ \mathrm{yr}^{-1}$. The following SFR trend is comparable to the one in the **BM_R** simulation, obtaining also in this case a SFR that stays more or less constant. For this reason, one might think that the stellar feedback is not particularly important for the evolution of the galaxy, but the third row of Figure 4.3 have shown the unrealistic disc structure in the **NOFEED_R** simulation. In the absence of stellar feedback a few large cavities are generated,

whereas high density filaments are absent and the gas is clustered in small clumps in the disc. Probably, the obtained SFR comes from the fact that in the absence of stellar feedback there is neither negative feedback (which would tend to lead to a lower SFR) nor positive feedback (which would tend to raise the SFR), given by the interaction between the galactic fountains and the corona. Despite the galactic fountains absence, the gas is still slowly accreted from the corona onto the disc. The balance between these two types of feedback combined with an accretion of gas from the corona thus gives rise to an approximately constant and similar SFR in the cases with and without feedback.

The **NOCOR** simulation features a SFR that goes from $\approx 3\ M_\odot\ \mathrm{yr}^{-1}$ to $\approx 0.5\ M_\odot\ \mathrm{yr}^{-1}$ at 2 Gyr. It is worth to turn the attention on the differences given by the presence of the coronal gas. In **BM_NR**/**BM_R** the SFR is higher and is declining more slowly, making the galaxy able to maintain an almost constant/slightly decreasing SFR. This behaviour is caused by the accretion of the coronal gas onto the disc, that keeps the density in the disc (maintaining in particular high-density filaments, see Figure 4.3), and, as a consequence, the SFR higher than in the no accretion scenario. This points out how the cold gas reservoir in the disc, that is used to form stars, is rapidly consumed if not replaced by an external source of gas, as expected from the depletion time (see Equation 4.2.2).

To further understand how this phenomenon occurs, in Figure 4.7 (right panel) I show the mass of gas in the disc (gas cells with $|z| < 2$ kpc and $R < 30$ kpc) in **BM_R** as a function of time. Gas has been divided in cold ($T < 10^4$ K, blue dashed line), warm ($10^4 \leq T \leq 5 \times 10^5$ K, grey line) and hot phases ($T > 5 \times 10^5$ K, red line). The black solid line represents the total gas mass in the disc. As a comparison, the dash-dotted and dotted blue lines represent the mass of cold gas in **NOCOR** and **NOFEED_R** simulations, respectively. In general, inside the disc, the majority of the gas is cold, but there is also a small fraction ($\sim 10^8$ $\mathrm{M}_\odot$) of warm and hot gas. The mass of cold gas starts from $\sim 6 \times 10^9$ $\mathrm{M}_\odot$ and is $\sim 7 \times 10^9$ $\mathrm{M}_\odot$ at the end of the simulation. Therefore, the mass of gas is not decreasing over time, but is rather increasing slightly, which would not be possible without the accretion of gas from the corona. In fact, in the **NOCOR** case the mass of cold gas decreases over time down to $\sim 4 \times 10^9$ $\mathrm{M}_\odot$ after 2 Gyr, since it is consumed to form stars without being replaced. This is in line with what was expected, with an average SFR of 1 $M_\odot\ \mathrm{yr}^{-1}$ a gas mass of 2×10^9 $\mathrm{M}_\odot$ is consumed. In **NOFEED_R** the mass of cold gas decreases rapidly in the first 0.5 Gyr, the negative feedback is

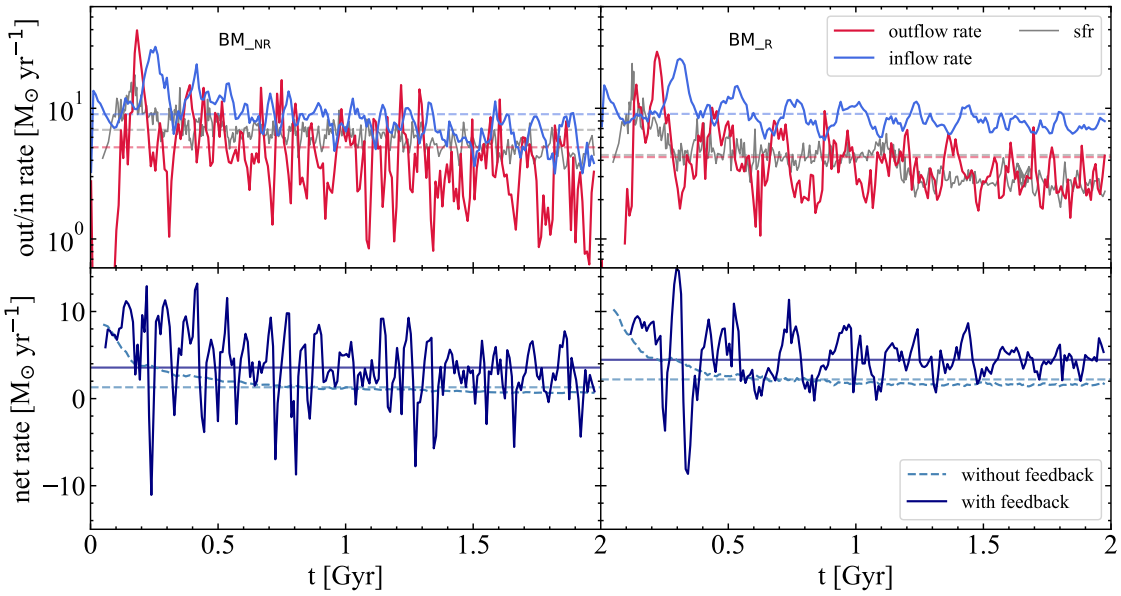

Figure 4.8: *Top row:* Outflow (red line) and inflow (blue line) rates computed for the **BM_NR** (left-hand panel) and **BM_R** (right-hand panel) simulations, from gas inside slabs with a 300 pc width located at ± 2 kpc from the plane of the disc. The grey dashed line represents the SFR. The three horizontal dashed lines represent the average value of the outflow rate (orange), inflow rate (light blue) and SFR (grey). The inflow and outflow rates highlight a strict connection between the formation of stars and the circulation of gas in the galaxy. *Bottom row:* net inflow rate for the same two simulations (solid blue lines), considering also two cases without feedback processes (dashed light blue lines): **NOFEED_NR** (left-hand panel) and **NOFEED_R** (right-hand panel). The net inflow rates are computed as $\dot{M}_{\rm net} = \dot{M}_{\rm in}(t) - \dot{M}_{\rm out}(t - t_{\rm cycle})$, with $t_{\rm cycle} = 100$ Myr. The average net inflow rates are depicted with horizontal lines. It is worth noticing that more gas (about twice as much) is accreted if stellar feedback is present in the simulation.

absent and stars are formed at a rate of over 10 $M_\odot$ yr^{-1}, which causes the disc to consume 4.5×10^9 M$_\odot$ in the time probed by the simulation. After that, the cold gas mass remains approximately constant, although with 5.5×10^9 M$_\odot$ less than in the presence of feedback. Despite the much smaller mass of gas, the SFR has a trend similar to **BM_R** (Figure 4.7), the difference is in how the gas is distributed in the disc, in **NOFEED_R** the gas can cluster in a few areas (in the center or in other clumps, Figure 4.3), increasing the efficiency of the gas-stars conversion process. The ability of the galaxy, in **BM_NR**/**BM_R**, in maintaining a higher SFR longer than in **NOCOR** can be attributed to the presence of the galactic corona that, accreting onto the disc, replenishes the disc with cold gas and slows down the emptying of the cold gas reservoir in the disc.

4.4.2 Galactic outflows and inflows

To understand the relationship between star formation and the gas ejected/accreted from/onto the disc of the galaxy, I analyze the outflow and inflow rates of gas, schematically depicted in Figure 4.2. We define the total inflow rate as

$$\dot{M}_{\rm in} = \dot{M}_{\rm in,\,fount} + \dot{M}_{\rm in,\,int} + \dot{M}_{\rm in,\,cor}. \tag{4.4.1}$$

I computed inflow and outflow rates as described in Marinacci et al. (2019): I took two slabs of width $\Delta z = 0.3$ kpc starting at an height from the plane of the disc of ± 2 kpc (see the shaded area around the dashed horizontal line in Figure 4.3) and sum up the contribution of all gas particles to the outflow/inflow rate

$$\dot{M}_{\rm out/in,\,i} = \frac{v_{z,i} m_i}{\Delta z}, \tag{4.4.2}$$

within the slab and with $R < 30$ kpc. In the above equation $v_{z,i}$ is the gas particle vertical velocity and m_i is the gas particle mass. The outflow rate is given by the gas particles that are moving away from the disc, i.e. particles with $v_z z > 0$; while the condition $v_z z < 0$ identifies the particles corresponding to an inflow.

In the top panels of Figure 4.8 I show the outflow (red line) and the inflow (blue line) rates at a height of 2 kpc over the disc plane for the **BM_NR** (left-hand panel) and **BM_R**

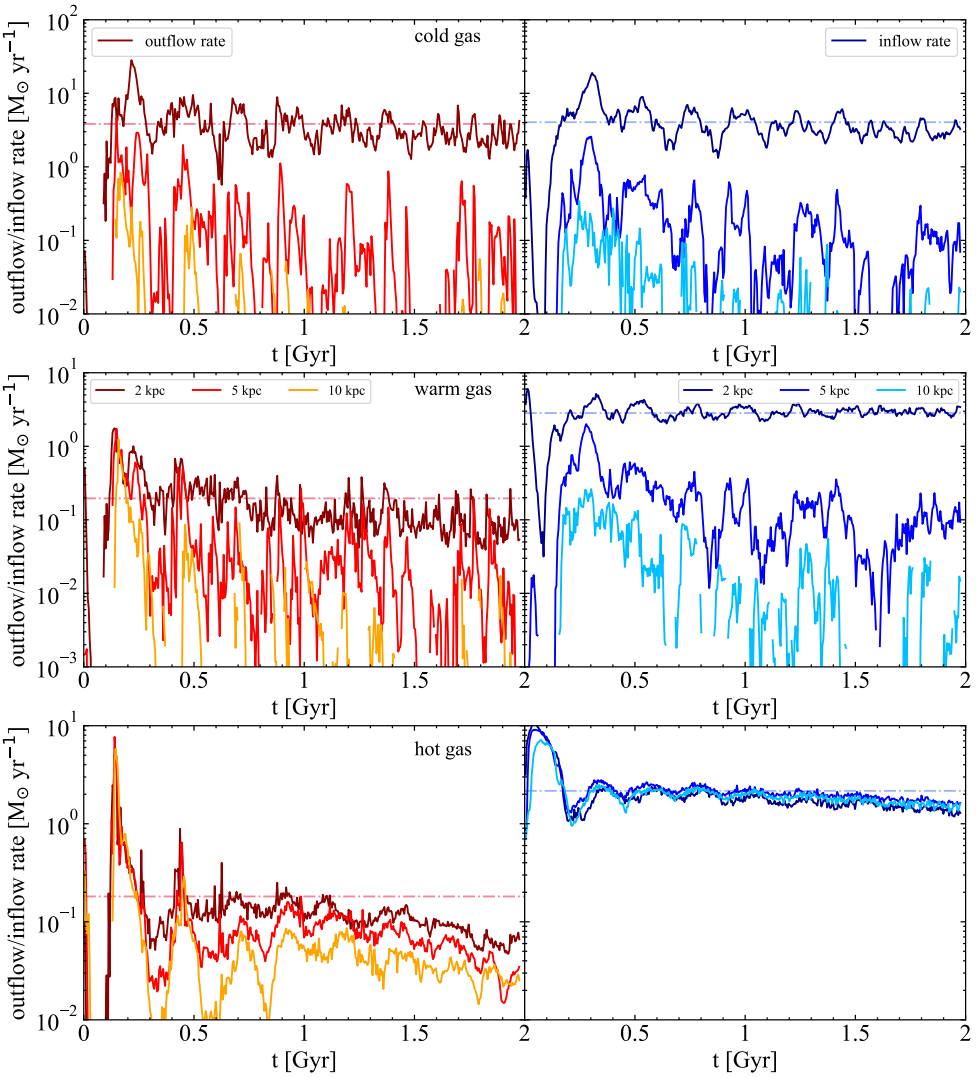

Figure 4.9: Outflow (red lines) and inflow (blue lines) rates for the **BM_R** simulation for three ranges of temperature at three different heights from the plane of the disc: 2 kpc, 5 kpc and 10 kpc (represented with three shades of red or blue, as described in the legend). The horizontal dashed lines represent the average value of the outflow/inflow rates at 2 kpc. *Top panel*: cold gas ($T < 10^4$ K), the inflow and outflow rate values are almost identical, this phase seems to be generated for the majority by the galactic fountains ejected from the disc thanks to stellar feedback. *Middle panel*: warm gas ($10^4 \leq T \leq 5 \times 10^5$ K), the outflow rate is low ($\approx 0.2\ M_\odot\ \mathrm{yr}^{-1}$) with respect to the inflow rate. This gas is formed at the disc-corona interface, the same region where the galactic fountains are present, therefore I speculate that it might be created by the interaction between the corona and the cold gas. *Bottom panel*: hot gas ($T > 5 \times 10^5$ K), the accretion of this gas derives from the cooling of the galactic corona. This accretion is almost spherical and the values of the inflow rate at different heights from the disc are very similar.

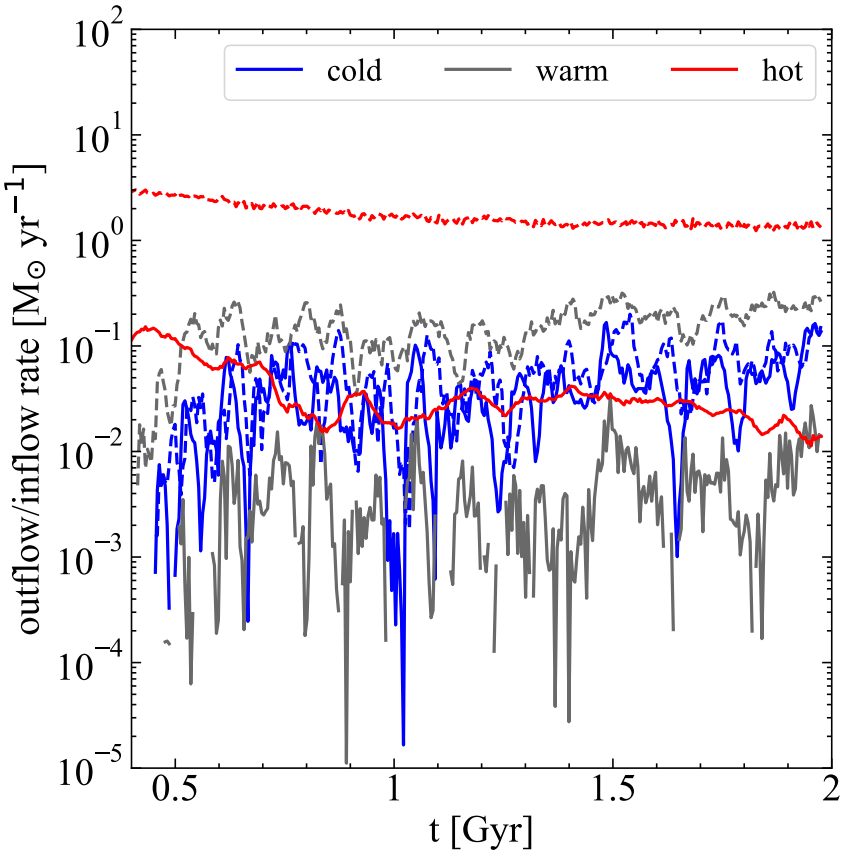

Figure 4.10: Outflow (solid lines) and inflow (dashed lines) rates of the simulation **NOFEED_R** computed at ± 2 kpc from the plane of the disc for the same three ranges of temperature of Figure 4.9. Only the inflow rate of hot gas has a non negligible value and there is almost no accretion of cold and warm gas. Furthermore, the outflow rates are also almost zero, due to the absence of stellar feedback no outflows are generated in the simulation.

(right-hand panel) simulations. The grey line represents the corresponding SFR. The three horizontal dashed lines represent the average values of the inflow (light blue) and outflow (orange) rates and the average SFR (grey).

In **BM_NR** the inflow rate ($\langle \dot{M} \rangle_{\rm in} \approx 9\ M_\odot\ {\rm yr}^{-1}$) is, on average, higher than the outflow rate ($\langle \dot{M} \rangle_{\rm out} \approx 5\ M_\odot\ {\rm yr}^{-1}$). The rates in **BM_R** are very similar, the average inflow and outflow rates are $\langle \dot{M} \rangle_{\rm in} \approx 9\ M_\odot\ {\rm yr}^{-1}$ and $\langle \dot{M} \rangle_{\rm out} \approx 4\ M_\odot\ {\rm yr}^{-1}$ respectively. It is worth noticing that in both simulations most of the peaks in the inflow rate correspond to depressions in the outflow rate and vice versa. This indicates the presence of a gas circulation at the interface between the disc and the halo (occupied by the corona) of the galaxy: the stellar feedback produces galactic fountains (outflows) that pass through the corona and then fall back onto the disc (inflows). This phenomenon is expected to drag also some coronal gas that could refill the disc and sustain the star formation.

Looking at the SFR, the first noticeable thing is that in both **BM_NR** and **BM_R** the average SFR ($\approx 6.8\ M_\odot\ {\rm yr}^{-1}$ in **BM_NR** and $\approx 4.4\ M_\odot\ {\rm yr}^{-1}$ in **BM_R**) is below the average inflow rate, implying that the supply of gas from the corona has a non negligible influence on the total gas budget of the galaxy, making it an important reservoir for star formation. Taking these numbers at face value, I can infer that star formation can be sustained entirely by the accretion of the coronal gas. Indeed, the inflowing gas is mostly caused by the accretion due to coronal gas. Computing the average net inflow rate as $\langle \dot{M}_{\rm net} \rangle = \langle \dot{M} \rangle_{\rm in} - \langle \dot{M} \rangle_{\rm out}$, I obtain $\approx 4\ {\rm M}_\odot\ {\rm yr}^{-1}$ in **BM_NR** and $\approx 5\ {\rm M}_\odot\ {\rm yr}^{-1}$ in **BM_R**, it follows that only a fraction of the inflows is accounted for by the gas that is ejected from the disc and that returns back on it ($\dot{M}_{\rm in,\ fount}$), the rest of the gas must be accreted from the corona ($\dot{M}_{\rm in,\ int} + \dot{M}_{\rm in,\ cor}$).

On average, the inflow rate in **BM_NR** and **BM_R** is almost identical. Therefore, the rotation of the coronal gas is not decreasing the rate at which the gas is falling onto the disc, but rather the distribution of this accreted gas appears to be different. The lower SFR in **BM_R** (Figure 4.7, left panel) tells us that the accreted gas is less efficient in forming new stars with respect to **BM_NR**. One hypothesis is that the gas is more easily accreted in the outermost areas of the disc rather than in the center, where the density of the gas is higher and therefore stars can be formed more easily.

Furthermore, it can be noticed that the SFR trend is linked to the outflow/inflow rates. Intervals of above average SFR are often followed by local outflow rate peaks and reciprocally

the SFR peaks follow the inflow rate peaks. The presence of this correlation between the SFR and outflow/inflow rate trends highlights the role of the star formation in the circulation of gas in the galaxy. The gas accreted from the corona can efficiently cool and form stars in the disc of the galaxy, which subsequently expel a fraction of gas from the disc. This underlines a strict connection between these phenomena, showing how the star formation is intimately linked to the accretion/ejection of gas from/into the external environment.

4.4.3 Positive feedback scenario

One fundamental phenomenon that has to be understood is whether or not the stellar feedback might act as a positive feedback for star formation. This has been already studied in the literature (e.g. Marinacci et al., 2010; Hobbs & Feldmann, 2020), and it is speculated that the galactic fountains originated from the stellar feedback can enhance the accretion of gas from the galactic corona, thanks to the mixing of the gas ejected from the disc with the hot gas that surrounds it. This can happen as a result of turbulence or of the generation of a Kelvin-Helmoltz instability in the wake of the galactic fountains. This newly generated mixture of gas has a lower cooling time with respect to the original coronal gas, ranging from a few hundred Myr to $\lesssim 1$ Myr (Marinacci et al., 2010) due to the lower temperature (between 10^4 and 10^6 K) and higher metallicity (between 0.1 and 1 $Z_\odot$), allowing a more rapid accretion.

To better investigate this phenomenon, to which I will refer as positive feedback scenario, I analyze the set of simulations without stellar feedback (**NOFEED_NR** and **NOFEED_R**, see Table 4.2), these have the same ICs of **BM_NR**/**BM_R**, but the stellar feedback processes are disabled. In this way, there is no injection of energy and momentum in the ISM, therefore no outflow is produced and there is almost no interaction between the disc and the coronal gas in the extra-planar region. I want to compare **BM_NR**/**BM_R** to **NOFEED_NR**/**NOFEED_R** in order to see if there are eventually differences in the accretion of gas. In doing so, I have to consider only the gas accreted from the galactic corona. I want to understand how much gas is accreted from this component without the galactic fountains (that are not present without stellar feedback) contribution (see Figure 4.2). In fact, the galactic fountain gas circulates outside and inside the galaxy, but does not change the quantity of gas stored in the disc, that can increase consequently to inflows of gas from the corona. Therefore, I need to subtract to the total inflow rate $\dot{M}_{\rm in}$ the inflow rate coming from the galactic fountains $\dot{M}_{\rm in,\,fount}$, that is

$\sim \dot{M}_{\rm out}$. For this reason, the net inflow rate has been computed as

$$\dot{M}_{\rm net} = \dot{M}_{\rm in}(t) - \dot{M}_{\rm out}(t - t_{\rm cycle}) \tag{4.4.3}$$

at each time t. As depicted in Figure 4.2, a large fraction of the inflowing gas is coming from the galactic fountains, the gas is ejected and then, after a typical time $t_{\rm cycle} \sim 100$ Myr (Fraternali, 2014), which is computed considering an average initial velocity of $70 - 80$ km s^{-1} (Marasco et al., 2012), falls back onto the disc. This time is in line with what I found in this Chapter, measuring the average time span between two consecutive outflow/inflow rate peaks. Choosing a different $t_{\rm cycle}$ in Equation (4.4.3) does not change significantly the results of following analysis.

In the lower panels of Figure 4.8 I show the net inflow rates for the couple of simulations **BM_NR**/**NOFEED_NR** (left-hand panel) and **BM_R**/**NOFEED_R** (right-hand panel) computed as in Equation (4.4.3). The horizontal lines represent the average value of the net inflow rate with (solid blue line) and without (dashed light blue line) stellar feedback. I can see that the mean net inflow rate without feedback is lower than the one with feedback in both cases. In the **NOFEED_NR** simulation the rate is $\dot{M}_{\rm net} \approx 1.3$ M$_\odot$ yr^{-1}. Without the stellar feedback $\dot{M}_{\rm net}$ is approximately half of the net inflow rate in **BM_NR** (≈ 3.6 M$_\odot$ yr^{-1}). Essentially the same yields for the **BM_R**/**NOFEED_R** simulations, in which the net rates are $\approx$ 2.2 M$_\odot$ yr^{-1} and ≈ 4.5 M$_\odot$ yr^{-1} respectively. The rates found without feedback are in line with a rough estimate of the accretion rate computed as the mass contained in the corona cooling radius, which is about $15 - 20$ kpc. Therefore, it is the mass of gas that is expected to cool in 2 Gyr in a pure radiative cooling scenario. The efficiency of gas accretion from the corona to the disc is higher if stellar feedback is present. Therefore, stellar feedback is increasing the rate at which the gas is falling onto the disc. This is due to the mixing between the two gas phases (the cold ISM and the hot corona) induced by the stellar feedback itself.

4.4.4 Gas phases at the disc-corona interface

The gas contained in the outflows and inflows is a complex medium composed of different phases. Understanding their evolution may allow us to better comprehend how the circulation of gas around the galaxy and the positive feedback scenario work. In Figure 4.9, where

I consider only the fiducial simulation **BM_R**, I show the outflow (red shades) and inflow (blue shades) rates in three ranges of temperatures, cold ($T < 10^4$ K, first panel), warm ($10^4 \leq T \leq 5 \times 10^5$ K, second panel) and hot ($T > 5 \times 10^5$ K, third panel) and at three heights from the plane of the disc (2 kpc, 5 kpc and 10 kpc, see the dashed horizontal lines in Figure 4.3), highlighted by the three shades of colour. These rates are computed as described in Section 4.4.2.

In the top panel of Figure 4.9, I show the cold phase. The cold ($T < 10^4$ K) outflow and inflow rates have a very similar trend, but shifted on average by $t_{\rm cycle} \sim 100$ Myr, which is the average time that a galactic fountain takes to return to the disc after the ejection, as already mentioned in Section 4.4.2. The average value of the outflow and inflow rates is also similar (≈ 4 M$_\odot$ yr^{-1}) and this gives us information on the origin of this phase of gas. I speculate that it represents the gas from the galactic fountains, that are mainly made by the cold gas of the disc: the gas that is ejected from the plane of the disc is re-accreted after a fountain cycle, this explains the periodic shifted trend of the ejected and accreted gas. This is corroborated by the fact that both outflow and inflow rates at 5 and 10 kpc are substantially lower, in fact the majority of the fountains stays in the first kpc from the disc, as it can be seen from the gas projections (see Figures 4.3, 4.4, 4.5) only the strongest fountains can reach heights $|z| > 10$ kpc.

The middle panel shows the warm phase ($10^4 \leq T \leq 5 \times 10^5$ K), this is particularly important for the positive feedback scenario as it can be argued that the warm gas is generated from the mixing between the cold galactic fountains and the hot corona. In fact, in this case there is a substantial difference between the gas that is accreted and the gas that is ejected. The inflow rate is much higher (≈ 3 M$_\odot$ yr^{-1}) with respect to the outflow rate, that is almost negligible (≈ 0.2 M$_\odot$ yr^{-1}), only a small fraction of the galactic fountains is composed by warm gas. Therefore, this gas phase is not lifted from the disc, but is rather generated at the disc-corona interface. The inflow rate of warm gas is lower at 5 and 10 kpc (below 0.2 M$_\odot$ yr^{-1}), similarly to the cold phase. Hence, it seems to be generated from the same region where the galactic fountains are present. This warm gas seems to be created for the most part in the first 2-3 kpc over the disc, and is then accreted onto the disc giving a non-zero inflow rate. This indicates how the accretion of warm gas is not generated by a cooling flow but is rather created thanks to the positive action of stellar feedback.

The bottom panel shows the hot gas ($T > 5 \times 10^5$ K). Only a small part of the ejected gas is made by this phase (coming from the gas shock-heated from the SNe), giving a outflow rate of ≈ 0.2 M$_\odot$ yr^{-1}. The inflow rate is stable at a value of ≈ 2 M$_\odot$ yr^{-1} at the three different heights. Therefore, the accretion has the same intensity at 2, 5 and 10 kpc over the plane of the disc. This gas is probably part of the galactic corona that is accreted onto the galaxy and it moves towards the central regions of the galaxy replacing the gas accreted onto the disc.

An interesting trend that can be noticed is that the gas with higher entropy ($s \propto T/\rho^{2/3}$) reaches higher distances from the disc than the cold gas. Since a gas distribution is convectively stable if entropy increases with radius, hotter and less dense gas can circulate towards higher distances with respect to cold gas. This behaviour is apparent looking at the outflowing gas in Figure 4.9: only a small fraction of the cold ejected gas ($\sim 0.5\%$) arrives at 10 kpc. This fraction increases with the temperature and is $\sim 10\%$ for the warm gas and $\sim 60\%$ for the hot gas.

One may argue that the intermediate warm phase of the accreted gas could come from the radiative cooling of the corona without the presence of cold galactic fountain gas that may act as a catalyst, and that this can happen near the disc where the density and the cooling function of the corona are higher. To rule out this possibility I have computed the same outflow/inflow rates at 2 kpc, shown in Figure 4.10, in the **NOFEED_R** simulation, where the cooling of the corona is present, but the stellar feedback is turned off. In this case the outflow rates (solid lines) are negligible because of the feedback absence. The only important accretion of gas (dashed lines) is in the hot phase (red colour) at rates of $2 - 3\ M_\odot$ yr^{-1}, that are very similar to the **BM_R** simulation. The accretion of cold (blue colour) gas is below $0.1\ M_\odot$ yr^{-1} because the galaxy is lacking the galactic fountains. A similar rate is present for the warm phase (grey colour), the absence of ejections of cold gas from the disc means that the warm gas cannot be formed.

Hence, I found that the warm gas found in my simulations is generated as a consequence of a gas circulation at the disc-corona interface, mediated by the galactic fountains ejected from the disc. This warm gas then can fall towards the galactic disc, fueling the galaxy with a non-negligible (≈ 3 M$_\odot$ yr^{-1}) amount of gas, that is necessary to sustain the SFR found in **BM_R** (≈ 4 M$_\odot$ yr^{-1}).

4.5 Comparison to previous works

In the last years different numerical works have been concerned with the study of the galactic corona, or with the circumgalactic medium in general, analyzing its properties (e.g. Lochhaas et al., 2020), the relation with outflows (e.g. Pandya et al., 2021) and numerical cooling flow solutions (e.g. Stern et al., 2019, 2020). In particular, Stern et al. (2020) hypothesizes that under a critical accretion rate $\dot{M}_{\rm crit}$ of $\approx 10\ M_\odot\ {\rm yr}^{-1}$ for a Milky Way-like galaxy, the gas is accreted onto the disc nearly at the virial temperature ($\sim 10^6$ K). This is consistent with my results in absence of feedback (**NOFEED** simulations), in fact, in this case in my simulations the accretion rate from the corona is lower than $\dot{M}_{\rm crit}$ and therefore it happens in the hot mode (see red dashed line in Figure 4.10), with a gaseous flow that stays hot until it reaches the interface region with the disc. In the simulations including feedback this hot gas can eventually mix with the gas ejected by stellar feedback and its accretion rate is enhanced.

Comparatively few works have focused on the interaction between the galactic fountains and the corona, and on the resulting positive feedback (e.g. Marinacci et al., 2010, 2011; Armillotta et al., 2016; Hobbs & Feldmann, 2020; Gronke et al., 2022). I focus, in particular, on Marinacci et al. (2010) and Hobbs & Feldmann (2020) whose aim is more similar to the analysis presented in this Chapter. Both papers found evidence of positive feedback coming from this galactic fountain-corona interaction.

Marinacci et al. (2010) developed 2D simulations, with the Eulerian code ECHO, of a galactic fountain cloud with $T = 10^4$ K moving through the galactic corona ($T = 2\times10^6$ K), with an initial velocity of 75 km s^{-1}. They found that for reasonable density ($n \approx 2 \times 10^{-3}$ cm^{-3}) and metallicity ($Z \approx 0.1$ Z$_\odot$) values of the corona, some coronal gas can condensate in the wake of the cloud, leading to a mass of cold gas that increases over time as the fountain passes through the hot gas. By extrapolating the result for a single fountain gas cloud to the whole galactic disc, they obtained a global accretion rate of ≈ 0.5 M$_\odot$ yr^{-1} for the Milky Way.

Hobbs & Feldmann (2020) investigated the positive feedback process simulating, with the GIZMO code, a portion of a star-forming disc in a small box of $2 \times 2 \times \pm 50$ kpc; therefore the resolution (23 M$_\odot$ for gas particles) is higher than in the simulations presented in this Chapter. The galactic corona has a constant number density of 6×10^{-4} cm^{-3} and a con-

stant temperature of $\approx 10^6$ K. They also take into account gas turbulence in the gaseous disc and use a different stellar feedback implementation (see Kim et al. 2014), in which SN feedback has a purely thermal component. Despite the differences in the ICs and in the models, their simulations suggest the presence of a positive stellar feedback mechanism as well. Furthermore, also in their case the mass of cold gas in the disc remains approximately constant as a consequence of coronal accretion. Hobbs & Feldmann (2020) developed an analytical model to examine the dependence of the accretion rate on the SFR. They found that negative feedback starts dominating over positive feedback when the SFR (extrapolated to the whole galactic disc) overcomes a value of $\approx 0.5\ M_\odot\ \mathrm{yr}^{-1}$. Above this value, an increase in the SFR will produce a decrease in the accretion rate. Although I would need more galaxy configurations to robustly investigate this aspect, it seems that my simulations behave differently as there is not an obvious trend between an increase/decrease of the SFR and a corresponding decrease/increase in the accretion rate (see Figure 4.8). My simulations appear to suggest that for a Milky Way-like galaxy positive stellar feedback continues to be important even at SFR above $\approx 0.5\ M_\odot\ \mathrm{yr}^{-1}$.

4.6 Summary

In this Chapter I studied the evolution of a series of multicomponent N-body hydrodynamical models representative of a Milky Way-like galaxy embedded in a hot gaseous atmosphere, the so-called corona, using state-of-the-art numerical simulations. In particular, I focused on the interaction between the disc and the corona caused by the gas exchanges between these two components mediated by stellar feedback. I studied several aspects of this interaction, such as the balancing between the star formation and the outflows/inflows of gas and the mixing between the disc and the corona. I analyzed these aspects employing the moving-mesh code Arepo and the explicit stellar feedback and ISM medium model *SMUGGLE* to carry out my simulations. I have successfully built a set of ICs for the hydrodynamical N-body simulations analyzed in this Chapter. These configurations have then been used to perform 'full-physics' simulations with the *SMUGGLE* model. The main results of these calculations can be summarized as follows.

(i) I found that the galactic corona is the main contributor to the material sustaining star

formation in the galaxy. The star formation takes place from the cold gas in the disc, whose mass is maintained at a nearly constant level by gas accretion from the corona; without this process the galaxy would have a lower SFR and would progressively deplete its gas content and lower its star formation rate in $\sim 1 - 2$ Gyr.

(ii) I studied the outflow/inflow rates from/onto the galactic disc. I have observed the formation of gaseous outflows thanks to the combined effects of the different stellar feedback processes implemented in the *SMUGGLE* model. The analyzed outflow rates are generated by the galactic fountains, which are composed mostly by cold metal-rich gas ($T < 10^4$ K), but possess also a fraction of warm and hot gas ($T \geq 10^4$ K). The alternation of the peaks in the outflow and inflow rates, for which each outflow-dominant phase is followed by an inflow-dominant phase, suggests the presence of a circulation of the gas between the galactic disc and the corona, in fact almost 50% of the inflow rate derives from the galactic fountains. The remaining inflow rate fraction is gas accreted onto the disc from the corona. I found a connection between the gas inflowing into the galaxy and star formation: the average SFR is below the average inflow rate, making the accretion of gas sufficient to entirely sustain star formation.

(iii) I have analyzed the *positive feedback scenario*: the accretion of gas might potentially be helped by the interaction between the galactic fountains and the coronal gas, favoring its cooling. In doing so, I made a comparison between simulations with and without stellar feedback. I found that stellar feedback helps in increasing the accretion rate of the coronal gas, which is two times larger than in the no feedback case. This increase of accretion is due to the generation of a warm gas phase (with an inflow rate of $\approx 3\ M_\odot\ \mathrm{yr}^{-1}$) at the disc-corona interface thanks to the action of positive stellar feedback. This warm gas then falls onto the disc, cools down and eventually fuels new star formation.

The type of simulations analyzed in this Chapter (and in this Thesis in general) represents a bridge between idealized small-scale simulations and cosmological simulations, allowing to obtain a high/intermediate resolution while still considering a realistic galactic setup. In the next Chapter I will analyze how the gas accreted from the CGM thanks to the galactic fountains interaction can become available for the formation of new stars.

Chapter 5

Understanding the Baryon Cycle: Fueling Star Formation via Inflows

5.1 Introduction

Understanding how CGM is accreted into the galactic disc is still puzzling. The goal of this Chapter is to understand how the CGM can become available for the formation of new stars in the center of the disc, therefore I investigate the distribution of vertical and radial outflow and inflows over the disc and how they are connected to the structure of the disc itself. To achieve this goal, I perform high-resolution hydrodynamical N-body simulations with the *SMUGGLE*model, an explicit ISM and stellar feedback model for the moving-mesh code Arepo. I simulate a set of 9 star-forming Milky Way-like galaxies including a hot gaseous halo surrounding the galactic discs. I vary the gas disc mass and size, in order to quantify the key properties of vertical and radial gas inflows/outflows and investigate their connection to the evolution of the whole galactic disc. The Chapter is organized as follows. In Section 6.2 I briefly introduce the numerical methods and how I built the initial conditions for the simulations. I analyze the distribution of vertical outflows and inflows in Section 5.3 and of radial outflows in Section 5.5. In Section 5.6 I study the evolution of the disc size over time. I compare these results with previous works in Section 5.7. Finally, Section 5.8 provides a brief summary of the Chapter. The results of this Chapter are based on the paper Barbani et al. (2025b, submitted to A&A).

Table 5.1: *Structural parameters of the fiducial Milky Way-like galaxy simulated in this Chapter.* From left to right: virial radius r_{200}; dark matter halo mass ($M_{\rm dm}$); dark matter halo scale length ($r_{\rm s}$); bulge mass ($M_{\rm b}$); bulge scale length (a); stellar disc mass ($M_\star$); stellar disc scale length ($h_\star$); stellar disc scale height ($z_\star$); gaseous disc mass ($M_{\rm g}$); gaseous disc scale length ($h_{\rm g}$); mass of the corona ($M_{\rm cor}$) computed within the virial radius r_{200}; corona core radius ($r_{\rm c}$). See Chapter 3 for a detailed description of these parameters.

r_{200} [kpc]	$M_{\rm dm}$ [$M_\odot$]	$r_{\rm s}$ [kpc]	$M_{\rm b}$ [$M_\odot$]	a [kpc]	$M_\star$ [$M_\odot$]
241	1.53×10^{12}	36.46	1.5×10^{10}	1.3	4.73×10^{10}
$h_\star$ [kpc]	$z_\star$ [pc]	$M_{\rm g}$ [$M_\odot$]	$h_{\rm g}$ [kpc]	$M_{\rm cor}$ [$M_\odot$]	$r_{\rm c}$ [kpc]
3.8	380	9×10^9	7.6	5×10^{10}	83

5.2 Numerical methods

The simulations presented in this Chapter are performed with the moving mesh code Arepo (Springel, 2010b) together with *SMUGGLE* (Marinacci et al., 2019), as extensively discussed in Chapter 2.

The generation of initial conditions is based on the method presented discussed in Chapter 3, which enables the creation of a multi-component galaxy in approximate equilibrium (see Springel et al., 2005). I consider galaxies including the following components: a dark matter halo and a stellar bulge, a thick stellar disc, a thick gaseous disc and a galactic hot corona. The galaxy components are modeled using the same functional profiles of the simulations presented in Chapter 4. The key difference are in the metallicity distribution of the disc and the galactic corona profile. For the disc I used an exponentially declining profile based on observation of the metallicity gradient in the Milky Way (Lemasle et al., 2018) with slope = -0.0447 dex kpc^{-1} and intercept = 0.3522 dex, thus the metallicity at the solar radius $R \sim 8$ kpc is $Z_\odot$, instead of a constant value $Z = Z_\odot$.

Figure 5.1 shows the number density profile for the galactic corona. Points with errorbars are observational data for the density of the Milky Way corona (Putman et al., 2021), which are obtained from dwarf galaxies observations by evaluating the coronal density necessary to strip the gas of the dwarf at the perigalacticon. Hence, they should be considered as lower

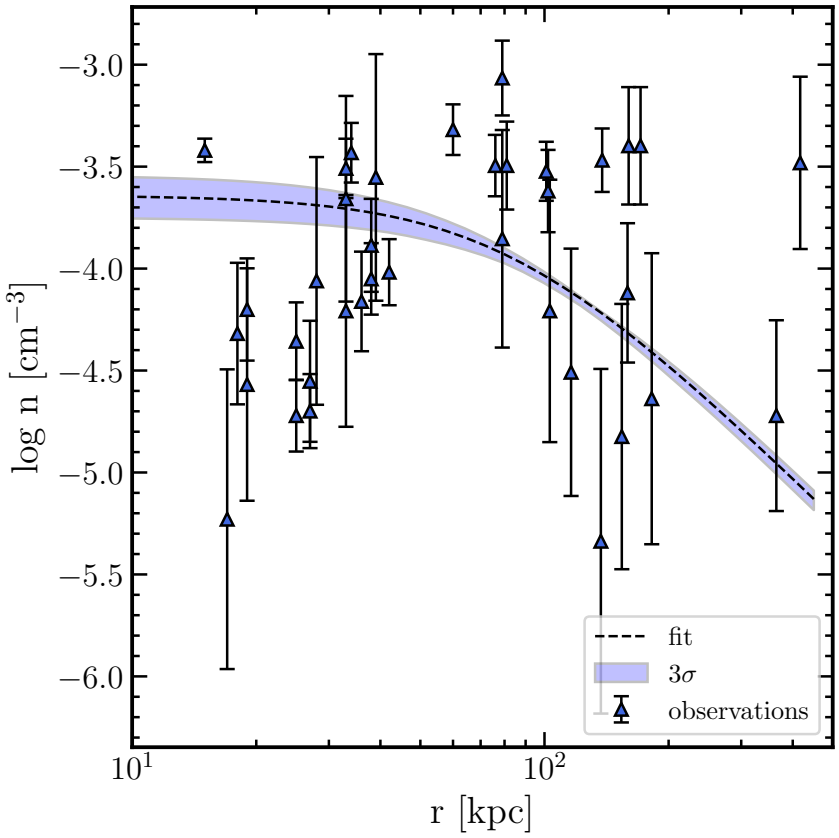

Figure 5.1: Number density of the coronal gas as a function of radius. The black dashed line is the median model obtained by fitting a beta model to Milky Way coronal gas observations (upward pointing triangles with errorbars) using a Markov chain Monte Carlo algorithm. The coloured shaded area represents the 3σ region. Observations, which should be considered as lower limits for the coronal density, are taken from Putman et al. (2021).

Table 5.2: Summary of the simulations investigated in this Chapter, each varying specific model parameters relative to the fiducial run (labeled as **gal**). The initial conditions differ in the mass of the gaseous disc, scaled by $f_{\rm M}$ relative to the fiducial value, and its scale length, scaled by $f_{\rm G}$. The fiducial values for these parameters are provided in Table 5.1.

Name	**gal_r05**	**gal**	**gal_r2**	**gal_m05r05**	**gal_m05**	**gal_m05r2**	**gal_m2r05**	**gal_m2**	**gal_m2r2**
$f_{\rm M}$	1	1	1	0.5	0.5	0.5	2	2	2
$f_{\rm G}$	0.5	1	2	0.5	1	2	0.5	1	2

limits for the density of the corona. The β model profile of the corona has formally infinite mass, but I truncated the resulting density distribution at $10\,R_{200}$. To obtain the central density ρ_0 and the core radius r_c I applied a Markov chain Monte Carlo algorithm using an affine-invariant ensemble sampler (EMCEE package, Foreman-Mackey et al. 2013). From the Markov chain Monte Carlo fit I found a core radius $r_c = 83$ kpc and a central density $\rho_0 = 3.3 \times 10^3$ M$_\odot$ kpc^{-3}. The effective equilibrium of each system has been verified by running adiabatic simulations, i.e. without dissipative processes such as radiative cooling. The metallicity of the coronal gas is set to Z $= 0.1$ Z$_\odot$, in line with observational estimates (e.g. Bogdán et al., 2017).

Table 5.1 lists the structural parameters of my fiducial Milky Way-like galaxy model, the other eight galaxies investigated in this Chapter are variations of this fiducial model. In Table 5.2 I summarize the different parameter variations that I consider in my runs. Specifically, I scale the mass of the gaseous disc $M_{\rm g}$, by a factor $f_{\rm M}$, and the gaseous disc scale length $h_{\rm g}$, by a factor $f_{\rm G}$, with respect to the fiducial values $9 \times 10^9\,M_\odot$ and 7.6 kpc – in practice my simulation set explores variations of a factor of two with respect to these reference values. The gravitational softening length is set at a minimum of $\epsilon_{\rm gas} = 10$ pc for the gas and at $\epsilon_\star = 21.4$ pc for the stars for all the nine runs. In the fiducial run there are $N_{\rm disc} = 3.2 \times 10^6$ particles in the stellar disc, $N_{\rm bulge} = 8 \times 10^5$ in the bulge and $N_{\rm gas} \simeq 1.1 \times 10^7$ gaseous particles, with $N_{\rm gas,d} = 3.2 \times 10^5$ gaseous particles in the disc and $N_{\rm gas,cor} \simeq 1.1 \times 10^7$ in the corona. This results in a mass resolution $m_{\rm gas} = 1.1 \times 10^4$ M$_\odot$, $m_{\rm disc} = 1.5 \times 10^4$ M$_\odot$ and $m_{\rm bulge} = 2 \times 10^4$ M$_\odot$ for the stellar disc and bulge particles, respectively. The number of gas particles in the disc in the simulations where the mass of this component is varied with respect to the reference value is changed accordingly to ensure the same mass resolution.

In the next Sections I discuss the main results of my simulations. In Section 5.3 I present the structure of the galaxies and of the gas in my simulations and I analyze the connection to the SFR. In Section 5.4 I focus on the vertical ejection/accretion of gas from/into the galactic disc, studying also the net accretion rate and how it changes between the 9 simulations. In Section 5.5 I analyze radial gas motions in the disc plane and their importance for the baryon cycle. Finally, in Section 5.6 I look at the disc size temporal evolution and its link to the vertical outflow/inflow rates.

5.3 Galaxy and outflow/inflow structure and distribution

I begin my discussion by presenting the general properties and the appearance of the gaseous discs in my runs. Figure 5.2 shows the gas projected density distribution (edge-on and face-on), after 1 Gyr of evolution, of all 9 simulations considered in this Chapter. Each row differs in the mass of the gaseous disc, whereas in columns only the initial scale length the gaseous disc is varied. The simulations are arranged, from left to right, as follows (see Table 5.2 for their main properties): **gal_m05r05**, **gal_m05** and **gal_m05r2** (first row), **gal_r05**, **gal** and **gal_r2** (second row), **gal_m2r05**, **gal_m2** and **gal_m2r2** (third row). In the second row, the central panel shows the fiducial galaxy; in the left panel the disc scale length is reduced by a factor $f_{\rm G} = 1/2$ relative to the reference case, whereas in the right panel the scale length is scaled by $f_{\rm G} = 2$ compared to the fiducial simulation. The first row displays simulations with a gaseous disc mass halved with respect to the second row ($f_{\rm M} = 1/2$), while the third row shows simulations with gaseous disc mass doubled relative to the reference value ($f_{\rm M} = 2$). Brighter colours represent higher surface density as indicated in the colorbar, which is kept the same in all panels to facilitate the comparison. The panels have the same physical size, 70×70 kpc for the face-on projections and 70×15 kpc for the edge-on projections. For subsequent analysis (see Sect. 5.4 and 5.5) it is useful to introduce a characteristic radius R_d representing the size of the gaseous disc. I define R_d as the radius at which the gas surface density drops below 1 $\mathrm{M_\odot\ pc^{-2}}$ (see also Di Teodoro & Peek, 2021). It is important to note that this definition generally results in R_d differing from the disc scale length $h_{\rm g}$ set in the initial conditions. This characteristic radius is shown as a white dashed circle in Figure 5.2 for the **gal_r05**, **gal** and **gal_r2** simulations (second row). The adopted R_d definition captures

well the disc extent in all the simulations analyzed here.

All nine simulations produce stable discs, with no evidence of bar formation. The resulting disc morphology is similar in all runs despite the different scale lengths, which however influence the overall disc extent. Looking at the face-on projections (top panels) it is worth to notice the formation of a multiphase ISM distributed in low density cavities and high density filaments, structures observed in recent JWST observations (Watkins et al., 2023; Thilker et al., 2023). Low-density cavities contain hot gas ($T \approx 10^6$ K) and are generated by SNe explosions in the galactic discs. These explosions heat and push the gas towards the edge of the cavities increasing, there, the cold gas surface density. Dense cold clumps are the environment in which new star formation is triggered. The newly formed stars can again inject momentum and energy in the ISM through feedback processes, disrupting cold gas clouds, eventually forming new cavities. These self-regulating mechanisms, implemented in *SMUGGLE*, can maintain the SFR stable over several Gyr.

Clustered SN explosions can generate large cavities (that can reach sizes up to 3 kpc, Egorov et al. 2017) in the ISM, also known as superbubbles (e.g. Reyes-Iturbide et al., 2014). These superbubbles may reach the vertical edge of the cold gaseous disc, eventually breaking through and pushing gas from the star-forming disc into the CGM. Stellar feedback processes in *SMUGGLE* are able to eject gas from the galactic disc, as clearly shown in the edge-on projections of Figure 5.2 (bottom panels). The majority of these outflows appears to be confined in the first $1 - 2$ kpc above the disc, but some of the ejected gas can reach distances up to $10 - 15$ kpc. This ejected gas is a manifestation of the so-called galactic fountain (Shapiro & Field, 1976; Fraternali & Binney, 2008), as typically it has a velocity that is insufficient to escape the galactic potential. As a result, such gas is bound to the galaxy and will eventually fall back onto the disc. Fountain flows are present in all nine simulations as their generation is a natural consequence of the formation of new stars and the associated feedback. The distribution and the intensity of these galactic fountains is analyzed in the following sections.

To demonstrate that *SMUGGLE* is able to regulate the SFR in my simulated galaxies, Figure 5.3 shows the evolution of this quantity as a function of time for the entire simulation set. The early evolution of the SFR should be treated with caution. While it is assumed that the corona is initially in equilibrium, cooling processes disrupt this balance, causing pressure loss and rapid accretion onto the disc. After about 0.3 Gyr, the SFR stabilizes due to the self-

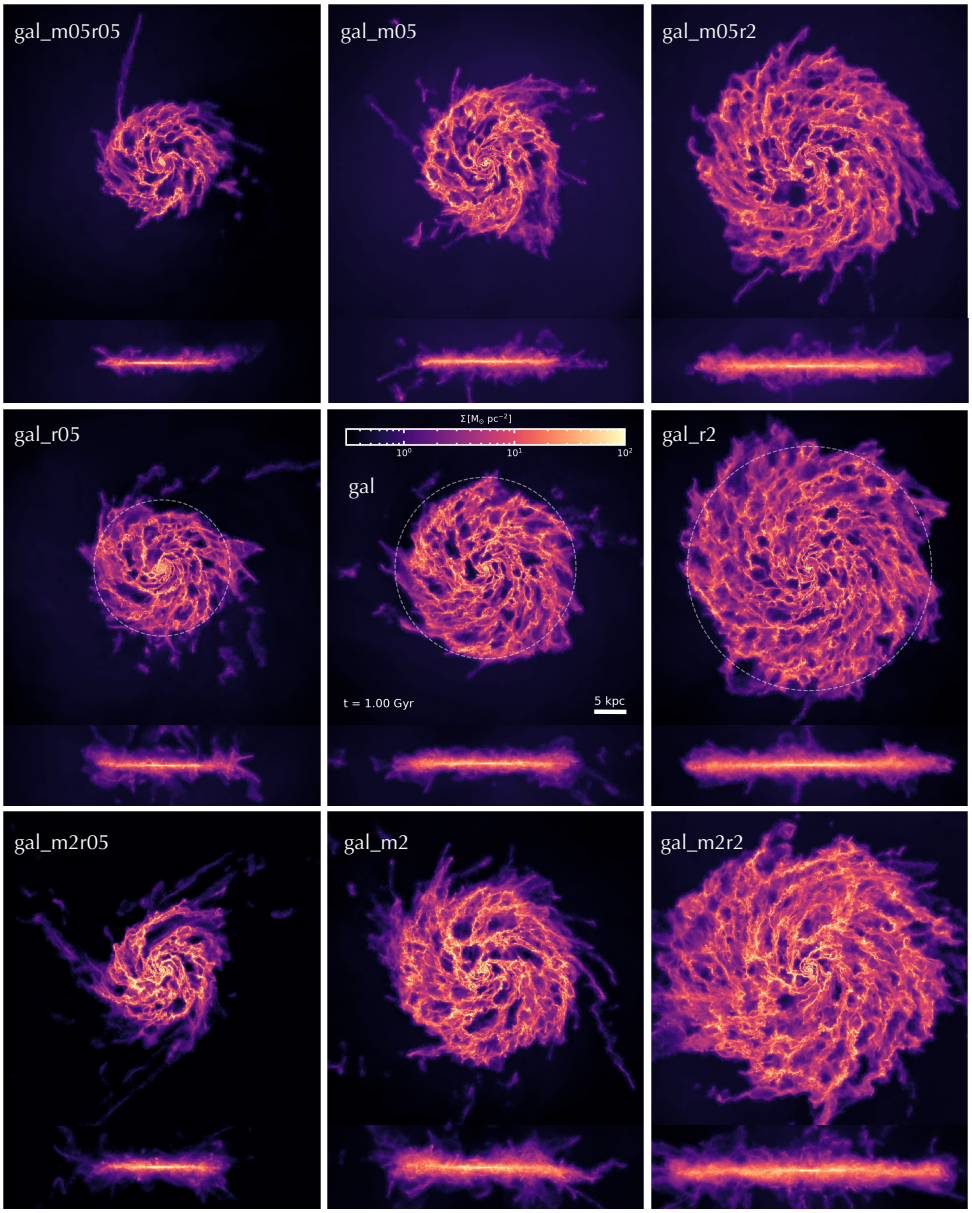

Figure 5.2: Gas column density face-on (top panels of each row) and edge-on (bottom panels of each row) projections computed using the *SMUGGLE* model at $t = 1$ Gyr for all the 9 simulations examined in this Chapter, as labelled in each panel. The simulations differ in the initial value of the scale-length and of the mass of the gaseous disc (see Table 5.2). Each panel is 70 kpc across and in projection depth with a total number of 1024 × 1024 pixels that give a resolution of $\sim$ 70 pc. Brighter colors correspond to higher column densities, as indicated in the colorbar. In the **gal_r05**, **gal** and **gal_r2** projection panels the dashed white circle shows the disc size R_d, defined as the radius at which the gas surface density drops below 1 $M_\odot$ pc^{-2} (not shown in the other projections for clarity).

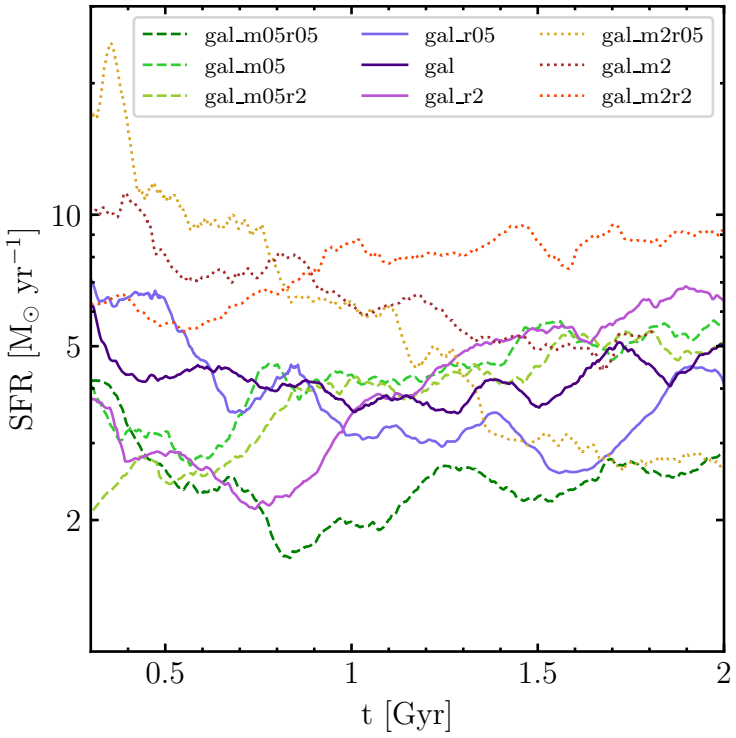

Figure 5.3: Star formation rate as a function of time for the 9 simulations analyzed in this Chapter. The SFR has a wide range of values ($\approx 2 - 10$ M$_\odot$ yr^{-1}) across the different simulations, but it remains approximately constant over time for each simulated system. The average SFR depends on the disc initial properties, with variations in each simulation staying within a factor of ~ 2 from the average value.

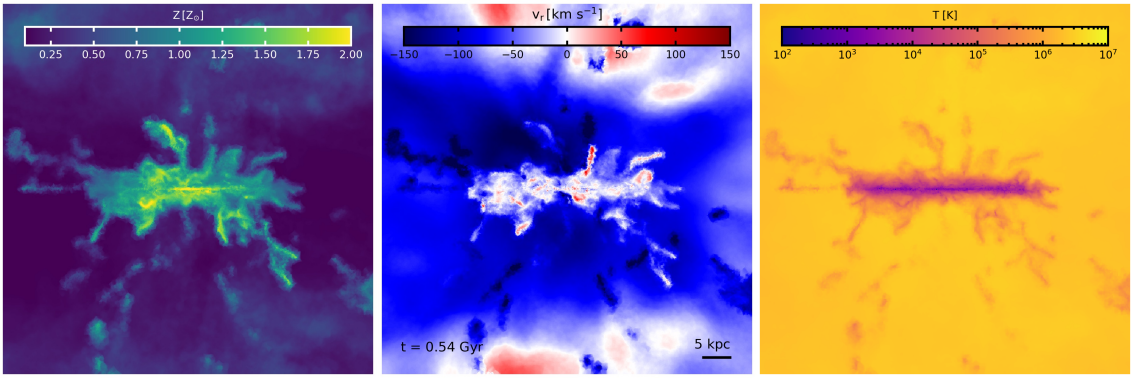

Figure 5.4: Gas metallicity, radial velocity and temperature (from left to right) in edge-on projections of the fiducial simulation at $t = 0.5$ Gyr. Each panel is 70 kpc across and in projection depth with a total number of 1024 × 1024 pixels that give a resolution of ~ 70 pc. These projections show the stark difference between the disc and the CGM properties.

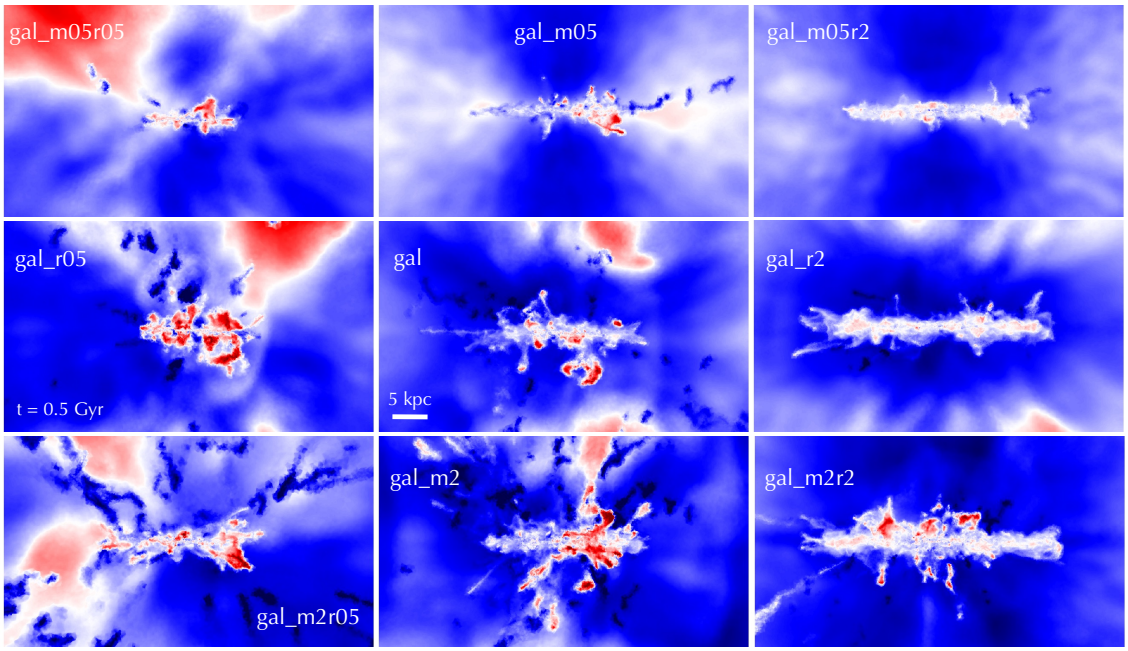

Figure 5.5: Gas radial velocity in edge-on projections of the 9 simulations at $t = 0.5$ Gyr. Each panel is 70 kpc × 40 kpc, with a projection depth of 70 kpc and a resolution of ~ 70 pc. The velocities go from -150 km s^{-1} (inflows, blue) to 150 km s^{-1} (outflows, red) as in central panel of Figure 5.4. These projections clearly show the presence of galactic fountains in the simulations.

regulation between star formation and feedback in the *SMUGGLE* model. The corona also becomes more stable, though it continues to accrete onto the disc through radiative cooling. All the runs display, after this transient period in the first $\sim$ 300 Myr (not shown in the figure), an approximately constant SFR spanning the range $2-10$ $M_\odot\,yr^{-1}$. The average level of SFR depends on the initial properties of the disc and SFR variations for each simulation are confined within a factor of ~ 2 from this average value. The **gal** simulation starts with a higher SFR that quickly stabilizes at around $4-5$ $M_\odot$ yr^{-1}. More specifically, the **gal_r05** simulation starts with a higher SFR because of its higher gas surface density (it has the same gas mass contained in a smaller disc) but ends up with a lower SFR compared to the fiducial **gal** simulation. **gal_r2** has the opposite behaviour, the SFR grows up over time surpassing the **gal_r05** simulation at $t \approx 1$ Gyr. Simulations with a larger disc mass have in general a higher SFR. Looking at the simulations with smaller disc mass: **gal_m05r05** simulation has a SFR lower than the $f_M = 1$ counterpart **gal_r05**, this does not happen for **gal_m05** and **gal_m05r2**. In this case, the SFR is lower in the first 0.8 Gyr and becomes slightly larger for the rest of the simulation.

To better highlight the presence of a galactic fountain cycle in my simulations, Figure 5.4 shows edge-on projections of the metallicity (left panel), radial velocity (middle panel) and temperature (right panel) of the gas for the fiducial run **gal** after 0.5 Gyr of evolution. Each panel has a physical size of 70×70 kpc. The colour mapping encodes metallicities between 0.2 $Z_\odot$ and 2 $Z_\odot$, radial velocities between -150 km s^{-1} and 150 km s^{-1} and temperatures between 10^2 K and 10^7 K (see the colourbar in each panel). As expected, the central region of the disc has a high metallicity ($1-2$ $Z_\odot$), which is consistent with the fact that the disc region is where the majority of the star formation is concentrated and stellar evolution can spread the bulk of metals in the ISM. The gas ejected by the galactic fountain has a metallicity consistent with the star-forming disc (≈ 1 $Z_\odot$), as it is expelled from that region by the action of stellar feedback. The CGM gas has an initial metallicity of $Z = 0.1$ $Z_\odot$, but there is the presence of metal-enriched gas (≈ 0.5 $Z_\odot$) at $\approx$ 30 kpc from the disc. This is the result of the mixing of disc gas, which is brought to these distances by the galactic fountain cycle, with the pristine coronal material. The middle panel shows the spherical radial velocity, red-coloured gas is moving radially away from the center of the galaxy while blue-coloured gas is moving towards it. The galactic fountain cycle is clearly visible: gas that was pushed outside

the galaxy (positive radial velocity) is then later re-accreted onto the disc (negative radial velocity). Looking at the metallicity projection it can be noticed that the gas moving towards the galaxy generally features a lower metallicity than the outflowing gas, which is consistent with the mixing scenario described above. Another important difference between the gas from the disc and the CGM is its temperature (right panel). The ISM is for the majority cold ($T \lesssim 10^4$ K) and this also the typical temperature of outflowing gas. As for the metallicity, when the fountain gas travels in the CGM it mixes and accretes material from it, forming an intermediate gas phase that subsequently cools and accretes onto the star-forming disc. As suggested in previous studies (see, e.g., Marinacci et al., 2010; Hobbs & Feldmann, 2020; Barbani et al., 2023), this fountain-driven gas accretion may represent an important source of fresh gas for star-forming galaxies, directly impacting their evolution. The presence of the galactic fountain cycle in each simulation is highlighted in Figure 5.5 which shows gas spherical radial velocity projections for the 9 simulations (as indicated in each panel). The color mapping is the same as in center panel in Figure 5.4. Each successive row (from top to bottom) increases the mass of the gaseous disc by a factor of 2, while each column from left to right represents a doubling of the disc scale length. The Figure emphasizes that simulations with a higher SFR (f_M = 2 simulations) have stronger ejections of gas from the disc, this results in clouds of cold gas that are pushed at larger distances from the disc and falling back into it after a larger time.

5.4 Vertical galactic fountain distribution

Galactic fountains play a fundamental role in galaxy evolution, by interacting with the CGM and bringing new gas to the disc (e.g. Marasco et al., 2022; Li et al., 2023). In this Section I present an analysis of the distribution of gaseous outflows and inflows over the galactic disc. Outflow and inflow rates are computed inside a slab centered at a height z_0 and with a thickness Δz above and below the plane of the disc (see also Barbani et al. 2023 and Chapter 4). If a gas cell inside the slab meets all the required conditions (see below), it is counted as inflowing/outflowing gas and its contribution to the total mass rate is summed up as

$$\dot{M}_{\rm in/out} = \sum_i \frac{m_i v_{z,i}}{\Delta z}, \tag{5.4.1}$$

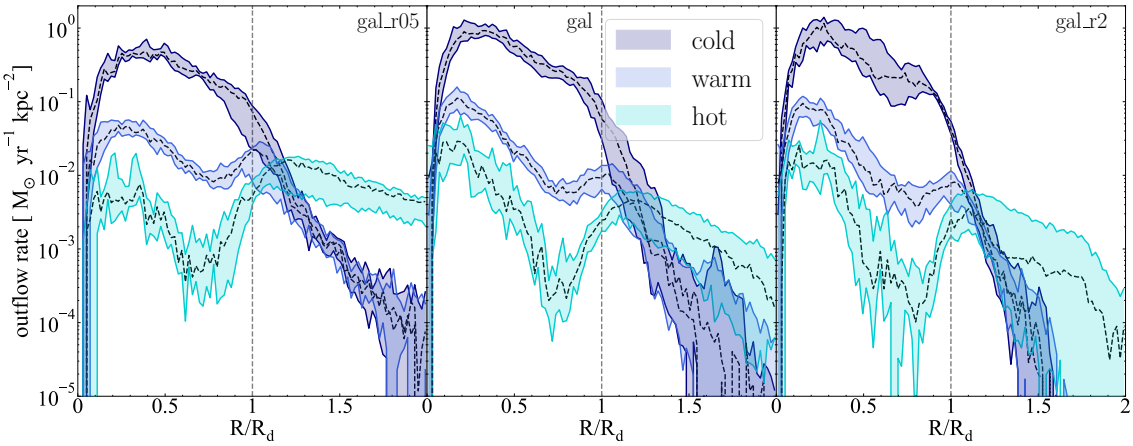

Figure 5.6: Outflow rate per unit area as a function of the cylindrical radius R (in units of the disc size R_d) for **gal_r05** (left panel), **gal** (center panel) and **gal_r2** (right panel) simulations. Each shaded area indicates the outflow rate profiles between the 25^{th} and the 75^{th} percentile, whereas the black dashed lines represent the median values. The rates are divided in cold ($T < 10^4$ K, dark blue shaded area), warm ($10^4 < T < 5 \times 10^5$ K, blue shaded area) and hot ($T > 5 \times 10^5$ K, light blue shaded area) gas and computed at a height $|z_0| = 0.5$ kpc inside a slab over the plane of the disc with a thickness $\Delta z = 0.1$ kpc and with $|v_z| > 30$ km s^{-1}.

where m_i is the mass of the gas cell and $v_{z,i}$ is the $z-$component of its velocity. I set a velocity threshold $v_{\text{thres}} = 30$ km s^{-1}, this value is chosen as an optimal compromise, ensuring that turbulent motions (tens of km s^{-1}) are not misclassified as inflows/outflows, while still accounting for most outflows with velocities in the range 50 km s^{-1}<v_z<100 km s^{-1}. If $v_{z,i} z_i > 0$ and $|v_{z,i}| > v_{\text{thres}}$, where z_i is the vertical distance from the disc plane of the gas cell, the gas in the cell is considered as a part of an outflow, whereas if $v_{z,i} z_i < 0$ and $|v_{z,i}| > v_{\text{thres}}$ it is counted as inflowing gas.

Figure 5.6 shows the outflow rate per unit area as a function of cylindrical radius normalized by R_d for the **gal_r05** (left panel), **gal** (middle panel) and **gal_r2** (right panel) simulations. The disc size R_d is defined as the radius at which the gas surface density drops below 1 M$_\odot$ pc^{-2} (see Figure 5.2), resulting in R_d values of ≈ 20 kpc for the fiducial galaxy, ≈ 15 kpc for **gal_r05** and ≈ 27 kpc for **gal**. These disc sizes are used to normalize the x-axis, which extends in the range $0 \leq R/R_d \leq 2$. The gas has been divided in cold ($T < 10^4$ K, dark blue shaded area), warm ($10^4 < T < 5 \times 10^5$ K, blue shaded area) and hot ($T > 5 \times 10^5$ K, light blue shaded area). The outflow rate profiles have been computed at each time in the simulation

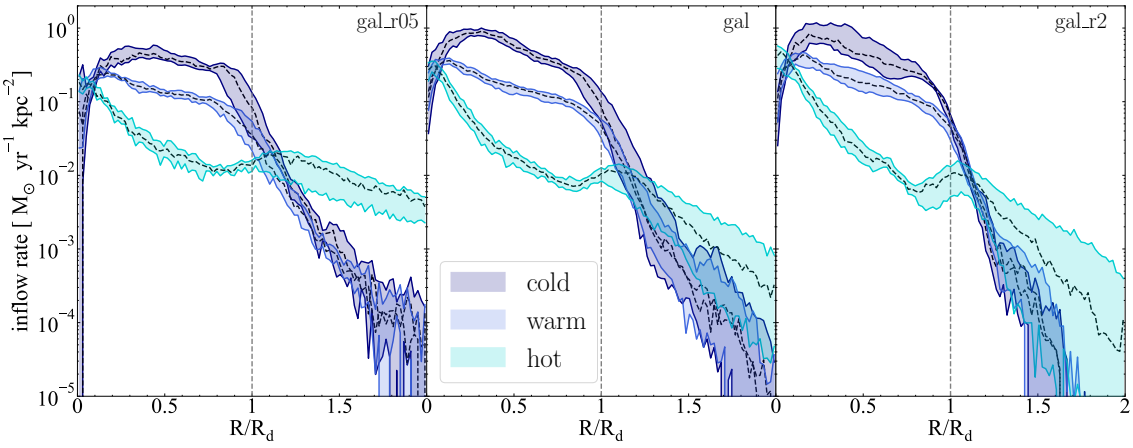

Figure 5.7: The same as Figure 5.6, but for inflow rates.

with a temporal resolution $\Delta t = 10$ Myr (temporal difference between each snapshot of the simulation), the radial bins width is $\Delta R = 0.02$ in R/R_d units. For each panel I evaluated the 25$^{\text{th}}$ and 75$^{\text{th}}$ percentiles of the resulting radial profiles and displayed their extent in the plot as the shaded coloured area, whereas the dashed black line indicates the median value. It is worth to notice that the outflows are dominated by the cold phase, which is on average at least one order of magnitude larger than the warm phase and two orders of magnitude larger than the hot one. Thus, the cold phase dominates the mass budget in the gas swept by SNe. The outflow rates are decreasing with the radius, following the distribution of gas and stars. At $R \lesssim 0.4R_d$, where more star formation is concentrated, the outflows are stronger. As expected, the distribution of the outflows is connected to the extension of the disc. All the simulations show a similar shape distribution with a break point at the edge of the disc R_d, beyond this radius the outflow rates drop significantly. In the fiducial simulation, the outflow rate is higher than 10^{-1} M$_\odot$ yr^{-1} kpc^{-2} until $R_d \approx 20$ kpc at all times. In **gal_r05**, that has a halved disc scale length, the outflows arrive to ≈ 15 kpc and in **gal_r2** they extend up to ≈ 30 kpc. At $t = 1$ Gyr these three runs have a very similar SFR ($4 - 5$ M$_\odot$ yr^{-1}, see Figure 5.3) and the intensity of the outflow rate in the first kpc is similar, but in **gal_r2** the outflow are more extended. Therefore, the global outflow rate is higher in this system, with direct consequences on its evolution. For instance, more outflows can interact with the hot gas in the CGM, consequently increasing also the accretion rate. During the 2 Gyr evolution there is not a large change in the outflow rate profile and therefore the shaded areas are very

close to the median value.

Figure 5.7 shows inflow rate per unit area as a function of cylindrical radius normalized by R_d for the same simulations and in the same temperature range of Figure 5.6. As this quantity is being computed at a relatively close distance to the disc mid-plane ($|z| = 0.5$ kpc), the accreted gas has time to cool down before entering the gaseous disc, therefore the inflowing gas is mostly cold. Similarly to the outflow rates, the extension of the inflow rate distribution is connected to the size of the disc, more extended discs have more extended inflows, showing a break in the distribution at $\approx R_d$, after which the inflow rates decline rapidly. This happens because a large fraction of the inflows is gas that was beforehand ejected from the disc and subsequently falls back into it. The analogy between outflow and inflow rate profiles is again suggesting an essential role of the galactic fountains in setting the spatial distribution of the gas onto the disc. In the **gal** simulation the inflow rate arrives to a lower radius with respect to **gal_r2**, indicating that the majority of the accreted gas comes from the recycling of the ejected gas in a galactic fountain cycle. The other 6 simulations (not shown) behave in a similar way.

My goal is to examine the net vertical mass inflow of gas onto the disc, considering that a significant portion of this inflowing gas was previously ejected from the disc as part of the galactic fountain process. Figure 5.8 shows the average net inflow rate, computed using Eq. (5.4.1) as $\dot{M}_{\rm net} = \dot{M}_{\rm in} - \dot{M}_{\rm out}$, divided in cold (red line), warm (orange line) and hot (yellow line) gas for the 9 simulations analyzed in this work (as indicated in each panel). The rates are computed at a height of $|z_0| = 0.5$ kpc from the disc plane with a $\Delta z = 0.1$ kpc width. Together with the net inflow rate I show the SFR radial profile (dashed grey line). As in the previous figure, the disc is divided into radial bins of width 0.02 in R/R_d units.

Figure 5.8 emphasizes the connection between accretion from the CGM and galactic disc structure. In all the simulations, the net inflow rates exhibit a bell-shaped distribution. These accretion rates extend up to $\approx 1.2\, R_d$ in all the simulations, which corresponds to ≈ 24 kpc in the $f_G = 1$ simulations, ≈ 18 kpc in the $f_G = 0.5$ simulations and ≈ 32.5 kpc in the $f_G = 2$ simulations, following the respective discs sizes R_d. It is worth to notice that the peak of the total net inflow rate is not located at the center of the galaxy, but is instead skewed towards larger radii. The peak distance from the center is increasing with disc size and is typically around $0.75\, R_d$. The grey dashed line shows the SFR as a function of radius, which

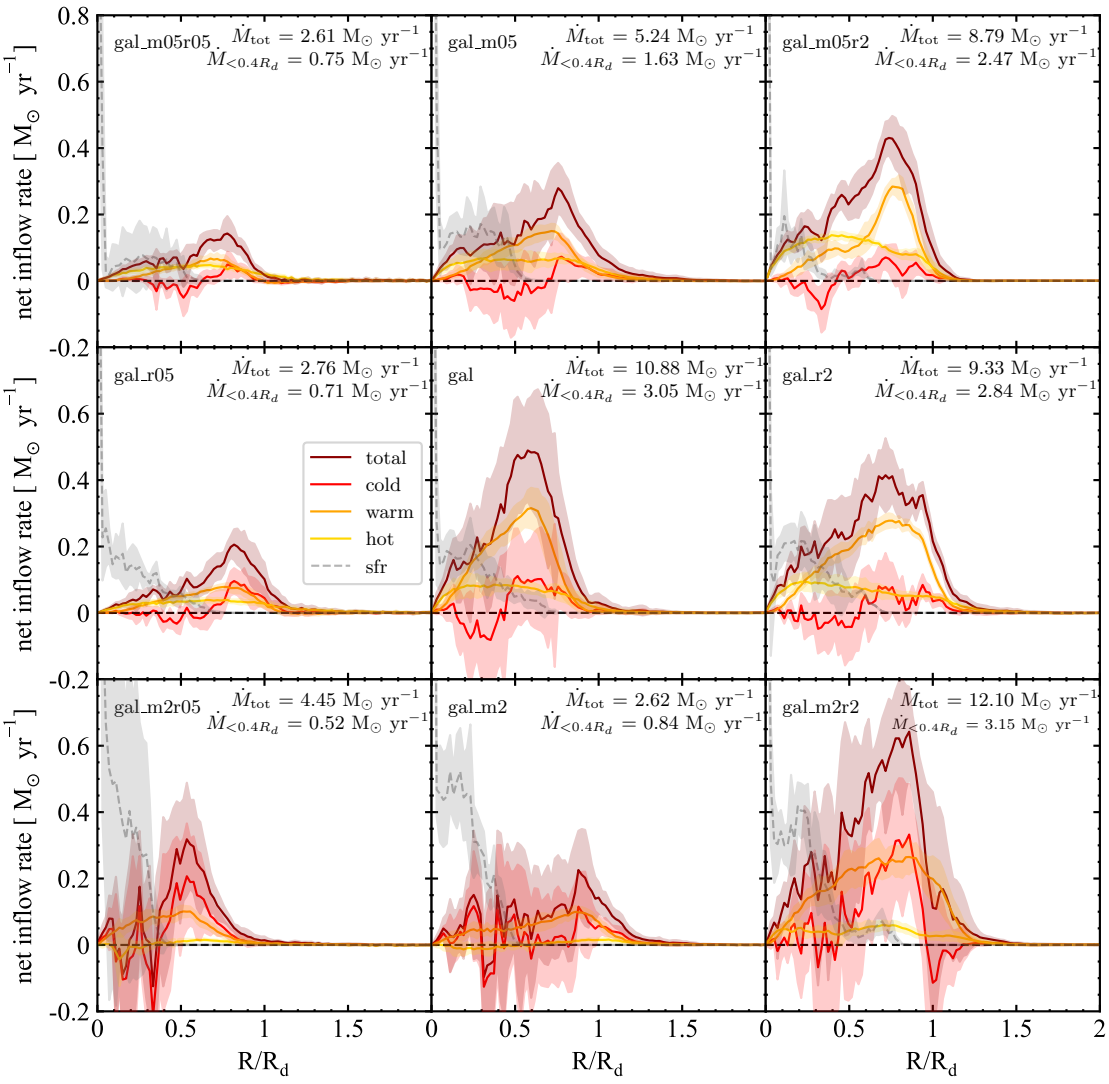

Figure 5.8: Net vertical inflow rate, computed as $\dot{M}_{\rm net} = \dot{M}_{\rm in} - \dot{M}_{\rm out}$, as a function of cylindrical radius R (in units of R_d) for the 9 simulations divided in cold ($T < 10^4$ K, red line), warm ($10^4 < T < 5 \times 10^5$ K, orange line) and hot ($T > 5 \times 10^5$ K, yellow line) gas. The dashed grey line is the SFR profile. The solid lines represent the profile averaged over the entire simulation and the shaded areas are the standard deviations. The rates are evaluated inside a slab over the plane of the disc with a width $\Delta z = 0.1$ kpc at a height $|z_0| = 0.5$ kpc. Each point represents the gas net inflow rate within a circular annulus with a radial width of 0.02 in R/R_d units and considering only gas cells with $|v_z| > v_{th} = 30$ km s^{-1}. In each panel I have indicated the average net vertical rate at $R < 0.4R_d$, this is roughly the region of the disc where 90% of the SFR is concentrated in all the 9 simulations. The net inflows can extend beyond R_d supplying the outer disc with fresh gas for star formation.

has a central peak and also a bell shape similar to the net inflow rate but is more concentrated in the inner region of the disc, where the gas surface density is higher. If the gas were to fall back to roughly the same radial position from which it was ejected, the inflow distribution would closely resemble the SFR distribution. Instead, the majority of the gas is accreted in the outer regions of the disc. This happens because the orbital paths of galactic fountain clouds increase with radius, due to the progressively weaker gravitational attraction moving toward the external regions of the galaxy (e.g. Li et al., 2023). Additionally, the region of the CGM affected by the fountain clouds passage – and where the warm gas phase is generated – expands with their orbital path, facilitating an easier accretion into the disc. The total net accretion rate $\dot{M}_{\rm tot}$ ($R < R_d$) is indicated in each panel. This total accreted gas would be enough to sustain the SFR (Figure 5.3), a fraction of this accretion in the external regions is used to grow the disc inside-out (see Section 5.6). While most of the gas is accreted in the outskirts of the disc, a fraction of it falls in the central region ($R < 0.4\,R_d$), in each panel of Figure 5.8 I indicated the average value of the net rate in this region. 90% of the SFR is located at $R < 0.4\,R_d$, thus gas accreted in these central regions can be directly available for the formation of new stars, whereas gas accreted at $R > 0.4\,R_d$ cannot be immediately used for star formation as the average gas density is not high enough. This average net rate, while not negligible, is still not sufficient to entirely sustain the SFR of the galaxy (see Figures 5.3 and 5.10). Therefore there needs to be an alternative mechanism that feeds the star formation in the center. The accretion budget and the comparison with the SFR are discussed in Section 5.5.

When examining the net inflow rate separated in hot, warm and cold components, several interesting features can be noticed. Previously, I have shown that the outflow rate of warm and hot gas is almost negligible (Figure 5.6), indicating that the net warm/hot inflow primarily originates from the CGM rather than just being gas previously ejected from the disc. In fact, as shown in Barbani et al. (2023), the warm gas phase is generated by the passage of the cold fountain clouds through the hot CGM. In all simulations, the hot gas has an almost flat distribution that slightly decreases with increasing radius, with values ranging from 0 to ~ 0.15 $\mathrm{M_\odot\ yr^{-1}}$. This likely represents gas directly accreted from the hot CGM via a cooling flow, showing no clear correlation with the cold and warm gas distributions. The warm and cold gas, however, are more closely connected, with their net inflow peaks

occurring at similar radii. The net cold inflow rate shows more discontinuous peaks and it is not consistently positive[1]. As shown in Figure 5.6, nearly all of the ejected gas is in the cold phase, leading to regions of the disc where the outflow rate exceeds the inflow rate (resulting in a negative net rate) and vice versa. This does not happen for the net warm inflow rate, which remains consistently positive and generally higher than the net cold inflow rate. The spatial distribution of cold and warm inflows appears interconnected, suggesting that cold outflows may enhance the formation of inflowing warm gas. As discussed extensively in Barbani et al. (2023), mixing between the cold fountain clouds and the hot CGM can reduce the cooling time of the gas mixture, allowing the gas to cool more rapidly and accrete onto the disc, thereby supplying fresh gas to sustain star formation.

The different disc sizes and gaseous masses also result in variations in the net inflow distribution. The simulations with the smaller discs (**gal_r05**, **gal_m05r05**, **gal_m2r05**) show the lowest net inflow rates, this is a combination of both a lower SFR (see average SFR indicated in each panel of Figure 5.10) and a smaller extent of the disc. The hot gas accretion rate increases with disc size, reflecting the slow accretion of the galactic corona; a larger disc is more capable of capturing and accreting more hot gas. The cold gas rate, that derives from stellar feedback, is also lower in smaller discs due to their lower SFR, which in turn reduces the generation of warm gas, formed from the mixing and condensation of CGM into the galactic fountain cloud. Consequently, the rates increase for larger discs, which also present on average a higher SFR. Therefore, if the mass of the gaseous disc decreases, gas accretion diminishes for the same reasons.

5.5 Radial gas motions

Figure 5.8 illustrates that the majority of the gas is accreted at a significant distance from the galactic center ($\approx 0.75 R_d$), near the edge of the gaseous disc. Star forming galaxies need to acquire gas from the external environment to keep forming stars with an almost constant SFR (e.g. Cignoni et al., 2006; Isern, 2019; Mor et al., 2019), as the gas within the disc is not sufficient. The majority of stars form in the central regions of the disc, where gas density

[1]In this Figure, I use the convention that a positive net inflow rate represents gas accretion onto the disc, whereas a negative rate is interpreted as gas ejection from the disc.

is the highest. Therefore, the accreted gas must travel from the disc outskirts to the center in order to be accessible for the formation of new stars (Schmidt et al., 2016; Di Teodoro & Peek, 2021).

A crucial aspect of understanding radial gas motion within the disc lies in the angular momentum distribution of both the disc and the CGM. Figure 5.9 presents the specific angular momentum profiles for different galaxy models, computed as $j = J/M$, where J is the total angular momentum and M is the total mass of the respective component. The angular momentum is evaluated near the disc ($|z| < 1$ kpc), with CGM gas selected by metallicity $Z < 1\,Z_\odot$ and disc gas by $Z > 1\,Z_\odot$. The figure highlights a consistent trend: the specific angular momentum of the disc is systematically higher than that of the CGM across all models, particularly in the inner regions. At small radii ($R/R_d \lesssim 1$), the gaseous disc exhibits significantly greater angular momentum than the surrounding CGM, reinforcing the expectation that the disc is rotationally supported, while the CGM consists of material undergoing accretion, turbulence, or interactions with outflows. The clear separation between the two components suggests that the disc angular momentum is primarily determined by ordered rotation, whereas the CGM lower angular momentum reflects a mix of inflows and weaker rotational coherence. At larger radii ($R/R_d \gtrsim 1$), the angular momentum difference between the disc and CGM varies depending on the model. In some cases, the profiles remain distinct, while in others, the CGM angular momentum approaches that of the disc. This convergence suggests angular momentum redistribution, likely due to mixing at the disc-CGM interface or the gradual acquisition of rotational support by CGM material as it settles into the disc. The impact of galaxy properties is evident in the figure. Increasing the total gas mass of the disc results in an overall increase in specific angular momentum at all radii. Similarly, variations in the disc scale length influence the angular momentum distribution, with larger scale lengths generally leading to more extended profiles. However, despite these differences, the higher angular momentum of the disc relative to the CGM in the inner regions remains a robust feature across all models.

To investigate the radial migration of gas I have computed the radial mass rate in each radial bin as $\dot{M}_{R,\,\mathrm{in/out}} = \sum_i v_{R,i} m_i / \Delta R$, where $v_{R,i}$ is the cylindrical radial velocity of the i-th gas particle and ΔR is the radial bin size. The particles are selected within a slab centered on the disc plane ($z_0 = 0$ kpc) with a thickness of $\Delta z = 0.5$ kpc to ensure that only

disc particles are included. The radial outflow (inflow) rate is determined by considering particles with $v_R > 0$ ($v_R < 0$). The net mass rate is computed as $\dot{M}_{R,\rm net} = \dot{M}_{R,\rm in} - \dot{M}_{R,\rm out}$. The radial velocity is computed averaging the cylindrical radial component of the velocity weighted by the mass of each gaseous cell. For both quantities, the disc is divided in annuli with a spatial extent $\Delta R = 0.02$ in R/R_d units and the profiles are computed in the radial range $0 \leq R/R_d \leq 2$.

Figure 5.10 shows the net radial mass rate of the gas for the 9 simulations, as indicated in each panel. The grey lines represent the net inflow rate profile at individual times, while the black line shows the average profile over a 2 Gyr time span, with the shaded area indicating the standard deviation. The average value of the gas mass rate is positive throughout the entire disc, indicating a significant radial mass flow towards the inner regions. When the accreted material has a specific angular momentum that is different than the one in the disc, radial flows will inevitably arise owing to angular momentum conservation (Mayor & Vigroux, 1981). Since the gas accreted from the CGM has a rotational velocity lower than that of the disc, it will naturally tend to migrate towards the inner regions of the disc, forming a radial flow that feeds the star formation. Generally, the gas net mass rate is near zero in the disc outskirts and it moves towards more positive values (indicating inflows) in the inner regions of the disc across all simulations, eventually approaching zero again at the center. This mass inflow becomes less prominent in the inner regions for two main reasons: the higher gas density at the center and the fact that a portion of the gas is consumed to form stars in these central regions. A consistent pattern emerges in all the simulations, a peak in the mass rate that is generally found roughly at the edge of the disc ($R \approx R_d$), except for simulations **gal_m2r05** and **gal_m05r05**. As the gas flows inwards the mass rate declines due to the increasing gas density and the presence of complex filamentary structures in the ISM.

When comparing simulations with the same gas disc scales, values of $\dot{M}_{R,\rm net}$ within a factor of 2 between each others are observed, except for the $f_G = 1$ simulations where the differences in the average mass rate value are almost negligible. The primary difference arises when the size of the gaseous disc is changed: the gas mass rate increases with larger disc sizes. A larger disc extends into regions where the CGM has lower angular momentum, facilitating easier inward motions towards the center of the disc. Overall, while the simulations show a non-negligible net inflow rate, this rate is generally lower than the average SFR. For instance,

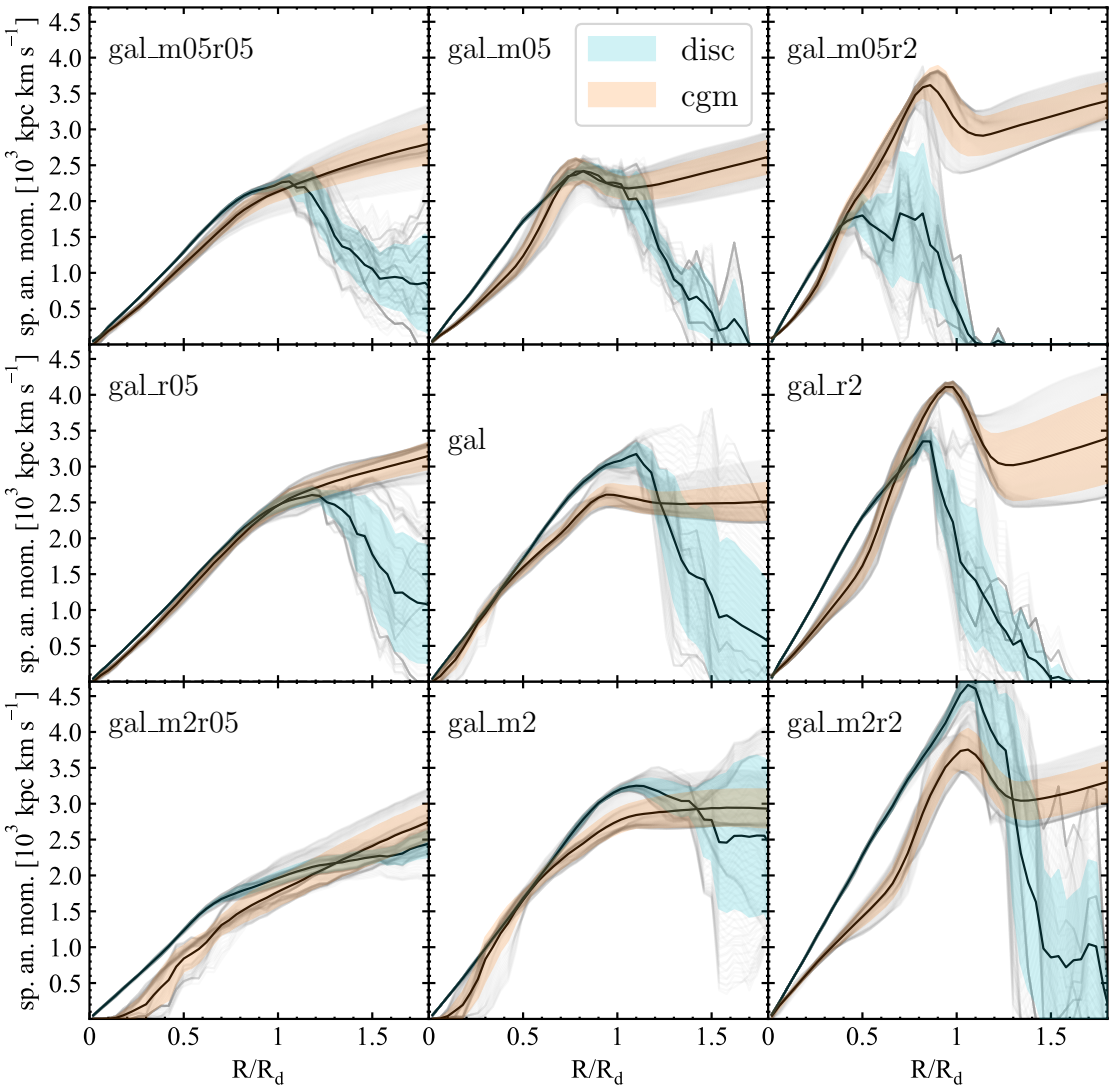

Figure 5.9: Specific angular momentum, computed as $j = J/M$, for the gaseous disc and the CGM computed as a function of cylindrical radius R (in units of R_d) for the 9 simulations. The angular momentum is measured near the disc ($|z| < 1$ kpc), with CGM gas selected by $Z < 1\,Z_\odot$ and disc gas by $Z > 1\,Z_\odot$. Each panel represents a different combination of disc mass and scale length, showing how these parameters influence the angular momentum distribution. Across all models, the disc maintains a systematically higher specific angular momentum than the CGM in the inner regions, while at $R/R_d \gtrsim 1$, the difference between the two components varies, indicating potential angular momentum redistribution or mixing at the disc-CGM interface.

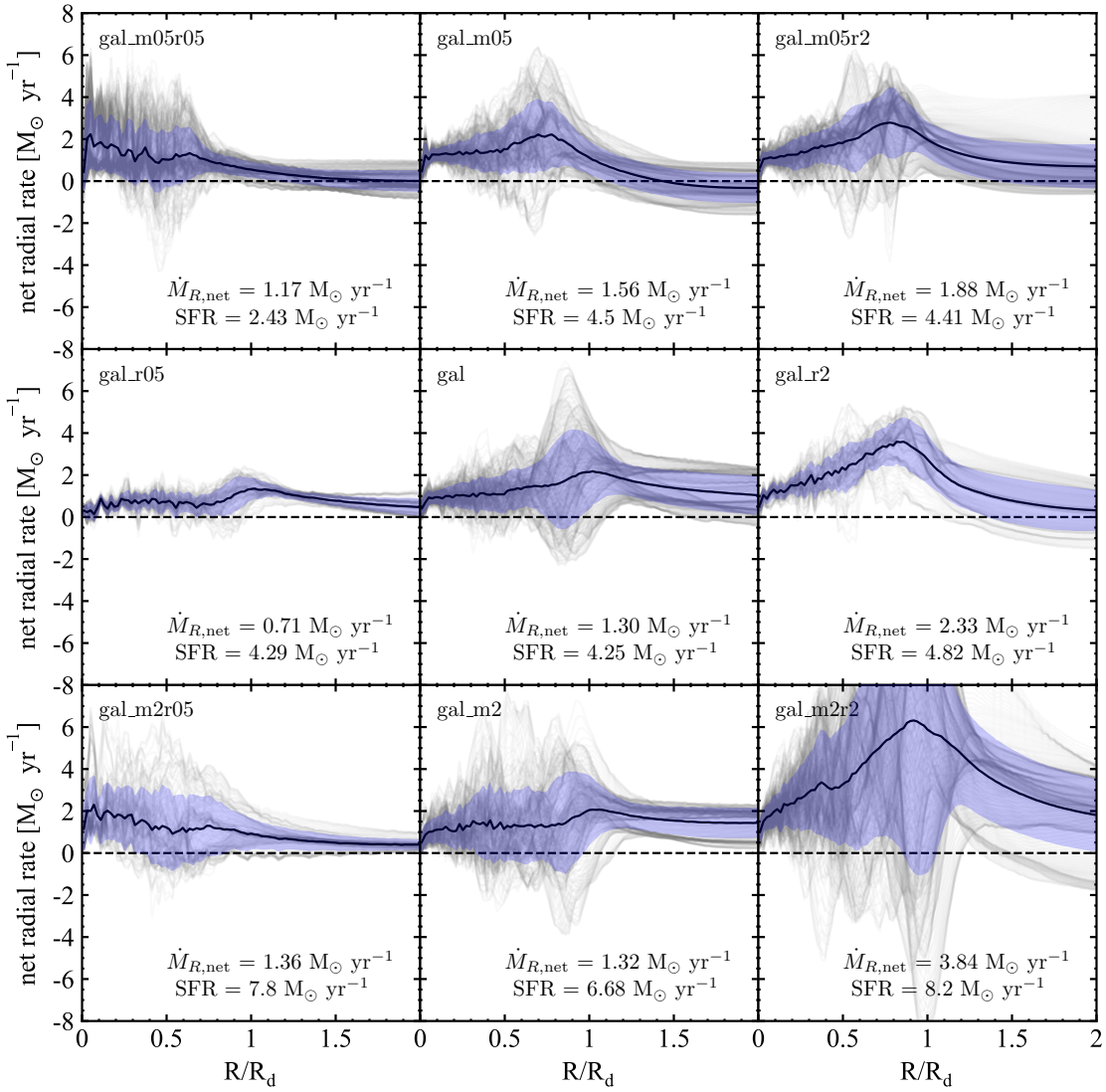

Figure 5.10: Gas net radial mass rate for the simulations analysed in this Chapter. In each panel, the grey lines represent the mass rate profile at a given time averaged in a time span of 100 Myr. The black line is the average mass rate and the blue shaded area represents the standard deviation. On top of each panel the net radial mass rate averaged within the radial range $0 \leq R/R_d \leq 1$ and the average SFR, computed in the temporal range $0.3 < t < 2$ Gyr, are indicated.

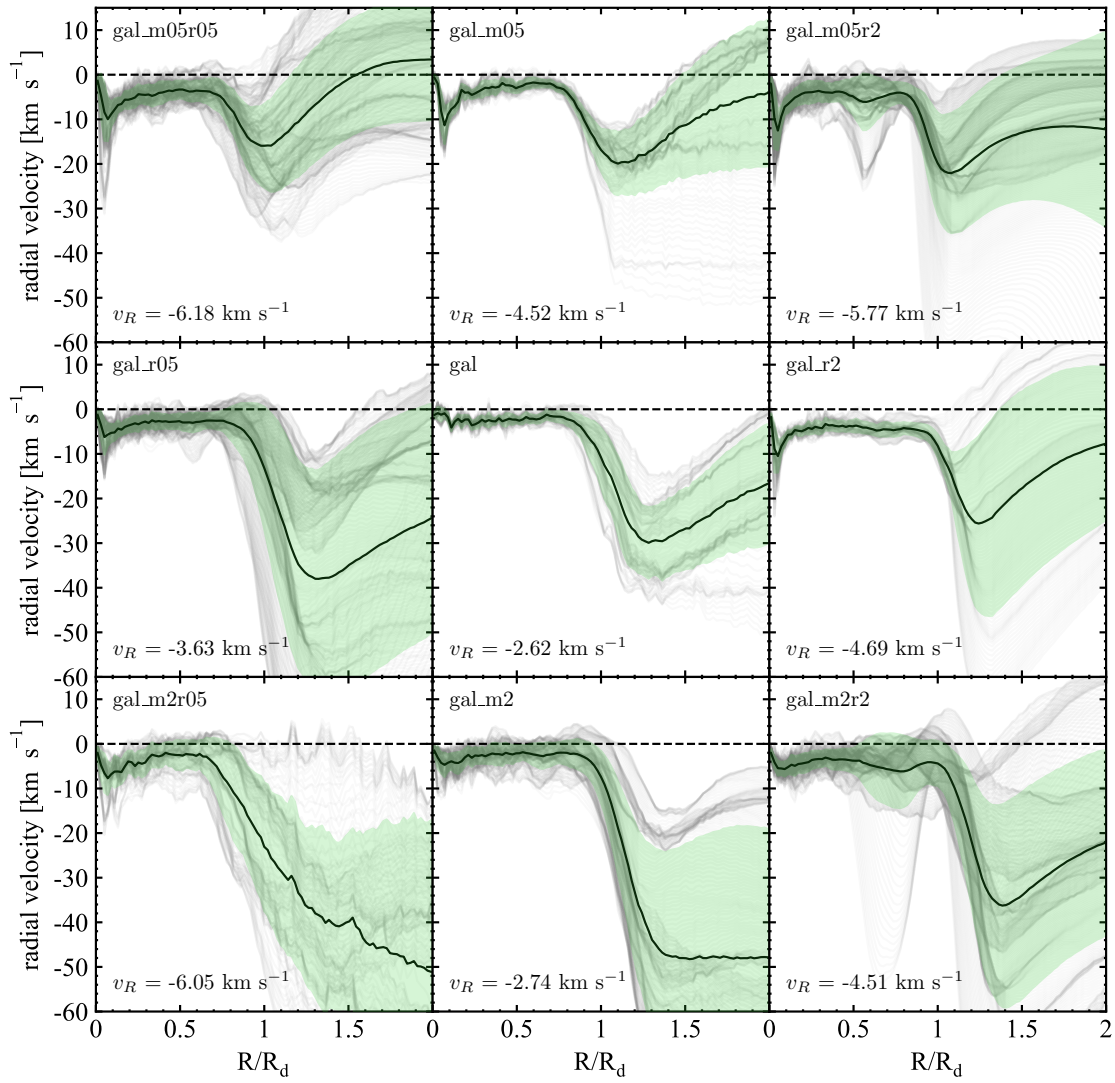

Figure 5.11: Gas cylindrical radial velocity for the simulations analysed in this Chapter. In each panel, the grey lines represent the (mass weighted) radial velocity profile at a given time averaged in a time span of 100 Myr. The black line is the average cylindrical radial velocity and the green shaded area represents the standard deviation. On the bottom left corner the radial velocity averaged within the radial range $0 \leq R/R_d \leq 1$ is indicated.

the net radial inflow rate is 1.39 $M_\odot$ yr^{-1} for the fiducial run and 0.77 $M_\odot$ yr^{-1} and 1.65 $M_\odot$ yr^{-1} for **gal_r05** and **gal_r2** respectively, compared to the average SFR of 4.5 $M_\odot$ yr^{-1}, 4 $M_\odot$ yr^{-1} and 4.5 $M_\odot$ yr^{-1} for these cases. Thus, radial mass motion towards the center alone may not fully sustain the SFR over time. However, it is important to note that not all gas is accreted at the edge of the disc; a significant fraction, approximately 25% of the total accreted gas, is directly deposited in the inner regions ($R < 0.4R_d$, see Figure 5.12), where 90% of star formation takes place. Combined with radially transported gas, this could be sufficient to sustain the global SFR of the galaxy. Therefore, for the SFR to be fueled by these two phenomena in conjunction the galaxy would need to have $\dot{M}_{\rm SFR} = \dot{M}_{z,\rm net}(R < 0.4R_d) + \dot{M}_{R,\rm net} \approx$ SFR. In fact, this is true for most of the 9 simulations analysed in this work. More specifically, in **gal_m05r05** I find $\dot{M}_{\rm SFR} \approx 1.92$ $M_\odot$ yr^{-1}, which has to be compared with the average SFR ≈ 2.43 $M_\odot$ yr^{-1}. Even though strictly speaking the rate of replenishment of gas is below the SFR, the two values are comparable. Moreover, it should be noted that $\dot{M}_{\rm SFR}$ and SFR are averaged over a 0.3-2 Gyr time span, meaning that my analysis is smoothing what occurs over the evolution of the galaxy. Therefore, these values should be interpreted with some caution, but nonetheless they provide insight into whether the formation of new stars can be sustained by gas accretion from the CGM. Other systems show a similar behaviour. In **gal_m05** I find $\dot{\rm M}_{\rm SFR} \approx 3.19$ $M_\odot$ yr^{-1} to be compared with SFR ≈ 4.5 $M_\odot$ yr^{-1} and I obtain $\dot{\rm M}_{\rm SFR} \approx 4.35$ $M_\odot$ yr^{-1} (SFR ≈ 4.4 $M_\odot$ yr^{-1}) in **gal_m05r2**. Looking at the $f_M = 1$ simulations: in **gal_r05** I find $\dot{\rm M}_{\rm SFR} \approx 1.42$ $M_\odot$ yr^{-1} (SFR ≈ 4.29 $M_\odot$ yr^{-1}) which accounts for less than half of the average SFR, in **gal** I find $\dot{\rm M}_{\rm SFR} \approx 4.35$ $M_\odot$ yr^{-1} (SFR ≈ 4.25 $M_\odot$ yr^{-1}) and in **gal_r2** I obtain $\dot{\rm M}_{\rm SFR} \approx 5.2$ $M_\odot$ yr^{-1} (SFR ≈ 4.82 $M_\odot$ yr^{-1}). The largest discrepancies are found in the $f_M = 2$ simulations: in **gal_m2r05** I find $\dot{\rm M}_{\rm SFR} \approx 1.9$ $M_\odot$ yr^{-1} (SFR ≈ 7.8 $M_\odot$ yr^{-1}) and in **gal_m2** I find $\dot{\rm M}_{\rm SFR} \approx 2.16$ $M_\odot$ yr^{-1} (SFR ≈ 6.68 $M_\odot$ yr^{-1}), which differ widely from the average SFR. In **gal_m2r2** I have $\dot{\rm M}_{\rm SFR} \approx 7$ $M_\odot$ yr^{-1} (SFR ≈ 8.2 $M_\odot$ yr^{-1}). Overall, the majority of the simulations have $\dot{M}_{\rm SFR} \approx$ SFR except **gal_m2r05** and **gal_m2**, in these cases the SFR is partially sustained by the larger amount of gas that is present in the disc at the beginning of the simulations.

Figure 5.11 shows the average radial velocity, with values ranging between -4 and -6 km s^{-1}. All the simulations exhibit a similar radial velocity profile: the velocity remains almost constant within the gaseous disc ($R < R_d$), rapidly decreases outside the disc and then start

to slightly increase again (except in **gal_m2r05** and **gal_m2**). This profile shape appears to be independent of the disc structural characteristics. However, the magnitude of the velocity slightly changes between discs of different sizes. Specifically, the radial velocity increases with disc size, similarly to the mass rate. The average velocity inside the disc increases between $f_M = 1$ and $f_M = 0.5$ simulations, when the mass of the gaseous disc is smaller, probably because the lower average ISM density allows gas to flow more easily toward the inner regions. The velocity is larger in the outskirts, outside the galactic disc, where gas is accreted radially on the edge of the galaxy, allowing the disc to grow in size over time (see Figure 5.13). Moving inward, the radial velocity decreases and approaches zero at the center of the disc.

Figure 5.12 presents the radial net rate of the gas as a function of time for the three simulations with the standard gaseous disc mass (**gal_r05**, **gal** and **gal_r2**), the other 6 simulations are not shown as they all have a very similar trend. For each simulation, I computed the total radial net rate by averaging it over the whole galactic disc (i.e. at $R < R_d$ and $|z| < 0.5$ kpc) at each time (with a temporal resolution between each value of ≈ 10 Myr). The trend is consistent across all simulations, alternating between periods of negligible or negative net rate and periods of positive net rate. This fluctuation is likely connected with the stellar feedback cycle; when SNe explode the net rate is dominated by the outflowing gas. As negative stellar feedback reduces star formation, thereby decreasing the injection of energy from new SNe, fresh gas can flow towards the center once again, fueling star formation and repeating the cycle. Overall, the gas predominantly flows towards the center (positive net rate), suggesting that the radial gas flow phenomenon is independent of the gaseous disc size, given that the rotational velocity of the coronal gas has the same values at the beginning of all simulations.

To sum up, the simulations reveal a general inflowing trend that, while insufficient to sustain the star formation in the center alone, is nonetheless crucial for feeding the inner regions of the galaxy, working in conjunction with vertical gas accretion in the central regions ($R < 0.4R_d$).

5.6 Inside-out evolution

The vertical accretion in the outer regions of the disc, coupled with the subsequent radial motions, drives the gas from the periphery towards the disc center. Inevitably, this accretion

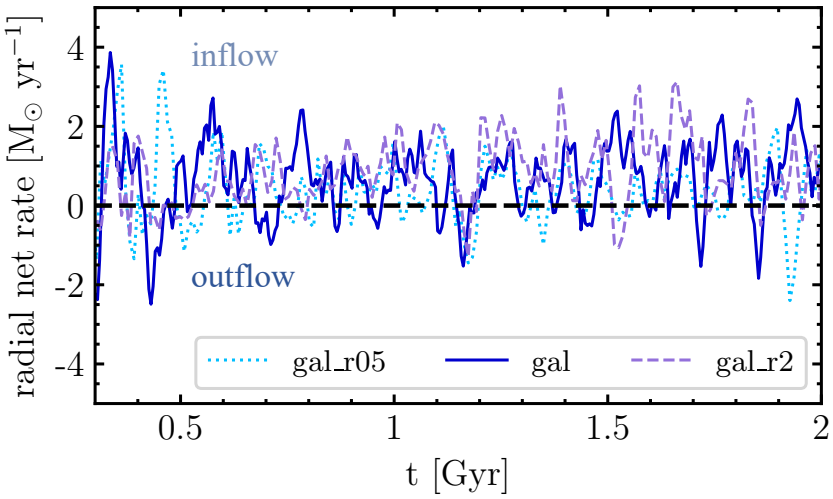

Figure 5.12: Radial gas net rate as a function of time for the **gal_r05** (dotted line), **gal** (solid line) and **gal_r2** (dashed line) simulations. At each time the radial net rate averaged within the disc, at $R < R_d$ and $|z| < 0.5$ kpc, is displayed. Overall the radial net rate is mostly positive, indicating a flow of gas towards the center of the disc.

increases the gas density in progressively more outer regions, consequently enhancing star formation activity in these external areas. Over time, this mechanism enables the disc to grow from the inside to the outside, creating what is known as inside-out evolution (e.g. Firmani & Avila-Reese, 2009; Brooks et al., 2011; Pezzulli & Fraternali, 2016; Li et al., 2023). To explore the relationship between gas accretion and disc growth, I analyzed the evolution of different scale lengths over time and their connection to the total outflow/inflow rates. The top panels of Figure 5.13 show the evolution of the scale lengths of stars (orange line), gas (light brown line) and SFR (brown line) for the 9 simulations as a function of time. These scale lengths are determined by computing the radius which encloses 90% of the stars/gas mass and of the SFR, with each value smoothed using a moving average over a 100 Myr interval. From left to right each panel shows the $f_G = 0.5$, $f_G = 1$ and $f_G = 2$ simulations respectively, with solid lines indicating the $f_M = 1$ runs, dashed lines indicating the $f_M = 0.5$ runs and dotted lines indicating the $f_M = 2$ runs. All the simulations show a periodic trend with oscillations that can be linked to the typical time scale of a fountain cycle in Milky Way-like galaxies ($t_{\rm fount} \approx 100$ Myr, e.g. Fraternali, 2014). Over a span of 2 Gyr all three scale lengths

have increased.

I start analysing these trends by focusing on the fiducial run **gal** (solid lines, central panel): the gas scale length has expanded from $\approx$ 12 kpc to $\approx$ 14 kpc, the star scale length from $\approx$ 8 kpc to $\approx$ 9 kpc and the SFR scale length from $\approx$ 6 kpc to $\approx$ 9 kpc. The gas scale length remains consistently larger than the stellar scale length by about a factor of $\approx$ 2. Notably, both the gas and stellar discs exhibit a concurrent growth, expanding steadily over a 2 Gyr period. The stellar scale shows higher peak frequencies, with approximately two peaks for every peak in the gas scale length. Interestingly, the peaks in the SFR do not coincide with those of the gas and star scales; rather, they tend to align with depressions in the gas scale length. The SFR exhibits the greatest amplitude variation, whereas the stellar scale remains more stable, with peaks that nearly disappear in the other simulations. An increase in the SFR spatial extent implies that more stars are being formed in the outer regions of the disc compared to previous times, leading to more outflows ejected from these areas. Consequently, these episodes of gas ejection may reduce the gas distribution scale length, with a fraction of these outflows eventually falling back onto the disc, thus increasing the gas scale and repeating the cycle again. The **gal_m05** (central panel, dashed lines) and **gal_m2** (central panel, dotted lines) simulations, with a gaseous disc mass halved and doubled, respectively, have similar behaviours. The values of the three scales are similar to **gal**, with the **gal_m05** scales slightly lower and the **gal_m2** scales slightly larger than the fiducial run scales. Also in these cases the peaks in the gas scale and in the SFR scale are misaligned. Similar features can be seen in the other simulations. The simulations with $f_G = 0.5$ (left panel) show lower values in all the three scales as expected and they are all increasing over the 2 Gyr of the simulations. In the $f_G = 2$ runs (right panel) the scales are higher than in the $f_G = 1$ runs, **gal_r2** gas scale is passing from $\approx$ 18 kpc to $\approx$ 20 kpc, whereas in **gal_m05r2** the gas scale stays almost constant at 16 kpc. Overall, the increasing trend in these scale lengths in all the simulations over time indicates the growth in the size of the star-forming disc, which is consistent with an inside-out evolution of the disc.

In the bottom panels, I display the total outflow (dark blue line) and inflow (light blue line) rates for the 9 simulations, computed at $z_0 = 0.5$ kpc, $\Delta z = 0.1$ kpc and $R < R_d$. In general, the inflow rate is larger than the outflow rate. In the fiducial run **gal** (central panel, solid line) the net inflow rate is $\dot{M}_{\rm net} = \dot{M}_{\rm in} - \dot{M}_{\rm out} \approx 10$ M$_\odot$ yr^{-1}. This net inflow is

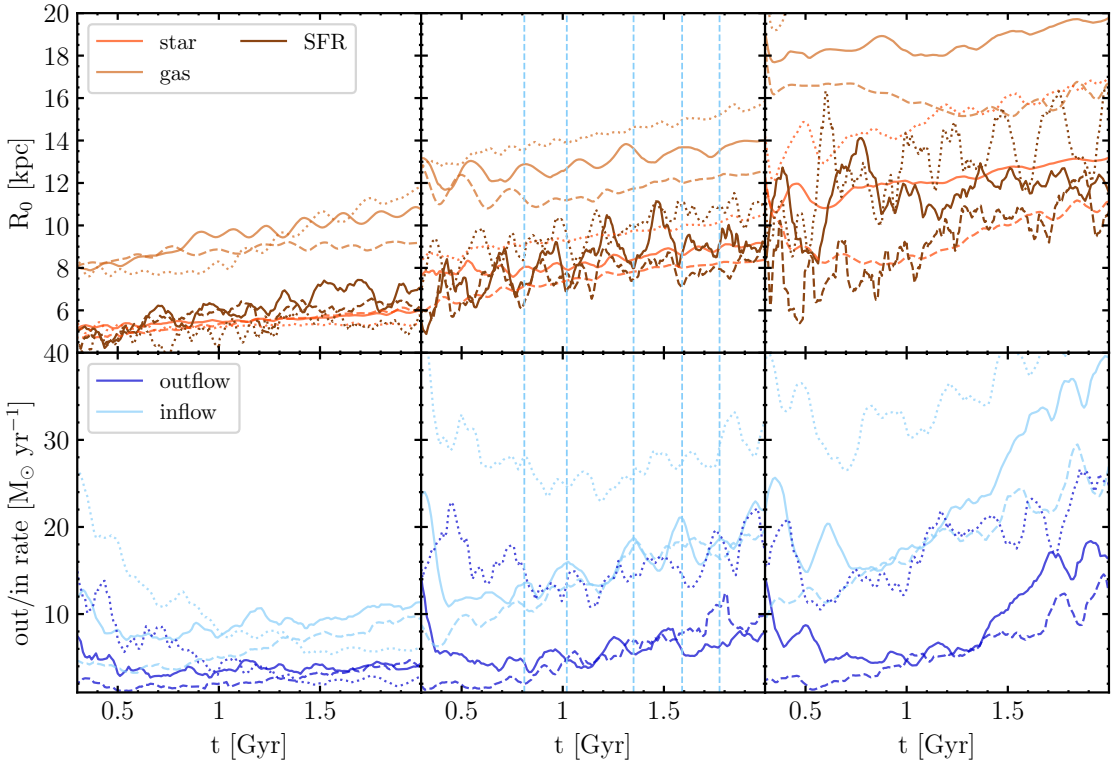

Figure 5.13: *Top panels*: star (orange line), gas (light brown line) and star formation rate (brown line) scale length for the **gal_r05** (solid), **gal_m05r05** (dashed), **gal_m2r05** (dotted, left panel), **gal** (solid), **gal_m05** (dashed), **gal_m2** (dotted, center panel) and **gal_r2** (solid), **gal_m05r2** (dashed), **gal_m2r2** (dotted, right panel) simulations as a function of time. These scale lengths are computed as the radius that encloses 90% of stars/gas mass or SFR. *Bottom panel*: total outflow (blue) and inflow (light blue) rates of the same simulations of the top panels as a function of time. The simulations with $f_M = 0.5$ are indicated with a dashed line and the simulations with $f_M = 2$ with a dotted line. Each of the scale is connected and they have an up-and-down trend linked to the gas outflow/inflow cycle.

larger than the average SFR observed in the fiducial simulation (see Figure 5.3), confirming that the formation of new stars is largely sustained by gas accretion from the CGM, the same applies to the other simulations. An important aspect to notice is that the outflow and inflow rates exhibit similar trends but with an offset in time, with depressions in the outflows corresponding to peaks in the inflows, and vice versa. This pattern arises due to the galactic fountain cycle: a certain amount of gas is ejected from the disc as a galactic fountain due to clustered type II SN explosions, creating a peak in the outflow rate. After a time interval of approximately $t_{\rm fount}$, the fountain gas falls back onto the disc, leading to a peak in the inflow rate. Periods of higher inflow rates result in an increased and more extended SFR, thereby enlarging the SFR scale length. This occurs because gas accretion is not concentrated in the disc inner regions but is rather shifted with respect to the peak of the SFR (see Figure 5.8). Vice versa, when the outflows are dominant, the SFR scale length diminishes.

In all the simulations I find that the peaks in the inflow rate roughly coincide with the peaks in gas and stellar scale lengths, I highlight these peaks for **gal** with dashed vertical lines in the central panel. In contrast, the peaks in the outflow rate correspond to the SFR scale peaks (see also Zhang et al., 2024a, for a similar effect on dwarf-mass galaxies). This shows the intricate connection between outflows/inflows and SFR, which is mediated by stellar feedback and the consequent gas circulation. As discussed earlier, vertical gas inflows are distributed throughout the disc plane, with the majority of the gas accreting at $\approx 0.75R_d$ (Figure 5.8). This accretion pattern increases gas density in these external regions, leading to an expansion in the size of the gaseous disc and consequently also the stellar disc. The SFR peaks, along with the associated stellar feedback, generate outflows, which are fundamental to the cyclical process of disc growth and evolution.

5.7 Comparison with previous works

Despite the challenges, gas accretion has been studied both in the Milky Way and in external galaxies. Evidence of cold gas accreting in the Milky Way is observed through intermediate velocity clouds (IVCs, $40 < v_{\rm LSR} < 90$ km s^{-1}) and high velocity clouds (HVCs, $v_{\rm LSR} > 90$ km s^{-1}) (e.g. Wakker & van Woerden, 1997; Lehner & Howk, 2010), gas clouds with anomalous kinematic with respect to the rotation of the disc. HVCs usually have higher velocities,

lower metallicities ($0.1 < Z/Z_{\odot} < 1$) and are located farther from the disc (up to 10 kpc) with respect to IVCs, that have higher metallicities ($Z \approx Z_{\odot}$) and are usually close to the disc (within 2 kpc). Historically, these differences have been interpreted as a dichotomy in the origin of these two populations of clouds: the IVCs are produced by the cycle of gas inside galactic fountains and the HVCs are coming from the accretion of gas from the CGM (Peek et al., 2008). However, in recent years this picture has been challenged and it has been proposed that HVCs and IVCs are both manifestation of the galactic fountain phenomenon at different velocities (Marasco et al., 2022; Lehner et al., 2022). The IVCs are outflows of gas ejected at lower velocity, therefore they are located closer to the disc and can maintain a metallicity similar to the ISM. HVCs are pushed farther away from the disc and therefore they can mix and decrease their metallicity. Zhang et al. (2024b) employed the *SMUGGLE* model in simulations of isolated Milky Way-like galaxies, without the inclusion of a CGM, to study OVI absorbers. Their findings suggest that key observational properties of low-velocity ($v_{\rm LSR} \lesssim 100$ km s^{-1}) OVI absorbers, such as column density and scale height, are well reproduced by the inclusion of galactic fountains driven by stellar feedback. However, the absence of the CGM in their simulations may lead to an underestimation of the column density of high-velocity ($v_{\rm LSR} \gtrsim 100$ km s^{-1}) OVI absorbers.

Extrapolating the accretion rate values of observed high- and intermediate-velocity clouds to the whole disc, observations find a maximum accretion rate for HVCs of 0.4 M$_{\odot}$ yr^{-1} (Putman et al., 2012) and of $1.3 - 4.3$ M$_{\odot}$ yr^{-1} for IVCs (Röhser et al., 2016), which would be enough to sustain the SFR in the Milky Way (SFR $\approx 1.5 - 3$ M$_{\odot}$ yr^{-1}, Chomiuk & Povich 2011; Licquia & Newman 2015; Elia et al. 2022). HVCs and IVCs are clearly visible in the gas projections of the simulations investigated in this Chapter (see Figures 5.4 and 5.5). Assuming that 40% of the total inflow rate, which averages between 10-20 M$_{\odot}$ yr^{-1} (see Figure 5.13), is attributed to HVCs and IVCs (Putman et al., 2012; Trapp et al., 2022), I find values consistent within a factor of 2 with observed data. It is important to note that the 9 simulated star-forming galaxies have significantly different SFR (higher than the Milky Way), which will be reflected in the resulting inflow rates.

Li et al. (2023) conducted a study on the extraplanar gas of the spiral galaxy NGC 2403, employing a dynamical galactic fountain model. Their findings suggest that fountain-driven accretion can be responsible for an inside-out evolution, effectively cooling the CGM at large

radii. In the absence of galactic fountains, cooling would occur predominantly at the center of the CGM, where gas density is the highest. However, their model applied to observations demonstrates that most gas is accreted at larger radii, a result that aligns closely with the outcomes of my simulations. They observed outflow/inflow rates per unit area similar to those in this Chapter (see Figure 5.6 and 5.7). In their case, the rates peak at the center. In contrast, my simulations show a central 'hole' due to the height at which the rates are computed. Li et al. (2023) derived the rates at $z = 0$ kpc, a condition that I cannot replicate in my simulations. They derived a coronal gas inflow rate whose shape can be compared to the net vertical inflow rate (Figure 5.8) that derived from my simulations. We both find a bell-shaped distribution, with the peak skewed towards larger radii. As already mentioned, this is likely due to the increased orbital path of the galactic fountains with radius and to the fact that the SFRD profile is declining with radius.

Different works have focused on the analysis of radial mass flows and their relation to galaxy evolution. Observationally, there is not a clear evidence of the existence of radial mass fluxes strong enough to sustain the formation of new stars in the central regions of disc galaxies. Some references find radial inflows that are comparable with the SFR of the host galaxy, whereas in other works such inflows are not present. For instance, Schmidt et al. (2016) studied 10 local spiral galaxies using the HI Nearby Galaxy Survey. They derived average radial gas mass rates of $\approx 1 - 3\ \mathrm{M_\odot\ yr^{-1}}$, which will be sufficient to explain the level of SFR in such galaxies. On the other hand, Di Teodoro & Peek (2021) analyzed a sample of 54 local spiral galaxies and found small inflow rates with velocities of a few km $\mathrm{s^{-1}}$ in only half the galaxies of the sample. They computed an average inflow rate over the entire sample of $(-0.3 \pm 0.9)\ \mathrm{M_\odot\ yr^{-1}}$ at radii larger than the optical disc (inside which most of the star formation occurs). They concluded that the radial inflows are not sufficient to sustain the star formation across the disc and therefore that a different mechanism in addition to secular accretion is necessary. I find that net radial mass rate value, averaged across my 9 simulations, is $\approx 1.72\ \mathrm{M_\odot\ yr^{-1}}$ with a standard deviation of $\approx 0.86\ \mathrm{M_\odot\ yr^{-1}}$, which lies somewhat in between the results of Schmidt et al. (2016) and Di Teodoro & Peek (2021). The net radial mass rates estimated from my numerical experiment can sustain a significant fraction of the SFR observed in simulations. This gas radial motion combined with gas accretion in the central regions of the disc can maintain an active level of star formation in the simulated

systems.

Finally, in recent years, some authors have been using cosmological simulations of Milky Way analogs to investigate vertical and radial gas inflows. For example, Trapp et al. (2022) studied gas accretion using FIRE-2 cosmological zoom-in simulations of 4 Milky Way-like galaxies. They found that gas is accreted preferentially in the outskirts of the galaxy, from where the gas moves towards the center with a mass rate comparable to the galaxy SFR. In their simulations, gas vertical inflows present a bell-shaped distribution and gas particles join the disc at $0.5 - 1R_d$, similarly to my results. Radial mass rate and velocities present trends broadly consistent with my findings, but in my case the radial gas motion is not sufficient to entirely sustain the star formation activity of the galaxy. Moreover, Trapp et al. (2022) show that most accretion occurs co-rotating and parallel to the disc plane, with only a subdominant contribution from HVCs and IVCs, whereas my results indicate that the majority of the gas is accreted vertically onto the disc, while still having significant radial inflows that move the gas towards the disc center.

5.8 Summary

In this Chapter I analyzed the baryon cycle in 9 spiral galaxies with different masses and disc sizes, surrounded by a hot CGM, using state-of-the-art N-body hydrodynamical simulations. In particular, I focused on the vertical and radial gas mass flows and on their connection to the structure of the disc. I analyzed the spatial distribution of outflows (forming the galactic fountain cycle) and inflows linking the vertical accretion and the formation of stars in the center through radial flows in the plane of the disc. In doing so, I employed the moving mesh code Arepo in conjunction with the explicit ISM and stellar feedback model *SMUGGLE*. The main results can be summarized as follows.

(i) I studied inflows and outflows per unit area divided in cold ($T < 10^4$ K), warm ($10^4 < T < 5\times10^5$ K) and hot ($T > 5\times10^5$ K) gas. I found that the cold phase is dominating both gas accretion and ejection followed by the warm and the hot phases. In each simulation I find a similar distribution, with a break point roughly corresponding to the disc size R_d, after which the outflow/inflow rates decline rapidly, showing how the outflow/inflow distribution is linked to the structure of the disc.

(ii) I found that gas is accreted vertically onto the disc in a bell-shaped distribution, with the peak skewed towards larger radii ($\approx 0.75 R_d$) compared to the SFR distribution. This offset is due to the orbital paths of galactic fountains and their interaction with the CGM, which increases the accreted material. The hot gas exhibits a flatter distribution and appears to be independent from the warm and cold gas, likely resulting from CGM accretion via a (subdominant in terms of mass) hot cooling flow. In contrast, the cold and warm gas distributions are closely linked. The cold gas is predominantly generated by the galactic fountain cycle, while the warm gas forms at the CGM-disc interface owing to the passage of the galactic fountain clouds, as found in Barbani et al. (2023) and confirmed by the simulations in this Chapter.

(iii) I examined the radial gas inflows in the disc. Net radial inflows are present with average values $\approx 0.7 - 3.8$ $M_\odot$ yr^{-1} across the 9 simulations. The gas is flowing inward and outward in a periodic trend with an overall inflowing flux in all the simulations over 2 Gyr. The shape of the radial net inflow distribution presents similarities in all the simulations. The mass rate has its peak at $\approx R_d$, it decreases going inside owing to the higher gas density and to the formation of stars in the central region of the disc. I found that these radial inflow rates have radial velocity $\approx -(3-6)$ km s^{-1} with an almost constant value inside R_d. The radial inflows alone are not sufficient to sustain the star formation in the center, but they can do it in conjunction with vertical inflows which fall at $R < 0.4 R_d$, where 90% of the SFR is concentrated. Thus, while the gas accreted from the CGM lands preferentially in the outer regions of the disc, the SFR can be fed by radial motions generated by the angular momentum difference between the CGM and the gas in the disc and by the gas vertically accreted in the center.

(iv) Gas accretion concentrated in the external regions of the disc causes an inside-out evolution scenario, where the galaxy is evolving growing from the inside to the outside. This is confirmed by the slow growth of both the stars and gas discs sizes over time in all 9 simulations. In particular gas and stellar discs grow together with an up-and-down trend linked to stellar evolution. Furthermore, the accretion and ejection of gas are deeply linked to the periodic growth of the disc: peaks in the inflow rate are connected to periods in which the disc is growing, the opposite happens for the outflow

rate.

The analysis carried out in this Chapter has linked different crucial aspects of gas dynamics in spiral galaxies, collectively known as the **baryon cycle**. Fresh gas is predominantly accreted from the circumgalactic medium in the outer regions of the disc. This infalling gas has a lower specific angular momentum compared to the gas already present in the disc, leading to an inward flow of gas due to the conservation of angular momentum. At the galaxy center, where gas density is the highest, a portion of this gas is converted into stars, sustaining the SFR. These newly formed stars impart feedback to the surrounding ISM, eventually driving cold gas clouds out of the disc and forming galactic fountains. As these fountains travel through and interact with the CGM, they create a warm gas phase that eventually cools down and accretes onto the disc at larger radii, thus continuing the baryon cycle. Looking ahead, the inclusion of additional physics, such as magnetic fields, could offer new insights on accretion dynamics.

While this work has focused on Milky Way-like galaxies, an important next step is to explore how the vertical and radial inflows behave in galaxies of different stellar masses. The set of simulations presented here was designed to isolate the impact of varying gaseous disc properties while keeping other galactic parameters unchanged. This approach provided a controlled environment to analyze the mechanisms driving inflows and their role in fueling star formation. However, galaxy mass is expected to play a crucial role in shaping these processes. Differences in the depth of the gravitational potential well (e.g. Zhang & Buta, 2012; Goldbaum et al., 2016), the overall angular momentum distribution (e.g. Hopkins & Quataert, 2011), and the interplay between inflows and feedback mechanisms (e.g. Sharda et al., 2024) could significantly modify the efficiency and structure of radial mass transport. Lower-mass galaxies, for instance, may exhibit more turbulent and less coherent inflows due to weaker gravitational confinement, while more massive galaxies might sustain more stable accretion flows. Extending this study to a broader range of stellar masses would provide insight into the mass dependence of gas cycling processes and their implications for galaxy evolution. Future simulations incorporating a more diverse sample of galaxy masses will help determine how universal the trends identified in this work are and whether additional dependencies emerge. This will be crucial for connecting my findings to observational constraints and understanding how inflows contribute to star formation across different galaxy popula-

tions.

Additionally, studying baryon cycle processes within a full cosmological framework will be crucial for advancing our understanding of spiral galaxies evolution. In this Chapter, the galaxies are evolved in isolation and are not inserted in a full cosmological context. Therefore, it would be desirable to extend this analysis to simulations including the cosmological context self-consistently. In this way, it will be possible to follow the evolution of star-forming galaxies like the Milky Way with a higher degree of physical fidelity, drawing a coherent picture of the formation and evolution of such objects and enabling us to make an important step forward towards a more physically faithful modelling of the evolution of star-forming galaxies. I will present a possible approach to include the cosmological context in the next Chapter.

Chapter 6

Hybrid Cosmological Simulations of Galactic Outflows in Milky Way-like Galaxies

6.1 Introduction

The aim of this Chapter is to analyze low-redshift properties of outflows in a Milky Way disc simulated within a realistic cosmological environment. In doing so, I simulated the galaxy in a cosmological zoom-in simulation from high redshift ($z = 127$) down to redshift $z = 0$, then I extracted the galactic halo and continued its evolution in isolated, non cosmological, box in order to decrease the computational time and being able to easily simulate runs with different feedback properties without significantly alter the evolution of the galaxy until $z = 0$. In particular, I doubled the energy injected per SN and I modified the scheme used to assign mass, energy and momentum to the gas that surrounds star particles.

This Chapter is structured as follows: in Section 6.2 I briefly describe the numerical methods used in this Chapter and how I have created the initial conditions for my cosmological simulations. In Section 6.3 I describe the structure of the CGM in my simulations, in Section 6.4 I analyze the outflow/inflow mass rates close to the galactic disc and in Section 6.5 I study mass, energy and momentum rates and loading factors at a larger distance from the disc. I

conclude and summarize them in Section 6.6.

This Chapter is based on an ongoing research, and the results presented here reflect the current status of the work. Further analyses and conclusions may evolve as the project progresses. These results will form the basis of a forthcoming peer-reviewed publication (Barbani et al., in prep.).

6.2 Numerical methods

6.2.1 Cosmological hybrid initial conditions

In this Chapter, I implemented a cosmological hybrid set up, which consists in simulating a galaxy in a zoom-in cosmological simulation down to redshift $z = 0$. Then, the galaxy is extracted and inserted in a cubic box to run it in 'isolation'. This has the advantage of decreasing the computational time while still having the full cosmological environment. Moreover, the feedback parameters can be easily changed while still having a realistic Milky Way-like system. The simulation box is extracted from a cosmological zoom-in simulation run with AREPO and *SMUGGLE*. The initial conditions are generated at redshift $z = 127$ with the MUSIC software (Hahn & Abel, 2011). The simulation follows a Λ cold dark matter cosmology with density parameters $\Omega_{\rm m} = \Omega_{\rm dm} + \Omega_{\rm b} = 0.3$, $\Omega_{\rm b} = 0.046$, $\Omega_\Lambda = 0.7$ and Hubble constant $\rm H_0 = 100\ \mathit{h}\ km\ s^{-1}\ Mpc^{-1} = 69\ km\ s^{-1}\ Mpc^{-1}$, consistent with WMAP results (Hinshaw et al., 2013), although small changes to these parameters do not significantly matter for the purpose of this Chapter. The target galaxy has been selected with a halo with a virial mass around $10^{12}\ \rm M_\odot$ at redshift $z = 0$ and with no other massive objects close to it. I run the zoom-in simulation until redshift $z = 0$ and then in order to run isolated simulations with a cosmological set up I extracted the galaxy from the cosmological simulation. All the particles are selected within $\rm 2R_{200} = 360$ kpc from the center of mass of the galaxy and are then inserted in a 857 kpc size cube. I then have add a background grid containing 16^3 cells filled with low density gas as the simulation volume needs to be filled with a Voronoi grid to avoid vacuum boundary problems (see Springel (2010b) for details on the implementation). During the simulation, the background grid is prevented from de-refining, disallowing de-refinement for cells with a volume greater than 10% of the mean gas cell volume. Thanks to

Table 6.1: Summary of the model variation of the Milky Way-like galaxy parameters in this Chapter. The fiducial simulations is **cosmo**. The other simulations are used as comparison with the main one.

Simulation name	$f_{\rm SN}$	weighting scheme
cosmo	1	normal
cosmo_feed2	2	normal
cosmo_weightm	1	mass
cosmo_weightv	1	volume

this isolated-cosmological hybrid set up it is possible to run simulations varying parameters quickly. In particular, I run 4 different simulations, changing the energy ejected from SNe and changing the implementation of how the feedback is distributed in the gas surrounding the star particle, i.e. the weighting scheme.

6.2.2 Feedback weighting schemes

A crucial aspect of modeling stellar feedback is how energy and momentum, as well as mass and metals, are distributed to the gas cells that surround star particles. In *SMUGGLE* this is done through weight functions. The number of neighbour cells is defined as

$$N_{\rm ngb} = \frac{4\pi}{3} h^3 \sum_i W(|\mathbf{r}_i - \mathbf{r}_s|, h), \tag{6.2.1}$$

where W is the standard cubic spline SPH kernel (Monaghan & Lattanzio, 1985), h is a search radius and $|\mathbf{r}_i - \mathbf{r}_s|$ is the distance between the gas cell and the star particle. Equation (6.2.1) is solved iteratively in order to find the parameter h with a predetermined value of $N_{\rm ngb}$. In my simulations I set $N_{\rm ngb} = 64$.

For each gas cell i the standard weights are defined as

$$w_i = \frac{\Delta\Omega_i}{4\pi} = \frac{1}{2}\left\{1 - \frac{1}{[1 + A_i/(\pi|\mathbf{r}_i - \mathbf{r}_s|^2)]^{1/2}}\right\}, \tag{6.2.2}$$

where $A_i = \pi\Delta x_i^2$ is the gas cell area. In this way each gas cell within $h_{\rm coupling}$ receives a fraction of energy and momenta (while mass and metals are returned within the scale h)

proportional to the fraction of the solid angle 4π covered by the cell as seen from the stellar particle position. The total energy and momentum is injected in each gas cell multiplied by the factor

$$\tilde{w}_i = \frac{w_i}{\sum_i w_i}, \tag{6.2.3}$$

which ensures that each cell receives a correct fraction of the total momentum and energy injected. Given the arbitrary nature of the momentum and energy distribution, I implemented other types of weights w_i, in order to analyze how they affect the nature of the outflows. In particular, the weights are chosen as the mass of each gas cell M_i

$$w_i = M_i, \tag{6.2.4}$$

and as the gas cell volume V_i

$$w_i = V_i. \tag{6.2.5}$$

These two different weighting schemes change significantly distribution of injected energy and momentum, as the more massive cells do not always correspond to the cells with bigger volumes.

6.2.3 Simulations set up

In Table 6.1 I summarize the different parameter variations I implemented in my runs. In particular, I changed the quantity of energy that each SN is injecting, parameterized by $f_{\rm SN}$, and the weighting scheme w_i (see eq 6.2.2). I made 4 parameter variations in the cosmo hybrid set-up: the fiducial simulations with the standard weighting scheme (**cosmo**), one simulation in which each SN is injecting 2×10^{51} erg into the ISM (**cosmo_feed2**) and two simulations respectively with a mass weighting scheme (**cosmo_weightm**) and a volume weighting scheme (**cosmo_weightv**). In each simulation there are $N_{\rm gas} \approx 2.4 \times 10^6$ gaseous particles with an average mass $\langle m_{\rm gas} \rangle \approx 2.4 \times 10^4\ M_\odot$, $N_\star \approx 1.4 \times 10^6$ with an average mass $\langle m_\star \rangle \approx 1.7 \times 10^4\ M_\odot$ and $N_{\rm dm} \approx 4.7 \times 10^6$ dark matter particles with an average mass $\langle m_{\rm dm} \rangle \approx 1.3 \times 10^5\ M_\odot$.

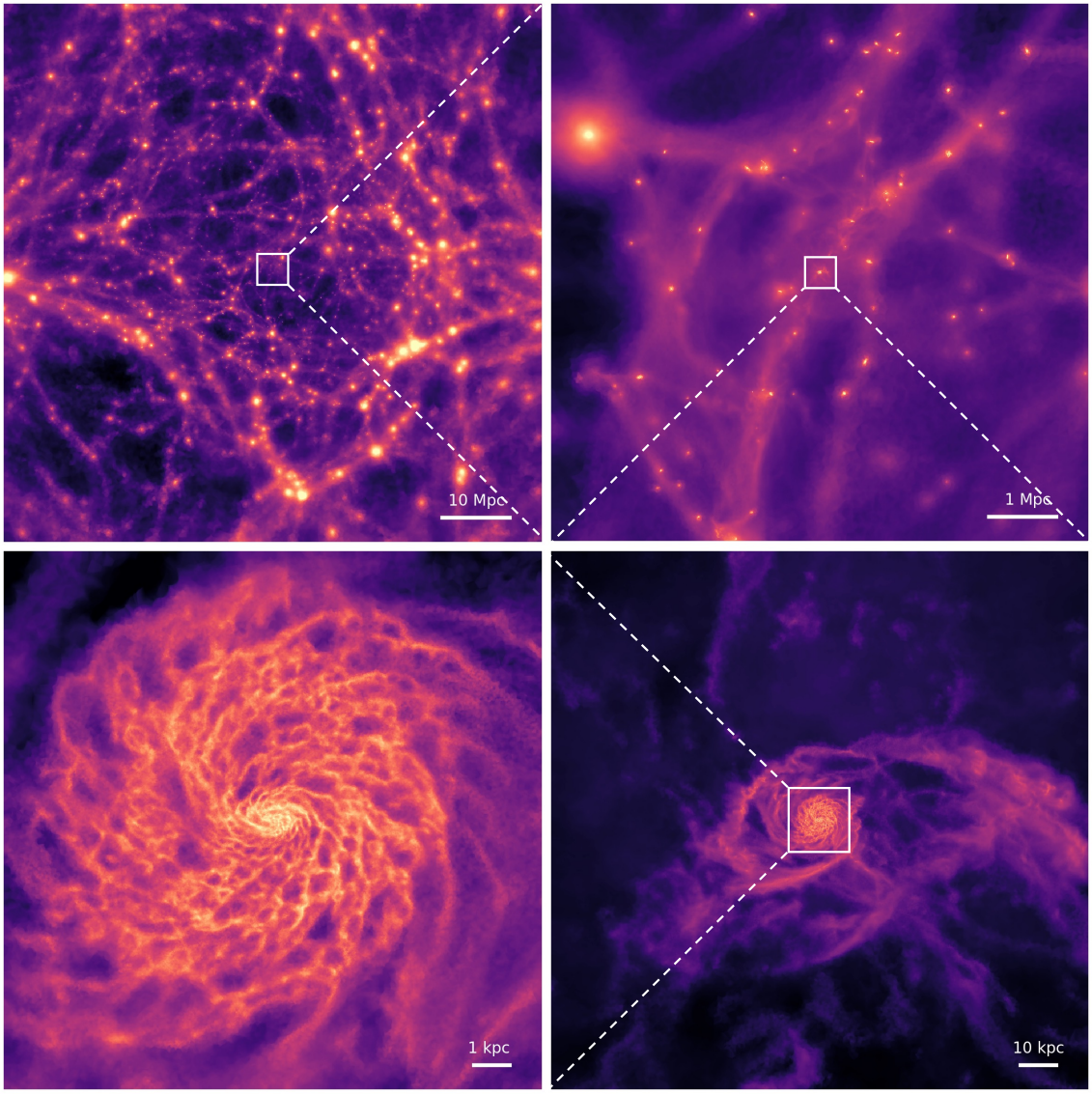

Figure 6.1: Gas column density projections computed at different scales for the cosmological simulation. *Top left*: the panel is 90 Mpc across and in projection depth with a resolution of $\sim$ 90 kpc. This panel shows clearly the cosmic web on a large scale. *Top right*: zoom-in view of the central 10 Mpc volume shown in the top left panel. *Bottom right*: panel with a size of 100 kpc. Inside the halo resides the spiral galaxies, it is possible to see the complex gas structures around the disc. *Bottom left*: zoom-in view of the central 10 kpc.

6.2.4 Rates and loading factors characterization

In this Chapter I analyze mass, momentum and energy rates and loading factors. In particular, these are analyzed in two main regions:

(i) disc region (2 kpc),

(ii) halo region ($0.25 r_{\rm vir} \sim 40$ kpc).

In this way it is possible to study outflows and inflows at different spatial scales: galactic fountains, which are usually confined in the regions closer to the galactic disc, and galactic winds, that are higher velocity outflows of gas that can reach higher distances from the galaxy. I briefly summarize the main processes involved in the baryon cycle of Milky Way-like galaxies as they are important for this analysis. At small scales the galactic fountains are the main gas recycling phenomenon close to the disc: cold high-metallicity gas ejected from the disc moves through the mainly hot and low-metallicity CGM, during this time ($\approx$ 100 Myr) the fountain gas mixes with the coronal gas letting a fraction of the CGM condense into it. The galactic fountains then fall into the disc again, bringing more gas than the one that was ejected and with different thermodynamical properties (see Chapter 4). For their nature galactic fountains typically join the disc in a different spot with respect to where they were ejected, therefore contributing to dilute gas properties in the disc and to bring fresh gas in the external regions of the disc (see Chapter 5). Not all the outflows are confined close to the disc, stronger outflows can have velocities higher than the galaxy escape velocity. Large galactic winds can quench a galaxy as the gas is only ejected and is not coming back. These winds can interact with the IGM bringing metals to the medium outside the galaxy.

Mass, momentum end energy rates are computed in two ways. The disc region is selected in an area within 2 slab at a height $|z| = 2$ kpc above and below the plane of the disc with a thickness Δx and with $R < 30$ kpc. In the halo region the rates are computed radially inside a shell sphere of thickness $\Delta x = 0.1$ $\rm r_{vir}$. Outflowing gas is identified with a radial velocity $v_r > 0$ km s^{-1} (vertical velocity $v_z > 0$ km s^{-1}) in the halo (disc) region, which means gas that is moving away radially (vertically) from the center (plane) of the galaxy. The opposite applies for the inflowing gas.

Mass, momentum and energy rates are defined as follows

$$\dot{M} = \sum_i \frac{v_i m_i}{\Delta x}, \tag{6.2.6}$$

$$\dot{p} = \sum_i \frac{m_i}{\Delta x}\left(v_i^2 + c_s^2\right), \tag{6.2.7}$$

$$\dot{E} = \sum_i \frac{v_i m_i}{\Delta x}\left(\frac{1}{2}v_i^2 + \frac{\gamma}{\gamma - 1}c_s^2\right), \tag{6.2.8}$$

where m_i is the gas cell mass, v_i is the gas cell radial (vertical) velocity, $c_s^2 = P/\rho$, γ is the adiabatic index and Δx corresponds to the radial/vertical width in which the rates are computed. These rates are computed inside the selected regions. The gas is divided in three main phases depending on the temperature: cold gas ($T < 10^4$ K), warm gas ($10^4 < T < 5 \times 10^5$ K) and hot gas ($T > 5 \times 10^5$ K).

To characterize the properties of the winds I computed the loading factors. In particular, the mass loading factor, that measures the efficiency in removing gas from the ISM compared to the formation of stars and the momentum and energy loadings, measuring how efficiently the momentum and energy ejected by stellar feedback can escape the ISM and be driven by the outflows. To compute these quantities I make the reasonable assumption that the energy and momentum are dominated by type II SNe. The reference rate values to compute the loading factors, similarly to Kim et al. (2020), are

$$\dot{M}_{\rm ref} = \mathrm{SFR}, \tag{6.2.9}$$

$$\dot{p}_{\rm ref} = \dot{N}_{\rm SN}\frac{E_{\rm SN}}{v_{\rm cool}}, \tag{6.2.10}$$

$$\dot{E}_{\rm ref} = \dot{N}_{\rm SN}E_{\rm SN} \tag{6.2.11}$$

It can be assumed that $\dot{N}_{\rm SN} = \mathrm{SFR}/100\ \mathrm{M}_\odot$, as around 1 SN explodes every 100 $\mathrm{M}_\odot$ of stars. I assume $E_{\rm SN} = 10^{51}$ erg except in the **cosmo_feed2**, which has a modified feedback energy, where it is equal to 2×10^{51}. The loading factors are then computed as $\eta_M = \dot{M}/\dot{M}_{\rm ref}$, $\eta_p = \dot{p}/\dot{p}_{\rm ref}$ and $\eta_E = \dot{E}/\dot{E}_{\rm ref}$.

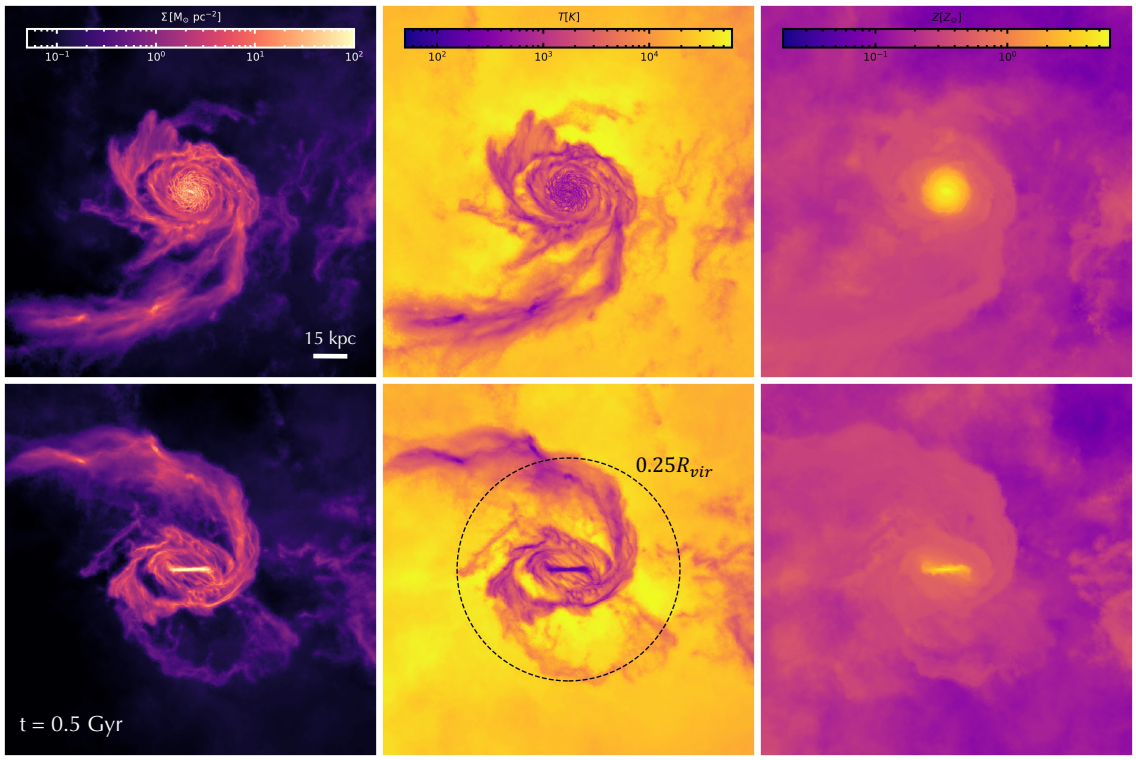

Figure 6.2: Gas surface density, temperature and metallicity (from left to right) in face-on (top panels) and edge-on (bottom panels) projections of the **cosmo** simulation at $t = 0.5$ Gyr. Each panel is 150 kpc across and in projection depth with a total number of 1024 × 1024 pixels that give a resolution of ~ 150 pc. These projections clearly show the multiphase nature of the CGM. The dashed black circle in the bottom central panel indicates $R = 0.25R_{\rm vir}$.

Figure 6.1 shows a gas surface density projection of the target galaxy for the hybrid cosmological simulation from large (tens of Mpc) to small (kpc) scales (from first panel going clockwise). Each colormap range has been re-scaled for visual interpretation. The surface density projections clearly show the large scale structure of the Universe, forming the so-called cosmic web. Zooming into the target halo for my simulations, the spiral galaxy resides at the center of it and its evolution is deeply influenced by the gas that accretes into it during its evolution. Figure 6.2 shows surface density (first column), temperature (second column) and metallicity (third column) projections. The multiphase nature of the CGM is apparent, showing a wide range of density, temperature and metallicity. Notably, a cold, high-density and low-metallicity filamentary structure swirling around the galactic disc is present.

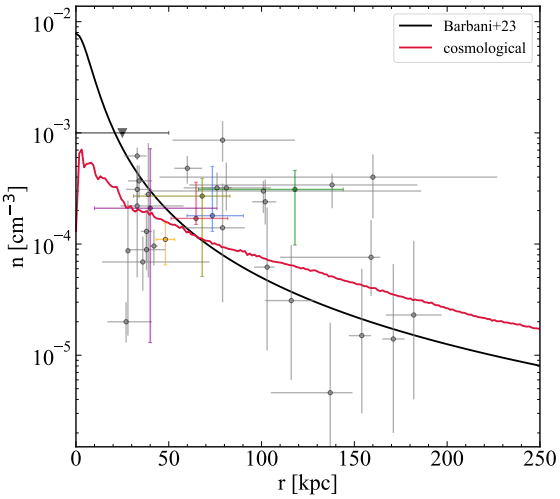

Figure 6.3: CGM number density profile of the isolated fiducial simulation of Chapter 4 (black solid line) and of the simulations in this Chapter at $t = 0$ Gyr (red line) compared with several observational constraints of the Milky Way (see Chapter 4).

6.3 Phase diagrams

In this Section I make a comparison of the gas properties between the cosmological simulation and the isolated simulations. Figure 6.3 shows the number density profile for the hot gas of the CGM in the isolated (black line, see Chapter 4) and in the hybrid cosmological (red line) simulations. The cosmological corona is originated naturally from a cosmological evolution of the galaxy, therefore there are no free parameters to be chosen and is more physically plausible. In particular it has a lower density in the central region (from 10^{-2} cm^{-3} to 10^{-3} cm^{-3}) and higher at larger radii ($r > 75$ kpc). One important difference between the isolated and the cosmological set up is the multiphase nature of the CGM. In the isolated ICs the coronal gas temperature profile is derived solving the hydrostatic equilibrium equation and therefore is intrinsically hot. It is known from observations that the CGM has a wide variety of gas phases inside it (e.g. Sameer et al., 2024). In Figure 6.4 I show phase diagrams of number density (first column), temperature (second column) and metallicity (third column) as a function of radius, for both the fiducial isolated (bottom row) and hybrid cosmological (top row) runs. The central region, with a density between 10^{-3} and 10^{3} cm^{-3}, is the disc. All the gas between 0 and 25 kpc is located at the interface between the disc and the CGM, the gas

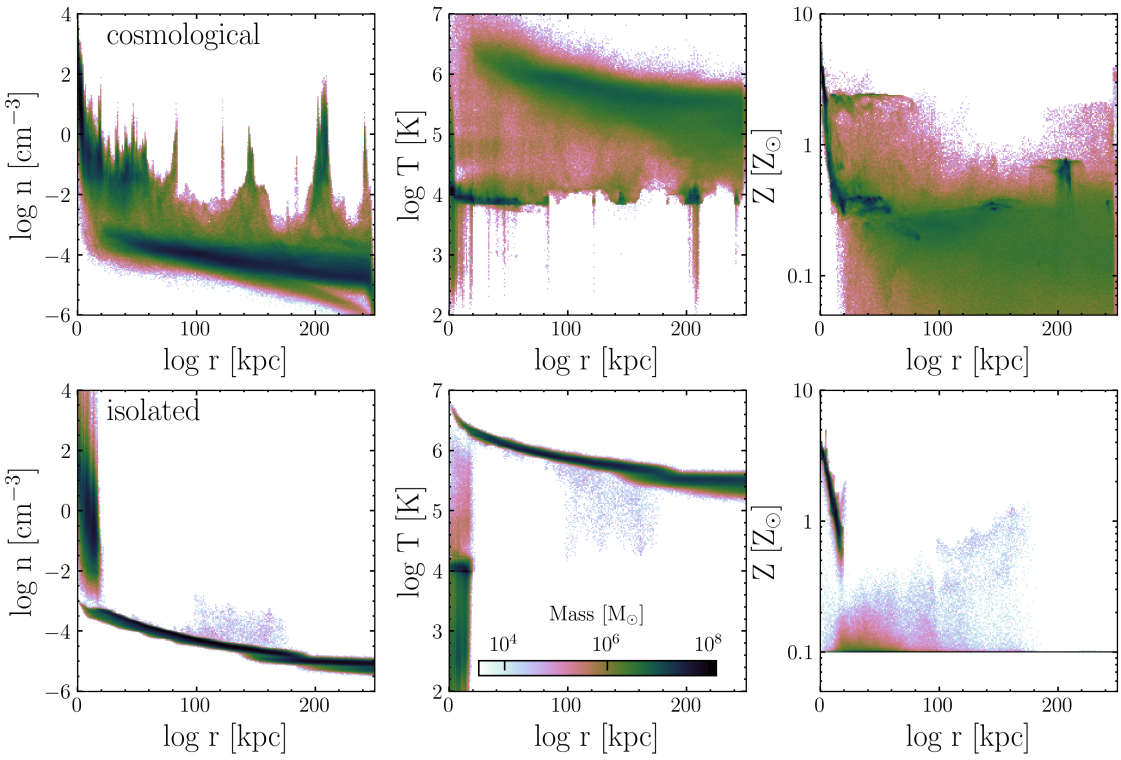

Figure 6.4: Number density-radius (first column), temperature-radius (second column) and metallicity-radius (third column) diagrams for the fiducial hybrid cosmological simulation (top row) at $t = 0$ Gyr and isolated simulation (bottom row) of Chapter 4 at $t = 0$ Gyr.

here is composed by outflows that are ejected from the disc and by gas that is accreted from the CGM. I analyze this region and the interchange between the disc and the inner CGM in the first part of this Chapter. The region with $n < 10^{-3}$ cm^{-3} represents the CGM, which extends over the virial radius, this is constituted mostly by low density gas, the two overdensity regions at 150 and 200 kpc are satellites galaxies. In the bottom panel the same phase diagram is shown for the isolated simulation of Chapter 4 at $t = 2$ Gyr, this is done to let the galaxy evolve from the initial conditions. The difference in the CGM is apparent, at each radius the range of number densities is very tight, showing the initial density profile set for the corona. Some higher density gas coming from stellar feedback is around the central disc and at high radii ($100 - 150$ kpc). In the second column the temperature is shown. The gas in the disc is mainly at 10^4 K but can go from 100 K to around 10^6 K. The CGM is on average hot (10^5-10^7 K) but also lower temperature gas is present very far from the disc, showing the multiphase nature of this medium. Looking at the isolated simulation, the disc has a very similar structure but almost only one phase of gas is present in the CGM, because of how the ICs were built. The third column shows the metallicity phase diagram. The cosmological simulation shows a wide range of metallicities as seen by observations (Cooper et al., 2021), going from low metallicity gas accreted from the intergalactic medium to more metal rich gas ejected from the galaxy thanks to stellar evolution. A very different scenario is shown in the isolated run, where the metallicity of the CGM is set to 0.1 $Z_\odot$ in the ICs. After 2 Gyr of evolution there is a higher metallicity, between 0.1 and 1 $Z_\odot$ until 150 kpc, this gas richer in metallicity has been pushed outside of the galaxy thanks to stellar feedback processes. The main structures, the central galactic disc and the CGM, are visible in both cosmological and isolated runs, but in the cosmological one it is more self-consistent and realistic. The advantage of using an isolated run is that outflows and inflows can be studied easily and in more detail, because there is less interference by filament accretion and tidal streams.

6.4 Small scale outflow/inflow rates

Figure 6.5 shows outflow (solid lines) and inflow (dashed lines) rates for the cosmological simulation computed in the disc region. The rates are computed summing up $v_i m_i / \Delta z$ inside a slab centered in $|z| = 1$ kpc and with a width $\Delta z = 0.15$ kpc (see Section 6.2.4). In

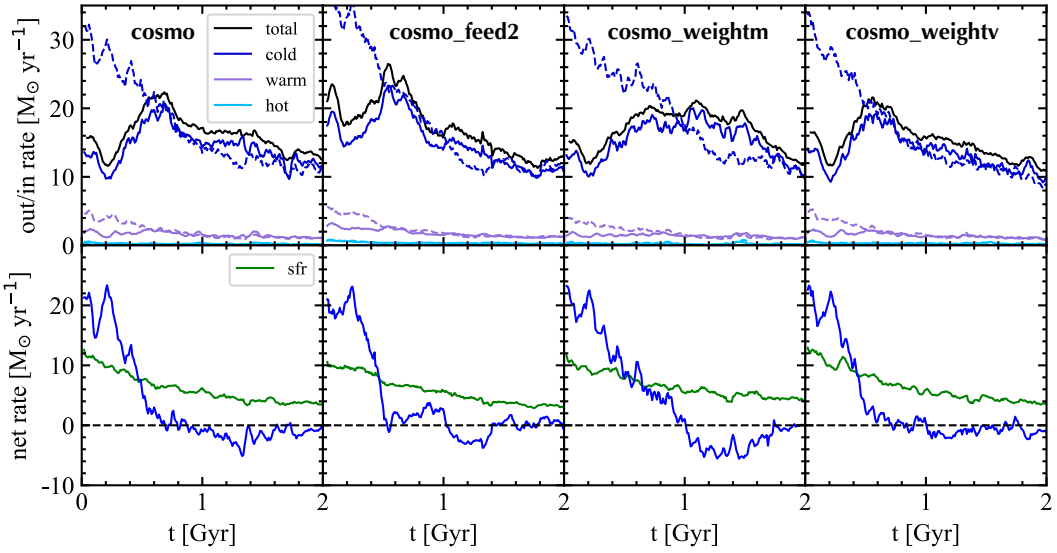

Figure 6.5: *Top row*: outflow (solid lines) and inflow (dashed lines) mass rates for cold (blue line), warm (purple line) and hot (light blue line) gas for the **cosmo** (first panel), **cosmo_feed2** (second panel), **cosmo_weightm** (third panel) and **cosmo_weightv** (forth panel) simulations. *Bottom row*: net inflow rate (blue line) compared with the SFR (green line) for the same simulations.

all the simulations, the majority of outflows is constituted by cold gas, as expected from SNe explosions. The same can be said about inflows which are almost only cold. This happens for two reasons, a significant fraction of the inflows is composed by recycled gas that was previously ejected from the disc and the majority of the outflows from the disc are cold. Also, the CGM gas has to cool down in order to be accreted into the galactic disc. Therefore, the fraction of warm and hot inflows is very low. The outflow and inflow rates have an up-and-down trend but slightly tilted between each other: the ejected gas (peak in the outflow rate) is then re-accreted onto the disc (peak in the inflow rate), circulating the gas between the disc and the CGM. There are no huge differences changing the feedback implementation. The **cosmo** simulation has a small peak around $t = 0$ Gyr which decreases and then rises again reaching to the maximum in the outflow rate at $t = 0.5$ Gyr. The same happens in **cosmo_feed2** and **cosmo_weightv**, whith **cosmo_feed2** having slightly higher rates. In **cosmo_weightm** the shape of the outflow rate is different, reaching a peak at $t = 1$ Gyr, but the average values are similar. The inflow rates is decreasing in all the simulations from a value ≈ 30 $M_\odot$ yr^{-1} (≈ 35 $M_\odot$ yr^{-1} for **cosmo_feed2**) at the beginning of the simulations to ≈ 10 $M_\odot$ yr^{-1} after

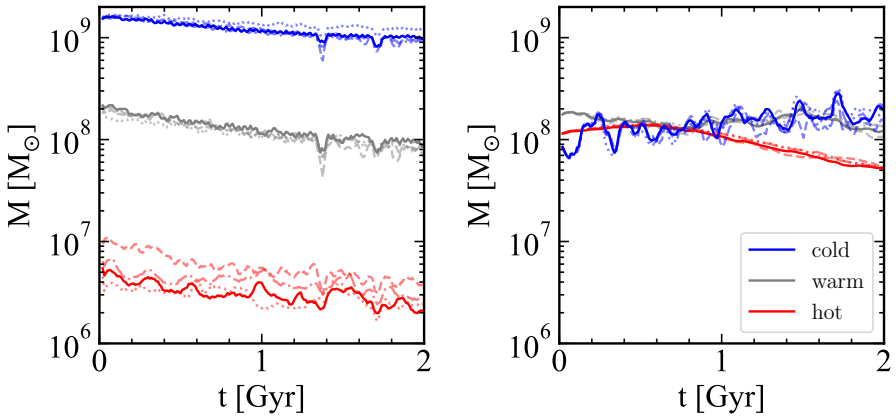

Figure 6.6: *Left panel*: gas mass at $R < 20$ kpc divided in cold (blue), warm (grey) and hot (red). *Right panel*: gas mass at $R > 20$ kpc divided in cold, warm and hot. In both panel the masses are computed for the **cosmo** (solid line), **cosmo_feed2** (dashed line), **cosmo_weightm** (dotted line) and **cosmo_weightv** (dash-dotted line) simulations.

2 Gyr. An important quantity to look at is the net inflow rate. In the bottom panel of Figure 6.5, the net inflow rate (blue line) is compared to the SFR of the galaxy (green line). To sustain the star formation of a galaxy over a long period of time the SFR and the net inflow need to be roughly the same order of magnitude. In all 4 simulations a peak in the net inflow rate is present in the first 0.5 Gyr, followed by a negligible net rate oscillating around 0 $M_\odot$ yr^{-1}.

Figure 6.6 shows the mass of gas in the CGM (left panel) and the mass of gas in the inner regions of the CGM and in the galactic disc (right panel) for the **cosmo** (solid line), **cosmo_feed2** (dashed line), **cosmo_weightm** (dotted) and **cosmo_weightv** (dash-dotted). The mass of gas in the inner regions is monotonically slightly decreasing over time from $\approx 2 \times 10^9$ $M_\odot$ yr^{-1} to $\approx 10^9$ $M_\odot$ yr^{-1}. The cold gas is dominant with one order of magnitude more than the warm gas (changing from $\approx 2 \times 10^8$ $M_\odot$ yr^{-1} to $\approx 10^8$ $M_\odot$ yr^{-1} in all the simulations). This is indicating that the reservoir of gas in the disc is slowly consumed to form new stars owing to the gas that is accreted from the CGM. The hot gas is the less massive component, with only $2 \times 10^6 - 5 \times 10^7$ $M_\odot$, the **cosmo_feed2** simulation have almost two times the mass with respect to the other simulations. In the right panel the mass at $R > 20$ kpc is displayed. There is no significant difference between the 4 simulations. The mass of the cold gas has a fluctuating trend, increasing over time from 10^8 to 2×10^8 $M_\odot$, indicating that a fraction of

outflows are traveling at these distances from the disc. Partially the oscillatory trend is also due to the filamentary cold structure visible in Figure 6.2 rotating around the galactic disc. The warm gas stays constant at $\approx 10^8$ $M_\odot$, whereas the hot gas decreases from $\approx 10^8$ $M_\odot$ to $\approx 5 \times 10^7$ $M_\odot$.

6.5 Large scale mass, momentum and energy rates

In this section I analyze mass, momentum and energy rates for the 4 simulations, focusing on differences arising from various stellar feedback implementations.

Figure 6.7 shows the mass outflow (solid lines) and inflow (dashed lines) rates at $0.25r_{\rm vir} \sim 160$ kpc, as shown in the first row, for the simulations listed in Table 6.1. The rates are again divided in cold ($T < 10^4$ K, blue line), warm ($10^4 < T < 5 \times 10^5$ K, purple line) and hot ($T > 5 \times 10^5$ K, light blue line) gas. As shown in Figure 6.5, the SFR decreases from 10 $M_\odot$ yr^{-1} to ≈ 2 $M_\odot$ yr^{-1} over the 2 Gyr period. Starting with **cosmo** simulation (first column), cold and warm gas dominate the outflow rate, with a significant contribution from hot gas as well. Cold and warm outflow rates exhibit oscillatory behavior over time, with values between 1-5 $M_\odot$ yr^{-1}, approximately the same order of magnitude of the SFR. Hot outflows and inflows, though less variable, range from 2 $M_\odot$ yr^{-1} to 1 $M_\odot$ yr^{-1}, ultimately contributing for almost 50% of the total outflow rate at $0.25r_{\rm vir}$ by the end of the simulation. Cold and warm inflows are slightly lower than the outflows, maintaining rates between 1-4 $M_\odot$ yr^{-1}. In the **cosmo_feed2** simulation (second column), outflow and inflow peaks appear similar to those in **cosmo**, with a slight increase in the hot gas outflow. Comparatively, the **cosmo_weightm** (third column) and **cosmo_weightv** (fourth column) simulations show minimal differences.

The second row of Figure 6.7 shows the energy rate (Eq. 6.2.8) as a function of time for the same simulations and in the same range of temperatures. The energy rate varies between 10^{46} and 10^{49} erg s^{-1}. The picture that is outlined is very different with respect to the mass rates, in this case the hot component is dominating the energy budget of the outflows with an energy rate $\approx 5 \times 10^{48}$ erg s^{-1} declining over time. Hot inflows show a lower energy rate of $\approx \times 10^{48}$ erg s^{-1}. This points out that the hot outflows are accelerated by the feedback processes in the central galaxy. Warm and hot outflows have lower and similar values between 10^{46} and 10^{48} erg s^{-1}. In **cosmo_feed2**, the energy of the hot outflowing gas is notably higher, at around

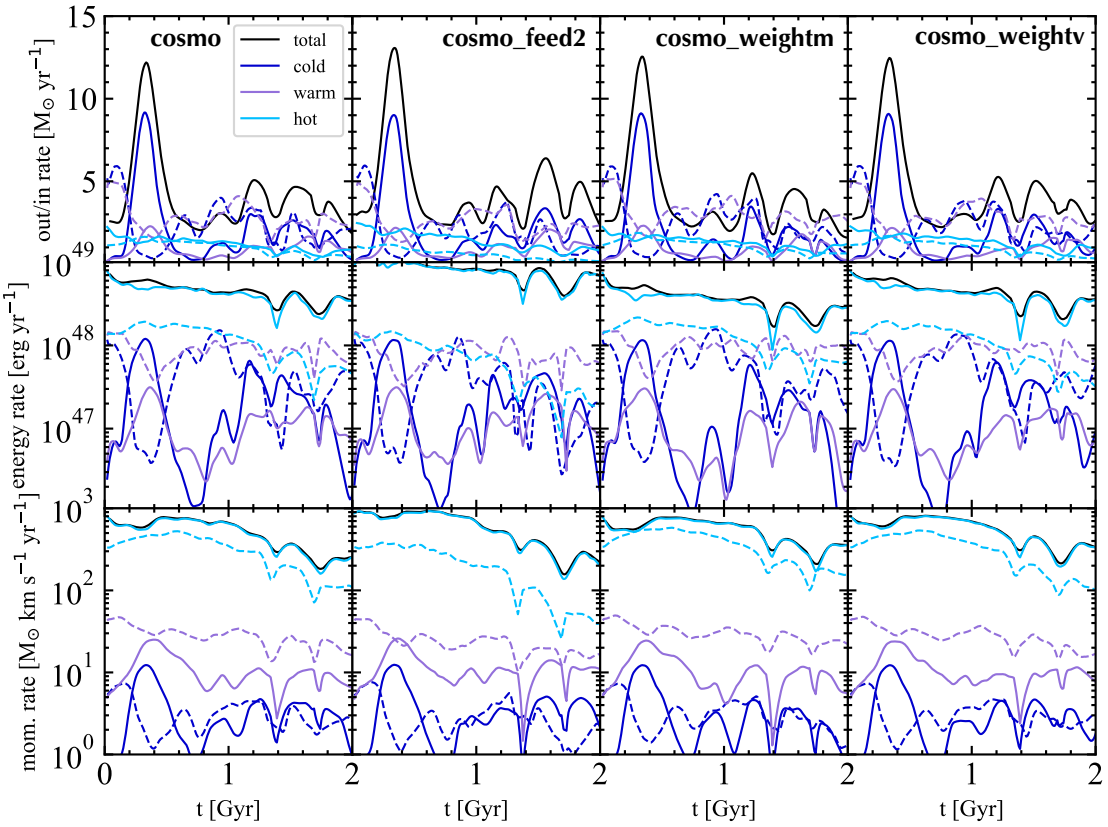

Figure 6.7: *First row:* outflow (solid lines) and inflow (dashed lines) mass rates. *Second row:* outflow (solid lines) and inflow (dashed lines) energy rates. *Third row:* outflow (solid lines) and inflow (dashed lines) momentum rates. All the rates are divided cold (blue line), warm (purple line) and hot (light blue line) gas for the **cosmo** (first panel), **cosmo_feed2** (second panel), **cosmo_weightm** (third panel) and **cosmo_weightv** (forth panel) simulations.

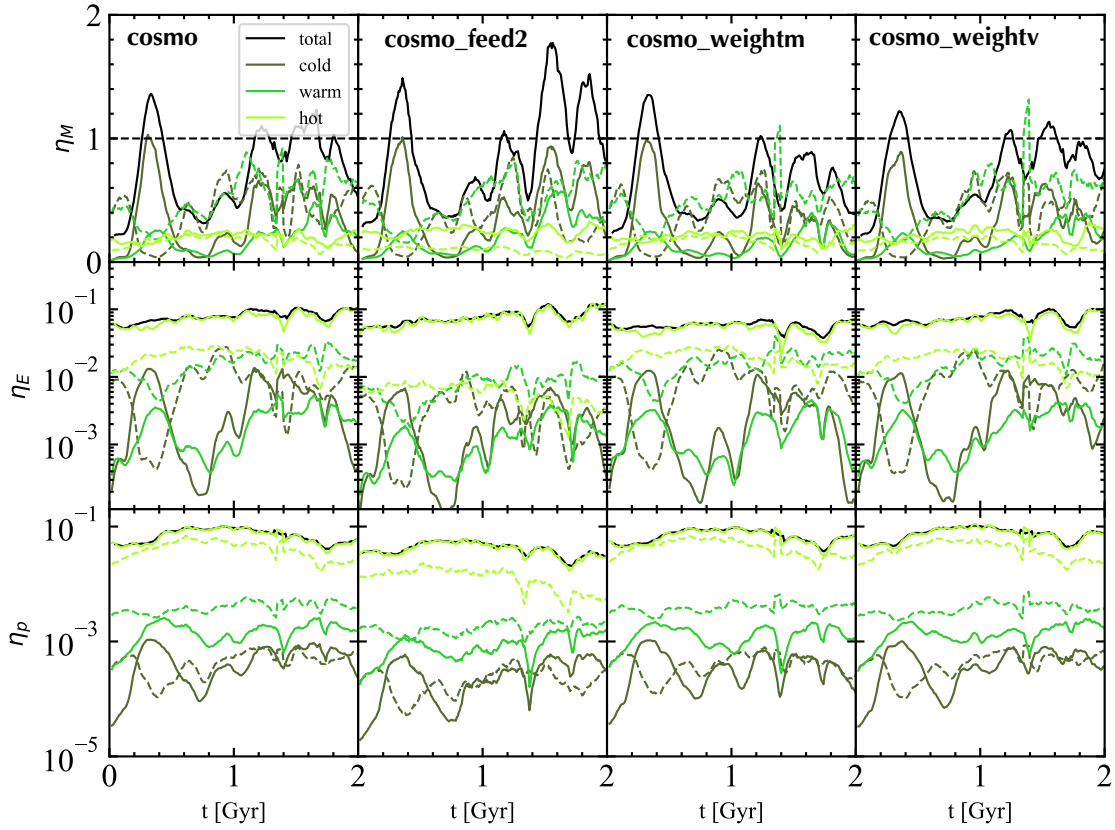

Figure 6.8: *First row:* outflow (solid lines) and inflow (dashed lines) mass loading factor. *Second row:* outflow (solid lines) and inflow (dashed lines) energy loading factor. *Third row:* outflow (solid lines) and inflow (dashed lines) momentum loading factor. All the loading factors are divided cold (blue line), warm (purple line) and hot (light blue line) gas for the **cosmo** (first panel), **cosmo_feed2** (second panel), **cosmo_weightm** (third panel) and **cosmo_weightv** (forth panel) simulations. The mass loading factor is computed as $\eta_M = \dot{M}/\mathrm{SFR}$. A dashed horizontal line indicates $\eta_M = 1$.

10^{49} erg s^{-1}, indicating that changes in the energy released from SNe significantly impact the large scale energetics of the gas around the galaxy. The **cosmo_weightm** and **cosmo_weightv** simulations have values similar to those seen in **cosmo**.

The third row displays the momentum rate as a function of time, computed as in Eq. (6.2.7). Also in this case the dominant component is the hot gas, carrying most of the total outflowing momentum, ranging from 9×10^3 to 3×10^2 $M_\odot$ km s^{-1} yr^{-1}. This is because, while hot gas has a lower mass, it has higher temperature and velocity. The inflowing gas has values that are roughly half of the outflowing ones.

Figure 6.8 shows mass loadings (first row), energy loadings (second row) and momentum loadings (third row) as a function of time. In the **cosmo** simulation the cold mass loading (dark green) stabilizes around 0.5, with warm mass loading between 0 and 0.4. The mass loading of the hot phase is $\approx$ 0.2 , consistent with findings from other simulations (Kim et al., 2020), and as expected from superbubble evolution (Kim et al., 2019). The total mass loading fluctuates from 0.2 to 1.4 with a more constant value around 1 in the last Gyr of the simulation. These values are higher in **cosmo_feed2**, where the cold and hot mass loadings have larger values, reaching almost 2 at 1.8 Gyr, indicating an outflow rate that is two times the SFR. In **cosmo_weightm** exhibits a lower total mass loading. The second row displays the energy loading, which is totally dominated by the hot component in all the simulations. This component has an energy loading that increases from 0.06 to 0.1 in **cosmo**, **cosmo_feed2** and **cosmo_weightv**, whereas is constant at 0.7 in **cosmo_weightm**. The warm and cold energy loading are under 0.01 in all the simulations.

The third row shows the momentum loading, also in this case the hot gas is the dominant phase with values around 0.1 in most simulations, although slightly lower in **cosmo_feed2**.

6.6 Summary

In this Chapter I presented an analysis of a Milky Way-like galaxy with a cosmological environment simulated applying an innovative technique, which consists of first simulating the galaxy in a zoom-in cosmological simulation and then extracting it to run isolated simulations while still maintaining the realistic environment. I run 4 different simulations varying stellar feedback parameters in order to study how the quantity of energy injected and how

it is distributed to the ISM is affecting the outflows structure. The main findings of this Chapter are outlined below.

- I found that the gas surrounding the galaxy is a multiphase medium with a large range of densities, temperatures and metallicities (Figure 6.4), deriving from the previous evolution of the galaxy.
- Close to the disc ($|z| = 2$ kpc) outflow and inflow mass rates are prevalently cold ($10 - 20$ $M_\odot$ yr^{-1}), with low mass rates of warm and hot gas (< 6 $M_\odot$ yr^{-1}). The net inflow rate is sufficient to sustain the SFR in the first Gyr but becomes almost zero in the last Gyr of the simulation.
- Looking at the outflows, I found that most of the mass at $R = 0.25R_{\rm vir}$ is carried by the cold and partially by the warm phases, whereas the hot gas is transporting almost all the energy and the momentum. This means that to realistically simulate outflows both phases are necessary.

The results presented in this chapter are part of ongoing research and will be completed in future work.

Chapter 7

Summary and Conclusions

In this Thesis work, I have extensively studied gas circulation between the disc and the CGM in star-forming galaxies and how this circulation affects their mutual evolution, both on small and large scales. To analyze gas circulation, I made use of high-resolution hydrodynamical N-body simulations of Milky Way-like galaxies with the inclusion of an observationally-motivated galactic corona. To perform these simulations, I employed *SMUGGLE*, an explicit ISM and stellar feedback model coupled with the moving-mesh code Arepo. After a detailed discussion of the algorithms implemented in the Arepo code and a presentation of the key features of the *SMUGGLE* model in Chapter 2, I have described, in Chapter 3, the procedure to build a set of initial conditions for the hydrodynamical N-body simulations analyzed in this Thesis that picture an equilibrium configuration for my multicomponent galaxies containing a hot CGM. The remaining part of this Thesis is devoted to the investigation of crucial aspects of the disc-CGM gas circulation. The main findings of this analysis are outlined below.

- In **Chapter 4**, I studied the gas circulation between the disc and the corona of star-forming galaxies like the Milky Way. I find that the reservoir of gas in the galactic corona is capable to entirely sustain star formation: the gas accreted from the corona is the primary fuel for the formation of new stars, helping in maintaining a nearly constant level of cold gas mass in the galactic disc. Stellar feedback generates a gas circulation between the disc and the corona (the galactic fountain) by ejecting different gas phases that are eventually re-accreted onto the disc. The accretion of coronal gas is

promoted by its mixing with the galactic fountains at the disc-corona interface, causing the formation of intermediate temperature gas that enhances the cooling of the hot corona. I find that this process acts as a positive feedback mechanism, increasing the accretion rate of coronal gas onto the galaxy (with an inflow rate of $\approx 3\ M_{\odot}\ \mathrm{yr}^{-1}$).

- In **Chapter 5** I extended the results of the previous Chapter studing gas circulation on a larger sample of galaxies. I performed hydrodynamic N-body simulations of 9 different galaxies surrounded by a hot ($T \sim 10^6$ K) CGM. Each simulation has a different structure of the gaseous disc in terms of mass and scale length, which enables a detailed study of how the dynamics of the gas can be affected by the disc structure. My goal was to understand how gas in the CGM is accreted onto the inner regions of the star-forming disc, making it available for the formation of new stars. Specifically, I explored the connection between stellar feedback and gas accretion from the CGM in Milky Way-like galaxies, focusing on the distribution of vertical and radial gas flows to and from the disc as a function of galactocentric radius, and I examined the implications of these processes for the evolution of such galaxies. I found evidence of a crucial link between stellar feedback processes and gas accretion from the CGM, which together play an essential role in sustaining ongoing star formation in the disc. In particular, the ejection of gas from the plane of the disc by stellar feedback leads to the generation of a baryon cycle in which the CGM gas is preferentially accreted onto the external regions of the disc ($\approx 3 - 10\ \mathrm{M}_{\odot}\ \mathrm{yr}^{-1}$ of gas is accreted over the entire disc). From these regions it is then transported to the center with radial mass rates $\approx 1-4\ \mathrm{M}_{\odot}\ \mathrm{yr}^{-1}$ on average, owing to angular momentum conservation, forming new stars and starting the whole cycle again. I found that both vertical accretion onto the inner regions of the disc and the radial transport of gas from the disc outskirts are necessary to sustain star formation.

- In **Chapter 6** I employed an innovative technique which consists in running a cosmological zoom-in simulation and consequently extracting a small box containing the galaxy to run isolated simulations. In this way it is easier to change feedback parameters in the simulations and to have a more computationally efficient simulation while still retaining the realistic cosmological environment around the galaxy. This realis-

tic environment is found in the simulations, where a multiphase medium is present around the galactic disc. I found that galactic outflows are a multiphase medium with cold, warm and hot phases of gas. The cold phase is carrying most of the mass, not reaching high distances from the disc, whereas the hot phase carries most of the energy and the momentum of the outflows, with higher velocities and lower masses that allow this phase to reach high distances from the disc ($R > 0.25R_{\rm vir}$). Therefore, to accurately simulate outflows driven by stellar feedback, both the cold and the hot phases are necessary.

My Thesis work could be expanded along different lines of research to reach a more complete understanding of baryon cycle in galaxies. Below, I outline potential future directions that could yield to a more comprehensive understanding of the processes involved.

- **Impact of numerical resolution on the results**. This remains an important aspect to explore. While the simulations presented in this work achieve relatively high gas mass resolution (10^4 $M_\odot$), key quantities like gas accretion rates may still be affected by numerical diffusion, potentially leading to resolution-dependent results (e.g. Armillotta et al., 2016). A detailed convergence study is necessary to assess the robustness of inflow properties, requiring simulations at multiple resolutions. A critical issue is the mixing of gas phases, which is influenced by unresolved small-scale physics, affecting inflow structure and efficiency. Higher resolutions could improve phase separation and inflow realism. Previous *SMUGGLE* model tests (Marinacci et al., 2019) suggest that global galaxy properties remain largely unaffected by resolution, but the behavior of gas inflows and mixing processes still needs verification.

- **Inclusion of black hole feedback**. The most straightforward progress would be the implementation of Active Galactic Nuclei (AGN) feedback in my simulations. While an implementation of AGN feedback is already available for *SMUGGLE* (Sivasankaran et al., 2022), its effects on the CGM have not been investigated in detail yet. Therefore, simulations with a central supermassive black hole and the associated AGN feedback can be run. Indeed, this type of feedback can influence the accretion dynamics of the galactic corona by providing a source of heat for the coronal gas in the central regions of the galaxy, potentially decreasing gas accretion and star formation in the center.

- **Changing galaxy properties**. Galaxies with different masses will be considered to explore the effect of the initial coronal temperature on its accretion onto the disc. Indeed, the total mass of the galaxy determines the temperature of the corona. So, since more massive galaxies have hotter coronae, the condensation and accretion of the coronal gas onto the disc may become more difficult (Armillotta et al., 2016). This could explain the dichotomy between spiral and elliptical galaxies, at a higher temperature the disc-corona interaction mediated by galactic fountains become inefficient, effectively quenching the star formation in the disc. Galaxies with different masses could be selected from cosmological simulations, following the method outlined in Chapter 6, in this way a realistic CGM will be associated with each galaxy.

- **Inclusion of additional physics**. Magnetic fields will be included, that could lead to a different dynamics of gas and have an effect on the star formation efficiency and feedback. Also, thermal conduction will be added because the strong temperature gradients between the fountain clouds and the CGM make it an extremely important process (Armillotta et al., 2016). Theoretically, thermal conduction could be suppressed by the presence of magnetic fields (Kooij et al., 2021), which can reduce the mean free path of the electrons (that transfer most of the heat flux). Studying the effective range of suppression will be an important step for understanding the effective accretion rate of coronal gas.

This project thus provides a crucial step toward a deeper understanding of the complex baryon cycle in star-forming galaxies like the Milky Way. By incorporating additional physical processes and refined parameters, this framework not only offers a coherent picture of the formation and evolution of such galaxies but also opens avenues for future studies to explore galaxy evolution across a diverse range of galactic environments and masses. Ultimately, these insights could help bridge the gap between simulated and observed galaxy properties, advancing our grasp of the dynamic interplay between the CGM and galactic discs and how it fuels, regulates, or quenches star formation across cosmic time.

Bibliography

Ackermann M., et al., 2014, ApJ, 793, 64

Afruni A., Pezzulli G., Fraternali F., 2022, MNRAS, 509, 4849

Agertz O., Teyssier R., Moore B., 2011, MNRAS, 410, 1391

Agertz O., Kravtsov A. V., Leitner S. N., Gnedin N. Y., 2013, ApJ, 770, 25

Alibés A., Labay J., Canal R., 2001, A&A, 370, 1103

Alzate J. A., Bruzual G., Díaz-González D. J., 2021, MNRAS, 501, 302

Anderson M. E., Bregman J. N., 2010, ApJ, 714, 320

Anderson M. E., Bregman J. N., 2011, ApJ, 737, 22

Anderson M. E., Churazov E., Bregman J. N., 2016, MNRAS, 455, 227

Anderson L. D., Luisi M., Liu B., Linville D. J., Benjamin R. A., Hurley-Walker N., McClure-Griffiths N. M., Zucker C., 2024, ApJ, 969, 43

Armillotta L., Fraternali F., Marinacci F., 2016, MNRAS, 462, 4157

Asplund M., Grevesse N., Sauval A. J., Scott P., 2009, ARA&A, 47

Bahcall J. N., Soneira R. M., 1980, ApJS, 44, 73

Baldry I. K., Balogh M. L., Bower R., Glazebrook K., Nichol R. C., Bamford S. P., Budavari T., 2006, Monthly Notices of the Royal Astronomical Society, 373, 469

Balsara D. S., 2004, ApJS, 151, 149

Barbani F., Pascale R., Marinacci F., Sales L. V., Vogelsberger M., Torrey P., Li H., 2023, MNRAS, 524, 4091

Barbani F., Torrey P., Rose J. C., Marinacci F., Pascale R., Sales L. V., Li H., Vogelsberger M., 2025a, A&A

Barbani F., Pascale R., Marinacci F., Torrey P., Sales L. V., Li H., Vogelsberger M., 2025b, A&A

Barnes J., Hut P., 1986, Nature, 324, 446

Beane A., et al., 2023, ApJ, 953, 173

Bernard E. J., 2017, Proceedings of the International Astronomical Union, 13, 158–161

Bertelli G., Nasi E., Girardi L., Marigo P., 2009, A&A, 508, 355

Besla G., Kallivayalil N., Hernquist L., van der Marel R. P., Cox T. J., Kereš D., 2012, MNRAS, 421, 2109

Bhowmick A. K., et al., 2024, MNRAS, 533, 1907

Binney J., Tremaine S., 2008, Galactic Dynamics: Second Edition

Binney J., Tremaine S., 2011, Galactic dynamics. Princeton university press

Binney J., Nipoti C., Fraternali F., 2009, MNRAS, 397, 1804

Bland-Hawthorn J., Cohen M., 2003, ApJ, 582, 246

Bland-Hawthorn J., et al., 2019, ApJ, 886, 45

Bode P., Ostriker J. P., 2003, ApJS, 145, 1

Bode P., Ostriker J. P., Xu G., 2000, ApJS, 128, 561

Bogdán Á., Forman W. R., Kraft R. P., Jones C., 2013, ApJ, 772, 98

Bogdán Á., et al., 2015, ApJ, 804, 72

Bogdán Á., Bourdin H., Forman W. R., Kraft R. P., Vogelsberger M., Hernquist L., Springel V., 2017, ApJ, 850, 98

Bolatto A. D., et al., 2013, Nature, 499, 450

Bolatto A. D., et al., 2021, ApJ, 923, 83

Bordoloi R., et al., 2011, ApJ, 743, 10

Boselli A., Fossati M., Sun M., 2022, A&A Rev., 30, 3

Bowen D. V., Chelouche D., Jenkins E. B., Tripp T. M., Pettini M., York D. G., Frye B. L., 2016, ApJ, 826, 50

Box G. E. P., Muller M. E., 1958, The Annals of Mathematical Statistics, 29, 610

Bregman J. N., Anderson M. E., Miller M. J., Hodges-Kluck E., Dai X., Li J.-T., Li Y., Qu Z., 2018, ApJ, 862, 3

Brooks A. M., et al., 2011, ApJ, 728, 51

Burchett J. N., Rubin K. H. R., Prochaska J. X., Coil A. L., Vaught R. R., Hennawi J. F., 2021, ApJ, 909, 151

Burger J. D., Zavala J., Sales L. V., Vogelsberger M., Marinacci F., Torrey P., 2022, MNRAS, 513, 3458

Burrows A., Vartanyan D., 2021, Nature, 589, 29

Castrillo A., et al., 2021, MNRAS, 501, 3122

Cavaliere A., Fusco-Femiano R., 1978, A&A, 70, 677

Cen R., 1992, ApJS, 78, 341

Chabrier G., 2003, PASP, 115, 763

Chiappini C., Matteucci F., Romano D., 2001, ApJ, 554, 1044

Chisholm J., Tremonti C. A., Leitherer C., Chen Y., Wofford A., Lundgren B., 2015, ApJ, 811, 149

Chomiuk L., Povich M. S., 2011, AJ, 142, 197

Cignoni M., Degl'Innocenti S., Prada Moroni P. G., Shore S. N., 2006, A&A, 459, 783

Cimatti A., Fraternali F., Nipoti C., 2019, Introduction to Galaxy Formation and Evolution: From Primordial Gas to Present-Day Galaxies. Cambridge University Press

Cioffi D. F., McKee C. F., Bertschinger E., 1988, ApJ, 334, 252

Ciotti L., Ostriker J. P., 1997, ApJ, 487, L105

Cohen M., Kuhi L. V., 1979, ApJS, 41, 743

Colavitti E., Matteucci F., Murante G., 2008, A&A, 483, 401

Colella P., Woodward P. R., 1984, Journal of Computational Physics, 54, 174

Conselice C. J., Mundy C. J., Ferreira L., Duncan K., 2022, ApJ, 940, 168

Cooper T. J., et al., 2021, MNRAS, 508, 4359

Courant R., Friedrichs K., Lewy H., 1967, IBM journal of Research and Development, 11, 215

Courteau S., de Jong R. S., Broeils A. H., 1996, ApJ, 457, L73

Dahlen T., et al., 2004, ApJ, 613, 189

Dai W., Woodward P. R., 1994, Journal of Computational Physics, 115, 485

Dai X., Anderson M. E., Bregman J. N., Miller J. M., 2012, ApJ, 755, 107

Das S., Mathur S., Gupta A., 2020, ApJ, 897, 63

De Jong R. S., Davies R. L., 1997, Monthly Notices of the Royal Astronomical Society, 285, L1

Dekel A., Birnboim Y., 2006, MNRAS, 368, 2

Di Teodoro E. M., Peek J. E. G., 2021, ApJ, 923, 220

Di Teodoro E. M., McClure-Griffiths N. M., Lockman F. J., Denbo S. R., Endsley R., Ford H. A., Harrington K., 2018, ApJ, 855, 33

Dobler G., Finkbeiner D. P., Cholis I., Slatyer T., Weiner N., 2010, ApJ, 717, 825

Duffell P. C., MacFadyen A. I., 2011, ApJS, 197, 15

Eastwood J., Hockney R., 1981, New York: Mc GrawHill

Ebeling H., Kalita B. S., 2019, ApJ, 882, 127

Efstathiou G., 1992, MNRAS, 256, 43P

Egorov O. V., Lozinskaya T. A., Moiseev A. V., Shchekinov Y. A., 2017, MNRAS, 464, 1833

Elia D., et al., 2022, ApJ, 941, 162

Faucher-Giguere C.-A., Lidz A., Zaldarriaga M., Hernquist L., 2009, ApJ, 703, 1416

Ferland G., Korista K., Verner D., Ferguson J., Kingdon J., Verner E., 1998, Publications of the Astronomical Society of the Pacific, 110, 761

Ferriere K. M., 2001, Reviews of Modern Physics, 73, 1031

Field G., Goldsmith D., Habing H., 1969, ApJ, 155, L149

Fielding D. B., Bryan G. L., 2022, ApJ, 924, 82

Firmani C., Avila-Reese V., 2009, MNRAS, 396, 1675

Foreman-Mackey D., Hogg D. W., Lang D., Goodman J., 2013, PASP, 125, 306

Fraser-McKelvie A., Merrifield M., Aragón-Salamanca A., 2019, MNRAS, 489, 5030

Fraternali F., 2014, in IAU Symposium. pp 228–239

Fraternali F., Binney J. J., 2006, MNRAS, 366, 449

Fraternali F., Binney J. J., 2008, MNRAS, 386, 935

Freeman K. C., 1970, ApJ, 160, 811

Fukugita M., Peebles P., 2006, ApJ, 639, 590

GRAVITY Collaboration et al., 2019, A&A, 625, L10

Gatto A., Fraternali F., Read J. I., Marinacci F., Lux H., Walch S., 2013, MNRAS, 433, 2749

Genel S., et al., 2014, MNRAS, 445, 175

Gingold R. A., Monaghan J. J., 1977, MNRAS, 181, 375

Gnedin N. Y., Hollon N., 2012, ApJS, 202, 13

Godunov S. K., 1959, Math. Sbornik, 47, 271

Goldbaum N. J., Krumholz M. R., Forbes J. C., 2016, ApJ, 827, 28

Gómez F. A., White S. D. M., Grand R. J. J., Marinacci F., Springel V., Pakmor R., 2017, MNRAS, 465, 3446

Grand R. J. J., et al., 2017, MNRAS, 467, 179

Grcevich J., Putman M. E., 2009, ApJ, 696, 385

Greengard L., Rokhlin V., 1987, Journal of Computational Physics, 73, 325

Greggio L., 2005, Astronomy & Astrophysics, 441, 1055

Gronke M., Oh S. P., Ji S., Norman C., 2022, MNRAS, 511, 859

Grudić M. Y., Guszejnov D., Hopkins P. F., Lamberts A., Boylan-Kolchin M., Murray N., Schmitz D., 2018, MNRAS, 481, 688

Guo F., Oh S. P., 2008, MNRAS, 384, 251

Gupta A., Mathur S., Krongold Y., Nicastro F., Galeazzi M., 2012, ApJ, 756, L8

Gutcke T. A., 2024, ApJ, 971, 103

Habing H., 1968, Bull. Astron. Inst. Netherlands, 19, 421

Hahn O., Abel T., 2011, MNRAS, 415, 2101

Haywood M., 2014, Mem. Soc. Astron. Italiana, 85, 253

Heckman T. M., Alexandroff R. M., Borthakur S., Overzier R., Leitherer C., 2015, ApJ, 809, 147

Herbig G. H., 1962, in , Vol. 1, Advances in Astronomy and Astrophysics. Elsevier, pp 47–103

Hernquist L., 1990, ApJ, 356, 359

Hernquist L., 1993, ApJS, 86, 389

Hinshaw G., et al., 2013, ApJS, 208, 19

Hobbs A., Feldmann R., 2020, MNRAS, 498, 1140

Hodges-Kluck E. J., Bregman J. N., 2013, ApJ, 762, 12

Hopkins P. F., 2015, MNRAS, 450, 53

Hopkins P. F., Grudić M. Y., 2019, MNRAS, 483, 4187

Hopkins P. F., Quataert E., 2011, MNRAS, 415, 1027

Hopkins P. F., et al., 2018, MNRAS, 480, 800

Howard C. S., Pudritz R. E., Harris W. E., 2016, MNRAS, 461, 2953

Hubble E. P., 1926, ApJ, 64, 321

Hubble E. P., 1936, Realm of the Nebulae

Ikeuchi S., Ostriker J., 1986, ApJ, 301, 522

Isern J., 2019, ApJ, 878, L11

Jacob S., Pakmor R., Simpson C. M., Springel V., Pfrommer C., 2018, MNRAS, 475, 570

Jahn E. D., et al., 2021, MNRAS, p. arXiv:2110.00142

Janhunen P., 2000, Journal of Computational Physics, 160, 649

Jenkins E. B., Tripp T. M., 2001, ApJS, 137, 297

Ji J., Irwin J. A., Athey A., Bregman J. N., Lloyd-Davies E. J., 2009, ApJ, 696, 2252

Kaaret P., et al., 2020, Nature Astronomy, 4, 1072

Kannan R., Marinacci F., Vogelsberger M., Sales L. V., Torrey P., Springel V., Hernquist L., 2020, MNRAS, 499, 5732

Kannan R., Vogelsberger M., Marinacci F., Sales L. V., Torrey P., Hernquist L., 2021, MNRAS, 503, 336

Karakas A. I., 2010, MNRAS, 403, 1413

Katz N., Weinberg D. H., Hernquist L., 1996, ApJS, 105, 19

Kereš D., Katz N., Fardal M., Davé R., Weinberg D. H., 2009, MNRAS, 395, 160

Kim C.-G., Ostriker E. C., 2018, ApJ, 853, 173

Kim J.-h., et al., 2014, ApJS, 210, 14

Kim J.-G., Kim W.-T., Ostriker E. C., 2019, ApJ, 883, 102

Kim C.-G., et al., 2020, ApJ, 900, 61

Kong S., Smith R. J., Whitworth D., Hamden E. T., 2024, arXiv e-prints, p. arXiv:2408.14417

Kooij R., Grønnow A., Fraternali F., 2021, MNRAS, 502, 1263

Krumholz M. R., Matzner C. D., 2009, ApJ, 703, 1352

Krumholz M. R., Tan J. C., 2007, ApJ, 654, 304

Lacey C. G., Fall S. M., 1985, ApJ, 290, 154

Larson R. B., 1972, Nature Physical Science, 236, 7

Lee J. C., et al., 2023, ApJ, 944, L17

Lehner N., Howk J. C., 2010, ApJ, 709, L138

Lehner N., Howk J. C., Wakker B. P., 2015, ApJ, 804, 79

Lehner N., Howk J. C., Marasco A., Fraternali F., 2022, MNRAS, 513, 3228

Lehnert M. D., Heckman T. M., Weaver K. A., 1999, ApJ, 523, 575

Lemasle B., et al., 2018, A&A, 618, A160

Leroy A. K., et al., 2015, ApJ, 814, 83

Li J.-T., Li Z., Wang Q. D., Irwin J. A., Rossa J., 2008, MNRAS, 390, 59

Li Z., et al., 2011, ApJ, 730, 84

Li H., Vogelsberger M., Marinacci F., Sales L. V., Torrey P., 2020, MNRAS, 499, 5862

Li H., Vogelsberger M., Bryan G. L., Marinacci F., Sales L. V., Torrey P., 2022, MNRAS, 514, 265

Li A., Fraternali F., Marasco A., Trager S. C., Pezzulli G., Mancera Piña P. E., Verheijen M. A., 2023, MNRAS, 520, 147

Licquia T. C., Newman J. A., 2015, ApJ, 806, 96

Liu Z.-W., Röpke F. K., Han Z., 2023, Research in Astronomy and Astrophysics, 23, 082001

Liu W., et al., 2024, MNRAS, 531, 2063

Lochhaas C., Bryan G. L., Li Y., Li M., Fielding D., 2020, MNRAS, 493, 1461

Lockman F. J., Di Teodoro E. M., McClure-Griffiths N. M., 2020, ApJ, 888, 51

Lopez L. A., Krumholz M. R., Bolatto A. D., Prochaska J. X., Ramirez-Ruiz E., 2011, ApJ, 731, 91

Lopez L. A., Mathur S., Nguyen D. D., Thompson T. A., Olivier G. M., 2020, ApJ, 904, 152

Lucy L. B., 1977, AJ, 82, 1013

Mannucci F., Della Valle M., Panagia N., 2006, MNRAS, 370, 773

Maoz D., Mannucci F., Brandt T. D., 2012, MNRAS, 426, 3282

Marasco A., Fraternali F., Binney J. J., 2012, MNRAS, 419, 1107

Marasco A., Fraternali F., Lehner N., Howk J. C., 2022, MNRAS, 515, 4176

Marinacci F., Binney J., Fraternali F., Nipoti C., Ciotti L., Londrillo P., 2010, MNRAS, 404, 1464

Marinacci F., Fraternali F., Nipoti C., Binney J., Ciotti L., Londrillo P., 2011, MNRAS, 415, 1534

Marinacci F., Grand R. J. J., Pakmor R., Springel V., Gómez F. A., Frenk C. S., White S. D. M., 2017, MNRAS, 466, 3859

Marinacci F., et al., 2018, MNRAS, 480, 5113

Marinacci F., Sales L. V., Vogelsberger M., Torrey P., Springel V., 2019, MNRAS, 489, 4233

Martini P., Leroy A. K., Mangum J. G., Bolatto A., Keating K. M., Sandstrom K., Walter F., 2018, ApJ, 856, 61

Martizzi D., Faucher-Giguère C.-A., Quataert E., 2015, MNRAS, 450, 504

Martizzi D., Fielding D., Faucher-Giguère C.-A., Quataert E., 2016, MNRAS, 459, 2311

Martynenko N., 2022, MNRAS, 511, 843

Matteucci F., Francois P., 1989, MNRAS, 239, 885

Matzner C. D., 2002, ApJ, 566, 302

Mayor M., Vigroux L., 1981, A&A, 98, 1

McClure-Griffiths N. M., Green J. A., Hill A. S., Lockman F. J., Dickey J. M., Gaensler B. M., Green A. J., 2013, ApJ, 770, L4

McQuinn M., 2016, ARA&A, 54, 313

Miller M. J., Bregman J. N., 2013, ApJ, 770, 118

Mo H., Mao S., White S. D., 1998, MNRAS, 295, 319

Monachesi A., Gómez F. A., Grand R. J. J., Kauffmann G., Marinacci F., Pakmor R., Springel V., Frenk C. S., 2016, MNRAS, 459, L46

Monaghan J. J., Lattanzio J. C., 1985, A&A, 149, 135

Mor R., Robin A. C., Figueras F., Roca-Fàbrega S., Luri X., 2019, A&A, 624, L1

Morganti R., et al., 2006, Monthly Notices of the Royal Astronomical Society, 371, 157

Moster B. P., Macciò A. V., Somerville R. S., Naab T., Cox T. J., 2011, MNRAS, 415, 3750

Mott A., Spitoni E., Matteucci F., 2013, MNRAS, 435, 2918

Muñoz D. J., Kratter K., Springel V., Hernquist L., 2014, MNRAS, 445, 3475

Murray N., Quataert E., Thompson T. A., 2009, ApJ, 709, 191

Murray N., Quataert E., Thompson T. A., 2010, ApJ, 709, 191

Naiman J. P., et al., 2018, MNRAS, 477, 1206

Navarro J. F., Frenk C. S., White S. D., 1997, ApJ, 490, 493

Nelson D., Vogelsberger M., Genel S., Sijacki D., Kereš D., Springel V., Hernquist L., 2013, MNRAS, 429, 3353

Nelson D., et al., 2018, MNRAS, 475, 624

Nipoti C., 2010, MNRAS, 406, 247

Nobels F. S. J., Schaye J., Schaller M., Ploeckinger S., Chaikin E., Richings A. J., 2024, MNRAS, 532, 3299

Ocvirk P., Pichon C., Teyssier R., 2008, MNRAS, 390, 1326

Oppenheimer B. D., Davé R., Kereš D., Fardal M., Katz N., Kollmeier J. A., Weinberg D. H., 2010, MNRAS, 406, 2325

Owocki S., 2013, in Oswalt T. D., Barstow M. A., eds, , Vol. 4, Planets, Stars and Stellar Systems. Volume 4: Stellar Structure and Evolution. p. 735, doi:10.1007/978-94-007-5615-1_15

Pakmor R., Kromer M., Taubenberger S., Springel V., 2013, ApJ, 770, L8

Pakmor R., Springel V., Bauer A., Mocz P., Munoz D. J., Ohlmann S. T., Schaal K., Zhu C., 2016, MNRAS, 455, 1134

Pandya V., et al., 2021, MNRAS, 508, 2979

Pascale R., Bellazzini M., Tosi M., Annibali F., Marinacci F., Nipoti C., 2021, MNRAS, 501, 2091

Pawlik A. H., Schaye J., 2008, MNRAS, 389, 651

Peek J. E. G., Putman M. E., Sommer-Larsen J., 2008, ApJ, 674, 227

Peek J. E. G., Ménard B., Corrales L., 2015, ApJ, 813, 7

Peng Y.-j., et al., 2010, The Astrophysical Journal, 721, 193

Pezzulli G., Fraternali F., 2016, MNRAS, 455, 2308

Pillepich A., et al., 2018, MNRAS, 475, 648

Planck Collaboration et al., 2020, A&A, 641, A6

Ponti G., et al., 2019, Nature, 567, 347

Portinari L., Salucci P., 2010, A&A, 521, A82

Portinari L., Chiosi C., Bressan A., 1998, A&A, 334, 505

Privatus P., Goswami U. D., 2025, Physics of the Dark Universe, 47, 101802

Prochaska J. X., et al., 2017, ApJ, 837, 169

Putman M. E., Peek J. E. G., Joung M. R., 2012, ARA&A, 50, 491

Putman M. E., Zheng Y., Price-Whelan A. M., Grcevich J., Johnson A. C., Tollerud E., Peek J. E. G., 2021, ApJ, 913, 53

Rahmati A., Pawlik A. H., Raičević M., Schaye J., 2013, MNRAS, 430, 2427

Rasmussen J., Sommer-Larsen J., Pedersen K., Toft S., Benson A., Bower R. G., Grove L. F., 2009, ApJ, 697, 79

Rauch M., Haehnelt M. G., 2011, MNRAS, 412, L55

Rees M. J., Ostriker J. P., 1977, MNRAS, 179, 541

Reyes-Iturbide J., Rosado M., Rodríguez-González A., Velázquez P. F., Sánchez-Cruces M., Ambrocio-Cruz P., 2014, AJ, 148, 102

Rickard M. J., et al., 2022, A&A, 666, A189

Roediger E., Hensler G., 2005, A&A, 433, 875

Röhser T., Kerp J., Lenz D., Winkel B., 2016, A&A, 596, A94

Rosen A. L., Krumholz M. R., McKee C. F., Klein R. I., 2016, MNRAS, 463, 2553

Rubin K. H. R., Weiner B. J., Koo D. C., Martin C. L., Prochaska J. X., Coil A. L., Newman J. A., 2010, ApJ, 719, 1503

Rubin K. H. R., Hennawi J. F., Prochaska J. X., Simcoe R. A., Myers A., Lau M. W., 2015, ApJ, 808, 38

Ruszkowski M., Yang H. Y. K., Zweibel E., 2014, in Sjouwerman L. O., Lang C. C., Ott J., eds, IAU Symposium Vol. 303, The Galactic Center: Feeding and Feedback in a Normal Galactic Nucleus. pp 390–394 (arXiv:1311.6159), doi:10.1017/S1743921314000994

Rybicki G. B., Lightman A. P., 1991, Radiative processes in astrophysics. John Wiley & Sons

Ryu D., Jones T., 1995, ApJ, 442, 228

Ryu D., Jones T., Frank A., 1995, ApJ, 452, 785

Saintonge A., et al., 2013, ApJ, 778, 2

Salem M., Besla G., Bryan G., Putman M., van der Marel R. P., Tonnesen S., 2015, ApJ, 815, 77

Salpeter E. E., 1955, ApJ, 121, 161

Sameer et al., 2024, MNRAS,

Scannapieco C., Tissera P. B., White S., Springel V., 2005, MNRAS, 364, 552

Schawinski K., et al., 2014, Monthly Notices of the Royal Astronomical Society, 440, 889

Schmidt T. M., Bigiel F., Klessen R. S., de Blok W. J. G., 2016, MNRAS, 457, 2642

Semenov V. A., Kravtsov A. V., Gnedin N. Y., 2017, ApJ, 845, 133

Shapiro P. R., Field G. B., 1976, ApJ, 205, 762

Sharda P., Ginzburg O., Krumholz M. R., Forbes J. C., Wisnioski E., Mingozzi M., Zovaro H. R. M., Dekel A., 2024, MNRAS, 528, 2232

Silk J., 1977, ApJ, 211, 638

Sivasankaran A., et al., 2022, MNRAS, 517, 4752

Smith B., Sigurdsson S., Abel T., 2008, MNRAS, 385, 1443

Smith R. J., Glover S. C. O., Clark P. C., Klessen R. S., Springel V., 2014, MNRAS, 441, 1628

Smith A., et al., 2022, MNRAS, 517, 1

Sofue Y., Handa T., 1984, Nature, 310, 568

Sormani M. C., Sobacchi E., 2019, MNRAS, 486, 215

Spitoni E., Calura F., Silva Aguirre V., Gilli R., 2021, A&A, 648, L5

Spitzer Jr L., 1942, ApJ, 95, 329

Spitzer Jr L., Baade W., 1951, The Astrophysical Journal, 113, 413

Springel V., 2000, MNRAS, 312, 859

Springel V., 2005, MNRAS, 364, 1105

Springel V., 2010a, ARA&A, 48, 391

Springel V., 2010b, MNRAS, 401, 791

Springel V., 2016a, in , Star Formation in Galaxy Evolution: Connecting Numerical Models to Reality. Springer, pp 251–358

Springel V., 2016b, Saas-Fee Advanced Course, 43, 251

Springel V., Hernquist L., 2003, MNRAS, 339, 289

Springel V., White S. D. M., 1999, MNRAS, 307, 162

Springel V., Di Matteo T., Hernquist L., 2005, MNRAS, 361, 776

Springel V., et al., 2018, MNRAS, 475, 676

Springel V., Pakmor R., Zier O., Reinecke M., 2021, MNRAS, 506, 2871

Steinmetz M., Müller E., 1994, A&A, 281, L97

Stern J., Fielding D., Faucher-Giguère C.-A., Quataert E., 2019, MNRAS, 488, 2549

Stern J., Fielding D., Faucher-Giguère C.-A., Quataert E., 2020, MNRAS, 492, 6042

Stinson G. S., Brook C., Macciò A. V., Wadsley J., Quinn T. R., Couchman H. M. P., 2013, MNRAS, 428, 129

Strickland D. K., Heckman T. M., 2007, ApJ, 658, 258

Strolger L.-G., et al., 2004, ApJ, 613, 200

Su M., Slatyer T. R., Finkbeiner D. P., 2010, ApJ, 724, 1044

Tacconi L. J., et al., 2018, ApJ, 853, 179

Thielemann F.-K., et al., 2003, Nuclear Physics A, 718, 139

Thilker D. A., et al., 2023, ApJ, 944, L13

Tielens A. G., 2005, The physics and chemistry of the interstellar medium. Cambridge University Press

Toro E. F., 2013, Riemann solvers and numerical methods for fluid dynamics: a practical introduction. Springer Science & Business Media

Toro E. F., Spruce M., Speares W., 1994, Shock waves, 4, 25

Tosi M., 1988, A&A, 197, 47

Trapp C. W., et al., 2022, MNRAS, 509, 4149

Travaglio C., Hillebrandt W., Reinecke M., Thielemann F.-K., 2004, A&A, 425, 1029

Troitsky S., 2017, MNRAS, 468, L36

Tumlinson J., et al., 2011, Science, 334, 948

Tumlinson J., Peeples M. S., Werk J. K., 2017, ARA&A, 55, 389

Twarog B. A., 1980, ApJ, 242, 242

Van Der Kruit P., Searle L., 1981, A&A, 95, 105

Vandenbroucke B., De Rijcke S., 2016, Astronomy and Computing, 16, 109

Veilleux S., Maiolino R., Bolatto A. D., Aalto S., 2020, A&A Rev., 28, 2

Vogelsberger M., Sijacki D., Kereš D., Springel V., Hernquist L., 2012, MNRAS, 425, 3024

Vogelsberger M., Genel S., Sijacki D., Torrey P., Springel V., Hernquist L., 2013, MNRAS, 436, 3031

Vogelsberger M., et al., 2014, MNRAS, 444, 1518

Wakker B. P., van Woerden H., 1997, ARA&A, 35, 217

Walch S., Whitworth A., Bisbas T., Wünsch R., Hubber D., 2012, MNRAS, 427, 625

Wang J., et al., 2014, MNRAS, 441, 2159

Ward Thompson D., André P., Kirk J., 2002, MNRAS, 329, 257

Ward S. R., Costa T., Harrison C. M., Mainieri V., 2024, MNRAS, 533, 1733

Watkins E. J., et al., 2023, ApJ, 944, L24

Weinberger R., Springel V., Pakmor R., 2020, ApJS, 248, 32

Weldon A., et al., 2024, arXiv e-prints, p. arXiv:2404.05725

Werk J. K., et al., 2014, ApJ, 792, 8

White S. D. M., Rees M. J., 1978, MNRAS, 183, 341

Wiersma R. P., Schaye J., Theuns T., Dalla Vecchia C., Tornatore L., 2009, MNRAS, 399, 574

Wolfire M. G., Hollenbach D., McKee C. F., Tielens A., Bakes E., 1995, ApJ, 443, 152

Wolfire M. G., McKee C. F., Hollenbach D., Tielens A., 2003, ApJ, 587, 278

Wong T., Blitz L., Bosma A., 2004, ApJ, 605, 183

Woosley S. E., Weaver T. A., 1986, ARA&A, 24, 205

Yao Y., Shull J. M., Wang Q. D., Cash W., 2012, ApJ, 746, 166

York D. G., et al., 2000, The Astronomical Journal, 120, 1579

Zachary A. L., Colella P., 1992, Journal of Computational Physics, 99, 341

Zhang X., Buta R. J., 2012, arXiv e-prints, p. arXiv:1203.5334

Zhang E., et al., 2024a, arXiv e-prints, p. arXiv:2406.10338

Zhang Z., et al., 2024b, ApJ, 962, 15

Ziegler U., 2004, Journal of Computational Physics, 196, 393

van den Bergh S., 1962, AJ, 67, 486